UNIVERSITY OF TRENTO

DEPARTMENT OF PHYSICS

DOCTORAL THESIS

DISSOCIATIVE CHARGE TRANSFER OF ORGANIC MOLECULES INDUCED BY COLLISIONS WITH THE He^+ CATION. A JOINT EXPERIMENTAL AND THEORETICAL STUDY OF RELEVANCE FOR THE INTERSTELLAR MEDIUM EVOLUTION

Author:
Andrea CERNUTO

Tutor:
Daniela ASCENZI
Co-Tutor:
Paolo TOSI

XXX PhD Cycle

"Now many moons and many Junes,
Have passed since we made land.
A Salty Dog, the seaman's log,
Your witness, my own hand."

A Salty Dog - Procol Harum

Abstract

Collisions with He^+ are an important pathway for the destruction of complex organic molecules in the interstellar medium (ISM). We have carried out dissociative charge transfer reactions of He^+ with two oxygen containing organic molecules, ubiquitous in ISM: dimethyl ether (DME, CH_3OCH_3) and methyl formate (MF, $HCOOCH_3$). Since they have a prebiotic relevance, several models were developed to explain how these molecules are formed and destroyed in the ISM.

The reactions have been investigated by using the home-built Guided-Ion Beam Mass Spectrometer (GIB-MS) apparatus. Absolute cross sections and branching ratios of the products have been measured as a function of the collision energy in the hyperthermal energy range (i.e. from about $0.1\,\mathrm{eV}$ to $7\,\mathrm{eV}$). The presence of the molecular ion was not observed among the products for these reactions, which means that the nascent DME and MF radical cations are formed in a dissociative state. Insights on both the charge transfer processes have been obtained by investigating the nature of the non-adiabatic transitions between the reactant and product potential energy surfaces (PES). The PES has been represented by using a semi-empirical method to model the inter-molecular interactions. To explain the experimental evidence, two excited states of DME and MF radical cations have been invoked: He^+ captures an electron from inner valence orbitals of both the organic molecules, having binding energies $\sim 10\,\mathrm{eV}$ higher than the HOMO. An improved Landau-Zener-Stückelberg model has been developed to obtain the total integral cross-section to be compared with the experimental results. Inter-molecular interaction and electron densities of the orbitals involved in the reaction turned out to be key points to describe the dynamics of the two studied dissociative charge transfers. A very good agreement is obtained between the experimental and calculated total cross-sections at low collision energy, which is the most relevant range for the interstellar environment. These results represent a significant starting point to estimate rate constants for the total dissociation of DME and MF by collisions with He^+ ions in the ISM at low temperatures.

Contents

List of Abbreviations

AO	**A**tomic **O**rbital
B68	**B**arnard68
BO	**B**orn-**O**ppenheimer
BR	**B**ranching **R**atio
cc-pVTZ	**C**orrelation-**C**onsistent **P**olarized **V**alence **T**riple **Z**eta
cc-pVQZ	**C**orrelation-**C**onsistent **P**olarized **V**alence **Q**uadruple **Z**eta
CISD	**C**onfiguration **I**nteraction including **S**ingle and **D**ouble excitations
CM	**C**enter-of-**M**ass
COD	**C**oefficient **O**f **D**etermination
COMs	**C**omplex **O**rganic **M**olecules
CRESU	**C**inétique de **R**éaction en **E**coulement **S**upersonique **U**niforme
DC	**D**irect **C**urrent
DFT	**D**ensity **F**unctional **T**heory
DME	**D**i**M**ethyl **E**ther
EA	**E**lectron **A**ffinity
EI	**E**lectron **I**onization
ESO	**E**uropean **S**outhern **O**bservatory
ECT*	**E**uropean **C**enter for **T**heoretical **S**tudies*
FA	**F**lowing **A**fterglow
FBK	**F**ondazione **Bruno K**essler
GC	**G**as **C**hromatography
GGA	**G**eneralized **G**radient **A**pproximation
GIB-MS	**G**uided **I**on **B**eam-**M**ass **S**pectrometer
HF	**H**artree-**F**ock
h-GGA	**H**ybrid-**G**eneralized **G**radient **A**pproximation
HOMO	**H**ighest **O**ccupied **M**olecular **O**rbital
ICR	**I**on **C**yclotron **R**esonance
I.E.	**I**onization **E**nergy
ILJ	**I**mproved **L**ennard-**J**ones
IP	**I**onization **P**otential
ISM	**I**nter**S**tellar **M**edium
KIDA	**KI**netic **D**atabase for **A**strochemistry
LDA	**L**ocal **D**ensity **A**pproximation
LSDA	**L**ocal **S**pin **D**ensity **A**pproximation
MECP	**M**inimum **E**nergy **C**rossing **P**oint
MF	**M**ethyl **F**ormate

m-GGA	**M**eta-**G**eneralized **G**radient **A**pproximation
MO	**M**olecular **O**rbital
MSE	**M**ean **S**igned **E**rror
MUE	**M**ean **U**nsigned **E**rror
NAO	**N**atural **A**tomic **O**rbital
NBO	**N**atural **B**ond **O**rbital
NIST	**N**ational **I**nstitute of **S**tandards and **T**echnology
O	**O**ctopole
OSU2009	**O**hio **S**tate **U**niversity 2009 Database
PA	**P**roton **A**ffinity
PB	**P**er **B**ond
PE	**P**otential **E**nergy
PES	**P**otential **E**nergy **S**urface
Q	**Q**uadrupole
QMS	**Q**uadrupole **M**ass **S**pectrometer
RF	**R**adio **F**requency
RSS	**R**esidual **S**um of **S**quare
SIFT	**S**elected **I**on **S**ift **F**low **T**ube
TPEPICO	**T**hreshold **P**hoto**E**lectron-**P**hoto**I**onization **CO**incidence spectroscopy
TQDO	**T**riple-**Q**uadrupole **D**ouble-**O**ctopole
TS	**T**ransition **S**tate
TSS	**T**otal **S**um of **S**quare
UMIST	**U**niversity of **M**anchester **I**nstitute of **S**cience and **T**echnology
UV	**U**ltra **V**iolet
VUV	**V**acuum **U**ltra **V**iolet

Chapter 1

Introduction

"Controllori di volo pronti per il decollo
Telescopi giganti per seguire le stelle
Navigare navigare nello spazio nello spazio, di più
Seguimmo per istinto le scie delle Comete
Come Avanguardie di un altro sistema solare."

No Time No Space - F. Battiato

1.1 The Space is not empty

Recent cosmological observations [1, 2] cast light on the composition of the Universe [3]. The 95.4% of its total mass is composed by dark energy and dark matter, and the remaining 4.6% comprises atoms and molecules, which make possible the formation of galaxies, stars and planets. The 98% of the "ordinary matter" (in opposition to the dark matter) is formed by atomic hydrogen and helium with ratios relative to hydrogen nuclei (shown also in Table 1.1) respectively of 1 and 0.085 [4, 5] ($\sim$ 90.3% of the total composition for H and $\sim$ 7.7% for He), while the remaining 2% is the contribution of "heavy" atoms such as carbon, nitrogen and oxygen (relative abundances reported in Table 1.1). Despite their low abundances, these elements control the variety of complex compounds revealed in the Universe. Heavier elements show lower abundances depending on the nucleosynthetic processes occurring in stars. However, the abundances of these elements is lower in the gas-phase and higher in dust grains. In fact, the interstellar matter consists not only of gas but also of dust particles (of typical size around $0.1\,\mu\mathrm{m}$), formed by silicate and carbonaceous compounds. In particular, the dust-to-gas mass ratio is 0.01 in the Solar System, but this ratio can vary among galaxies and even within the Milky Way, our galaxy.

The galaxies are characterized by the presence of "clouds", clumps or filament of interstellar matter. Here, the physical conditions (of densities and temperatures) are extreme, ranging from 10 to $150\,\mathrm{K}$ in temperature and from 1 to $10^6\,\mathrm{cm}^{-3}$ in density and the respective data for some classes of interstellar clouds are reported in Table 1.2 [6]. In particular, it is worth noting the case of the diffuse clouds, in which atomic and molecular hydrogen coexist, but decreasing the temperature the density increases. These clouds, therefore, start to be opaque to interstellar ultraviolet radiation and H_2 becomes the dominant form of hydrogen. In other words, at lower temperatures the diffuse

Table 1.1: Abundances of elements in interstellar matter near the solar neighborhood [4], defined as the space associated with a cylinder centered at the Sun and perpendicular to the Milky Way disk. The atoms are sorted by increasing atomic number. It is worth to note that the abundances of heavier elements correspond to the dust grain abundances, because they tend to exist in dust grains.

Element	Relative Ab.	Element	Relative Ab.
H	1	Si	3.24×10^{-5}
He	0.085	P	2.57×10^{-7}
Li	1.12×10^{-11}	S	1.32×10^{-5}
Be	2.40×10^{-11}	Cl	3.16×10^{-7}
B	5.01×10^{-10}	Ar	2.51×10^{-6}
C	2.69×10^{-3}	K	1.07×10^{-7}
N	6.76×10^{-5}	Ca	2.19×10^{-6}
O	4.90×10^{-4}	Sc	1.41×10^{-9}
F	3.63×10^{-8}	Ti	8.91×10^{-8}
Ne	8.51×10^{-5}	V	8.51×10^{-9}
Na	1.74×10^{-6}	Cr	4.37×10^{-7}
Mg	3.98×10^{-5}	Mn	2.69×10^{-7}
Al	2.82×10^{-6}	Fe	3.16×10^{-5}

Table 1.2: Physical conditions in interstellar clouds [6]. The n_H parameter indicates the volume density of hydrogen nuclei.

Property	Cloud Type		
	Diffuse atomic	Diffuse molecular	Dense molecular
Typical n_H [cm^{-3}]	1-100	100-500	10^4-10^6
Typical T [K]	30-150	30-100	10-50

atomic clouds tend to become diffuse *molecular* clouds, generally considered as formation sites of new stars and cradles of rich molecular chemistry.

Characteristic of the interstellar clouds is that they are weakly ionized and the main causes of ionization are photons and cosmic-rays. In general, the ionization degree for diffuse clouds is high as $\sim 10^{-4}$ because the UV radiation can easily penetrate, while it decreases down to $\sim 10^{-8}$ in dense clouds, where only cosmic rays can contribute. Due to the already mentioned large

number of H atoms (I.E.[1] = 13.598 eV [7]), it is interesting to note that UV radiation with energy higher than 13.60 eV is absent in the interstellar medium (ISM) [3]. Hence, species (such as N, O atoms) with ionization potential higher than that of H atoms escape from photo-ionization, that is efficient only for species with I.E. lower than 13.60 eV (*e.g.* C atom). On the contrary, in molecular clouds where the density is higher, the interstellar UV radiation can not penetrate deeply. This is the reason why photo-dissociation of molecular hydrogen is inefficient in the cloud core and most of the hydrogen is in the H_2 form. These types of clouds are defined "dark" because they can be recognized as black areas obscuring the light of background stars (as the photograph of the dark molecular cloud Barnard 68 shows in Figure 1.1). Since the UV radiation can not contribute to cloud heating in which cosmic-rays play the major role, the gas kinetic temperature in the cloud core (around 10-15 K) is much lower than that of a diffuse cloud (see Table 1.2).

To date, almost 200 molecules up to 12 atoms have been detected [9, 10, 11]. Most of these species have been identified by radio observations of their rotational spectral lines, whereas others by optical or infrared observations of their electronic or vibration-rotational spectra. In this "molecular zoo", it is interesting to note the presence of:

- free radicals or molecular ions, very strong reactive species that can survive for a long time in the ISM thanks to the extreme conditions of the clouds (very low density and temperature);
- large number of unsaturated hydrocarbons (*e.g.* CH_3CCH) despite the ISM conditions dominated by hydrogen;
- ionic species (*e.g.* HCO^+, H_3^+, C_6H^-) allowed by the feature of the clouds to be weakly ionized plasmas;
- complex organic molecules (in astrochemical jargon, the term complex refers to molecules containing at least six atoms [12] and the abbreviation COMs is commonly used), such as $HCOOCH_3$ and CH_3OCH_3 suggesting an unexpected chemical evolution in interstellar clouds despite the extreme physical conditions.

1.2 CH_3OCH_3 and $HCOOCH_3$: an interstellar brotherhood

Among all of the interstellar COMs (defined as organic molecules containing at least six heavy atoms [12]) two noteworthy molecules are dimethyl ether (CH_3OCH_3, DME) and methyl formate ($HCOOCH_3$, MF). These O-bearing molecules can be considered potential building blocks of biological molecules, such as sugars. Therefore, the prebiotic nature of these species evokes a potential connection with the origin of life molecules on the Earth. Their detection in the ISM is of paramount interest [13], opening the discussion on the life formation to the exogenous theory, in which the organic matter should be delivered by meteorites and comets.

The observations show that these two molecules are ubiquitous in the ISM. In fact, hey have been identified in:

- hot cores [14, 15, 16] and hot corinos [17, 18] (characterized by high density, $> 10^6$ cm^{-3}, and high temperatures, 100 - 500 K) associated with high- and low-mass star-forming regions;
- Galactic center cold clouds (T $\sim$ 50 - 200 K and an mean density of 10^4 cm^{-3}) [19, 20];

[1] Ionization Energy

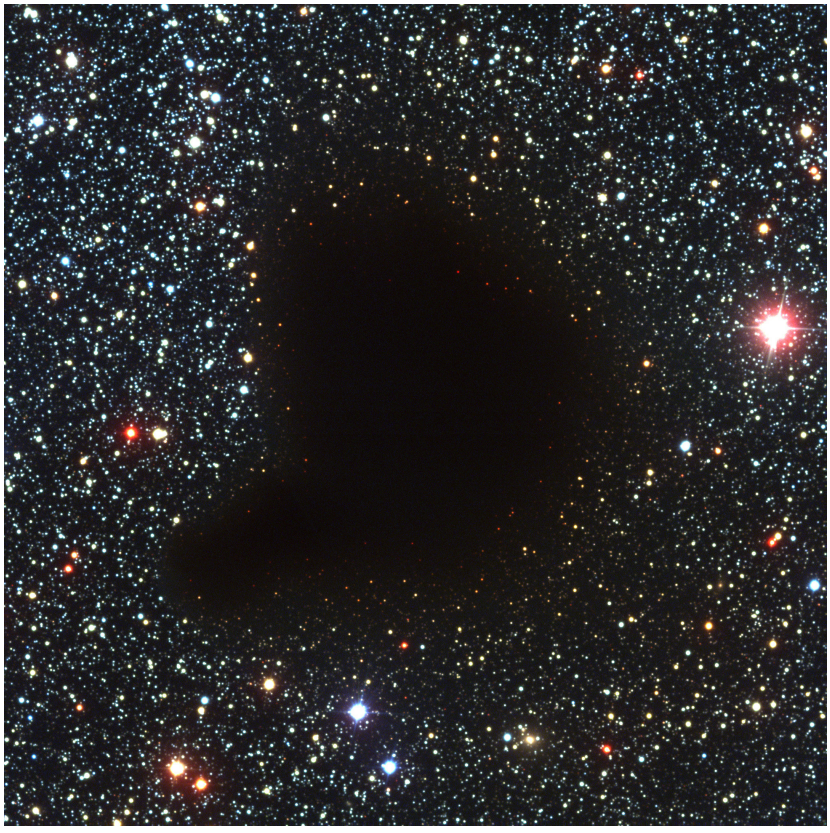

Figure 1.1: Photograph of Barnard 68 (B68), dark molecular cloud that represents very well the case of a compact, opaque and defined object against the background star field (Image Credit: ESO [8]).

- prestellar cores ($T \leq 30$ K) [21, 22, 23, 13, 24].

Abundances with respect to methanol (CH_3OH) for some example of ISM sources are summarized in Table 1.3 [12].

[2]based on [17]
[3]based on [18]
[4]based on [19, 20]
[5]based on [14]
[6]based on [21]

Table 1.3: Abundance ratios of MF ($HCOOCH_3$) and DME (CH_3OCH_3) with respect to CH_3OH are report for some representative ISM sources. Methanol abundances vary between 10^{-7} - 10^{-5} with respect to H_2 [12] .

Species	Low mass		High mass		Pre-stellar Core
	I16293[2]	N13 4A[3]	GC[4]	G327.3[5]	B1-b[6]
MF	0.30	0.56	~ 0.04	0.08	2.3
DME	0.20	< 0.22	~ 0.04	~ 3	≤ 0.8

Furthermore, from the observations of different ISM sources, a linear correlation between MF and DME abundances can be derived, covering almost five orders of magnitude [24]. The correlation implies that the two molecules must have the same precursor or one of the two must be the precursor of the other. This conclusion about a common progenitor has been included recently in astrochemical models.

In particular, the DME and MF detection in colder environments poses a real challenge to determine the origin and abundances of these organic molecules. In fact, in warm and dense regions (such as the high-mass protostars with $T \geqslant 100\,K$ and density higher than $10^6\,cm^{-3}$), the presence of COMs was established by several models [25, 26, 27] in which a "warm" gas-phase chemistry is involved after heating of the ices and the emission in the gas phase of simple hydrogenated molecules (*e.g.* H_2CO, CH_3OH, NH_3). However, observation and experiments suggest that grain-surface chemistry should be the responsible for the formation of most the observed COMs. In this case, radicals trapped in the ices can react and acquire mobility when the dust temperature is around $30\,K$ [28]. On the contrary, in pre-stellar cores, where DME and MF have been recently detected [23, 13], the temperature ($T < 30\,K$) is not sufficient to give mobility to radicals. For this reason, a new model has been formulated according to which DME and MF are formed by gas-phase chemistry starting from the progenitor methoxy radical after desorption of methanol by the ices *via* non-thermal processes [29].

1.3 Chemistry in ISM: the role of He^+ ions

After discoveries of interstellar molecules, the new challenge is which chemical processes are at basis of their production. For this reason, astrochemical networks are developed to interpret *via* numerical simulations the observational data.

Constraints on reactions in interstellar clouds originate from the extreme conditions of the ISM with low temperature (from 10 to $150\,K$) and low density (from 1 to $10^6\,cm^{-3}$) in comparison with the terrestrial ones. First, due to the low density, binary association reactions are not efficient. In fact, considering the reaction:

$$A + B \longrightarrow C \tag{1.1}$$

the excess energy produced by the C formation is not easily discarded by the new molecule, unless a third body takes it away or the molecule spontaneously emits a photon. Since the probability of a collision with a third body is negligible in ISM conditions, the unstable molecule tends to dissociate. This is the case of the molecular hydrogen formation, that requires a gas phase-grain surface process to occur. On the other hand, when surface chemistry is not involved, the most general type of effective binary reactions is:

$$\mathrm{A} + \mathrm{B} \longrightarrow \mathrm{C} + \mathrm{D} \tag{1.2}$$

which gives two or more products, that, moving in opposite directions, can dissipate the redundant energy through their kinetic energy.

Another requirement for interstellar reactions is that they must be exothermic without energy barriers towards the products. In fact, since the kinetic temperature of the gas can be as low as 10-100 K for most cases, endothermic reactions can not proceed, as well as exothermic reactions with an activation barrier sufficiently higher than the thermal energy of the reactants.

The ion-molecule reaction satisfies these conditions and for this reason, it plays a relevant role in producing various molecules. For instance, it is worth noting the reactions of H_3^+, one of the most important species involved in the chemical evolution of the ISM. The life of the trihydrogen cation starts from the ionization of H_2 molecules, formed by association of H atoms adsorbed on the surface of grains, *via* cosmic-rays:

$$\mathrm{H_2} + \text{cosmic rays} \longrightarrow \mathrm{H^+} + \mathrm{H} + \mathrm{e} \tag{1.3}$$

$$\longrightarrow \mathrm{H_2}^+ + \mathrm{e} \tag{1.4}$$

The rate coefficients for H^+, H_2^+ formation are 1.2×10^{-17} and $2.9 \times 10^{-19}\,\mathrm{s}^{-1}$, respectively [3]. The H_2^+ ions can further react with H_2 to give H_3^+ ions:

$$\mathrm{H_2}^+ + \mathrm{H_2} \longrightarrow \mathrm{H_3}^+ + \mathrm{H} \tag{1.5}$$

The H_3^+ chemistry is dominated by proton transfer to other molecules:

$$\mathrm{H_3}^+ + \mathrm{A} \longrightarrow \mathrm{AH}^+ + \mathrm{H_2} \tag{1.6}$$

This type of reactions proceed very efficiently if the proton affinity of A is larger than that of H_2. More complex molecules can be therefore formed from AH^+ species.

Besides formation processes also the destruction (unconventional term of the astrophysical jargon that refers to the complete dissociation/fragmentation of a molecule) ones play a decisive role in interstellar chemistry. Since in molecular clouds photo-dissociation processes are negligible, one of the main fragmentation mechanism of molecules (in addition to cosmic-rays and X-ray photons) is reactions with energetic ions such as He^+ and H^+, *i.e. ionic destruction*. In particular, He^+ ion efficiently extracts one electron from the neutral molecular reactant, ionizing and then destroying the molecule. The efficiency of this charge transfer is so much dominated by the high ionization potential of helium (I.E. $\sim 24.6\,\mathrm{eV}$ [7]) that the difference in I.E. between He and the neutral target can be mostly assimilated as electronic excitation of the ionized molecule, leading to dissociation. On the contrary, due to the low I.E. of atomic hydrogen the dissociation by H^+ is not as effective as that by He^+, despite the higher abundance. The H^+ only transfers the charge, ionizing the molecule without dissociation in many cases and furthermore, a fraction of the ionized

species tend to return to neutral species for electron recombination.

The timescale of neutral molecule (such as CO, the most abundant molecule other than H_2 with relative abundance $\sim 1.4 \times 10^{-4}$) fragmentation by helium ons can be estimated as follows [3]. Cosmic rays are the main ionization factor for He, while He^+ is mainly lost by collisions with neutral CO:

$$\mathrm{He} + \mathrm{Cosmic\,Rays} \longrightarrow \mathrm{He}^+ + \mathrm{e}^- \tag{1.7}$$

$$\mathrm{He}^+ + \mathrm{CO} \longrightarrow \mathrm{C}^+ + \mathrm{O} + \mathrm{He} \tag{1.8}$$

The reaction of He^+ with H_2 to form H^+ and $H_2{}^+$ is not efficient (with rate constants in the range 10^{-14} to $10^{-13}\,\mathrm{cm}^3\,\mathrm{s}^{-1}$ [30, 31, 32] between 16-300 K). For this reason, this reaction can be neglected in this estimate. The rate equation for He^+ is therefore:

$$\frac{d[\mathrm{He}^+]}{dt} = \zeta_{\mathrm{He}}[\mathrm{He}] - k_{\mathrm{He}}[\mathrm{He}^+][\mathrm{CO}] \tag{1.9}$$

where ζ_{He} is the effective ionization rate for He (equal to $6.5 \times 10^{-18}\,\mathrm{s}^{-1}$ [3]) including ionization by cosmic-ray-induce photons; k_{He} is the rate coefficient for the He^+ + CO reaction (k=1.5×10^{-9} $\mathrm{cm}^3\,\mathrm{s}^{-1}$ at 8 K [33]). Therefore, the He^+ abundance can be obtained under the *steady-state approximation* (although the molecular cloud is not always in chemical equilibrium):

$$\frac{d[\mathrm{He}^+]}{dt} = \zeta_{\mathrm{He}}[\mathrm{He}] - k_{\mathrm{He}}[\mathrm{He}^+][\mathrm{CO}] = 0$$

$$[\mathrm{He}^+] = \frac{\zeta_{\mathrm{He}}[\mathrm{He}]}{k_{\mathrm{He}}[\mathrm{CO}]}$$

From the latter equation, the timescale for destruction by He^+ can be written as:

$$t = \frac{1}{k_{\mathrm{He}}[\mathrm{He}^+]} = \frac{[\mathrm{CO}]}{\zeta_{\mathrm{He}}[\mathrm{He}]}$$

where the $k_{\mathrm{He}}[\mathrm{He}^+]$ term can be considered the frequency of the reaction expressed in s^{-1}.

The timescale is therefore evaluated to be $3 \times 10^6\,\mathrm{year}$ (assuming [CO]/[He] = 7×10^{-4}), much longer than the photo-dissociation timescale in diffuse clouds ($100\,\mathrm{year}$). Since corresponding timescales for reaction with H^+ are comparable or shorter than that for He^+ reactions and the dissociation *via* H^+ is not efficient, the fragmentation timescale of neutrals in molecular clouds can be approximated by the calculated timescale for He^+ destruction.

In conclusion, as already explained, the modeling of the abundances of COMs, such as DME and MF, is not trivial. New pathways of formation have been proposed, but accurate models must consider also the dissociation processes, which are really efficient in the interstellar environment. Furthermore, it is necessary that astrochemical models should be based on experimental rate constants in order to minimize errors coming from estimates. For the best knowledge of the author, experiments on DME and MF destruction *via* He^+ collision have not been performed until now. For this reason, the final aim of this thesis is the experimental study of the reactions between He^+ and DME/MF, supported by a theoretical study able to cast light on the details that dominate the charge exchange process and to give rate constant values at typical temperatures of the ISM.

Chapter 2

Experimental Techniques and Procedures

"Hoping for the best, but expecting the worst."

Forever Young - Alphaville

In this section, a brief overview of the experimental techniques for studying the ion-neutral reactions will be reported. Furthermore, it will be described the Trento apparatus giving details on the methods utilized to analyze and to interpret the rough data. The used set-up is a home-built guided ion beam-mass spectrometer (GIB-MS). In this work, the mentioned tandem mass spectrometer was used to investigate the products of the gas-phase reactions between an ion, selected in terms of its mass to charge (m/z), and a neutral species. The most important parameters that can be controlled during the experiments are the pressure of the neutral reactants and the relative kinetic energy.

2.1 Experimental Techniques for Ion-Neutral Reactions

2.1.1 Laboratory Measurements

Laboratory experiments can provide different information. From experiments in which reactants are thermalized at defined T, rate coefficient as a function of the temperature *k(T)* can be obtained. For a second-order process (units of $cm^3\ s^{-1}$), *k(T)* is measured from the variations in concentration of the reactants with time. On the other hand, reactive total cross-section (σ_{rxn}, from now on defined just as σ) can be measured from single collision experiments at controlled collision energy. In fact, for collisions between two generic $\boldsymbol{A}$ and $\boldsymbol{B}$ species it is possible to define the effective cross-sectional area, σ_{coll}, that the centers of the two reactants must lie within if they are to collide (the definition of cross-section will be explained more in detail in Chapter 3). This parameter, which depends on energy, has therefore units of $\AA^2$. Since not all collisions lead to products, the probability that after collision the system will evolve to give any reaction product (*i.e.* the total reactive cross-section σ), is a fraction of σ_{coll}. Therefore, σ is the microscopic or single-collision

version of the rate constant and represents the reaction probability as an effective cross-sectional area within which the reactants must collide in order for the reaction to occur.

Product yields for different reaction channels are another important result from both laboratory experiments. In fact, it is possible to define the branching ratio (*BR*) for a particular product channel as the ratio of the yield of a product ion (P_i) formed by one channel with respect to the amount of the total set of the possible products (Eqn. 2.1).

$$BR_i = \frac{P_i}{\sum_{i=1}^{N} P_i} \tag{2.1}$$

These parameters will be treated in detail thereafter.

2.1.2 Laboratory Methods

The experimental methods developed to obtain data on ion-neutral reactions can be divided in two categories: those that measure rate constants and those that have the measuring of absolute integral cross-section as final aim.

In 60s and 70s, many studies on ion-neutral reactions were carried out using *ion cyclotron resonance* (ICR) or *flowing afterglow* (FA) methods. In ICR technique, ions are contained by a combination of electric and magnetic fields: after the introduction of a neutral reactant, at a selected time delay the ions are transferred from the source region through an analyzer region [34, 35]. The study of kinetics of ion-neutral reactions with this method was limited to room temperature measurements [36]. For this reason, other trapping methods have been developed to measure rate constants also at temperatures lower than room temperature, for instance using a Penning ion trap [37, 38, 32, 39]. Gerlich and co-workers have started to work with 22-pole traps [40, 41, 42], allowing study of ion-molecule reactions at low pressures and very low temperatures (down to $\sim 10\,\mathrm{K}$). To reach the thermal equilibrium the technique of the buffer gas cooling is used. Such a technique works, indeed, best if the interaction of the ion with the confining electric field of the trap is limited to a minimum [43]. The radio frequency multipole traps satisfy this requirement, offering a suppressed electric field in their center and an effective potential that increases steeply moving away from the center.

In the FA method [44, 45, 46], the ions are obtained by a plasma afterglow in a suitable carrier gas, usually helium, which transports them along a Pyrex tube ($\sim$100 cm in length and $\sim 8\,\mathrm{cm}$ of internal diameter). As the mixture of buffer gas and reactant flows in the reactor, reactions are carried out with a neutral co-reactant, introduced with one or more injectors. In the end of the reaction vessel, both primary and product ions are sampled by a mass spectrometer. Since the reaction time is calculated through the ratio between the distance between the point of introduction of the reactant gas and the mass spectrometer and the flow velocity, the depletion of the primary ion signal and the increase in the product signal can be interpreted in terms of rate coefficients.[44, 45, 46] Furthermore, in more recent set-ups it is possible to vary the temperature from 82 to 600 K [46].

The simple FA has been supplanted by the *selected ion flow tube* (SIFT), developed by Adams and Smith in 1976 [47, 48, 6]. In this technique a mass-selected positive ion beam, created by a low-pressure microwave discharge in an appropriate gas, is focused into a quadrupole mass filter, that allows mass selection of the reactant ions. After selection, the ion species of interest are focused into a stainless-steel flow tube ($100\,\mathrm{cm}$ in length and $\sim 7\,\mathrm{cm}$ of internal diameter), where they are thermalized by collisions with a carrier gas and where they can react with neutral species. At the

end of the reaction area the ions are sampled by a second quadrupole mass filter and detected. Using a thermal and microwave discharge sources, this technique allows to study also reactions in which radicals are involved. Furthermore, it is possible to cool (using liquid nitrogen) or to heat (using a series of resistive heater) the flow tube, allowing to measure rate constants between 85-500 K [49, 50]. The entire heated (or cooled) region is surrounded by a vacuum box that acts as a large Dewar.

Another major development of flow methods is represented by CRESU (*Cinétique de Réaction en Ecoulement Supersonique Uniforme*, literally reaction kinetics in uniform supersonic flow) apparatus [51, 52, 53, 54, 55, 56]. This set-up uses a supersonic jet generated by a convergent-divergent Laval nozzle, that allows to prepare dense (from 10^{16} to $2 \times 10^{17}\,\mathrm{cm}^{-3}$) and strongly cooled gaseous beam (to 8 K). The possibility to cool down the reactant species provides important information about the temperature dependency of the rate constants over an extended range. While originally ions were created by irradiating the gas with an electron beam just outside the Laval nozzle, recently they are formed by resonance-enhanced multiphoton ionization [57]. Furthermore, the ion selection of parent and products is again operated with a mass spectrometer.

Another useful technique is the GIB-MS [58, 59, 60, 61, 62], that allows accurate measurements of absolute cross-sections of ion-neutral reactions as a function of the collision energy (in the center-of-mass frame). A guided ion beam experiment is defined as that in which the reaction of interest is carried out inside a rf-only beam guide of *n*-pole (the octopole is the most common configuration as it will be described) that cylindrically surrounds the ion beam path [59]. This type of device permits to overcome two problems associated with integral cross-sections measurement: the efficiency in the collection of all products and the possibility to study reactions at low energy (below about 1 eV in laboratory). In fact, the ion guide acts as a transversal trap for the ions, permitting an efficient collection, regardless of their scattering angle. Furthermore, the beam guide allows experiments at low ion kinetic energies, avoiding space-charge effects that would disperse the ion beam [59, 58]. Moreover, it is possible to couple this type of apparatus with a photoionization source, allowing the preparation of state- or energy-selected reactant ions. In fact, by using this technique the photon energy is finely controlled and ions in their ground states (or in selected higher states) can be prepared with 100% purity. For this purpose, Ng and co-workers developed a triple-quadrupole double-octopole (TQDO) photoionization mass spectrometer for state-selected and state-to-state ion-molecule reaction studies [63]. The apparatus consists of a VUV photo-ionization source (a discharge lamp that produces VUV radiation in the range from 7.5 to 21.4 eV with a wavelength resolution of 3-6 Å), a reactant quadrupole mass spectrometer (QMS), a lower RF octopole ion guide reaction gas cell, a middle QMS, an upper RF octopole ion guide reaction gas cell and a product QMS. In the VUV photo-ionization source, the neutral precursor molecules are introduced in the form of a free jet.

2.2 The Trento GIB-MS

The guided ion beam mass spectrometer represents the method used for the work of this thesis and details of this experimental set-up are treated in this section. In particular, the Trento apparatus is a tandem mass spectrometer with an O1-Q1-O2-Q2 configuration (where Q stands for quadrupole and O for octupole) [64, 65] and the scheme of the set-up is shown in Figure 2.1. The primary positive charged ions are produced in an *electron ionization source* (EI, described in detail in Sec. 2.2.1). Then, the ions are extracted by a set of conical extractor lenses and injected into a

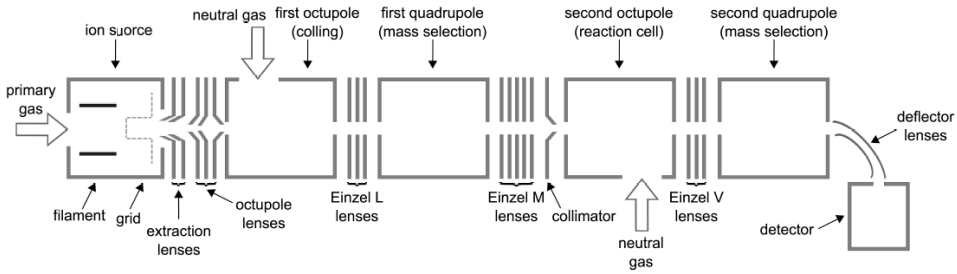

Figure 2.1: Scheme of the Trento GIB-MS

first octopole O1 (functioning and details of this device will be explained in Sec. 2.2.3). Since O1 is surrounded by a cell, which is possible to be filled with an inert gas (*e.g.* He or Ar), this octopole is generally used as energy quencher chamber, where excited ions can be cooled to the ground state by collisions with the inert partner, reducing some of their internal energy (*i.e.* vibrational or electronic). The presence of an unknown amount of ions in excited states represents a complication in the interpretation of the experimental results, because of the possibility to open endothermic channel avoided at the nominal collision energy. The first quadrupole Q1, connected with O1 via a set of *einzel lenses*, is used to mass-select just the parent ion beam under investigation and the chosen cations are subsequently directed towards the second octopole O2 ion guide through a series of cylindrical lenses, the last of which operates as collimator of the beam, reducing its divergence before the reaction chamber. The second octopole O2 is used again as guide: the ions inside are trapped in the two transversal directions and forced to move towards the end of the set-up. O2 is surrounded by a scattering cell, where the incoming parent ions collide and react with a neutral target (either a gas or the vapor pressure of a liquid chemical). The pressure of the neutral compound inside the reaction chamber is monitored by a pressure gauge (spinning rotor vacuum gauge system *SRG2 MKS instrument* [66]). This device works by measuring, on a magnetically-levitated spinning metal sphere, the viscosity drag, which is directly correlated to the number of particles (atoms or molecules) and therefore to the pressure. The pressure inside the scattering cell is regulated to ensure the single-collision regime inside the cell (for multiple collision effects see Appendix A).

Finally, the second quadrupole Q2 mass-selects the ionic products, focused as well as the primary ion beam by a series of lenses. These lenses transport efficiently the ions exiting the octopole O2, taking into account that the ions have a wide transversal velocity range due to the oscillating trajectories imparted by the RF field of O2. At the end of the GIB-MS, the ions are defecleted by 90° and transmitted to an electron multiplier, placed off axis with respect to the ion source to avoid spurious signals hitting the detector.

2.2.1 EI ion source

EI [67] is a well known ionization method in which atoms or molecules are bombarded with a high-energy beam of electrons forming ions, as described by the following reaction:

$$\mathrm{M} + \mathrm{e}^- \longrightarrow \mathrm{M}^{\bullet +} + 2\,\mathrm{e}^-$$

where M is a general particle (atom or molecule) and $\mathrm{M}^{\bullet +}$ is its radical cation. Primary products of ionization are positive ions unitary charged, formed when the high energy electrons collide with the neutral particles, which lose an electron *via* electrostatic repulsion. Electrons are emitted usually by a filament of tungsten or rhenium and accelerated by a potential in the range 40 to $100\,\mathrm{V}$ applied between the filament and an anode. The low mass and the very high energy of the emitted electrons cause a vibro-rotational excitation of the particles. In the case of molecular ionization, the relaxing of these excited states produces a huge fragmentation, forming cations at several masses lower than the radical cation.

In the GIB-MS set-up, there are two rhodium-tungsten filaments placed in small compartments and only one filament is operated at each time, emitting electrons in all the directions. A gas or a vapor pressure of a neutral target is injected in the center of the source, in a cylindrical zone where the filaments are facing. In this zone a cylindrical grid is placed and kept at a positive potential with respect to the filament so that the emitted electrons are extracted and accelerated towards the grid by a potential that can be changed from $40\,\mathrm{V}$ to $100\,\mathrm{V}$. The design of this source part is properly optimized to allow the creation of a constant field area. In the region of the cylindrical grid, the ions are created by the interaction between the neutral particles and the ionizing electrons. The whole source system (filaments and grid) is contained in a steel-iron box, kept at a negative potential with respect to filament and grid permitting the repulsion of the electrons. After the grid there are two lenses as already said in Sec. 2.2: the first one repels the electrons and squeezes the created ions to the latter that finally extracts the ions from the source system.

2.2.2 Quadrupole mass analyzer

Quadrupole mass analyzers are mass filters that allow to pass just ions of a certain mass-to-charge ratio. The functioning principle of quadrupole mass filter is fully described by the Mathieu equation [62]. In particular, it consists of four cylindrical electrodes that are positioned in a radial array, as shown in Figure 2.2. The opposite rods are connected to static (DC) and radio-frequency (RF) oscillating voltages. With proper electric fields, a stable path is created for ions of a certain m/z ratio: in fact, only ions within a narrow mass region (generally $1\,\mathrm{u}$) are allowed to pass through the device, while the trajectories of all the other ions are unstable, leading the ions to collide against the rods. In general, this device has some advantages: small physical dimensions compared to the resolving power, linearity in the mass scale, fast scanning, simplicity of construction and robustness during use.

2.2.3 Octopole ion beam guide

After quadrupoles, octopole ion beam guides are the second most used RF devices in mass spectrometry [62]. In this case, the device is formed by eight rods placed in an octagonally symmetric array around the beam path. RF electric potentials applied in opposite phases to alternate rods

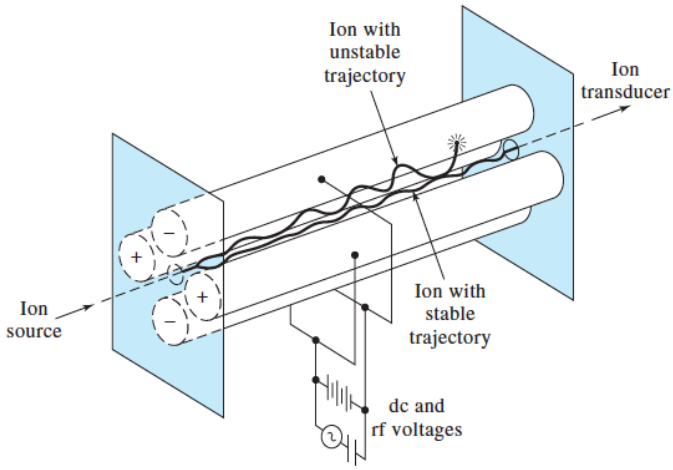

Figure 2.2: General scheme of a quadrupole mass analyzer [67].

produce an heterogeneous field which creates an effective radial potential well. The octopole traps the ions in transversal directions not affecting the axial ion velocities. Furthermore, the trapping ensures that ionic products are collected in spite of scattering angle, that could decrease the collection efficiency. The most impressive application of beam guide is that it allows operation at very low kinetic energies (<0.1 eV in the lab-frame), where space-charge seriously affects the convergence of the ion beam [58, 59]. The expression for the effective radial potential [68] for a multipole ion trap is:

$$V_{eff} = \frac{n^2 q^2 V_0^2}{4m\omega^2 r_0^2} \cdot \left(\frac{r}{r_0}\right)^{2n-2} \tag{2.2}$$

where $2n$ is the number of poles, q is the charge of the ion, m its mass, r is the radial distance from the center-line and r_0 is the inner radius of the multipoles. The RF potential applied to the alternate rods is $\pm V_0 cos(\omega t)$. From this formula it is easy to infer that the effective potential for an octopole ($n = 4$) is proportional to r^6. It follows that the octopole guide has a large tubular trapping volume with steep walls near the poles and a low potential near the center, as shown in Figure 2.3, in which the differences between a quadrupole and octopole potential are highlighted. Results of these characteristics are a very effective ion trapping with only small perturbations of the kinetic energies of the ions traveling into the octopole. On the other side, a quadrupole ($n = 2$) varies as a function of r^2, which leads to large perturbations of the kinetic energy and less effective trapping power. In fact, it is possible to conclude that for the same applied RF field, an octopole has a maximum trapping potential four times higher than a quadrupole [59] and in general, the larger is the number of electrodes, the more homogeneous is the trapping field.

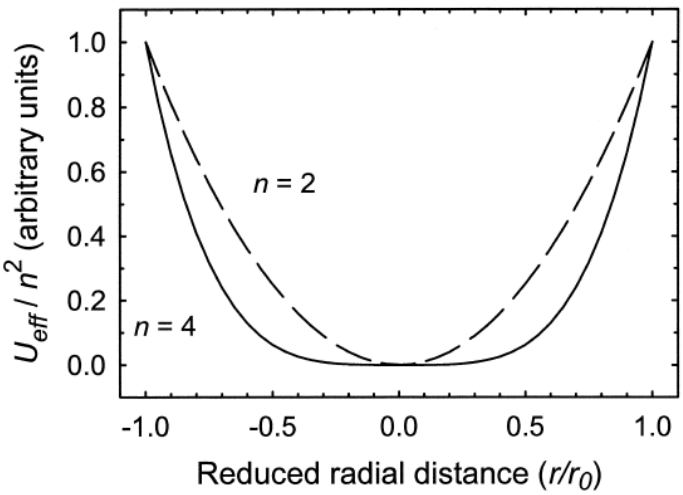

Figure 2.3: Relative effective potential scaled for n^2 as a function of the ratio r/r_0 for a quadrupole (dashed line) and for an octopole (continous line). [59]

2.3 Theoretical procedures of data analysis

In a typical GIB-MS experiment, it is possible to measure:

- Mass spectra of the resulting ions using the quadrupole mass filter in order to determine which products are formed; the measures are performed under different experimental conditions of neutral gas pressure and collision energy.
- Ion intensities of the reactant and product ions, measured as a function of the collision energy at a fixed pressure of the neutral target; in this case, the ion kinetic energy is varied, including the region where the reactant ions no longer have enough energy to pass through the octopole.
- Intensity of reagent and products signals as a function of the pressure of the neutral target at a fixed collision energy.

To convert the raw data in a more usable form independent of the instrument used to acquire them, several transformations are required. One involves the conversion of the kinetic energy of the ion, the *laboratory energy*, in the *center-of-mass energy* (CM energy), the energy available to the reaction system for chemical transformations. A second transformation involves the conversion of the relative product ion intensities into the cross-sections, which represent the intrinsic probability for the studied reaction.

2.3.1 Absolute Zero of Energy and the Ion Energy Calibration

One of the principal features of GIB experiments is the possibility to control the collision energy of the reaction. Hence, it is of paramount importance to have a reliable technique to measure the collision energy and the zero of the energy scale. Experimentally, this can be difficult because the effective potential values of the ion source and the collision cell may not equal to the applied potentials: differences might be produced as consequences of contact potentials, field effects, space-charge effects and surface charging [60].

In the mentioned apparatus, the octopole ion guide (the second octopole in Figure 2.1) can be used as a highly efficient retarding field energy analyzer to accurately measure the zero of the collision energy scale and the energy spread of the primary ion beam. In early ion beam experiments, retarding methods were difficult because, due to the slow motion, ions were very easily lost. In this case, the problem is solved by using the trapping characteristic of the octopole ion guide. More in detail, the zero of the ion energy is calculated by measuring the reactant ion intensity as a function of the DC bias potential applied to the second octopole as this is varied to the zero of energy. This variation gradually cuts off the ions at lower energy than the applied DC voltage, that literally repels such ions, so they no longer reach the detection system. It is possible to note that the zero of energy formally corresponds to the potential applied to the source, where the ions are formed. Since the retarding field and cross-section measurements for the ion-molecule reaction under study are performed using the same physical part of the set-up, the deviations produced by contact potentials and field, space charge and surface charging effects in the ion source (already mentioned above) are eliminated.

The black line in Figure 2.4 is an example of retarding field curve for a beam of He^+ ions. In order to obtain a direct measure of the distribution of the ion kinetic energies, the resulting retarding curve is differentiated. In general, the derivative (red curve in Figure 2.4) has a shape close to that of a Gaussian function. The center of the peak is equal to the absolute value of the zero energy (x_C in Figure 2.4) and the full width at half maximum is the energy spread of the ion beam. This latter value depends on several factors, *e.g.* electron energy and pressure in the ion source, and widths of $\approx 1\,\mathrm{eV}$ are usually obtained.

2.3.2 The Laboratory and Center-of-Mass Energy

In measuring reactive cross-sections and branching ratios, it is fundamental to know how much energy is available to the reaction system. The translational energy of two colliding particles can be divided into two parts:

1. The relative translational motion of the two reactants;
2. The motion of the entire collision system in the laboratory reference frame.

Since the total mass of the system can not change during the reaction and the linear momentum is conserved, the energy involved in the second part remains constant and therefore, unavailable to induce chemical reactions. Hence, the fraction of the kinetic energy available for the chemistry during the collision is the CM energy E_{CM}. In GIB-MS experiments the *stationary target limit* is effective, *i.e.* the neutral reactant is essentially stationary ($v = 0$) whereas the ions have an appreciable velocity ($v \neq 0$). The laboratory energy, E_{LAB}, is therefore defined as:

$$E_{LAB} = \frac{1}{2} m_I v_I^2 + \frac{1}{2} m_N v_N^2 \cong \frac{1}{2} m_I v_I^2 \tag{2.3}$$

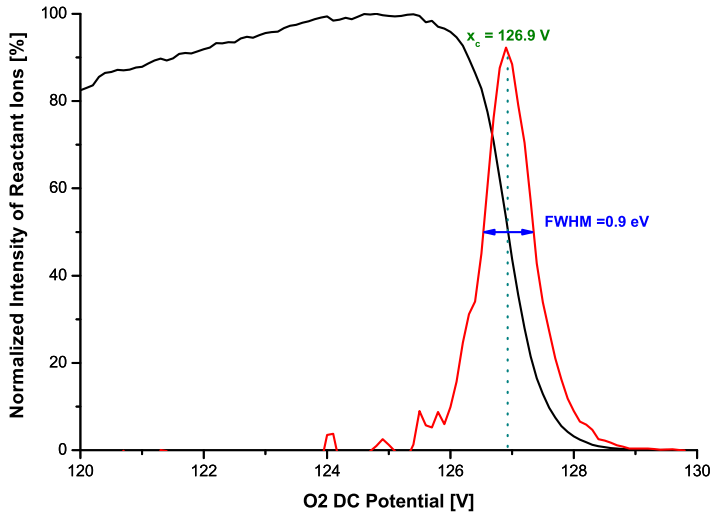

Figure 2.4: Retarding field analysis of a reactant beam of He^+ ions mass-selected with Q1 at $4\,m/z$ from electron ionization of He with the EI source (in black). In the x axis are shown the O2 DC potential values in V. The retarding field curve is differentiated and the result is shown in red. The FWHM corresponds to the spread in energy of the ion beam and x_C is the absolute zero of energy.

where m_I and m_N are the masses of ion and neutral target and v_I and v_N are their velocity, respectively. The kinetic energy of the reactant ion is measured in the laboratory frame as the potential difference between the ion source anode and the interaction region (*i.e.* the DC intensity of the second octopole). Hence, the total kinetic energy of the system is defined as sum of a contribution associated with the velocity of the CM of the collision partners ($v = \frac{m_I v_I + m_N v_N}{m_I + m_N} \equiv \frac{m_I v_I}{m_I + m_N}$) and a contribution associated with their relative velocity ($v_{REL} = v_I - v_N \equiv v_I$):

$$E_{LAB} = E + E_{CM} \tag{2.4}$$

where E is the kinetic energy of the CM, while E_{CM} is the kinetic energy in the CM frame. From Eqn. 2.4, E_{CM} can be obtained:

$$\begin{aligned}
E_{CM} &= E_{LAB} - E = \\
&= \frac{1}{2} m_I v_I^2 - \frac{1}{2}(m_I + m_N)v^2 = \\
&= \frac{1}{2} m_I v_I^2 - \frac{1}{2}\cancel{(m_I + m_N)} \frac{m_I^2}{\cancel{(m_I + m_N)^2}} v_I^2 = \\
&= \frac{1}{2} m_I v_I^2 - \frac{1}{2} \frac{m_I^2}{m_I + m_N} v_I^2 = \\
&= \frac{1}{2} \left(m_I - \frac{m_I^2}{(m_I + m_N)} \right) v_I^2 = \\
&= \frac{1}{2} \left(\frac{\cancel{m_I^2} + m_I m_N - \cancel{m_I^2}}{m_I + m_N} \right) v_I^2 = \\
&= \frac{m_N}{m_I + m_N} \cdot \frac{1}{2} m_I v_I^2
\end{aligned} \tag{2.5}$$

Therefore, from Eqn. 2.5 the laboratory energy can be converted into the collision energy in the CM frame by using the following simple expression:

$$E_{CM} = \frac{m_N}{m_N + m_I} \cdot E_{LAB} \tag{2.6}$$

This formula accurately describes the mean collision energy of the reactants.

2.3.3 Exothermic and Endothermic Reactions

An other information available studying ion-neutral reactions with the GIB-MS is whether they are exothermic or endothermic processes, *i.e.* if they release or require energy in making products, respectively. In case of exothermic reactions the energy requirement is related to the presence or absence of energy barriers to cross over a transition state. Specifically, in rarefied environments, such as the gas phase, the long-range attractive interactions between charged particles often overcomes barriers associated with reactions in condensed phases [61]. Consequently, exothermic ion-neutral reactions are often observed to be barrier-less and occur with high efficiency. As for any exothermic barrier-less process, increasing the amount of energy available will decrease the probability of the reaction. In other words, barrier-less exothermic reactions occur with the highest efficiency at the smallest collision energies. In fact, when the collision energy is low, there is enough time for long-range interactions to act on the particles, meaning large values of cross-section. Increasing the collision energy, the attractive forces between the reactants are less efficient due to the low time of interaction. In this case, the cross-sections is smaller than the one of the first case.

2.3.4 Determination of Cross-Sections

The total reaction cross-section is, as already mentioned, the intrinsic property of any reacting systems and it describes the probability that two particles (in our case an ion and a neutral target)

upon collisions will react to form all the possible products. For a reaction between two general species A^+ and B evolving into the products P_i, each one has a probability defined as σ_i:

$$\begin{aligned} \mathrm{A}^+ + \mathrm{B} &\rightarrow \mathrm{P}_1 \ \ \sigma_1 \\ &\rightarrow \mathrm{P}_2 \ \ \sigma_2 \\ &... \\ &... \\ &\rightarrow \mathrm{P}_\mathrm{N} \ \ \sigma_\mathrm{N} \end{aligned}$$

the total cross-section is defined as:

$$\sigma = \sum_{i=1}^{N} \sigma_i$$

The definition of cross-sections starting from the ion intensity follows an expression that is equivalent to the *Lambert-Beer Law* for light absorption through a sample. In fact, an ion beam with intensity I_R, defined as the number of reactant ions observed per unit time, is attenuated by collisions as it passes through the collision cell filled with a gas at a pressure *P*. The intensity of ions passing through the chamber that is not affected by collision is given by the following equation:

$$I_0 = I_R \cdot exp(-\rho \cdot \sigma_{coll} \cdot l) \tag{2.7}$$

where I_0 is the fraction of not attenuated beam, σ_{coll} is the collision cross-section and *l* is the effective length of the reaction chamber; furthermore, the neutral target density ρ is directly connected with its pressure *P* by the *Ideal Gas Law*:

$$\rho = \frac{P}{N_A \cdot R \cdot T} \tag{2.8}$$

where ρ is given in $\mathrm{particles\,cm^{-3}}$, N_A is the *Avogadro Number*, *R* is in $\mathrm{mbar\,cm^3\,K^{-1}\,mol^{-1}}$, *T* in K and *P* in mbar. The intensities of ions that have undergone at least one collision, for example a general product ion intensity, I_P, is given by:

$$I_P = I_R \cdot [1 - exp(-\rho \cdot \sigma_{rxn} \cdot l)] \tag{2.9}$$

where:

$$I_R = I_0 + I_P$$

In the *thin target limit*, where the probability of collisions is small either for low pressures or for small cross-sections or for a short interaction length (*i.e.* $\rho\sigma_{rxn}l \ll 1$), the Eqn. 2.9 is simplified in:

$$I_P = I_R \cdot (\rho \cdot \sigma_{rxn} \cdot l) \tag{2.10}$$

Since *P*, *T* and *l* are known, the absolute reaction cross-section is easily determined by measuring the ion intensities as a function of the neutral reactant pressure. In this way, the absolute cross-section accuracy is primarily limited by measurement procedure of *l* and ρ. From this assumption, it is possible to estimate and fix the accuracy within 30 %.

It is interesting to note that in GIB-MS experiments the effective path length l is not equal to the real physical length of the scattering cell ($10\,\mathrm{cm}$). In fact, the vacuum pumping takes place just outside the cell, which is closed with exception for the entrance and exit apertures for the ions; this implies that the neutral target pressure does not fall down immediately outside the chamber, permitting more collisions before and after it. For this reason, the effective length has been determined from a calibration process using the following reaction [58] as reference:

$$\mathrm{Ar}^{+} + \mathrm{H}_2 \rightarrow \mathrm{ArH}^{+} + \mathrm{H} \tag{2.11}$$

To determine the effective length l in the Eqn. 2.10, experimental data as a function of the collision energy were compared to the values of [58]. Results (shown in Figure 2.5) can be superimposed to literature values when using an effective length of the cell equal to $(8.0 \pm 0.4)\,\mathrm{cm}$.

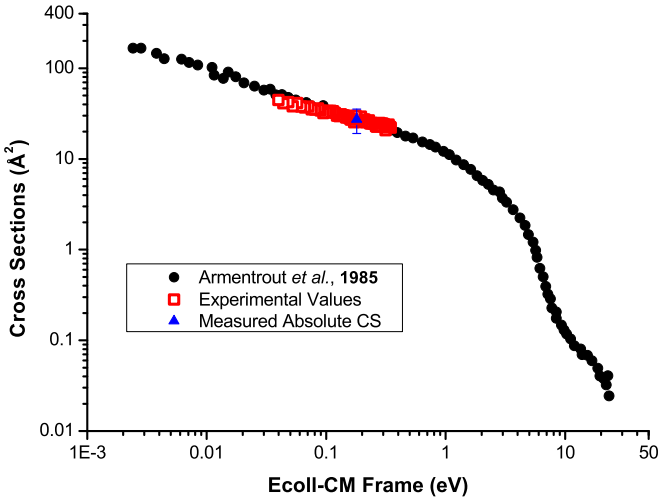

Figure 2.5: Experimental data of cross-section as a function of collision energy in the CM frame for the reaction channel $Ar^+ + H_2 \longrightarrow ArH^+ + H$: red-empty squares are values from our measurements while black circles are from literature [58]. In blue is shown the resulting absolute value of the cross-section.

2.3.5 From Cross-Sections to Rate Constants

In the simplest form, the cross-section can be converted to a rate constant simply multiplying by the velocity. Therefore, the phenomenological rate constant is given by the following expression:

$$k(v_0) = v_0 \cdot \sigma(v_0) \tag{2.12}$$

with the nominal relative velocity v_0 of the reactants defined as:

$$v_0 = \left(\frac{2E}{\mu}\right)^{1/2} \tag{2.13}$$

and the reduced mass of the reactants μ is:

$$\mu = \frac{m_I \cdot m_N}{m_I + M_N} \tag{2.14}$$

Because of the kinetic energy distribution of the reactants, the rate constants are better characterized as a function of the mean relative energy of the reactants:

$$\langle E \rangle = E + \frac{3}{2}\left(\frac{\mu}{m} \cdot k_B \cdot T\right) \tag{2.15}$$

Generally, rate constants measured with under equilibrium methods (*e.g.* at room temperature) are functions of *T*, not of *E*. Since the beam guide technique should allow very low ion energies, the rate constant nearly at room temperature could be obtained directly from the data at lowest interaction energy. Unfortunately, this is not the case for our experiments due to the fact that with our set-up it is not possible to reach so low collision energies.

Alternatively, true thermal rate constants as a function of temperature are obtained by averaging the cross-section over a *Maxwell-Boltzmann distribution* of relative energies (Eqn. 2.16). Since only the translational energy of the reactants is varied in GIB experiments, the results are actually $k(T_k)$, the rate constant as a function of translational temperature.

$$k(T) = \left(\frac{1}{\pi\mu}\right)^{1/2} \cdot \left(\frac{2}{k_B T}\right)^{3/2} \cdot \int_0^\infty \sigma(E) \cdot E \cdot e^{-E/k_B T} dE \tag{2.16}$$

The derivation of this formula will be treated in detail in the following Chapter.

Chapter 3

Theoretical Methodologies

"If there's a God or any kind of justice under the sky
If there's a point, if there's a reason to live or die
Ha, if there's an answer to the questions we feel bound to ask."

Innuendo - Queen

To understand the second part of this doctoral thesis, the attention of the author is moved to the theoretical aspects used to interpret the experimental evidences and the mechanisms at their basis. In particular, the aim of the considerations reported in this chapter was to develop a theoretical framework for describing and understanding the chemical changes involved in the studied ion-molecule reactions and for extending these insights to the astrophysical context.

In addition to the concepts essential to study the dynamics of the reactions object of this doctoral thesis and to calculate cross-sections to compare with the experimental data, in this chapter the tools for a realistic representation of the potential energy surface (PES) for the reactive system are also reported. Furthermore, quantum mechanical methods used to identify the electron densities and the partial charges of the molecules are described.

3.1 Dynamics of reactive collisions

The molecular reaction dynamics has the final aim to deeply understand the chemical reactivity and it represents a "bridge" between experiment and theory. The key concept in reaction dynamics is the PES, that describes the potential energy of the system of interest as a function of the nuclear coordinates of each atom involved in the reaction and of the electronic state of the system. Theoretically, once the PES is known, the dynamics of a reaction that involves just one electronic state of the system may be understood completely. On the other hand, if multiple electronic states are involved in the reactions, it is necessary to consider multiple PESs.

Another key point of the dynamics is the cross-section, since a chemical event may be imagined in terms of a collision in which the involved species are transformed through the cleavage and formation of chemical bonds. In fact, this is a concept that is commonly considered in situations in which the collision energy is well defined or when the system is not at thermal equilibrium.

Therefore, studying the cross-sections of a colliding system and their dependence on energy is of high interest to understand the chemical reactivity.

3.1.1 The theory of collisions

In this section we will examine in more details the concept of cross-section for collisions among two atoms/molecules, as already mentioned in Sec. 2.1.1. The simple model of a binary collision between two reactants A and B, of mass m_A and m_B, respectively, is shown in Figure 3.1, where the distance of closest approach in the absence of interaction between the two species is defined as the impact parameter b. The parameter b can not be controlled experimentally, but it plays a

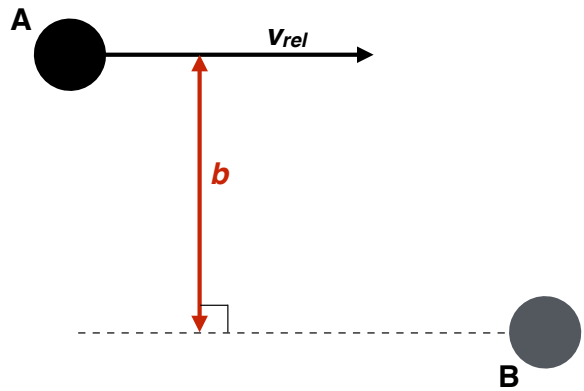

Figure 3.1: Representation of a colliding system between two reactants A and B. In the figure, the impact parameter b is also reported.

crucial role in the collision as will be explained thereafter. In the colliding system, the two species approach each other with a fixed velocity ($v_{rel} = v_A - v_B$, where v_A and v_B are the velocities of the two reactants with respect a reference frame, *e.g.* in the laboratory). Classically, the impact parameter can be directly linked to the orbital angular momentum, $\overrightarrow{L}$, of the two reactants with the following equation:

$$| \overrightarrow{L} | = | \overrightarrow{R} \times \overrightarrow{p} | = \mu v_{rel} b \tag{3.1}$$

where μ is the reduced mass of A and B (see Eqn. 2.14), $\overrightarrow{R}$ is the relative position of B with respect to A, and $\overrightarrow{p}$ is the momentum. In quantum mechanic theory, the orbital angular momentum is defined as:

$$| \overrightarrow{L} | = \hbar \sqrt{l\,(l+1)} \tag{3.2}$$

where $\hbar$ is the reduced Plank constant and l is the orbital angular momentum quantum number. From Figure 3.1, it is clear that the probability of the scattering event depends on the impact parameter (or on the orbital angular momentum).

For reactions, the variation in the probability of the process with the impact parameter is known as *opacity function*, $P(b)$. Therefore, the reaction cross-section is given by integrating the reaction probability as a function of the impact parameter from $b = 0$ (*head on* collision) to some maximum value, b_{max} (*i.e.* the highest b for which a reaction can happen):

$$\sigma = \int_0^{b_{max}} P(b) 2\pi b db \tag{3.3}$$

where the volume element $2\pi bdb$ is illustrated in Figure 3.2.

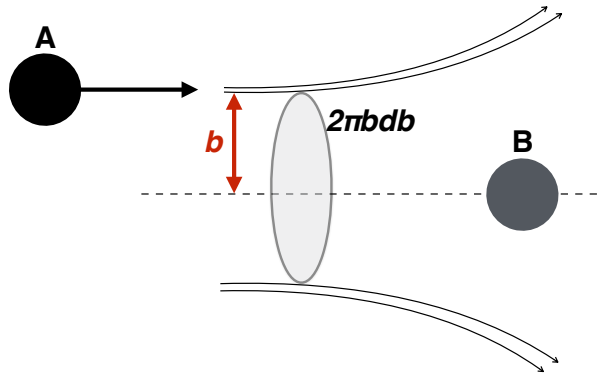

Figure 3.2: The figure shows the approach of two spherical particles A and B at impact parameter b. As discussed in the text, the cross-section is defined as the integral of the reaction probability over all impact parameters in the volume element $2\pi bdb$. In the figure, the impact parameter b is also reported.

In order to determine $P(b)$ in detail, the simplest approximation is a unit step function:

$$P(b) = \begin{cases} 1 & b \leqslant b_{max} \\ 0 & b > b_{max} \end{cases} \tag{3.4}$$

where b_{max} is therefore the *cut-off* impact parameter. So using Eqn. 3.3, σ is simply:

$$\sigma = \pi b_{max}^2 \tag{3.5}$$

The resulting cross-section has the correct dimensions of area, as expected. Therefore, the cross-section σ can be imagined as an effective target area within which the colliding particles must

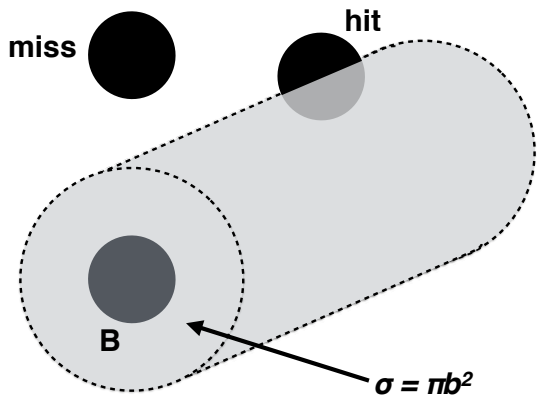

!ht

Figure 3.3: Simple collision theory: the cross-section can be thought as the effective target area of the reactants.

approach for occurring the processes of interest, as shown in Figure 3.3. Different types of collisional process have different cross-sections, reflecting the different effective target areas. Reactions characterized by PES with high barriers tend to have small reactive cross-sections, since the reaction probability is small unless the system has sufficient energy to approach. On the other hand, reactions on attractive surfaces (*e.g.* those occurring between an ion and a molecule with large dipole moment, as in our cases) have large cross-section values.

Quantum mechanically, the integral in Eqn. 3.3 can be transformed to a sum over l, since from equation 3.1 and 3.1 the relation between b and l is known as:

$$b = \frac{\hbar\sqrt{l\,(l+1)}}{\mu v_{rel}} \tag{3.6}$$

Furthermore, the momentum associated with the relative motion of the colliding particles can be written as $p = \mu v_{rel} = k\hbar$, where k is the wavenumber ($k = 2\pi/\lambda$, where λ is the wavelentgh). Hence, the corresponding quantum expression of Eqn. 3.3 for the cross-section is:

$$\sigma = \frac{\pi}{k^2}\sum_{l} P(l)(2l+1) \tag{3.7}$$

in which σ is expressed as the weighted sum of reaction probabilities for each orbital angular momentum.

In the *classical capture model*, the reaction can occur with unitary probability ($P(b) = 1$), if the colliding system has sufficient translational energy to overcome the energy barrier for the reaction. For reactions without an energy threshold, the only barrier is the *centrifugal* one. Since the reaction dynamics is the solution of nuclear motion under forces, it is necessary to solve the Newton's

equation to define these forces:

$$\overrightarrow{F} = \mu \frac{d\overrightarrow{v}}{dt} = \mu \frac{d^2\overrightarrow{R}}{dt^2} = -\frac{dV(R)}{dR}\widehat{R} \tag{3.8}$$

As written, the forces can be represented by the derivative of the inter-particle potential ($V(R)$) directed along the vector $\overrightarrow{R}$.

During the time evolution of the vector $\overrightarrow{R}$, a conservation condition must be active. For this reason, it is more advisable to speak in terms of angular momentum $\overrightarrow{L}$, that from Eqn. 3.1 can be written as:

$$\overrightarrow{L} = \overrightarrow{R} \times \mu \frac{d\overrightarrow{R}}{dt} \tag{3.9}$$

$\overrightarrow{L}$ is the vector perpendicular to the plane defined by the position and momentum vectors (*Right-hand Rule*) and during a collision of particles, it does not change over time:

$$\frac{d\overrightarrow{L}}{dt} = \frac{d\overrightarrow{R}}{dt} \times \mu \frac{d\overrightarrow{R}}{dt} + \overrightarrow{R} \times \mu \frac{d^2\overrightarrow{R}}{dt^2} = 0 \tag{3.10}$$

Therefore, the magnitude and the direction of $\overrightarrow{L}$ are constant in time. This condition implies that there is a particular plane in which the collision is confined. Before the collision, this plane is defined by $\overrightarrow{R}$ and $\overrightarrow{v}$ (initial relative velocity of the particle) and $\overrightarrow{L}$ is normal to this plane. Since the direction of angular momentum is constant in time, also the time evolution of $\overrightarrow{R}$ will be confined to the same single plane defined by the initial conditions. Thus, the position $\overrightarrow{R}$ can be

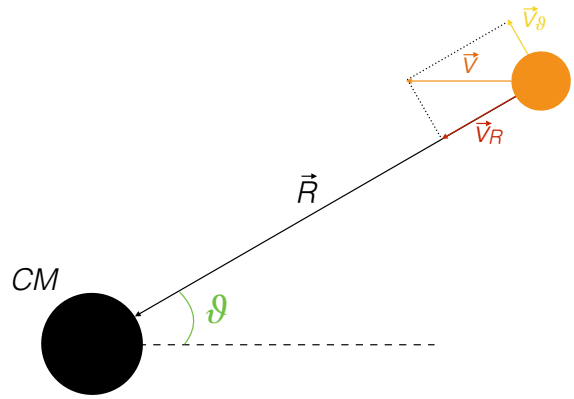

Figure 3.4: Relative motion of a particle (in orange) respect of the CM. In the figure, the velocity v and its components (v_ϑ and v_R) are indicated in orange, yellow and red, respectively.

represented by its length R and its orientation ϑ with respect the CM, as shown in Figure 3.4. If the particle moves with a velocity $\overrightarrow{v}$, its kinetic energy (E_K) in the CM frame is:

$$E_K = \frac{1}{2}\mu \overrightarrow{v}^2$$

Considering the velocity along the line centers (the *radial velocity*, v_R) and the angular tangential velocity ($v_\vartheta = R\frac{d\vartheta}{dt}$), the kinetic energy formula can be re-written as:

$$\begin{aligned} E_K &= \frac{1}{2}\mu(\overrightarrow{v_R}^2 + \overrightarrow{v_\vartheta}^2) = \\ &= \frac{1}{2}\mu\left[\left(\frac{d\overrightarrow{R}}{dt}\right)^2 + \left(\overrightarrow{R}\frac{d\vartheta}{dt}\right)^2\right] = E_R + E_\vartheta \end{aligned} \tag{3.11}$$

where E_R is the colliding energy along the line between the particle and the CM, while the E_ϑ can be defined in term of angular momentum of the system. The angular velocity ($\frac{d\vartheta}{dt}$) is defined as:

$$\frac{d\overrightarrow{\vartheta}}{dt} = \frac{\overrightarrow{L}}{|\overrightarrow{I}|} = \frac{\overrightarrow{L}}{\mu R^2} \tag{3.12}$$

where $\overrightarrow{I}$ is the moment of inertia.

Therefore, E_ϑ can be written as:

$$\begin{aligned} E_\vartheta &= \frac{1}{2}\mu\left(\overrightarrow{R}\frac{d\vartheta}{dt}\right)^2 = \\ &= \frac{|\overrightarrow{L}^2|}{2\mu R^2} = \frac{Eb^2}{R^2} \end{aligned} \tag{3.13}$$

and in terms of the quantum angular number, Eqn. 3.13 can be rewritten as:

$$E_\vartheta = \frac{\hbar^2 l(l+1)}{2\mu R^2} \tag{3.14}$$

In this form, E_ϑ becomes formally potential energy and it corresponds to the centrifugal potential ($E_\vartheta \equiv V_C$). Since it is positive for each value of R and l (or b), the centrifugal potential V_C is repulsive, forming a barrier to overcome to reach a reactive collision. Therefore, the effective interaction potential for two colliding structure-less and spherical atoms can be written as:

$$V_{eff} = V(R) + \frac{Eb^2}{R^2} = V(R) + \frac{|\overrightarrow{L}^2|}{2\mu R^2} \tag{3.15}$$

where E is the relative kinetic energy, R the distance between the colliding particles, $\overrightarrow{L}$ is the angular momentum (see Eqn. 3.1 for the relation between $\overrightarrow{L}$ and b) and μ the reduced mass of the system. In this model, it is assumed that all the trajectories having sufficient energy to overcome the centrifugal barrier will lead to reaction, and the cross-sections are completely determined by long range attractive interactions between the approaching reactants. In this sense, when $b = 0$ all the collisions are reactive, while when $b > 0$ the system has non-zero angular momentum and

Table 3.1: n and long range potential coefficients C_n. In table, it also reported the type of interaction [69]. With I_i is indicated the ionization potential of the interaction species.

n	Interaction	C_n
2	ion-dipole	$\frac{\mu_1 q_2}{4\pi\varepsilon_0}$
3	dipole-dipole	$\frac{\mu_1 \mu_2}{2\pi\varepsilon_0}$
4	ion-induced dipole	$\frac{\alpha_1 q_2^2}{8\pi\varepsilon_0}$
5	dipole-induced dipole	$\frac{\mu_1 \alpha_2}{4\pi\varepsilon_0}$
6	induced dipole-induced dipole	$\frac{\alpha_1 \alpha_2 I_1 I_2}{2(I_1+I_2)}$

reactive collisions are only those with sufficient energy to pass over the centrifugal barrier.

In the capture model, $V(R)$ is approximated only using the long range interaction between two particles , expressed as:

$$V_n(R) = -\frac{C_n}{R^n} \tag{3.16}$$

where C_n is the long range coefficient depending on the charges (q), dipole moments (μ), polarizabilities (α) and ionization potentials (I) of the two interacting species and n depends on the type of the interaction (expressions of C_n are reported in Table 3.1). Therefore, the maximum of the effective potential that occurs at a distance R_{max} can be evaluated by imposing the condition that the first derivative of $V_{eff}(R)$ should be equal to zero, as follows [69]:

$$\frac{d}{dR}[V_{eff}(R)]\bigg|_{R=R_{max}} = \frac{nC_n}{R^{n+1}} - \frac{|\overrightarrow{L}|^2}{\mu R^3} = 0 \tag{3.17}$$

Resolving Eqn. 3.17, an expression for R_{max} is obtained as a function of $\overrightarrow{L}$:

$$R_{max} = \left(\frac{nC_n\mu}{|\overrightarrow{L}|^2}\right)^{\frac{1}{n-2}} \tag{3.18}$$

Substituting Eqn. 3.18 in Eqn. 3.15, we can obtain an analytic expression for the effective potential:

$$V_{eff}(R_{max}) = -\frac{C_n}{R_{max}^n} + \frac{|\overrightarrow{L}|^2}{2\mu R_{max}} = \left(\frac{|\overrightarrow{L}|^2}{\mu}\right)^{n/(n-2)} \frac{n-2}{2n}(nC_n)^{-2/(n-2)} \tag{3.19}$$

The trajectories are reactive when $V_{eff}(R_{max}) \leq E$, condition to have a maximum value for $|\overrightarrow{L}|$:

$$|\overrightarrow{L}_{max}|^2 = \mu n (C_n)^{2/n} \left(\frac{2E}{n-2}\right)^{(n-2)/n} \tag{3.20}$$

From the relation between the orbital angular momentum and the impact parameter (Eqn. 3.1), the corresponding maximum impact parameter is:

$$b_{max} = \frac{|\overrightarrow{L}_{max}|}{\mu v} \tag{3.21}$$

Assuming $P(b, E) = 1$, from Eqn. 3.5 we have:

$$\sigma = \pi b_{max}^2 = \frac{\pi}{2} n \left(\frac{2}{n-2}\right)^{(n-2)/2} \left(\frac{C_n}{E}\right)^{2/n} \tag{3.22}$$

This expression of σ can be used to calculated the rate constant of the process. As already said above and in Sec. 2.3.5, thermal rate constants are linked to the cross-sections (σ). In fact, considering the binary process:

$$\mathrm{A} + \mathrm{B} \longrightarrow \mathrm{C} \tag{3.23}$$

the evolution in time of the concentrations [A], [B] and [C] (in $\mathrm{molecules\,cm^{-3}}$) is given by:

$$-\frac{d[\mathbf{A}]}{dt} = -\frac{d[\mathbf{B}]}{dt} = \frac{d[\mathbf{C}]}{dt} = k(T)[\mathbf{A}][\mathbf{B}] \tag{3.24}$$

where $k(T)$ is the temperature dependent reaction rate ($\mathrm{cm^{-3}s^{-1}molecule^{-1}}$).

Since the concept of rate constant implies that the system is at thermal equilibrium, each state is populated according to the Boltzmann distribution law. Therefore, it can be obtained from the integral cross-section by averaging over the Maxwell-Boltzmann distribution of velocities ($f(v_{rel})$):

$$k(T) = \int_0^\infty v_{rel} \sigma(v_{rel}) f(v_{rel}) dv_{rel} \tag{3.25}$$

For a particle with mass m, the Maxwell-Boltzmann velocity distributions (normalized so that $\int_0^\infty f(v_{rel}) = 1$) is given by:

$$f(v_{rel}) = 4\pi \left(\frac{m}{2\pi k_B T}\right)^{3/2} v_{rel}^2 e^{-\frac{m v_{rel}^2}{2 k_B T}} \tag{3.26}$$

Alternatively, the rate constant can be written as the integral over the relative kinetic energy ($E = \frac{1}{2}\mu v_{rel}^2$):

$$k(T) = \sqrt{\frac{8 k_B T}{\pi \mu}} \frac{1}{(k_B T)^2} \int_0^\infty \sigma(E) e^{-\frac{E}{k_B T}} E dE \tag{3.27}$$

From equations 3.25 and 3.27, it is possible to deduce that the thermal rate constant is a highly

averaged quantity and for this reason, to gain the most insight into the dynamics of a reactions and to quantify its rates it is better to use cross-sections. Therefore, from equations 3.22 and 3.27, we have that:

$$k(T) = \sqrt{\frac{2\pi}{\mu}} n \left(\frac{2}{n-2}\right)^{(n-2)/2} C_n^{2/n} (k_B T)^{(n-4)/2n} \Gamma\left(2 - \frac{2}{n}\right) \tag{3.28}$$

where the Gamma function Γ is defined as:

$$\Gamma(n) = \int_0^\infty x^{n-1} e^{-x} dx \tag{3.29}$$

The $\Gamma(n)$ has the following properties:

- $\Gamma(1/2) = \sqrt{\pi}$;
- it satisfies the relation $\Gamma(n+1) = n\Gamma(n)$, *e.g.* $\Gamma(3/2) = \frac{1}{2}\sqrt{\pi}$;
- for integer values we have $\Gamma(n+1) = n!$.

The results as a function of n are summarized in Table 3.2.

In case of a ion-neutral system, the formulation of the cross-section has been studied by Langevin in 1905 [70, 71]. Assumptions at the basis of this model are:

- the neutral reactant has not dipole moment;
- the ion is represented as a point charge and therefore, it has no dipole moment (μ) neither polarizability (α).

Hence, the reaction case is $n = 4$ (*i.e.* between an ion and an induced dipole, Table 3.1) and the long range coefficient C_4 is (Table 3.2):

$$C_4 = \frac{1}{2} \frac{\alpha q^2}{4\pi\varepsilon_0} \tag{3.30}$$

where q is the charge of the ion and α is the polarizability in m^3. From Eqn. 3.22, the cross-section is thus:

$$\sigma(E) = q\sqrt{\frac{\pi\alpha}{2\varepsilon_0 E}} \tag{3.31}$$

Substituting C_4 into the capture rate coefficient (Table 3.2) (or integrating σ with Eqn. 3.27), we obtain:

$$k_{Langevin}(T) = \frac{2\pi q}{4\pi\varepsilon_0}\sqrt{\frac{\alpha}{\mu}} \tag{3.32}$$

It is interesting to note that $k_{Langevin}$ is independent of the temperature.

Until now, the mentioned treatment regards only isotropic potentials that describe very well the interaction between two closed-shell atoms. The isotropic approximation fails when molecular systems are considered: in this case, the potential depends on the orientation of the molecule, even when it is apolar (anisotropic interaction). This is always true for short-range potentials, while it can be neglected when only long-range interactions are considered. For this reason, the simple "capture" model (for which the cross-section depends only on the dispersion term of the

Table 3.2: Cross-sections $\sigma_n(E)$ and rate constants $k_n(T)$ for classical capture theory. [69]

n	$\sigma_n(E)$	$k_n(T)$
2	$\frac{\pi C_2}{E}$	$2\sqrt{\frac{2\pi}{\mu}}C_2(k_BT)^{-1/2}$
3	$3\pi\left(\frac{C_3}{2E}\right)^{2/3}$	$4\sqrt{\frac{\pi}{3\mu}}\Gamma(1/3)(C_3)^{2/3}(k_BT)^{-1/6}$
4	$2\pi\sqrt{\frac{C_4}{E}}$	$2\pi\sqrt{\frac{2C_4}{\mu}}$
5	$\frac{5\pi}{2}\left(\frac{2}{3}\right)^{3/5}\left(\frac{C_5}{E}\right)^{2/5}$	$3\sqrt{\frac{2\pi}{\mu}}\Gamma(3/5)(2/3)^{3/5}(C_5)^{2/5}(k_BT)^{1/10}$
6	$3\pi\left(\frac{1}{2}\right)^{2/3}\left(\frac{C_6}{E}\right)^{1/3}$	$2^{11/6}\Gamma(2/3)\sqrt{\frac{\pi}{\mu}}(C_6)^{1/3}(k_BT)^{1/6}$

potential) can be applied not only to atom-atom systems, but also when apolar molecules are involved, assuming that the long-range potential is isotropic. On the contrary, for polar molecules the potential is always anisotropic, depending on the orientation of the permanent dipole and on the distance between the reactants. For this reason, a model as the Langevin one is incomplete for polar systems and an interesting case of study has been to extend the proposed model for for ion-polar molecule reactions. The interaction of an ion with a molecule possesing a permanent dipole was first investigated in the 60s by Hamill and co-workers [72, 73]. They pointed out two conditions:

1. if no alignment of the dipole with the incoming ion occurs, the ion-dipole interactions should average out to zero and only the ion-induced dipole interaction would be important. In this case, the expressions obtained by the Langevin model for σ (Eqn. 3.31) and $k(T)$ (Eqn. 3.32) would be applied;
2. if there is alignment between the dipole and the ion, and in particular, the molecule dipole "locks-in" as the ion approaches, this ion-dipole interaction must be added to the long range potential used by Langevin.

Hence, for the "locked-in" case, the interaction potential is given by:

$$V(R) = -\frac{\alpha q^2}{8\pi\varepsilon_0}\frac{1}{R^4} - \frac{q\mu_D}{R^2} \tag{3.33}$$

where μ_D is the dipole moment of the molecule. Therefore, obtaining the maximum impact parameters from equations 3.17-3.21 and knowing the effective interaction potential, cross-section (Eqn. 3.34) and rate constant (Eqn. 3.35) expressions for the *locked-in* case have been obtained.

$$\sigma(R_max, E) = \pi R_{max}^2 + \frac{\pi q^2\alpha}{2ER_{max}} + \frac{\pi q\mu_D}{E} \tag{3.34}$$

$$k(T) = q\sqrt{\frac{\pi\alpha}{\varepsilon_0\mu}} + \frac{\mu_D q}{2\varepsilon_0}\sqrt{\frac{2}{\mu k_B T\pi}} \tag{3.35}$$

Since the *locked-in* of the dipole does not necessarily occur [74], the values obtained with this approximation are overestimated. Hence, a more appropriate extension of Eqn. 3.33 should be the following expression:

$$V(R) = -\frac{1}{2}\frac{\alpha q^2}{4\pi\varepsilon_0} - \frac{q\mu_D}{R^2}cos\theta \tag{3.36}$$

where θ is the angle that the dipole makes with the direction R of the incoming ion. For $\theta = 0°$, Eqn. 3.36 becomes Eqn. 3.33. Most theories assume that θ has a distribution of values as a function of R: specifying this distribution, the anisotropic potential becomes a central potential. In 1973, Su and Bowers [75] proposed the *average dipole orientation* theory, assuming that the sum of the ion-dipole interaction and the rotational energy of the dipole is a constant. With this approximation, θ could be determined as an average of angles ($\bar{\theta}$) of alignment between the dipole and the ion.

Searching a definitive solution, Su and Chesnavich [76] parametrized the results for extensive trajectory calculation by using the classical equations of motion. They obtained [77, 78] a simple formulation for the rate constant in terms of the Langevin one:

$$\frac{k}{k_L} = 0.4767x + 0.6200 \quad with\ x \geq 2$$
$$\frac{k}{k_L} = \frac{(x + 0.5090)^2}{10.526} + 0.9754 \quad with\ x < 2$$

The formula is based on the parameter x, defined as:

$$x = \frac{\mu_D}{\sqrt{2\alpha k_B T}}$$

Explicating the dependence of k on T, the k can be written as:

$$k = c_1 + c_2 T^{-1/2} \quad with\ x \geq 2 \tag{3.37}$$

where $c_1 = 0.62k_L$ and $c_2 = 2.1179\frac{\mu_D e}{\sqrt{\mu k_B}}$. For $x < 2$:

$$k = k_L + b_1 T^{-1/2} + b_2 T^{-1} \quad with\ x < 2 \tag{3.38}$$

where $b_1 = 0.4296\frac{\mu_D e}{\sqrt{\mu k_B}}$ and $b_2 = \frac{\mu_D^2 \pi e}{10.526 k_B \sqrt{\alpha\mu}}$. In Eqn. 3.37 if the second term (c_2) is much greater than the first one (c_1) (*e.g.* at low temperatures), the Eqn. 3.37 reduces to $c_2 T^{-1/2}$. In the astrochemical databases (such as KIDA, OSU2009, UMIST), these formulas are used for giving rate constant values to reactions in the situation where no experimental informations are available.

3.1.2 The charge transfer process

Of fundamental importance for this thesis it is to understand the dynamics of an electron transfer. The *charge transfer* between charged (A^+) and neutral (B) species to form the neutral (A) and charged (B^+) counterparts is a typical example of a non-adiabatic process. Therefore to understand this process, it is necessary to introduce new elements not considered by the simple collision theory treated until now.

Since in the collision process and more generally in the chemical reaction a transformation from reagent to product is involved , it is necessary to know the interaction energy of the configuration of the system during this rearrangement. For this reason, it is appropriate to finally introduce the concept of potential energy surface. Considering a simple case of an atom-diatom collision, A + BC, the potential energy, interpreted as inter-atomic potential, is a function of the three inter-atomic distances. Further simplifying the system in a collinear configuration (A – B – C), only two independent inter-atomic distances remain to be considered, whereas the third one (A – C) is equal to the sum of the other two (A – B and B – C). In this case, it is possible to build the potential as a function of these two coordinates as a *potential contour map* (Figure 3.5), showing equipotential lines in a two-dimensional plot as a topographical maps.

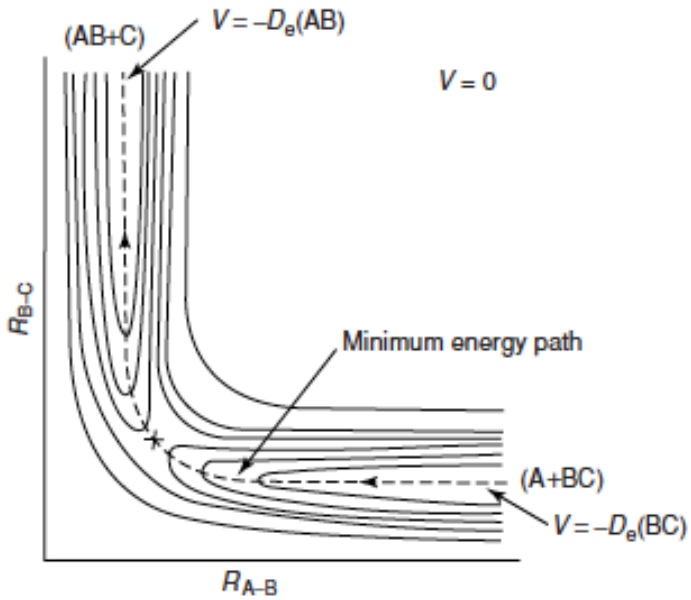

Figure 3.5: Contour map for the PES of the reaction A + BC. The solid lines are contours of given potential energy and the dashed line shows the minimum reaction path. [79]

In the potential plotted as a function of the two bond distances, we can have the *old* A – B bond distance, in the reactant region where C is a infinite distance, and the *new* B – C bond one, in the

product region with A far away. The reaction happens in the middle of these two regions (shown with a **X** in Figure 3.5), where the potential energy surface mediates between the reactants' and products' configuration. This region is at higher energy (*threshold energy* for the reaction) with respect to the other two and the threshold energy represents the cost in energy required to cross over from the reactants' to the products' regions. Because the reaction path passes through the local minima of the surface (dashed line in Figure 3.5), near the activation barrier of the reaction the potential surface has the form of a saddle. Therefore, the configuration of the system in the saddle point of the PES is the *transition state region*, the height of the barrier along the minimum reaction path is the lowest maximum of the potential between the reactants' and products' valleys.

Since molecular species are composed by electrons and atomic nuclei, the motion of these particles is determined by the molecular Hamiltonian, $\hat{H}$. This Hamiltonian contains the nuclear kinetic energy ($\hat{T}_n$), the electron kinetic energy ($\hat{T}_e$), the Coulomb attraction of the electrons and nuclei ($\hat{V}_{ne}$) and the electron-electron ($\hat{V}_{ee}$) and nuclear-nuclear ($\hat{V}_{nn}$) Coulomb repulsion. In atomic unit ($e = \hbar = m_e = 1$), the Hamiltonian can be written as:

$$\begin{aligned}\hat{H} &= \hat{T}_n + \hat{T}_e + \hat{V}_{ne} + \hat{V}_{ee} + \hat{V}_{nn} \\ &= \sum_{\alpha=1}^{N} \frac{\hat{P}_\alpha \cdot \hat{P}_\alpha}{2M_\alpha} + \sum_{i=1}^{N_e} \frac{\hat{P}_i \cdot \hat{P}_i}{2} + \sum_{\alpha=1}^{N}\sum_{i=1}^{N_e} \frac{Z_\alpha}{R_{i\alpha}} + \sum_{i=1}^{N_e}\sum_{j<i}^{N_e} \frac{1}{R_{ij}} + \sum_{\alpha=1}^{N}\sum_{\beta<\alpha}^{N} \frac{Z_\alpha Z_\beta}{R_{\alpha\beta}}\end{aligned} \tag{3.39}$$

where N is the number of atomic nuclei, N_e of the electrons, M_α is the mass and Z_α the charge of nucleus α, $\hat{P}_\alpha$ is the operator for a Cartesian momentum vector for nucleus α, $\hat{P}_i$ is that for the momentum electron i, $R_{i\alpha}$ is the distance between nucleus α and electron i, R_{ij} is the distance between electrons i and j, and $R_{\alpha\beta}$ is the distance between nuclei α and β. The motion of the nuclei is then completely described by the time-dependent Schrödinger equation:

$$i\frac{\delta}{\delta t}\Psi(x, X, t) = \hat{H}\Psi(x, X, t) \tag{3.40}$$

where x and X represent the Cartesian coordinates of all electrons and nuclei, respectively. Equivalently, the time-independent Schrödinger equation (Eqn. 3.41) can be used to obtain any observable associated with molecular motion.

$$\hat{H}\Psi(x, X) = E\Psi(x, X) \tag{3.41}$$

It is interesting to note that in the atomic units the nuclear mass is expressed in terms of electron mass (m_e = 9.31 $\times$ 10^{-31} kg). Therefore, M_α in Eqn. 3.39 is a large number (in the range 10^3-10^5) and therefore, $\hat{T}_n$ is much smaller than the other four terms in the Hamiltonian. Defining the electronic Hamiltonian, $\hat{H}_e$ as:

$$\hat{H}_e = \hat{T}_e + \hat{V}_{ne} + \hat{V}_{ee} + \hat{V}_{nn} \tag{3.42}$$

the total Hamiltonian can be written as:

$$\hat{H} = \hat{T}_n + \hat{H}_e \tag{3.43}$$

Anticipating that $\hat{T}_n$ is small, it is possible to find the eigenfunctions of $\hat{H}_e$ alone ignoring the nuclear kinetic energy and fixing X:

$$\hat{H}_e\psi_i(x;X) = E_i(X)\psi_i(x;X) \quad \text{with } i = 0, 1, 2, ... \tag{3.44}$$

Even if the nuclear coordinates are fixed, the electronic energy (E_i) is different for different nuclear positions. Considering $\hat{T}_n$ in Eqn. 3.43 as a perturbation, the wavefunctions $\psi_i(x;X)$ form a useful basis set for the total wavefunction:

$$\Psi(x,X) = \sum_{i=0}^{\infty} \chi_i(X)\psi_i(x;X) \tag{3.45}$$

where the coefficients $\chi_i(X)$ must be functions of the nuclear coordinates. Including Eqn. 3.45 in the Schrödinger equation, Eqn. 3.41 becomes:

$$(\hat{T}_n + \hat{H}_e)\sum_{i=0}^{\infty} \chi_i(X)\psi_i(x;X) = E\sum_{i=0}^{\infty} \chi_i(X)\psi_i(x;X) \tag{3.46}$$

Dropping x and X from the notation of the wavefunctions for clarity, this gives:

$$\sum_{i=0}^{\infty}\left[\sum_{\alpha=1}^{N}\frac{1}{2M_\alpha}\bigtriangledown_\alpha^2 + \hat{H}_e\right]\chi_i\psi_i = E\sum_{i=0}^{\infty}\chi_i\psi_i$$

$$\sum_{i=0}^{\infty}\left[\sum_{\alpha=1}^{N}\frac{1}{2M_\alpha}\bigtriangledown_\alpha\left(\psi_i\bigtriangledown_\alpha\chi_i + \chi_i\bigtriangledown_\alpha\psi_i\right) + \chi_i\hat{H}_e\psi_i\right] = E\sum_{i=0}^{\infty}\chi_i\psi_i$$

$$\sum_{i=0}^{\infty}\left\{\sum_{\alpha=1}^{N}\frac{1}{2M_\alpha}\left[\psi_i\left(\bigtriangledown_\alpha^2\chi_i\right) + 2\left(\bigtriangledown_\alpha\chi_i\right)\left(\bigtriangledown_\alpha\psi_i\right) + \chi_i\left(\bigtriangledown_\alpha^2\psi_i\right)\right] + \chi_i E_i\psi_i\right\} = E\sum_{i=0}^{\infty}\chi_i\psi_i$$

Pre-multiplying this equation by ψ_j^* and integrating over the electron coordinates (knowing that different eigenfunctions are orthogonal), one can find that:

$$\sum_{\alpha=1}^{N}\frac{1}{2M_\alpha}\bigtriangledown_\alpha^2\chi_j + E_j(X)\chi_j -$$
$$-\sum_{i=0}^{\infty}\sum_{\alpha=1}^{N}\frac{1}{2M_\alpha}\left\{2\langle\psi_j \mid \bigtriangledown_\alpha \mid \psi_i\rangle\left(\bigtriangledown_\alpha^2\chi_i\right) + \langle\psi_j \mid \bigtriangledown_\alpha^2 \mid \psi_i\rangle\chi_i\right\} = E\chi_i \tag{3.47}$$

The terms in curly brackets couple the nuclear wavefunction for the j^{th} electronic state to nuclear wavefunctions for all the other electronic states. In the Born-Oppenheimer (BO) approximation, all these terms are neglected. Due to the fact that the nuclear masses are larger than the electron ones, this is an accurate approximation, as long as the energy $E_j(X)$ is not too close to the energy of the other electronic states. Therefore, considering the remaining terms in Eqn. 3.47, after the BO

approximation for each electronic state we have the nuclear Schrödinger equation:

$$\hat{H}_{nuc}\chi_j = \left[\sum_{\alpha=1}^{N} \frac{1}{2M_\alpha} \bigtriangledown_\alpha^2 + E_j(X)\right] \chi_j(X) = E\chi_i(X) \tag{3.48}$$

The Hamiltonian for the nuclear motion is the sum of the kinetic energy operator and the potential energy ($E_j(X)$), which is the total electronic energy for electronic state j. It is possible to assume that the general $E(X)$ refers to the energy of any electronic state of interest and it is simply the potential energy experienced by the nuclei (usually detonated with the symbol $U(R)$).

Qualitatively, the BO approximation is built on the fact that the nuclei are thousand times more massive than electrons, and then move much more slowly. Therefore, the electron and nuclear motions can be treated separately: the nuclei move in an average potential formed by the electrons, while the electrons adjust instantaneously to a change in the nuclear geometry. This separation is called *adiabatic* and consequently, when a chemical reaction does not involve different electronic state, but its dynamics occurs on a single PES, it shows an adiabatic behavior. In the adiabatic approach, the electrons have all the time to adjust for each configuration of the atom. In this case, as said, the BO approximation is valid and the Hamiltonian is diagonalized with the nuclei in fixed coordinates. Solution of the Hamiltonian diagonalization is $U(R)$, *i.e.* the electronic potential energy surface in which the nuclei move.

On the other hand, a charge transfer is a non-adiabatic process, meaning that the BO approximation fails under some circumstances and the nuclear dynamics occurs on two or more coupled PES. During the collision, the nuclei moves at a velocity not negligible with respect to the velocity of the electrons. This is the condition because of the adiabatic approximations fails because the electrons have not enough time to adjust. Hence, for the *charge transfer* between charged (A^+) and neutral (B) species to form the neutral (A) and charged (B^+) counterparts, the evolution from reactants to products occurs in a time scale comparable to the electron motion. Furthermore, reactants and products constitute two different electronic states and for this reason, the charge transfer happens in presence of coupling between the two different system configurations corresponding to the different position of an electron. For a multi-surface reaction, as in this case, the terms in curly brackets of Eqn. 3.47 can not be neglected and the treatment is very challenging, because the couplings change rapidly with nuclear coordinates. Therefore, it is preferable a *diabatic* representation of the PESs, in which the electronic configuration evolves smoothly with changes to the nuclear coordinates, retaining predominant reactant or product character. In this work, the diabatic PESs corresponding to reactant and product configurations have been developed by using *semi-empirical* method and the detailed procedure will be treated in detail thereafter in this Chapter.

For a chemical reaction, the diabatic curves of the different electronic states can cross, as shown by the dashed lines in Figure 3.6. On the other hand, for the adiabatic PESs (solid lines in Figure 3.6) the crossing is avoided (*non-crossing rule*). This can be demonstrated taking into account two uncoupled, diabatic states, ϕ_1 and ϕ_2, orthornomal eigenstates of the Hamiltonian operator, $\widehat{h}$. They are mixed together by an additional weak coupling term ($\widehat{V}$) in a Hamiltonian operator $\widehat{H} = \widehat{h} + \widehat{V}$. The new Hamiltonian has eigenstates ϕ (*i.e.* the adiabatic states), that can be expressed by linear combination of the diabatic basis functions:

$$\phi = c_1\phi_1 + c_2\phi_2 \tag{3.49}$$

where, c_1 and c_2 are two constants that describe the amounts of each diabatic state for contributing

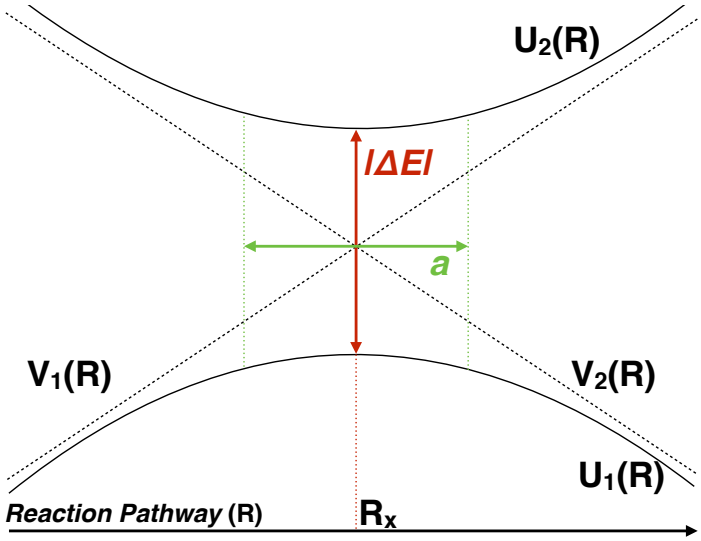

Figure 3.6: Schematic illustration of the crossing of diabatic states ($V(R)_1$ and $V(R)_2$, dashed lines) and the avoided crossing of the adiabatic states ($U(R)_1$ and $U(R)_2$, solid lines) in a narrow region centered in R_x of interaction between of the two electronic states, defined by the parameter a (in green). In red the energy gap (| ΔE |) between the adiabatic curve in the crossing region is reported.

to the adiabatic state. Inserting the linear combination into the Schrödinger equation, multiplying from the left the resultant equation by either ϕ_1 and ϕ_2, and integrating, the energy levels can be determined by solving the secular equation:

$$\begin{bmatrix} H_{11} - E & H_{12} \\ H_{21} & H_{22} - E \end{bmatrix} = 0 \tag{3.50}$$

where:

$$H_{ij} = \langle \phi_i | \widehat{H} | \phi_j \rangle \tag{3.51}$$

Therefore, solutions are:

$$E_{1,2} = \frac{1}{2} \left(H_{11} + H_{22} \right) \pm \sqrt{\left(H_{11} - H_{22} \right)^2 + 4 |H_{12}|^2} \tag{3.52}$$

The resulting energies are a function of the nuclear coordinates because the diabatic wavefunctions, the Hamiltonian operators and the coupling terms all depend on the nuclear geometry. The

two values of E of Eqn. 3.52 are equal only if the two following conditions are satisfied simultaneously:

$$H_{11} = H_{22}$$
$$H_{12} = 0$$

In a diatomic molecule where only the inter-atomic distance R can be varied, this is impossible, because the two conditions require two independently variable nuclear coordinates: hence, the non-crossing of the two curves. However, avoided crossing are also possible in polyatomic systems [80]. Therefore, if the BO approximation fails, the electrons retain their configuration (either reactant or product character) and the nuclear trajectory stays on the same diabatic curve at the barrier. In the adiabatic approach, this is equivalent to a transition from one adiabatic curve to the other one. Furthermore, the two electronic states are separated asymptotically by a fixed energy gap, nevertheless a minimum distance between the two PESs exists in a localized region in the configuration space of the nuclei (| $\Delta E(R_x)$ |). In fact, there is a distance R_x, where the electronic energy is the same for the two different diabatic states. Near R_x the system can change its electronic state with only a very slight change in the kinetic energy of the nuclei [79], that makes the process efficient. The convergence of two non-adiabatic PE curves in the coordinate R_x is known as *curve crossing*. In this case, the adiabatic curves (under the BO approximation) do not cross, but converge and then diverge at R_x.

The cross-section of a non-adiabatic event can be obtained by the semi-classical formulation of Eqn. 3.3, equivalent to Eqn. 3.7. Therefore, it is necessary to define the probability $P(l)$ of Eqn. 3.7 for the non-adiabatic transition, obtained by the following procedure.

To obtain $P(l)$, it results convenient to introduce an *adiabaticity parameter* (ξ) defined by the ratio between the time of a perturbation (linked to the duration of collision, τ_c) and the time scale that a system needs to adjust its electronic configuration (τ_e) [79]:

$$\xi = \frac{\tau_c}{\tau_e} \tag{3.53}$$

In case of short collision time or in other words, for high-velocity collision (*sudden* or *non-adiabatic* limit) , we have that:

$$\tau_c < \tau_e \tag{3.54}$$

For collisions occurring at low velocities, the system is better described following the *adiabatic* limit, when the collision time is longer than the period of oscillation:

$$\tau_c > \tau_e \tag{3.55}$$

The collision time τ_c is defined as:

$$\tau_c = \frac{a}{v} \tag{3.56}$$

where a is the narrow region of the diabatic crossing (Figure 3.6) and v is the relative velocity during the collision. With a slow perturbation, the system has all the time to re-adjust into its instantaneous state, *e.g.* the way in which the electrons adiabatically adjust after a motion of the nuclei in the BO approximation.

The system that crosses the region R_x in a generic time τ has an indefiniteness in energy h/τ. We can have two cases:

1. if $h/\tau > \mid \Delta E(R_x) \mid$, the system can "jump" to the other curve, changing its adiabatic state;
2. if $h/\tau < \mid \Delta E(R_x) \mid$, the system remains on its own curve, maintaining the adiabatic state.

Therefore, the condition for an adiabatic behavior is that the passage through the crossing region R_x must be sufficiently slow. Since in Eqn. 3.55 the time of the collision τ_c must be greater than the time that the system needs to adjust its electronic state (τ_e), τ_e can be assumed as $\frac{h}{|\Delta E(R_x)|}$. The adiabaticity parameter can be rewritten from Eqn. 3.53 as

$$\xi = \tau_{R_x} \frac{\mid \Delta E(R_x) \mid}{h} \tag{3.57}$$

where τ_{R_x} refers not to the whole time of the collision (τ_c), but to the time in which the nuclei are in the region R_x where the gap is small. Therefore, the transition between the two curves occurs only during the time spent in vicinity of R_x and for this reason, v of Eqn. 3.56 becomes the radial velocity at R_x. To evaluate τ_{R_x}, it is necessary to define the spatial parameter a, that can be estimated describing the diabatic curves as linear functions of R close to R_x. The adiabatic gap can be thus defined as difference between the two potential energy curves ($V(R)_1$ and $V(R)_2$ in Figure 3.6) in R:

$$\Delta E(R) = V_1(R) - V_2(R) \tag{3.58}$$

that can be expanded as a Taylor series in R_x:

$$\Delta E(R) = V_1(R_x) + (R - R_x) \left.\frac{dV_1}{dR}\right|_{R_x} - V_2(R_x) - (R - R_x) \left.\frac{dV_2}{dR}\right|_{R_x} \tag{3.59}$$

Knowing that $V_1(R_x) = V_2(R_x)$ and $(R - R_x) = a/2$, we have:

$$|\Delta E(R_x)| = \frac{a}{2} \left| \frac{dV_1}{dR} - \left.\frac{dV_2}{dR}\right|_{R_x} \right| \equiv \frac{a}{2} |\Delta F_x| \tag{3.60}$$

$|\Delta F_x|$ is the absolute value of the differences in slopes at R_x. From Eqn. 3.60, it is possible to obtain a

$$a = \frac{2|\Delta E(R_x)|}{|\Delta F_x|} \tag{3.61}$$

Since τ_{R_x} can be expressed in terms of a and radial velocity (from the relation of Eqn. 3.61), the Eqn. 3.57 becomes:

$$\xi = 2\frac{|\Delta E(R_x)|^2}{hv|\Delta F_x|} \tag{3.62}$$

Therefore, to define the semi-classical probability of a single non-adiabatic transition p, *i.e.* corresponding to approach the crossing region on adiabatic state and exiting on the other adiabatic state, the Landau-Zener-Stückelberg formula [81, 82, 83, 84] (Eqn. 3.63) has been used. It represents the non-adiabatic transition probability (p) at an avoided crossing of adiabatic PESs taking

into account the non-adiabatic jump at the crossing point (R_x) of the diabatic curves and it is based on the adiabatic parameter ξ:

$$p = exp\left(-2\pi^2\xi\right) = exp\left(-\frac{2\pi|\Delta E(R_x)|^2}{\hbar v|\Delta F_x|}\right) \tag{3.63}$$

where $|\Delta E(R_x)|^2$ is associated to the non-adiabatic coupling term between the two adiabatic potential curves, H_x. The radial velocity v is given in terms of orbital angular momentum quantum number l:

$$\begin{aligned} v^2 &= \frac{2}{\mu}\left[E\left(1-\frac{b^2}{R_x^2}\right) - E_x\right] = \\ &= \frac{2}{\mu}\left[E\left(1-\frac{l(l+1)}{k^2R_i^2}\right) - E_i\right] \end{aligned} \tag{3.64}$$

where E is the collision energy of the system, b the impact parameter, μ the reduced mass, k the wavenumber already defined above as $k = 2\pi/\lambda$. The impact parameter b has been substituted knowing the relation:

$$b = \frac{[l\,(l+1)]^{1/2}}{k}$$

The total cross-section $\sigma(E)$ is obtained by applying the Eqn. 3.7 in the range 0 to l_{max}. l_{max}, that is given by the maximum value of l for which v is real:

$$l_{max} = kR_x\left(1-\frac{E_x}{E}\right)^{1/2} \tag{3.65}$$

Therefore, the probability $P(l)$ in Eqn. 3.7 is the total probability associated to the formation of products after the charge transfer. In presence of just one crossing, $P(l)$ would be the combination of single probabilities (Eqn. 3.63) to jump or not between the two diabatic potential curves. Thus, we can have two situations:

1. the system passes the crossing remaining on the diabatic curve of the reactants ($1-p$), but passing again the crossing after the *turning point* and jumping to the other diabatic curve (p);
2. the reactants system jumps to the products potential (p), but after the *turning point*, it remains on this curve ($p-1$).

The total probability $P(l)$ is thus:

$$P(l) = p(p-1) + (p-1)p = 2p(p-1) \tag{3.66}$$

At this point, cross-sections of charge transfer processes are still far to be calculated, since the method to represent the diabatic PESs of the electronic states corresponding to reactant and product configuration is still not reported. In fact, to apply the Landau-Zener-Stückelberg formula (Eqn. 3.63), it is necessary to know the crossing parameters (R_x, v and $|\Delta F_x|$). As already

introduced above, the *semi-empirical* method has been chosen to determine the potential energy interactions between the neutral and the charge particle. In the following Section, the fundamental instruments used for this purpose are thoroughly reported.

3.2 Semi-empirical potential energy surfaces

The *ab initio* methods are grounded to the solution of the Schrödinger equation without any reference to experimental data. On the contrary, the semi-empirical method allows to represent the potential energy surfaces from the global physical properties of the molecules. This method is a valid choice for large inter-atomic and -molecular distances at which the two particles can be considered as two distinct entities without any perturbations on their physical properties. In general, the interaction V between atomic or molecular systems is represented by several contributions. For example, the interactions between charges (q), dipoles (μ) and multipoles (Q) define the *electrostatic components* of the inter-molecular forces. Furthermore, q, μ, Q of a molecule might cause phenomena of *induction* on another molecule, which will be characterized by μ_{Ind} and Q_{Ind}. Also the induced multipole- induced multipole interaction plays a role in the total potential, determining the *dispersion contribution*. These three components have the common characteristic to arise already for long particle distance and for this reason, they are called *long range* contributions; the combination of these terms gives often an attractive potential, except when there are strong repulsive electrostatic interactions between, for example, charges of the same sign. To these *long range* terms, it is requested to sum the other *short range* components:

- **Repulsive contribution**: it arises from the repulsion between nuclei and valence electrons of the interacting species;
- **Chemical contribution**: coming from the possibility of two systems to share one or more electrons.

The combination of attractive and repulsive contributions allows the formation of a potential well, with depth ε_m (shown in red in Figure 3.7). In other words, starting from large inter-molecular distances and reducing R, $V(R)$ tends first to decrease, passing to a well with ε_m depth at a certain distance r_m and then, it raises for the repulsive interactions at short r.

Focusing only on the long range contributions, we have the Eqn. 3.67.

$$V = V_{Electr} + V_{Ind} + V_{Disp} \tag{3.67}$$

Before defining each single contribution of V, it is necessary to identify which parameters and physical quantities are fundamental for the interaction potential. The first property that needs to be mentioned is the total charge q_i of each atom of a system. In case of distribution of partial charges in non-spherically symmetric molecules, it is also important to consider, as already said, the *permanent dipole moment* (μ_p) and the *permanent quadrupole moment* (Q_p). Other important properties are the ionization potential (I_i) and the electronic affinity (A_i).

Furthermore, the *polarizability* (α) represents an essential property to describe the interactions, because it quantifies the possibility of chemical species to create instantaneous dipoles and to deform its charge distribution, forming induced dipoles in presence of an external charge q_i.

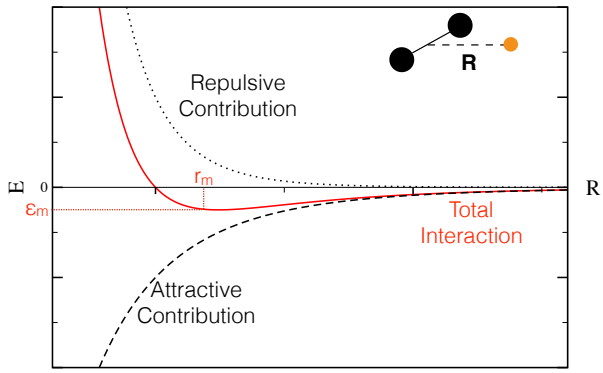

Figure 3.7: Example of interaction potential between a homonuclear diatomic molecule and an atom (*e.g.* an ion) as a function of **R** distance between the two species. In red the characteristic parameters, ε_m and r_m, of the potential are highlighted. The decreasing dashed line indicates the attractive contribution, while the increasing pointed line the repulsive one.

Considering a spherical atom in an electric field $\overrightarrow{\xi}_e$, the atom will be subjected to a deformation of its electronic distribution, forming an induced dipole moment ($\overrightarrow{\mu}_{ind}$):

$$\overrightarrow{\mu}_{ind} = \alpha \overrightarrow{\xi}_e \tag{3.68}$$

from which it is possible to define the potential created by the induced dipole in the electric field (V_{ind}):

$$V_{ind} = -\int_0^{\overrightarrow{\xi}_e} \overrightarrow{\mu}_{ind} d\overrightarrow{\xi}_e = -\frac{1}{2}\alpha \overrightarrow{\xi}_e^2 \tag{3.69}$$

On the other hand, in a Cartesian coordinate system, the polarizability of poly-atomic molecules can be defined as a tensor in terms of the three principal components, α_{xx}, α_{yy} and α_{zz}. The simplest case is that of a diatomic homonuclear molecule with the inter-nuclear axis aligned along the z-axis and exposed to a electric field $\overrightarrow{\xi}_e$, generated *e.g.* by an ion (Figure 3.8). Due to the alignment between the bond and the z-axis, the tensor can be simplified in terms of parallel ($\alpha_\parallel = \alpha_{zz}$) and perpendicular ($\alpha_\perp = \alpha_{xx} = \alpha_{yy}$) components. From a mathematical point of view, the polarizability tensor is described by the *diagonal matrix*, $\underline{\alpha}$ [85]:

$$\underline{\alpha}_j = \begin{bmatrix} \alpha_{1\perp} & 0 & 0 \\ 0 & \alpha_{2\perp} & 0 \\ 0 & 0 & \alpha_\parallel \end{bmatrix} \tag{3.70}$$

Defined ϑ as the angle formed by the direction of the approaching atom and the bond of the diatomic molecule in the CM (Figure 3.8), the angle-dependent polarizability can be written as:

$$\alpha(\vartheta) = \alpha_{\parallel} cos^2(\vartheta) + \alpha_{\perp} sin^2(\vartheta) \tag{3.71}$$

The average value of the polarizability for the diatomic molecule corresponds to the average of

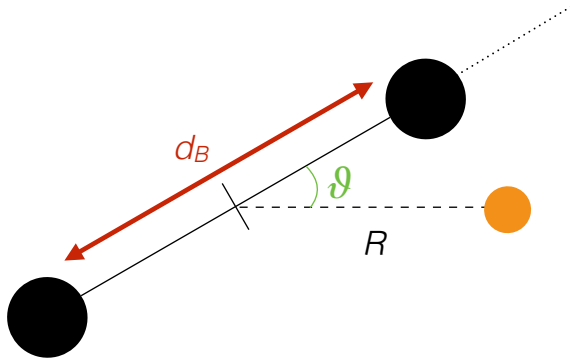

Figure 3.8: Homonuclear diatomic molecule of bond length d_B, which interacts with an ion, that produces an electric field. The angle ϑ defines the direction of the approaching atom.

the three principal tensor components:

$$\overline{\alpha} = \frac{\alpha_{1\perp} + \alpha_{2\perp} + \alpha_{\parallel}}{3} \tag{3.72}$$

A way to predict the polarizability of a polyatomic molecule is to consider the electronic charge distribution around each molecular bond and then to sum each polarizability contribution to obtain the total polarizability [86]. Therefore, the average molecular polarizability $\overline{\alpha}_{tot}$ is the sum of each j average bond component:

$$\overline{\alpha}_{tot} = \sum_j \overline{\alpha}_j \tag{3.73}$$

3.2.1 Electrostatic Potential (V_{Electr})

The first element of Eqn. 3.2 to define is V_{Electr}, the electrostatic component that arises from the interaction between charges and/or permanent dipoles and/or permanent multi-poles in the interaction species. The interaction between two simple diatomic linear molecules, represented in Figure 3.9, can be evaluated. In the figure, **O** and **P** are the CM of the molecules and q_1, q_2, q_1', q_2' the charges. Defining R as the distance between the centers of mass, if $R >>> z_1, z_2, z_1', z_2'$, V_{Elect}

Figure 3.9: System of two collinear diatomic molecule with charge distributions.

is described as a multipole expansion:

$$V_{Electr} = \frac{1}{4\pi\varepsilon_0}\left(\frac{qq'}{R} + \frac{\mu q' - \mu' q}{R^2} + \frac{qQ' + q'Q}{R^3} + \frac{3\mu Q' - 3\mu' Q}{R^4} + \frac{6QQ'}{R^5}\right) \tag{3.74}$$

where ε_0 is the *vacuum permittivity*. In Eqn. 3.74, the physical quantities are:

- $q = q_1 + q_2$ and $q' = q'_1 + q'_2$: the total charges of the two molecules;
- $\mu = q_2 z_2 - q_1 z_1$ and $\mu' = q'_2 z'_2 - q'_1 z'_1$: the electric dipole moments;
- $Q = q_1(z_1)^2 + q_2(z_2)^2$ and $Q' = q'_1(z'_1)^2 + q'_2(z'_2)^2$: the electric quadrupole moments.

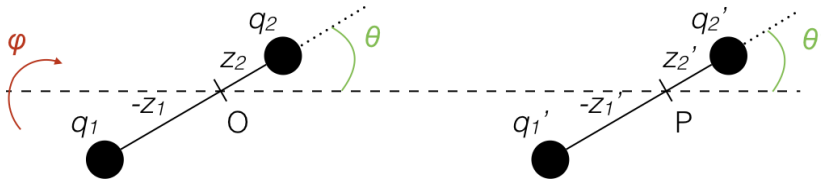

Figure 3.10: System of two not collinear diatomic molecule with charge distributions.

If the molecules are not collinear, the terms of Eqn. 3.74 have to be weighted for the different configurations as a function of $\theta_1, \theta_2, \varphi$, defined in Figure 3.10.

For example, assuming $q, q', Q, Q' = 0$, Eqn. 3.74 becomes:

$$V_{Electr}(R, \theta_1, \theta_2, \varphi) = -\frac{\mu\mu' A_r(\theta_1, \theta_2, \varphi)}{4\pi\varepsilon_0 R^3} \tag{3.75}$$

with A_r:

$$A_r(\theta_1, \theta_2, \varphi) = 2cos\theta_1 cos\theta_2 - sin\theta_1 sin\theta_2 cos\varphi \tag{3.76}$$

These are the cases with fixed molecules. When it is requested to consider rotating molecules, it is necessary to do a weighted mean of all the possible orientations. If the configurations are equiprobable, all the terms in Eqn. 3.74 cancel out except the first one.

In case of a poly-atomic molecule interacting with an ion, the way to represent the electrostatic potential is to consider the interaction between the ion and each of the atoms of the molecule,

characterized by a net atomic charge (also called *partial charge*). The partial charge is generated by the asymmetric distribution of the electrons in a chemical bond, in which two electrically neutral atoms of different electronegativity are connected. Therefore, the total electrostatic potential can be written as:

$$V_{Electr} = \frac{q}{4\pi\varepsilon_0} \sum_{i}^{N} \frac{\delta q_i}{R_i} \tag{3.77}$$

where N is the total number of the atoms of the poly-atomic molecule, δq_i is the partial charge of the i atom, and R_i the distance between the ion and the i atom. Partial charges can be obtained experimentally, for example from measured dipole moments or by measuring the electron densities using high resolution X-ray, gamma ray, or electron beam diffraction experiments.

When experimental data are not available, it is necessary to assign partial atomic charges from quantum chemistry calculations. In this thesis, the *natural orbital* approach has been used for this purpose and the details are given at the end of the Chapter.

3.2.2 Induction Potential (V_{Ind})

This contribution to the total potential energy is due to the interaction between an induced multipole and the charges of the inducing species. If the electric field is produced by a charge q, the V_{Ind} is defined as:

$$V_{Ind} = -\frac{1}{2(4\pi\varepsilon_0)^2} \frac{q^2\alpha}{r^4} = -\frac{C_{4Ind}}{r^4} \tag{3.78}$$

where α is the polarizability of the molecule. The other terms, *e.g.* charge-induced quadrupole and charge-induced octupole, which vary as a function of r^{-6} and r^{-8}, respectively, are often ignored.

3.2.3 Dispersion Potential (V_{Disp})

The interaction between instantaneous multipoles and induced multipoles forms the dispersion potential, V_{Disp}, which is represented by the following expression:

$$V_{Disp}(r) = -f_6 \frac{C_{6Disp}}{r^6} - f_8(r) \frac{C_8}{r^8} - f_{10}(r) \frac{C_10}{r^{10}} - ... \tag{3.79}$$

where $f_i(r)$ are factors that tend to zero for short values of r, while $f_i(r) \to 1$ for $r \to \infty$. For r in the middle-long range, the resulting V_{Disp} is:

$$V_{Disp} = -\frac{C_{6eff}}{r^6} \tag{3.80}$$

The coefficient C_{6eff} includes the first term and all the other ones, *i.e.* dipole-dipole, dipole-multipole and multipole-multipole interactions. It tends to C_6 for large r.

Many attempts have been done to describe C_6 and C_{6eff} properly. In particular, Slater and Kirkwood [87] demonstrated in 1931 the following semi-empirical expression for C_{6eff}:

$$C_{6eff} = \frac{3eh}{2m_e^{1/2}\pi} \frac{\alpha_1\alpha_2}{(\frac{\alpha_1}{N_{e1}})^{1/2} + (\frac{\alpha_2}{N_{e1}})^{1/2}} \tag{3.81}$$

where e and m_e are the electron charge and mass, h is the Planck constant and α_1 and α_2 are the polarizability of the two interacting species, respectively. N_{e1} and N_{e2} are the numbers of electron on the species 1 and 2, respectively, that contribute to the dipole formations, and therefore, $\frac{\alpha_1}{N_{e1}}$ and $\frac{\alpha_2}{N_{e2}}$ are the electron density reciprocals.

The formula allows an easy calculation of C_{6eff} in terms of polarizability, but it requires a correct evaluation of the electron numbers N_{e1} and N_{e2}. As a general rule, the number of electrons of the outer shells has been used for N_{e1} and N_{e2}, but this approximation is too rude for many-electron systems, in which also *core* electrons might have a contribution in the dipole formations. In this context, Pitzer [88] first proposed to take different N_{e1} and N_{e2}, higher than the number of the valence shell electrons in order to consider the effect of inner electrons on the formation of dipoles. Succesively, Koutselos and Mason [89] indicated that N_{e1} and N_{e2} depend on the overall electronic structure of the atoms.

For atomic species, a progress has been achieved with a simple empirical formula [90] (Eqn. 3.82) to calculate N_{eff} (*effective electrons* determining the long-range interactions) only in terms of inner and outer orbital electron numbers (N_{inn} and N_{ext}, respectively). In fact, it is possible to consider that:

- N_{eff} must depend on the outer electron ratio $\frac{N_{ext}}{N_{tot}}$, since N_{ext} give the bigger contribution to the polarization;
- also the inner electrons contribute to the polarization;
- since the outer electrons are effected by "shield" phenomena, that might reduce the effective electron number, N_{eff} must depend on $N_{inn} - N_{ext}$.

On the basis of these observations, the authors of [90] proposed the following formula to calculate N_{eff}:

$$\frac{N_{eff}}{N_{ext}} = 1 + (1 - \frac{N_{ext}}{N_{inn}})(\frac{N_{inn}}{N_{tot}})^2 \tag{3.82}$$

with $N_{tot} = N_{ext} + N_{inn}$, the total number of the electrons of the atom. Eqn. 3.82 can be also expressed in the following form:

$$N_{eff} = N_{ext} + (\frac{N_{ext}}{N_{tot}})(\frac{N_{inn}}{N_{tot}})(N_{inn} - N_{ext}) \tag{3.83}$$

For molecular systems, the formulas are basically the same, considering an average polarizability, weighted for all the possible orientations (see equations 3.72 and 3.73). In this case, the effective numbers of electrons must be calculated taking into account the electrons effectively involved in the bonds (N_b) and the other external electrons not involved in bonds (N_{nb}). *Core* electrons are ignored due to the minor effect on long-range interactions. For molecules made up of

light atoms, an approximated formula can be written as follows:

$$\frac{N_{eff}}{N_t} = 1 - \frac{N_b N_{nb}}{N_t^2} \tag{3.84}$$

where the total external electron number (N_t) is given by the sum of N_b and N_{nb}. The remaining electrons are considered being part of the core. When all the external electrons give bond (*e.g.* in the molecule of H_2 or in the hydrocarbons), N_t coincides with N_{eff}.

The expressions for N_{eff} can be used in Eqn. 3.81 giving C_{6eff} coefficients in agreement with experimental values [90].

The Lennard-Jones Potential and its improved versions

A simple and computationally light potential function for the dispersion interaction is the Lennard-Jones one. In reduced unity, it is defined as:

$$v_{LJ}(x) = \frac{m}{n-m} x^{-n} - \frac{n}{n-m} x^{-m} \tag{3.85}$$

where $n = 12$ and $m = 6$ for neutral-neutral interaction and x is the reduced distance, $x = \frac{r}{r_m}$. The first term constitutes the repulsive contribution, while the second one is about the attraction. This function reproduces the characteristics of the potential well satisfactorily, but it fails in the representation of both the short-range repulsion (too repulsive) and the long-range attraction (overestimated as much as a factor two) [91]. Maitland and Smith suggested a correction in 1973 [92] with a $[n(x), 6]$ function instead of the $[12, 6]$ one. The suggestion of the authors [92] was to define $n(x)$ as:

$$n(x) = 13 + \gamma(x - 1) \tag{3.86}$$

where $2 \leqslant \gamma \leqslant 10$. From comparison between the behavior of the $[n(x), 6]$ and $[12, 6]$ potential models, the formulation of the potential allows a significant improvement of the log range attraction representation using a γ=10, but still incomplete for the repulsive wall. Lower γ values give a more reliable short range behavior, but determine a too large attraction.

In the 2000s, Pirani *et al.* [91, 93] proposed a modification of the Maitland formula with a $[n(x), m]$ function, called *Improved Lennard-Jones* potential, V_{ILJ}. According to this new formulation, the Eqn. 3.85 becomes:

$$v_{ILJ}(x) = \frac{V(r)}{\varepsilon} = \frac{m}{n(x)-m} x^{-n(x)} - \frac{n(x)}{n(x)-m} x^{-m} \tag{3.87}$$

where parameter m is 6 for all neutral-neutral systems, 4 for ion-neutral and 1 for ion-ion cases [93]. In this case, $n(x)$ has a more pronounced dependence on the reduced distance x:

$$n(x) = \beta + 4x^2 \tag{3.88}$$

The factor β is related to the hardness/softness (and thus to the polarizability α) of the interacting partners and it varies in a narrow range of values ($7 \leqslant \beta \leqslant 9$). The mentioned representation of $n(x)$ allows the correct characterization of the long-range attraction, as well as of the repulsive wall at short distance, attenuating this contribution with respect to the Maitland and Smith correction.

3.2.4 The correlation formulas

The correlation formulas allow the connection between the polarizability, α, and the properties of the PES well, *i.e.* the depth and its location. As already said, since the interaction potential is represented by attractive and repulsive contributions, in the intermediate region the balancing of the two forces creates the potential well. The *van der Waals* forces are especially affected by the polarizability, because it characterizes the long-range dispersion interactions. For this reason, depth (ε) and position (r_m) of the well are functions of α.

For neutral-neutral interactions between A and B species, it is possible to define r_m [90, 94] as

$$r_m = 1.767 \frac{\alpha_A^{1/3} + \alpha_B^{1/3}}{(\alpha_A \alpha_B)^{\gamma}} \tag{3.89}$$

where r_m is in Å, and polarizabilities α_A and α_B are in Å^3. The coefficient and the exponent ($\gamma = 0.095 \pm 0.005$), are empirical values. [94] In Eqn. 3.89 the numerator represents the effect of the repulsion, while the denominator is about the effect of the attraction. This formula and the following one are obtained by a statistical analysis of a large number of *van der Waals* systems. [94, 95]

Following the same procedure, the ε [90] is:

$$\varepsilon = 0.720 \frac{C_{6eff}}{r_m^6} \tag{3.90}$$

obtaining ε in meV from C_{6eff} (defined in Eqn. 3.81) in meV Å and r_m (Eqn. 3.89) in Å. The coefficient 0.720 is a empirical value [94].

For ion-neutral (I and B, respectively) interactions, it is possible to use the same approach used for the neutral-neutral systems. Again, since the polarizability is related to the size of the outer electronic orbitals, it used to represent the mutual repulsion. For the attractive contribution, in addition to the multipole dispersion interaction, it is necessary to add the ion-induced multipole interaction, function of the polarizability (Eqn. 3.78) and dominant at a large distance. [96] To evaluate the contribution of both the interactions, it is essential to define (Eqn. 3.91 [96]) a dimensionless parameter, ρ, as the ratio of the dispersion forces to the induction ones.

$$\begin{aligned} \rho = \frac{V_{Disp}}{V_{Ind}} = \frac{C_{6eff}/R_m^6}{C_{4eff}/R_m^4} = \\ = K \frac{\alpha_I \alpha_B}{[1 + (2\alpha_I/\alpha_B)^{2/3}]\alpha_B^{3/2}} \end{aligned} \tag{3.91}$$

where C_{6eff} and C_{4eff} are already defined in Eqn. 3.78 and Eqn. 3.81, respectively, and K is 1, if the polarizabilities are in Å^3. The exponent $3/2$ of α_B is related to the different R dependence of the attraction terms (R^{-6} for the dipole-dipole interaction in the dispersion and R^{-4} fro the ion-dipole interaction in the induction). In square brackets there is the normalization factor to take into account the relative weights of the interaction contributions for a single ionized ion. Considering the induction forces and the ρ term, R_m and ε can be obtained basically from the same formulas

of the neutral-neutral case. So, for r_m we can have:

$$r_m = 1.767 \frac{\alpha_I^{1/3} + \alpha_B^{1/3}}{(\alpha_I \alpha_B [1 + 1/\rho])^{\gamma}} \tag{3.92}$$

where γ and the coefficient 1.767 are the same of Eqn. 3.89. If the induction forces have a low contribution (*i.e.* $1/\rho \to 0$), Eqn. 3.92 becomes equal to Eqn. 3.89.

ε can be written as [96]:

$$\varepsilon = 5.20 \times 10^3 \frac{\alpha_B}{R_m^4}(1 + \rho) \tag{3.93}$$

As above, if $\rho \to 0$ (low contribution of dispersion forces), Eqn. 3.93 represents the effect of a point-like ion-multipole interaction. On the contrary, for large values of ρ, Eqn. 3.93 is equal to the neutral-neutral ε (Eqn. 3.90). It is interesting to note that, defining $\varepsilon = k\frac{C_4}{r_m^4}(1 + \rho)$, the empirical value k is the same of Eqn. 3.90 (0.72), meaning that in the well region the attraction and the repulsion play the same relative role in the ion-neutral and neutral-neutral cases [97].

From the correlation formulas, it is possible to summarize:

- the physical properties directly affecting the principal features of the interaction are α, μ and q (polarizability, dipole moment and charge);
- the correlation formulas are simple expressions for bond energies (ε_m);
- the bond energies are a defined percentage ($72 - 85\%$) of the total attraction evaluated in r_m;
- all the formulas reported can be used to estimate the spherical (*isotropic*) component of the interaction;
- introducing the reduced quantities, $x = \frac{r}{r_m}$ and $v(x) = \frac{V(x)}{\varepsilon_m}$, it is obtained that $v(x)$ has a similar behavior as a function of the parameter x for similar systems.

3.2.5 The anisotropic case

Until now, we have spoken only about atomic or spherically symmetrical molecular systems, characterized by isotropic potentials. In anisotropic systems, it is necessary to include the angular dependence in the potential expressions. Following the previously general definition of $\alpha(\vartheta)$ (Eqn. 3.71) for an ion-diatomic molecule, the depth (ε_m) and position (r_m) of the potential well can be expressed as a function of the angle (ϑ) [91]:

$$\varepsilon_m(\vartheta) = \varepsilon_{\perp} sin^2(\vartheta) + \varepsilon_{\parallel} cos^2(\vartheta)$$
$$r_m(\vartheta) = r_{\perp} sin^2(\vartheta) + r_{\parallel} cos^2(\vartheta)$$

Furthermore, in a anisotropic potential model the specific role of any atom-bond in the atom-molecule system has to be taken in account. In this case, the potential energy V of the many body system can be represented as:

$$V = \sum_{i>j} V_{ij} + \sum_{i>j>k} V_{ijk} + \cdots = \sum V_{2bodies} + \sum V_{3bodies} + \cdots \tag{3.94}$$

Often, it is considered only the first term, assuming that total interaction energy is simply derived from the sum of the all two bodies interactions, neglecting the higher order terms. V can be represented also by an atom-bond approach (the same used to define the polarizability, in which a poly-atomic molecule is conceived as an ensemble of diatoms, coinciding with the bonds) In this case, the potential maintains its additive formulation, including high-order effects, and it can be formed by atom-bond components V_{ab}, *e.g.* described by a ILJ potential (see Eqn. 3.87).

$$V = \sum_b V_{ab}(r_{ab}, \vartheta_{ab}) \tag{3.95}$$

where r_{ab} is the distance of the approaching probe atom a from the dispersion center localized on the b bond (R in Figure 3.8) and ϑ_{ab} is the angle ϑ of Figure 3.8.

3.3 Natural Bond Orbital (NBO) method

As already said, when experimental data are not available, the determination of the electronic configuration and net charges associated with each atom in a poly-atomic molecule is often the final goal of quantum chemical studies. The information concerning atomic charge distributions is important, for example, to represent the electrostatic potential when an ion interacts with a poly-atomic molecule (see Sec. 3.2.1). For this reason, the NBO analysis has been applied to obtain the net charges of the methyl formate. However, quantifying the atomic charges and orbital populations represents a challenging problem, even when accurate wave functions are available. One of the method proposed for atomic population analysis is that of Mulliken [98, 99], even if it fails to give a useful and reliable characterization of the charge distribution in many cases:

- Mulliken populations can have negative values, which have no physical significance [100];
- for compounds with significant ionic character, Mulliken populations seem to give an unreasonable physical picture of the charge distribution [101];

Weinhold and co-workers [102, 103, 104, 105, 106, 107, 108, 109] proposed an alternative method of population analysis, based on the construction of a set of "natural atomic orbitals" (NAOs) for a given molecule in an arbitrary atomic orbital basis set. The NAOs are the orthonormal atomic orbitals of maximal occupancy for the given wave function Ψ, and are obtained as eigenfunctions of the atomic first-order density matrix $\Gamma^{(1)}$ [110], derived by averaging over all but one of the N electronic space-spin coordinates:

$$\Gamma^{(1)} = N \int |\Psi(1, 2, ..., N)|^2 d\tau_2 d\tau_3 ... d\tau_N \tag{3.96}$$

The first order density matrix may be diagonalized, and the corresponding eigenvectors and eigenvalues are the natural orbitals (θ_k) and the occupation numbers, respectively.

$$\Gamma^{(1)}\theta_k = n_k\theta_k \tag{3.97}$$

where n_k is the occupancy (electronic population) of θ_k, subject to the *Pauli exclusion limit* ($0 \leq n_k \leq 2$), and defined as:

$$n_k = \langle\theta_k|\Gamma^{(1)}|\theta_k\rangle \tag{3.98}$$

The idea of Weinhold and co-workers was to deduce the shape of the atomic orbitals in the molecule from the one-electron density matrix and the type of molecular bonds from the electron density between the atoms. This idea is known as *Natural Atomic Orbital* (NAO) and *Natural Bond Orbital* (NBO) analysis.

Assuming that the basis functions have been arranged so that all orbitals located on center A are before those on center B, which are before those on center C , etc. (where A, B, C, etc. are the atoms of a poly-atomic molecule), the density matrix can be written in terms of blocks of basis functions belonging to a specific center:

$$\Gamma = \begin{bmatrix} \Gamma_{AA} & \Gamma_{AB} & \Gamma_{AC} & \cdots \\ \Gamma_{BA} & \Gamma_{BB} & \Gamma_{BC} & \cdots \\ \Gamma_{CA} & \Gamma_{CB} & \Gamma_{CC} & \cdots \\ \cdots & \cdots & \cdots & \cdots \end{bmatrix} \tag{3.99}$$

Therefore, the NAOs for a specific atom in the molecular environment can be obtained diagonalizing the density matrix block of the basis functions belonging to the specific atomic center (*i.e.* the NAOs of the atom A are those that diagonalize the Γ_{AA} block of matrix 3.99). In general, these NAOs are not orthogonal and the orbital occupancy does not correspond to the total number of electrons. Hence, the orbitals should be orthogonalized to have a well-defined division of system electrons.

The NAOs resemble the pure atomic orbitals as calculated for an isolated atom. Furthermore, they can be divided on the basis of the occupancy into a *natural minimal basis*, corresponding to the occupied atomic orbitals for the isolated atoms, and a set of *natural Rydberg orbitals*, corresponding to the remaining and formally unoccupied orbitals. The minimal set of NAOs is strongly occupied, while the Rydberg one is weakly occupied (the occupancies are not necessarily zero, but these orbitals play only a secondary role in describing the electron density associated with the atom). Therefore, the procedure is the following:

1. Each of the atomic blocks in the density matrix Γ is diagonalized, producing a set of non orthogonal NAOs (*pre*-NAOs);
2. the strongly occupied *pre*-NAOs for each center are made orthogonal to all the other *pre*-NAOs on the other centers by an occupancy-weighted procedure;
3. the weakly occupied *pre*-NAOs on each center are made orthogonal to the strongly occupied NAOs on the same center;
4. the weakly occupied NAOs are made orthogonal to all the weakly occupied NAOs on the other centers by an occupancy-weighted procedure.

The diagonal elements of the density matrix in this basis are the orbital populations: to obtain the atomic charge, all contributions from orbitals belonging to a specific atom have to be summed up.

From the off-diagonal blocks of the density matrix transformed to the NAO basis and their occupation number, it is possible also identify the type of bonds between the atoms. We can have different cases:

- the NAOs with occupation number close to 2 are *core orbitals*;
- if the occupation number is large (> 1.90), the NAOs are identified as *lone pair orbitals*;
- removing the previous contributions, only the two-by-two sub-blocks (of each pair of atoms) remain in the density matrix. In this case NBO are the eigenvectors with large eigenvalues (occupation number > 1.90);

At this point, the obtained NBOs can be written as linear combination of NAOs, knowing which atomic orbital are involved in the chemical bond.

For this thesis, the NBO analysis have been performed on geometric optimized dimethyl ether and methyl formate by using Gaussian09 software [111]. M06-2X functional with cc-pVTZ/cc-pVQZ basis sets have been chosen to perform the optimization of the molecule geometries. Details on this DFT functional and the chosen basis sets are reported in Appendix B.

Chapter 4

The Experimental Results

"Things get damaged
Things get broken
I thought we'd manage, but words left unspoken
Left us so brittle
There was so little left to give."

Precious - Depeche Mode

In this chapter, the results of the experiments on the reaction of He^+ with dimethyl ether (CH_3OCH_3, DME) and with methyl formate ($HCOOCH_3$, MF) will be presented and discussed.

4.1 Reaction of He^+ with CH_3OCH_3 (DME)

For both DME and MF reactions, helium ions have been generated by electron ionization (see Sec. 2.2.1) at electron energies in the range $90\,\mathrm{eV}$ to $100\,\mathrm{eV}$. The neutral reagent used to fill the reaction chamber was gaseous DME, purchased from SIGMA-ALDRICH ($\geq$ 99.9%, GC purity). The ionic products of the reaction He^+ + DME have been explored by recording mass spectra at different pressures of the neutral reagent and results are shown in Figure 4.1. The low pressure mass spectra are shown in detail on the right panel of Figure 4.1. The spectra were obtained at a collision energy in the CM frame of about $1.6\,\mathrm{eV}$, and with different pressures of DME inside the reaction cell: $1.9 \times 10^{-7}\,\mathrm{mbar}$ (black), $4.6 \times 10^{-7}\,\mathrm{mbar}$ (red), $9.9 \times 10^{-7}\,\mathrm{mbar}$ (blue), $4.9 \times 10^{-6}\,\mathrm{mbar}$ (green), and $1.01 \times 10^{-5}\,\mathrm{mbar}$ (orange) (Figure 4.1).

The first notable result is the absence, at all the explored pressure regimes, of a peak at *m/z* 46, corresponding to the DME radical cation ($H_3COCH_3^{\bullet+}$). In fact, the *charge transfer* process should potentially give the following products:

$$He^+ + H_3COCH_3 \longrightarrow He + [(H_3C)_2O]^{\bullet+} \qquad (m/z\,46) \qquad (4.1)$$

The absence of this product means that React. 4.1 ($\Delta_r H^\circ$=14.562 eV) is completely dissociative, leading to a series of products in which an ionic fragment is associated with one (or more) possible neutral partners.

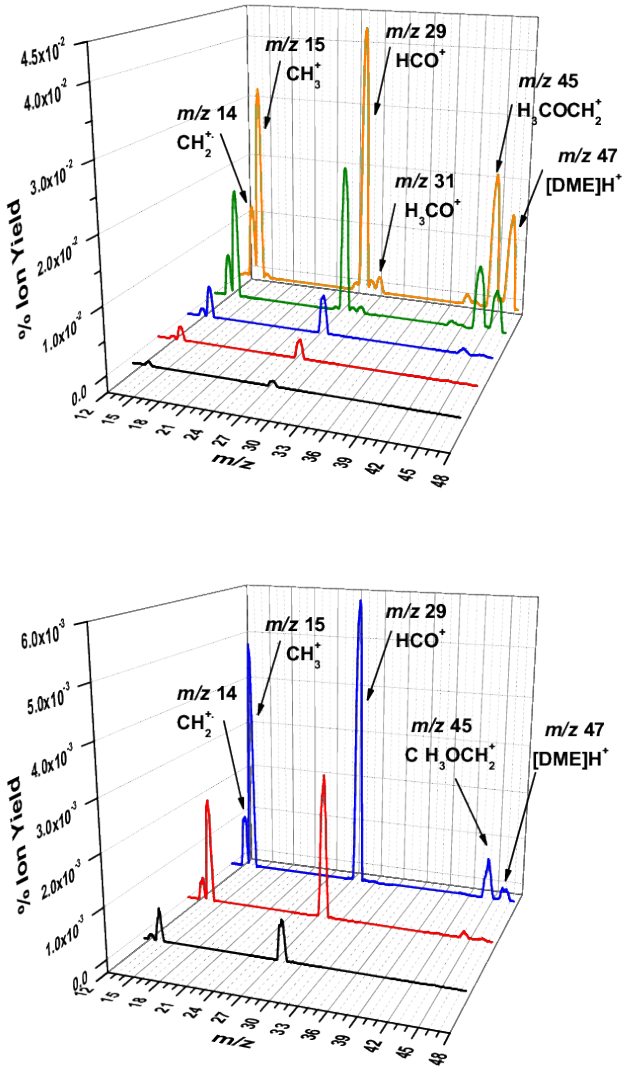

Figure 4.1: Mass spectra of selected He^+ ions reacting with DME at different pressures inside the reaction cell: 1.9×10^{-7} mbar (black), 4.6×10^{-7} mbar (red), 9.9×10^{-7} mbar (blue), 4.9×10^{-6} mbar (green), and 1.01×10^{-5} mbar (orange) (on the top). The collision energy in the CM-frame has been fixed at 1.6 eV and the signal intensity of the He^+ ion (100%) is not shown. On the bottom, it is shown a zoomed view of mass spectra in range 1×10^{-7} mbar to 1×10^{-6} mbar. Ionic products and respective *m/z* values are reported to facilitate reading.

By thermodynamic considerations (as it will be discussed in the following), the fragmentation channels that are compatible with the observed mass spectra and the detected ionic products are the following:

$$\mathrm{He^+ + H_3COCH_3} \longrightarrow \mathrm{He + CH_2{}^{\bullet +}}\ (m/z\,14) + \mathrm{CH_3O^\bullet + H^\bullet} \tag{4.2}$$
$$\longrightarrow \mathrm{He + CH_2{}^{\bullet +}}\ (m/z\,14) + \mathrm{CH_2O + 2\,H^\bullet} \tag{4.3}$$
$$\longrightarrow \mathrm{He + CH_3{}^+}\ (m/z\,15) + \mathrm{CH_3O^\bullet} \tag{4.4}$$
$$\longrightarrow \mathrm{He + CH_3{}^+}\ (m/z\,15) + \mathrm{CH_2O + H^\bullet} \tag{4.5}$$
$$\longrightarrow \mathrm{He + CH_3{}^+}\ (m/z\,15) + \mathrm{HCO^\bullet + 2\,H^\bullet} \tag{4.6}$$
$$\longrightarrow \mathrm{He + CH_3{}^+}\ (m/z\,15) + \mathrm{CO + 3\,H^\bullet} \tag{4.7}$$
$$\longrightarrow \mathrm{He + HCO^+}\ (m/z\,29) + \mathrm{CH_4 + H^\bullet} \tag{4.8}$$
$$\longrightarrow \mathrm{He + HCO^+}\ (m/z\,29) + \mathrm{CH_3{}^\bullet + H_2} \tag{4.9}$$
$$\longrightarrow \mathrm{He + HCO^+}\ (m/z\,29) + \mathrm{CH_3{}^\bullet + 2\,H^\bullet} \tag{4.10}$$
$$\longrightarrow \mathrm{He + HCO^+}\ (m/z\,29) + \mathrm{CH_2{}^\bullet + H^\bullet + H_2} \tag{4.11}$$
$$\longrightarrow \mathrm{He + HCO^+}\ (m/z\,29) + \mathrm{CH^\bullet + 2\,H^\bullet + H_2} \tag{4.12}$$
$$\longrightarrow \mathrm{He + CH_3O^+}\ (m/z\,31) + \mathrm{CH_3{}^\bullet} \tag{4.13}$$
$$\longrightarrow \mathrm{He + CH_3O^+}\ (m/z\,31) + \mathrm{CH_2{}^\bullet + H^\bullet} \tag{4.14}$$

At pressures higher than about 2×10^{-7} mbar, small peaks at *m/z* 45 and 47 are observed with intensities that increase with the pressure. These products are $CH_3OCH_2^+$ (*m/z* 45) and protonated (*m/z* 47) DME, respectively. According to Appendix A, their presence can be explained by the secondary collisions of the most abundant primary products (HCO^+ and CH_3^+) with DME. This hypothesis is validated by measurements of ion yields (*m/z* 45 and 47) as a function of the DME pressure inside the reaction cell (see Figures 4.2 and 4.3 where pressure values have been transformed into densities as explained in Chapter 2 in Sec. 2.3.4): in both cases, the yields show a quadratic dependence from pressure, a clear indication of secondary collisions (see Appendix A).

In order to have a quantitative indication of the best fit, the *adjusted R-square* parameter [1] (fitting software output values, shown in Table 4.1) of linear and second order polynomial fit might be used.

The *adjusted* R^2 values shown in Table 4.1 confirm that second order polynomial is the best fit and the ions are products of secondary collisions.

More specifically, the protonated DME ($[HO(CH_3)_2]^+$ at *m/z* 47) might result from the protonation of DME by HCO^+, *via* the reaction:

$$\mathrm{HCO^+ + H_3COCH_3} \longrightarrow \mathrm{CO + HO(CH_3)_2{}^+}\ (m/z\,47) \tag{4.15}$$

[1] The quality of linear and polynomial regressions can be measured by the *coefficient of determination* (COD or better known as R^2). The R^2 can be calculated as:

$$R^2 = \frac{SXY}{SXX \cdot TSS} = 1 - \frac{RSS}{TSS}$$

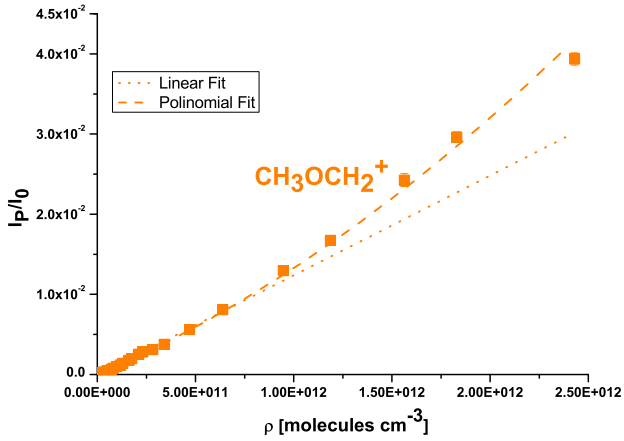

Figure 4.2: *m/z* 45 yield as a function of the DME density at $E_{CM} \sim 0.93\,\mathrm{eV}$. In the figure, linear (dot) and second order polynomial (dashed line) fits are reported. It is evident that the best fit is the quadratic one.

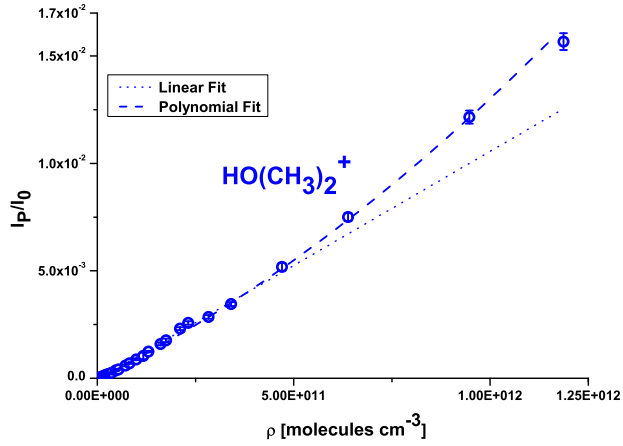

Figure 4.3: *m/z* 47 yield as a function of the DME density at $E_{CM} \sim 0.93\,\mathrm{eV}$. In the figure, linear (dot) and second order polynomial (dashed line) fits are reported. It is evident that the best fit is the quadratic one.

Table 4.1: The *adjusted* R^2 for the fits of the experimental data of *m/z* 45 and 47 ion yield products as a function of DME density are reported. The values confirm that second order polynomial is the best fit and the ions are products of secondary collisions.

m/z	*adj.* R^2	
	Linear Fit	2^{nd} Ord. Pol. Fit
45	0.97155	0.99587
47	0.97793	0.99469

It is known from previous investigations that React. 4.15 occurs efficiently and leads to the exclusive formation of protonated DME at thermal energies. Rate constants for the process are:

- $k = (2.1 \pm 0.5) \times 10^{-9}\,\mathrm{cm^3\,molecule^{-1}\,s^{-1}}$ at T=298 K [112];
- $k = 1.71 \times 10^{-9}\,\mathrm{cm^3\,molecule^{-1}\,s^{-1}}$ at T=300 K [113].

The $CH_3OCH_2^+$ product (sat *m/z* 45) can be generated by the hydride (H^-) abstraction reaction of CH_3^+ cation with DME:

$$CH_3^+ + H_3COCH_3 \longrightarrow CH_4 + CH_3OCH_2^+ \,(m/z\,45) \tag{4.16}$$

For this reaction, two different rate constant values are reported:

- $k = (3.5 \pm 0.7) \times 10^{-10}\,\mathrm{cm^3\,molecule^{-1}\,s^{-1}}$ at T=295 K [114];
- $k = 1.98 \times 10^{-9}\,\mathrm{cm^3\,molecule^{-1}\,s^{-1}}$ at T=300 K [113].

Relative yields for the various products (including those from secondary reactions) have been obtained by integrating the areas under the mass spectrum peaks registered at pressures in the range 2.0×10^{-6} to 4.9×10^{-6} mbar. The relative yields of HCO^+ and CH_3^+ products have been corrected taking into account the amounts of *m/z* 45 and 47 due to secondary reactions 4.15 and 4.16. The obtained BRs are reported in Table 4.2.

The proposed dissociative charge transfer reactions 4.2 - 4.14 are energetically favored. In Table 4.3, the reaction enthalpies ($\Delta_r H^\circ$) have been estimated using values for the standard heat of formation of reagent and products ($\Delta_f H^\circ$) [115]. Since the experimental set-up does not allow to detected the neutral partners in the reactions, we can not differentiate between different channels

---

where $SXY = \sum_{i=1}^{n}(x_i - \overline{x})(y_i - \overline{y})^2$, $SXY = \sum_{i=1}^{n}(x_i - \overline{x})^2$, RSS is the *residual sum of square* ($\sum_{i=1}^{n} e_i = \sum_{i=1}^{n} w_i(y_i - \widehat{y}_i)$, with w_i that is measurement error reciprocal and $\widehat{y}_i$, the fitted value) and TSS is the *total sum of square* ($\sum_{i=1}^{n}(y_i - \overline{y})^2$). Furthermore, the *adjusted* R^2 is defined as:

$$\overline{R}^2 = 1 - \frac{RSS/df_{error}}{TSS/df_{total}}$$

where df_{total} are the total n degrees of freedom of the system, while df_{error} are the $n-1$ degrees of freedom. The *adjusted* R^2 is a value between 0 and 1: a number close to 1 means that the fitting model has a high degree of confidence.

Table 4.2: Branching ratios of the products for the reaction He^+ + H_3COCH_3. Data have been obtained by averaging the experimental mass spectra taken at the same collision energy $E_{CM} \sim 1.6\,\mathrm{eV}$ and at different neutral pressures in the range $2.0 \times 10^{-7}\,\mathrm{mbar}$ to $5.0 \times 10^{-6}\,\mathrm{mbar}$. The values have been corrected for contributions from secondary reactions as outlined in the text.

m/z	**Product**	**BR (%)**
14	$CH_2^{\bullet+}$	7.3 ± 0.8
15	CH_3^+	38.5 ± 3.7
29	HCO^+	53.6 ± 5.3
31	OCH_3^+	0.4 ± 0.7

(*e.g.* with React. 4.2 - 4.3). For this reason, the proposed channels in React. 4.2 - 4.14 and Table 4.3 include all the energetically allowed fragmentation processes.

Table 4.3: Experimental reaction enthalpies ($\Delta_r H^\circ$) for the possible dissociative charge transfer channels of the reaction between He^+ and DME. $\Delta_r H^\circ$ values are obtained from the experimentally determined heat of formation ($\Delta_f H^\circ$) of reagents and products, as available in literature [115].

m/z	**Product** + He	**Eqn.**	$\Delta_r H^\circ$ eV
14	$CH_2^{\bullet+} + CH_3O^\bullet + H^\bullet$	4.2	-5.8
14	$CH_2^{\bullet+} + CH_2O + 2\,H^\bullet$	4.3	-5.0
15	$CH_3^+ + CH_3O^\bullet$	4.4	-11.2
15	$CH_3^+ + CH_2O + H^\bullet$	4.5	-10.3
15	$CH_3^+ + HCO^\bullet + 2\,H^\bullet$	4.6	-6.4
15	$CH_3^+ + CO + 3\,H^\bullet$	4.7	-5.7
29	$HCO^+ + CH_4 + H^\bullet$	4.8	-12.6
29	$HCO^+ + CH_3^\bullet + H_2$	4.9	-12.6
29	$HCO^+ + CH_3^\bullet + 2\,H^\bullet$	4.10	-8.1
29	$HCO^+ + CH_2^\bullet + H^\bullet + H_2$	4.11	-7.9
29	$HCO^+ + CH^\bullet + 2\,H^\bullet + H_2$	4.12	-3.4
31	$CH_3O^+ + CH_3^\bullet$	4.13	-10.3
31	$CH_3O^+ + CH_2^\bullet + H^\bullet$	4.14	-5.5

The exothermicity of the fragmentation channels can be invoked to explain why the formyl cation HCO^+ is observed as the most abundant fragment, followed by the methyl cation CH_3^+.

Indeed, reactions 4.9 and 4.8 are more exothermic than React. 4.4 leading to the formation of the methyl cation. At this level of the discussion a comparison with the electron ionization mass spectrum of DME (shown in Figure 4.4) might result interesting. From the NIST spectrum (Figure 4.4),

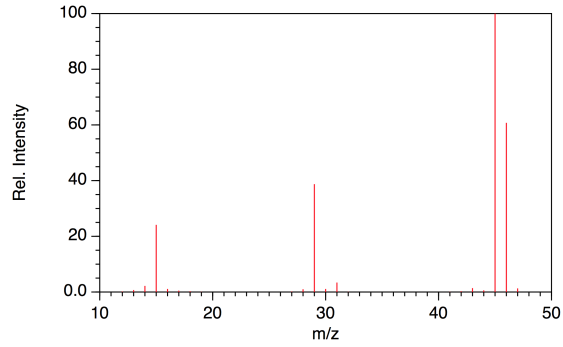

Figure 4.4: EI mass spectrum at 70 eV of DME from NIST database [115].

it is possible to observe that the most abundant products of the ionization at the nominal electron energy of 70 eV are the DME radical cation ($CH_3OCH_3^{\bullet+}$ at *m/z* 46) and the $CH_3OCH_2^+$ product (at *m/z* 45). Products at *m/z* 29, 15 are also observed, but with lower abundances. Since the products and their abundances are different between our experiments with He^+ and ionization by electrons, it can be inferred that the mechanisms leading to ionization and subsequent fragmentations are different in the two cases. For instance, in collisions with He^+, only the breaking of a C–O bond is responsible for the fragmentation, because of the absence of the $CH_3OCH_2^+$ as first collision product (C–H bond break). Furthermore, the absence of the $CH_3OCH_2^+$ product is mentioned in the works of Butler [116] and Nishimura [117], in which the dissociation of state-selected DME cation was studied by using *threshold photo-electron-photo-ionization coincidence spectroscopy* (TPEPICO). In fact, in the two experiments a sharp rise of the *m/z* 29 breakdown curve is observed in the photon energy range 14.0-14.9 eV, corresponding to a fall in the *m/z* 45 curve. This result indicates that the ion at *m/z* 29 might be formed from *m/z* 45 according to the following reaction (equivalent for our experiment to React. 4.8):

$$CH_3OCH_3^{\bullet+} \longrightarrow CH_3OCH_2^+ + H \longrightarrow HCO^+ + CH_4 + H \tag{4.17}$$

This means that HCO^+ ion is produced in a secondary process from the *m/z* 45 fragment ion. The CH_3^+ formation is also explained in terms of secondary ion dissociation from the *m/z* 45 (at photon energy higher than 14.4 eV) according to the reaction (equivalent for our experiment to React. 4.5):

$$CH_3OCH_3^{\bullet+} \longrightarrow CH_3OCH_2^+ + H \longrightarrow CH_3^+ + H_2CO + H \tag{4.18}$$

Therefore, in accord to the cited works it is possible to conclude that, when the DME is formed in a highly excited state, the formation of HCO^+ and CH_3^+ ions are favored to the detriment of $CH_3OCH_2^+$ ions.

The abundance of the HCO^+ might be further explained in terms of CH_3O^+ instability. In fact, this product at *m/z* 31 tends to fragment due to its instability into the resonance stabilised

HCO^+ cation by expelling an H_2 molecule [118, 119, 120, 121, 122]. The process is a uni-molecular decomposition of triplet methoxy cation ($^3CH_3O^+$) to give the hydrogen molecule plus the formyl cation (HCO^+), both singlet species. We can have two possibilities [121] (shown by the schematic PESs in Figure 4.5 [121, 123]):

1. the mechanism is *concerted*. The spin change and the [1,1]-elimination from the $^3CH_3O^+$ are simultaneous, *via* MECP1[2] (at $\sim 0.57\,\mathrm{eV}$ above the triplet methoxy cation) of Figure 4.5:

$$^3CH_3O^+ \longrightarrow {}^1HCO^+ + {}^1H_2 \tag{4.19}$$

2. the process occurs in a *stepwise* way:

$$^3CH_3O^+ \longrightarrow {}^1CH_2OH^+ \longrightarrow {}^1HCO^+ + {}^1H_2 \tag{4.20}$$

first the singlet hydroxymethyl cation ($^1CH_2OH^+$) is formed by the hydrogen shift *via* the MECP2 (at $\sim 0.62\,\mathrm{eV}$ above the triplet methoxy cation, as shown in Figure 4.5), concurrent with the spin change, and then the products HCO^+ + H_2 are formed by a [1,2]-elimination *via* a TS (at $\sim 0.11\,\mathrm{eV}$ with respect to the triplet methoxy cation).

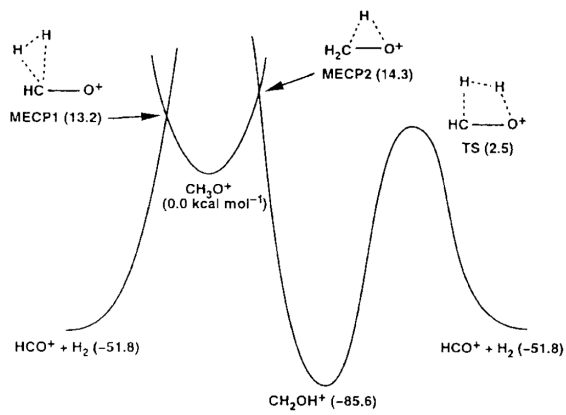

Figure 4.5: Schematic singlet and triplet PESs of the $[CH_3O]^+$ system calculated ate CCSD(T)/cc-pVTZ(-d)//B3LYP/6-31+G(d,p) level of theory [121, 123]. The energies are expressed in $\mathrm{kcal\,mol^{-1}}$. The figure is taken from [123].

Harvey and Aschi found that the concerted reaction occurs faster than the stepwise one, with rate constant higher by about one order of magnitude [123]. This conclusion is supported by the higher MEPC2 of the second pathway with respect to MEPC1 and by the presence of the TS. In conclusion, the fragmentation of the DME radical cation can occur according to SCHEME 4.1 and insights on the mechanism will be treated in detail in Chapter 5. The fragmentation of the methoxy cation will be resumed at the end of this Chapter to explain the BRs obtained for the MF.

[2] *minimum energy crossing point*

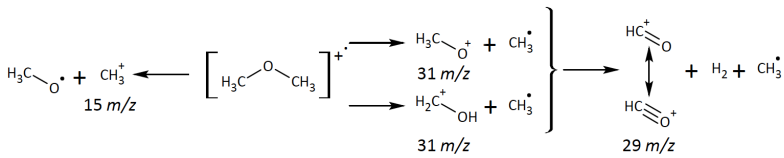

SCHEME 4.1: Fragmentation pathways of DME radical cation into CH_3^+, OCH_3^+ and HCO^+.

The absolute values of the reactive cross-section have been measured for the main channels, in order to have quantitative information on the ion product yields. Using the procedure already explained in Sec. 2.3.4, for ionic products of React. 4.4 - 4.14, the ratio I_P/I_0 has been measured as a function of the DME reagent pressure at fixed E_{CM}. Then, the absolute value of the cross-section has been extrapolated by the slope of the lines using the effective length of the scattering cell ((8.0 ± 0.4) cm). Data of I_P/I_0 for CH_3^+ and HCO^+ as a function of neutral gas density at fixed E_{CM} are reported in Figures 4.6 and 4.7.

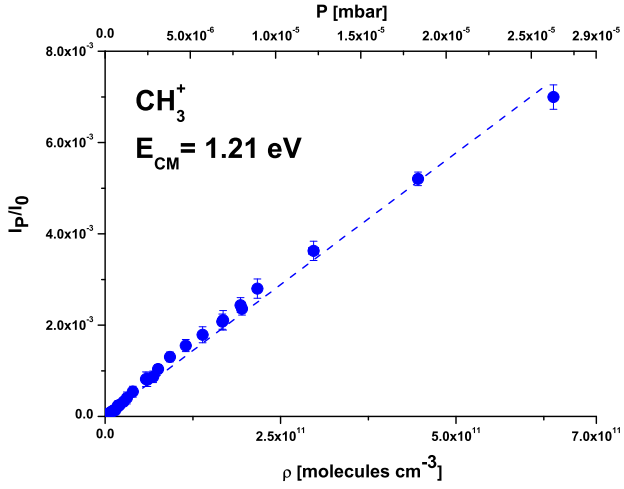

Figure 4.6: Density dependence of CH_3^+ product. The data have been recorded at E_{CM} = 1.21 eV. Dashed line is linear fit of the data.

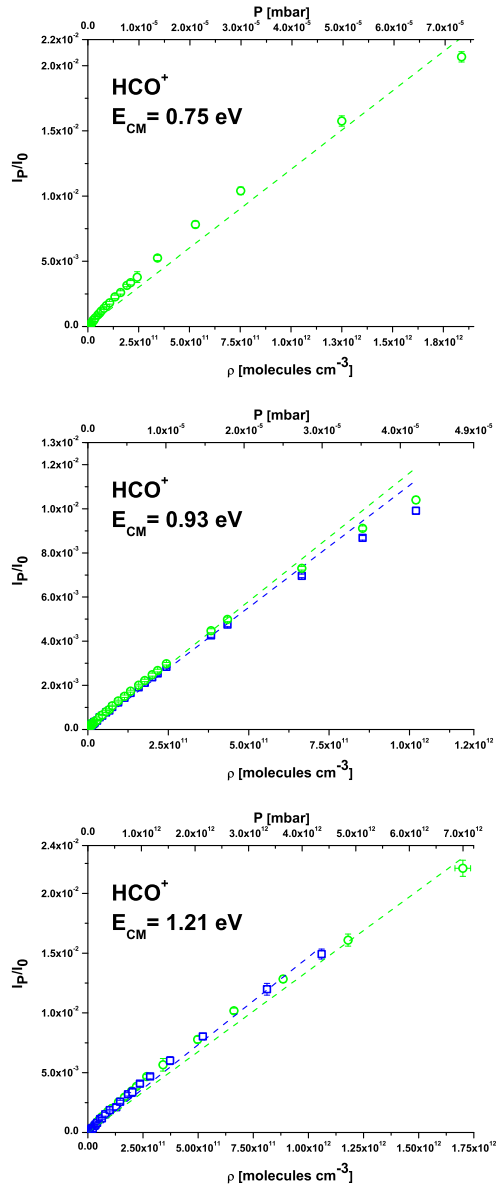

Figure 4.7: Density dependence of HCO^+ product. The data have been recorded at three different E_{CM} (0.75 eV, 0.93 eV and 1.21 eV). Dashed lines are linear fits of the data.

For the HCO^+ channel, a deviation from the linearity is observed at density higher than 5.0×10^{11} molecules cm^{-3} (corresponding to a DME pressure of $\sim 2.0 \times 10^{-5}$ mbar). This phenomenon is caused by the presence of secondary collisions that makes to decrease the intensity of the primary ion and thus, I_P/I_0. By using the linear fits, it is possible to estimate the absolute values of cross-section for the two measured products. The obtained values corrected for secondary reactions are summarized in Table 4.4.

Table 4.4: Absolute values of the reactive cross-section for the ionic products at *m/z* 15, 29 (CH_3^+, HCO^+, respectively) corrected for secondary reactions.

E_{CM} (eV)	σ (Å^2)	
	m/z 29	*m/z* 15
0.75	27.0 ± 10.8	x
0.93	23.37 ± 0.93	x
1.21	33.6 ± 13.4	19.21 ± 0.77

For all the channels, relative cross-sections have been measured as a function of the collision energy in the thermal- and hyperthermal-range (~ 0.050 eV to 7 eV). The relative cross-section values as a function of the collision energy have been re-scaled according to the absolute values measured at fixed energies in the CM frame (see data in Table 4.4), corrected for secondary reactions. The resulting absolute cross-sections are shown in Figure 4.8, in which the absolute value of cross-sections for CH_3^+, HCO^+ are also shown with light-blue and orange stars, respectively. We note that the absolute value for the CH_2^+ and CH_3O^+ channels have not been obtained by measurements of I_P/I_0 as a function of pressure, but it has been calculated using the branching ratio values (Table 4.2) that are constant in the explored energy range.

From Figure 4.8, we can observe that all the fragmentation channels show a decreasing trend and this observation confirms that all the channels are exothermic.

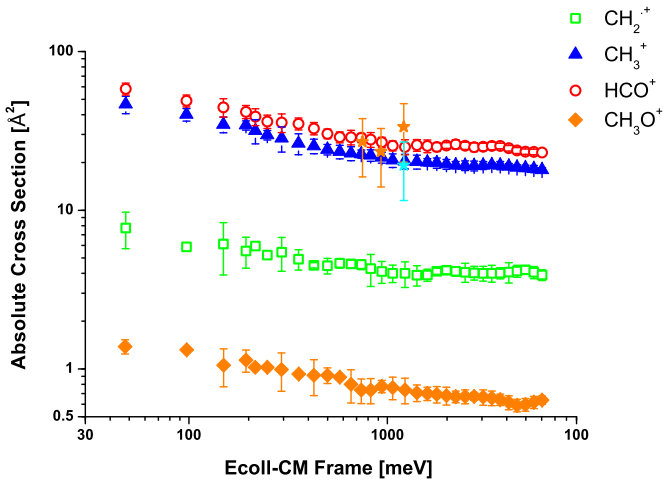

Figure 4.8: Absolute cross-sections in $Å^2$ for the production of HCO^+ (red open dots), CH_3^+ (blue filled triangles), $CH_2^{\bullet+}$ (green open squares) and CH_3O^+ (orange filled diamonds) ionic products are reported as a function of the collision energy, from the title reaction. The absolute values of cross-section for CH_3^+, HCO^+ are also shown with light-blue and orange stars, respectively.

4.2 Reaction of He^+ with $HCOOCH_3$ (MF)

For the reaction He^+ + $HCOOCH_3$, vapor pressure of MF has been used to fill the scattering cell. The reagent has been purchased from SIGMA-ALDRICH in anhydrous form at 99% of purity. The sample of the MF liquid once attached to the system has been additionally purified by *freeze-pump-thaw* cycles with liquid nitrogen, in order to remove dissolved gases. As already done for the reaction with the DME, mass spectra of the ionic products have been obtained at different pressures of MF inside the reaction octupole at fixed collision energy ($E_{CM} \sim 0.9\,\mathrm{eV}$). Spectra at 1.8×10^{-7} (black line), 5.0×10^{-7} (red line), 1.4×10^{-6} (blue line), 5.2×10^{-6} (green line), $1.61 \times 10^{-5}\,\mathrm{mbar}$ (orange line) are shown in Figure 4.9. Also in this case, a first important result is the absence of the MF radical cation peak ($[HCOOCH_3]^{\bullet+}$ at *m/z* 60, $\Delta_r H$=13.755 eV) at all the explored pressures is clear, speaking for a completely dissociative charge transfer process. By thermodynamic considerations (as it will be discussed later on), the possible fragmentation channels compatible with our experimental observations are the following:

$$He^+ + HCOOCH_3 \longrightarrow He + {CH_2}^{\bullet+}\,(m/z\,14) + HCOO^{\bullet} + H^{\bullet} \quad (4.21)$$

$$\longrightarrow He + {CH_2}^{\bullet+}\,(m/z\,14) + CO_2 + 2\,H^{\bullet} \quad (4.22)$$

$$\longrightarrow He + {CH_2}^{\bullet+}\,(m/z\,14) + CO_2 + H_2 \quad (4.23)$$

$$\longrightarrow He + {CH_2}^{\bullet+}\,(m/z\,14) + HCO^{\bullet} + OH^{\bullet} \quad (4.24)$$

$$\longrightarrow He + {CH_3}^{+}\,(m/z\,15) + HCOO^{\bullet} \quad (4.25)$$

$$\longrightarrow He + {CH_3}^{+}\,(m/z\,15) + CO_2 + H^{\bullet} \quad (4.26)$$

$$\longrightarrow He + {CH_3}^{+}\,(m/z\,15) + CO + OH^{\bullet} \quad (4.27)$$

$$\longrightarrow He + HCO^{+}\,(m/z\,29) + {OCH_3}^{\bullet} \quad (4.28)$$

$$\longrightarrow He + HCO^{+}\,(m/z\,29) + CH_2OH^{\bullet} \quad (4.29)$$

$$\longrightarrow He + CH_3O^{+}\,(m/z\,31) + HCO^{\bullet} \quad (4.30)$$

$$\longrightarrow He + CH_3O^{+}\,(m/z\,31) + CO + H^{\bullet} \quad (4.31)$$

$$\longrightarrow He + {CO_2}^{\bullet+}\,(m/z\quad 44) + CH_4 \quad (4.32)$$

$$\longrightarrow He + {CO_2}^{\bullet+}\,(m/z\quad 44) + CH_3 + H \quad (4.33)$$

Already at the lowest pressure ($1.8 \times 10^{-7}\,\mathrm{mbar}$), a notable peak at *m/z* 61 is observed. Considering the molecular weight of MF (60 u) and the absence of the molecular peak from the spectra, such a peak can reasonably be attributed to protonated MF. In the absence of H^+ as contaminant of our He^+ ion beam (that was carefully checked and avoided), the only way to generate the protonated MF ion is by secondary collisions of the most abundant primary product (HCO^+, *m/z* 29) with neutral MF, *via* the following reaction:

$$HCO^+ + HCOOCH_3 \longrightarrow CO + {CH_3C(OH)_2}^{+}\,(m/z\,61) \quad (4.34)$$

The React. 4.34 is very efficient at thermal energies and has as only product the protonated MF (rate constant is k=$(2.90 \pm 0.25) \times 10^{-9}\,\mathrm{cm^3\,molecule^{-1}\,s^{-1}}$ at T=300 K [112]). To demonstrate the origin of protonated MF via secondary reactions, the yield of *m/z* 61 ion was measured as function of MF density and a quadratic trend was expected. Unfortunately, all the recorded data show

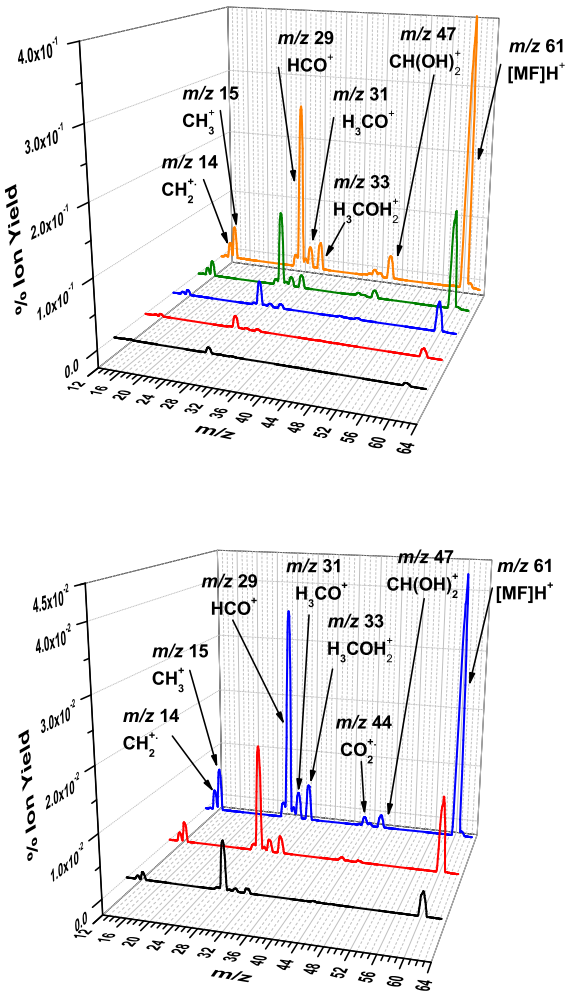

Figure 4.9: Mass spectra of selected He^+ ions reacting with MF at different pressures inside the reaction cell: 1.8×10^{-7} mbar (black line), 5.0×10^{-7} mbar (red line), 1.4×10^{-6} mbar (blue line), 5.2×10^{-6} mbar (green line) and 1.61×10^{-5} mbar (orange line) (on the top). The collision energy in the CM-frame has been fixed at 0.9 eV and the signal intensity of the He^+ ion (100%) is not shown. On the bottom, it is shown a zoomed view of mass spectra in range 1×10^{-7} mbar to 2×10^{-6} mbar. Ionic products and respective *m/z* values are reported in figure to facilitate reading.

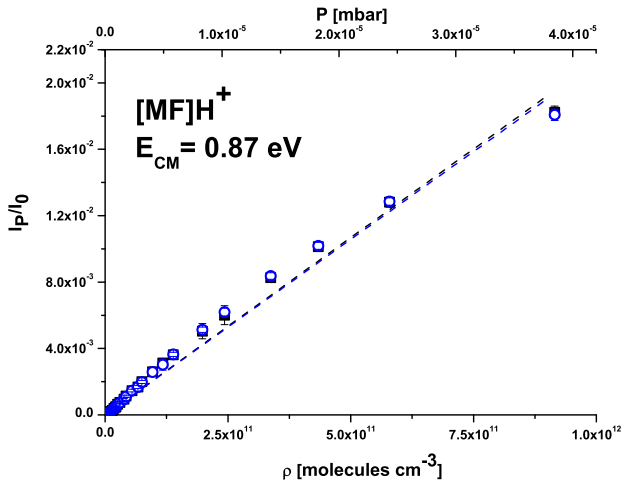

Figure 4.10: Density dependence of $[MF]H^+$ product at *m/z* 61. The data have been recorded at $E_{CM} = 0.87\,\text{eV}$. Dashed line is the linear fit of the data. The linear trend of the values is clearly visible.

a linear trend (Figure 4.10, with an *adjusted* $R^2 \sim 0.99$), but this unexpected behavior can be rationalized following the lines of what is reported in Appendix A. So, despite the linear trend with density, we can conclude that *m/z* 61 is formed by secondary collision of HCO^+ with MF. In addition to *m/z* 61, peaks unrelated to the title reaction appear at *m/z* 33 and 47. It is reasonable to assume that the 1% impurity of anhydrous MF is composed by methanol (CH_3OH, $32\,u$[3]) and formic acid (HCOOH, $46\,u$), reagent compounds for the synthesis of MF[4]. For this reason, the signal at *m/z* 33 might be caused by the secondary collision of HCO^+ with methanol, forming protonated methanol ($CH_3OH_2^+$, *m/z* 33) *via* the reaction:

$$HCO^+ + HOCH_3 \longrightarrow CO + CH_3OH_2{}^+ \,(m/z\,33) \tag{4.36}$$

[3]unified atomic mass unit, symbol: u

[4]The most common *esterification* is the treatment of a carboxylic acid (in this case, formic acid) with an alcohol (methanol) in presence of an acyd catalyst (H_2SO_4, $ArSO_3H$ or gaseous HCl) [124]. This process has the special name *Fischer esterification* from the German chemist, Emil Fischer (1852-1919). For the MF, we can have the following reaction:

$$HCOOH + CH_3OH \overset{H^+}{\rightleftharpoons} HCOOCH_3 + H_2O \tag{4.35}$$

The Fischer esterification allows to prepare esters in high yields. Using a large excess of the alcohol, the equilibrium is driven to the right, achieving a high conversion of carboxylic acid to its ester. Water can be removed by azeotropic distillation with a *Dean-Stark trap*.

that is very efficient and for which several different rate constants are reported in literature:

- k=from $1.4 \pm 0.3 \times 10^{-9}$ to $2.4 \pm 0.3 \times 10^{-9}$ $\mathrm{cm^3\,molecule^{-1}\,s^{-1}}$ at T=300 K [125, 126, 127];
- k=$2.70 \pm 0.15 \times 10^{-9}$ $\mathrm{cm^3\,molecule^{-1}\,s^{-1}}$ at T=298 K [112].

Although also *m/z* 33 comes from secondary collisions, the data as a function of density (Figure 4.11) show a linear trend (adjusted $R^2 \sim 0.99$), similar to what has been already observed for the *m/z* 61 peak. Hence, it is possible to conclude that, in case of very efficient secondary collisions as React. 4.34 and 4.36, the I_P/I_0 ratio can show a linear dependence on density. On the other hand, the ionic product at *m/z* 47 has a clear quadratic trend of I_P/I_0 as a function of the neutral density in the scattering cell as shown by data measured at E_{CM} = 0.89 eV and reported in Figure 4.12. The data have been fitted with a second order polynomial with *adjusted* $R^2 \sim 0.998$. The peak at *m/z* 47 can be assigned as protonated formic acid (second impurity of MF sample), coming from the secondary reaction of HCO^+ with HCOOH:

$$\mathrm{HCO^+ + HCOOH \longrightarrow CO + CH(OH)_2{}^+}\ (m/z\,47) \tag{4.37}$$

In this case, the proton-transfer process shows a clear quadratic trend. The rate constants measured at thermal energies confirm this conjecture, since for React. 4.37 we have:

- k= $1.80 \pm 0.15 \times 10^{-9}$ and $1.80 \pm 0.30 \times 10^{-9}$ $\mathrm{cm^3\,molecule^{-1}\,s^{-1}}$ at T=298 K [112, 128];
- k=$1.80 \pm 0.15 \times 10^{-9}$ and $1.90 \pm 0.30 \times 10^{-9}$ $\mathrm{cm^3\,molecule^{-1}\,s^{-1}}$ at T=300 K [126, 129].

Relative yields for the ionic products of the title reaction have been estimated by averaging mass spectrum results obtained at pressures in the range 2×10^{-7} to 5×10^{-6} mbar. The relative yield of HCO^+ has been corrected by considering the amounts of *m/z* 61, 33 and 47 due to secondary React. 4.34, 4.36 and 4.37, respectively. The obtained branching ratios are reported in Table 4.5.

Table 4.5: Branching ratios of the products for the reaction He^+ + $HCOOCH_3$. Data have been obtained by averaging the experimental mass spectra taken at the same collision energy $E_{CM} \sim 0.9$ eV and at different neutral pressures in the range 2.0×10^{-7} mbar to 5.0×10^{-6} mbar. The values have been corrected for contributions from secondary reactions as detailed in the text.

m/z	Product	BRs (%)
14	$CH_2{}^{\bullet+}$	3.6 ± 0.3
15	$CH_3{}^+$	7.3 ± 0.3
29	HCO^+	83.2 ± 2.0
31	$OCH_3{}^+$	4.2 ± 0.8
44	$CO_2{}^{\bullet+}$	1.3 ± 0.1

The proposed React. 4.21 - 4.33 are all energetically favored. The reaction enthalpies ($\Delta_r H^\circ$) at 298 K are reported for all the hypothesized fragmentation channels in Table 4.6. They have

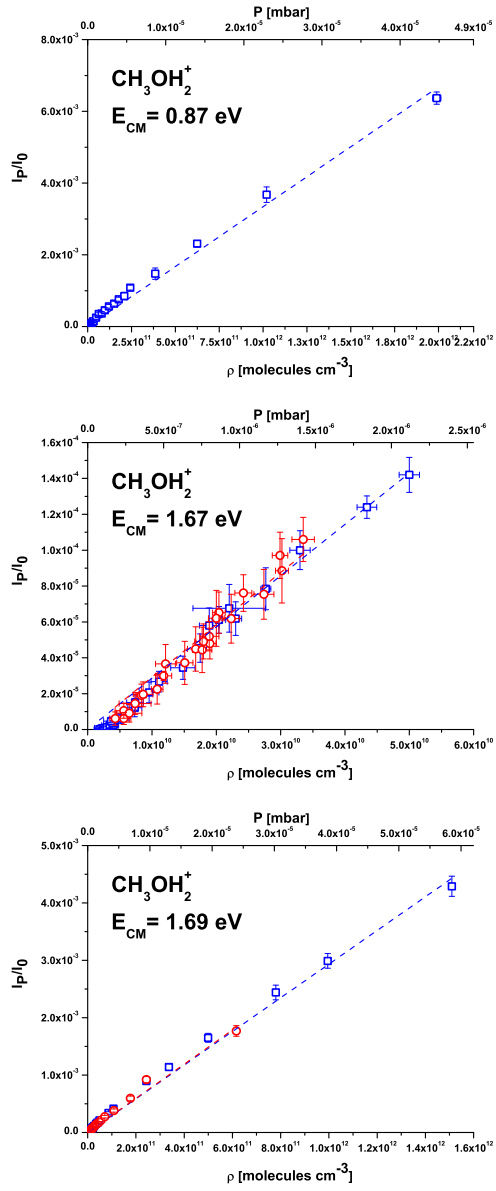

Figure 4.11: Density dependence of $CH_3OH_2^+$ product at *m/z* 33. The data have been recorded at E_{CM} = 0.87 eV, 1.67 eV and 1.69 eV. Dashed lines are the linear fits of the data.

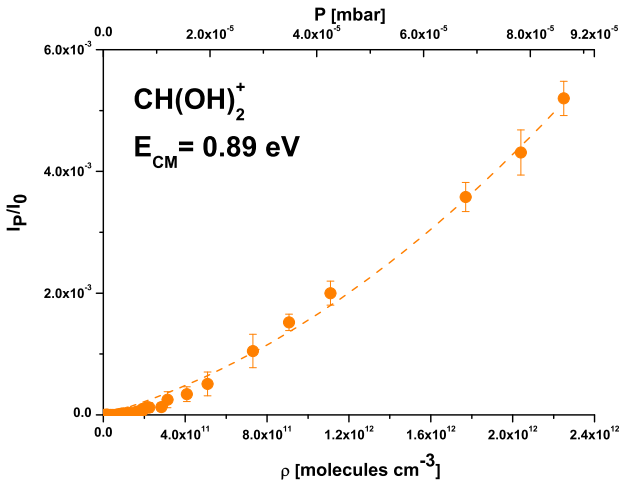

Figure 4.12: *m/z* 47 yield as a function of the pressure at $E_{CM} \sim 0.89\,\mathrm{eV}$. In the figure, the second order polynomial (dashed line) fit is reported.

been estimated (as done for the reaction of $He^+ + CH_3OCH_3$) using values for the standard heat of formation of reagent and products ($\Delta_f H^\circ$) [115, 130].

For products at *m/z* 29 and 31, the absolute values of the cross-section have been measured (Table 4.7). The ratio I_P/I_0 has been measured as a function of the neutral reagent pressure (MF) at fixed E_{CM}. Then, the absolute value of the cross-section has been extrapolated by the slope of the lines using the effective length of the scattering cell ($(8.0 \pm 0.4)\,\mathrm{cm}$). Data of I_P/I_0 for HCO^+ and CH_3O^+ as a function of neutral gas density at fixed E_{CM} are reported in Figure 4.13 and 4.14.

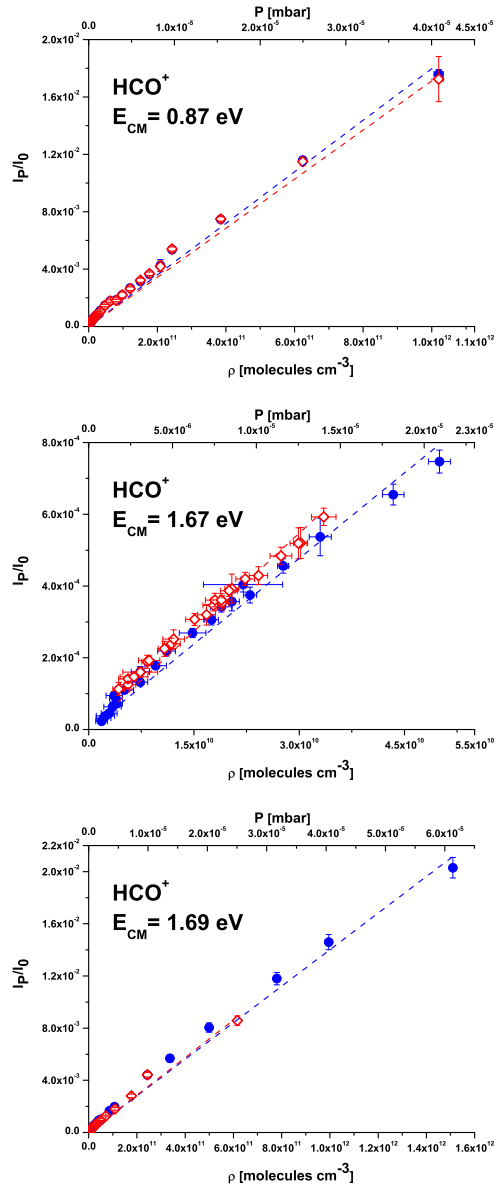

Figure 4.13: Density dependence of OCH^+ product. The data have been recorded at three different E_{CM} (0.87 eV, 1.67 eV and 1.69 eV). Dashed lines are linear fits of the data.

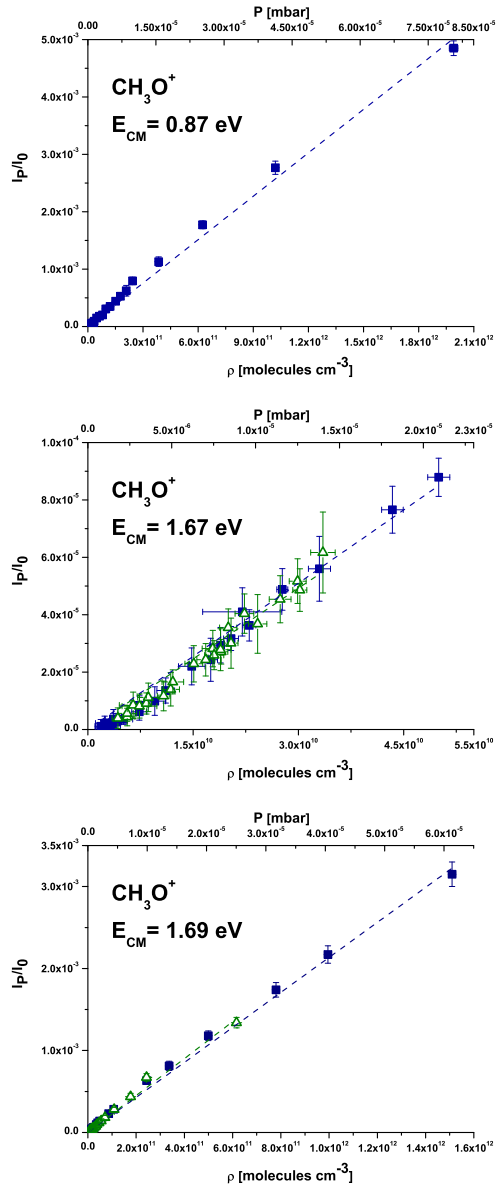

Figure 4.14: Density dependence of OCH_3^+ product. The data have been recorded at three different E_{CM} (0.87 eV, 1.67 eV and 1.69 eV). Dashed lines are linear fits of the data.

Table 4.6: Experimental reaction enthalpies ($\Delta_r H^\circ$) for the possible dissociative charge transfer channels of the reaction He^+ + MF. $\Delta_r H^\circ$ values are obtained from the experimentally determined heat of formation ($\Delta_f H^\circ$) of reagents and products, as available in literature [115, 130].

m/z	**Product** + He	**Eqn.**	$\Delta_r H^\circ$ eV
14	$CH_2^{\bullet+}$ + $HCOO^\bullet$ + $H^\bullet$	4.21	-5.7
14	$CH_2^{\bullet+}$ + CO_2 + 2 $H^\bullet$	4.22	-6.3
14	$CH_2^{\bullet+}$ + CO_2 + H_2	4.23	-10.8
14	$CH_2^{\bullet+}$ + $HCO^\bullet$ + $OH^\bullet$	4.24	-5.9
15	CH_3^+ + $HCOO^\bullet$	4.25	-11.1
15	CH_3^+ + CO_2 + $H^\bullet$	4.26	-11.6
15	CH_3^+ + CO + $OH^\bullet$	4.27	-10.5
29	HCO^+ + $OCH_3^\bullet$	4.28	-12.4
29	HCO^+ + $CH_2OH^\bullet$	4.29	-12.6
31	CH_3O^+ + $HCO^\bullet$	4.30	-9.8
31	CH_3O^+ + CO + $H^\bullet$	4.31	-9.1
44	$CO_2^{\bullet+}$ + CH_4	4.11	-12.2
44	$CO_2^{\bullet+}$ + CH_3 + H	4.12	-7.6

Table 4.7: Absolute values of the reactive cross-section corrected for secondary reactions for the ionic products at *m/z* 29, 31 (HCO^+ and OCH_3^+, respectively).

E_{CM} (eV)	σ (Å^2)	
	m/z 29	*m/z* 31
0.87	49.6 ± 19.8	3.2 ± 1.3
1.67	41.5 ± 16.6	2.1 ± 0.8
1.69	34.4 ± 13.8	1.4 ± 0.6

For the main channels, relative cross-sections have been measured as a function of the collision energy in the thermal- and hyperthermal-range ($\sim 0.050\,\mathrm{eV}$ to $7\,\mathrm{eV}$), and results are shown in Figure 4.15. By using the BRs reported in Table 4.5 relative cross-sections for all the other channels have been re-scaled to their absolute values and summed to give the total absolute cross-sections. From Figure 4.15, we can observe that all the fragmentation channels show a decreasing trend.

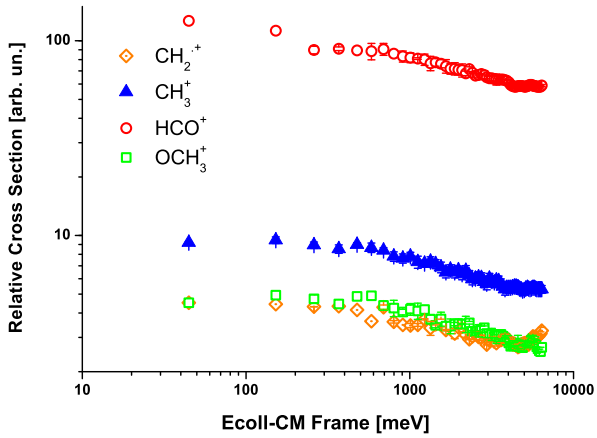

Figure 4.15: Relative cross-sections for the production of HCO^+ (red open dots), CH_3^+ (blue filled triangles), $CH_2^{\bullet+}$ (green open squares) and OCH_3^+ (orange open diamonds) ionic products as a function of the collision energy, from the title reaction. Cross-sections for the very minor channel $CO_2^{\bullet+}$ (data not shown) are in the range 1.0-0.7 arbitrary units.

According to Table 4.6, this observation confirms that all the channels are exothermic.

Again in the MF reaction, the formyl cation HCO^+ is the most abundant fragment and its formation reaction (React. 4.28) is the most exothermic. According to the work of Jackson *et al.* (based on collisions of Ar^+/N_2^+ with MF [131]), the fragmentation process can occur by breaking two different C–O bond. In fact, we can have:

1. the rupture of the $HC(O)-OCH_3$ bond can give either HCO^+ or CH_3O^+, that might again fragment giving the formyl cation (see Reactions 4.19 and 4.20);
2. the rupture of the $HC(O)O-CH_3$ gives exclusively the CH_3^+ fragment plus the formyloxyl radical HCOO; the formation of the formiloxyl ion is not preferred due to the instability of HCOO, that tends to fragment in CO_2 + H [131].

Despite the similarities with the experiments of Jackson *et al.* [131], in which the reaction of MF with Ar^+ and N_2^+ is completely dissociative, the BRs are quite different, suggesting different mechanisms of dissociation. In fact, in the SIFT experiment with Ar^+ and N_2^+ [131], CH_3O^+ ion is the

major product (BR ∼ 56-57%), with significant yields of HCO^+ (BR ∼ 25-26%), while CH_3^+ is a minor product (BR ∼ 15-17%) . On the contrary, in our guided ion beam experiment with He^+ the production of HCO^+ is largely preferred over the formation of CH_3^+ and CH_3O^+ (see BRs in Table 4.5). The difference in BR of the CH_3O^+ can be explained in term of differences in ionization energy of He and Ar/N_2. In fact, after removing an electron, the excess energy of the nascent MF radical cation is lower for Ar^+/N_2^+ ($\Delta_r H$=−4.9 eV for Ar^+ + MF, $\Delta_r H$=−4.7 eV for N_2^+ + MF), while for He^+ it is $\Delta_r H$=−13.8 eV for He^+ + MF. Such difference in energy can modify the pathway of MF fragmentation leading to reaction with He^+ to methoxy ion in triplet state ($^3CH_3O^+$), that dissociates rapidly in $HCO^+ + H_2$ (React. 4.19), while the reactions with Ar^+ and N_2^+ might lead preferentially to CH_2OH^+ (React. 4.20), that dissociates less easily. Therefore, in collisions with He^+ the production of HCO^+ might be enhanced by the direct dissociation of $^3CH_3O^+$, whereas in collisions with Ar^+ and N_2^+ the hydroxymethyl contributes to a minor extent to the HCO^+ formation.

Further considerations can be done when comparing our branching ratios with dissociative ionization products due to soft X-rays (at 288.3 eV and 532.2 eV) [132], electron interactions at 70 eV [115] and UV photons at 18 eV [133] (Figure 4.16). Since the ionization *via* electron at 70 eV and UV photons occurs in the valence shell while *via* soft X-rays in the inner shells, the differences in product ion yields between the various techniques are evident. The inner shell photoionization process induces instabilities on molecular structure with strong nuclear rearrangements [132], leading to small amounts of radical cation of MF and preferring the formation of fragments (in particular, HCO^+). This suggests that the ionization from inner and valence orbitals might lead

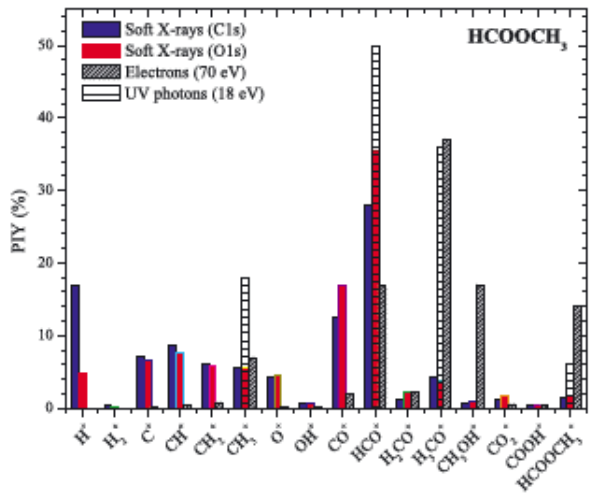

Figure 4.16: Comparison taken between mass spectra of MF fragments obtained by dissociation by electron ionization at 70 eV [115], by UV photons at 18 eV [133], and by soft X-rays at 288.3 eV and 532.2 eV[132]. The figure is taken from [132].

to peculiar dissociation pathways. Since the branching ratios for the title reaction are still different to the proposed cases, some similarities with the soft X-ray ionization products and yields evoke that in the reaction of He^+ + $HCOOCH_3$ some inner valence shell ionization should be involved. This will be confirmed by the theoretical considerations in Chapter 5.

From the calculated hypersurface of the fragmentation of the MF radical cation (Figure 4.17) [134] it is possible to infer further conclusions about the product BRs of He^+ + MF reaction. Heinrich and co-workers [134] characterized the following product formation channels (see Figure 4.17):

1. formation of CH_3OH^+ (*m/z* 32) *via* 1 $\longrightarrow$ 5 $\longrightarrow$ CH_3OH^+ + CO: this is the pathway at lowest energy, but no ion at *m/z* 32 is observed in our experiment;
2. formation of CH_2OH^+ (*m/z* 31) *via* 1 $\longrightarrow$ 2 $\longrightarrow$ 6 $\longrightarrow$ CH_2OH^+ + HCO at even higher energy;
3. at even higher energy the HCO^+ can be formed directly by the fragmentation of the radical cation; neutral counterparts can be the OCH_3 radical (the channel is endotermic of $39.9\,\mathrm{kcalmol^{-1}}$) or the CH_2OH ($35.8\,\mathrm{kcalmol^{-1}}$). In our experiment, the formation of HCO^+ (Reactions 4.28 and 4.29) is exothermic of $\sim -12\,\mathrm{eV}$ (Table 4.6).
4. CH_3^+ and $CH_2^{\bullet+}$ can be produced *via* the fragmentation of CH_3OH^+ (giving CH_3^+ + CO + OH) and CH_2OH^+ (giving $CH_2^{\bullet+}$ + OH + HCO), possible at even higher energy, as suggested by Heinrich and co-workers [134]. This might explain the presence of these two ionic products in our experiment (Reactions 4.24 and 4.27) and the low abundance of CH_3^+ and the absence of $CH_2^{\bullet+}$ in the Jackson's experiment [131]. In fact, with Ar^+/N_2^+ instead of He^+ the CH_3^+ production remains exothermic ($\sim -1.7\,\mathrm{eV}$), while $CH_2^{\bullet+}$ formation becomes endothermic ($\sim 3\,\mathrm{eV}$) and therefore, not possible for the Jackson's experiment.

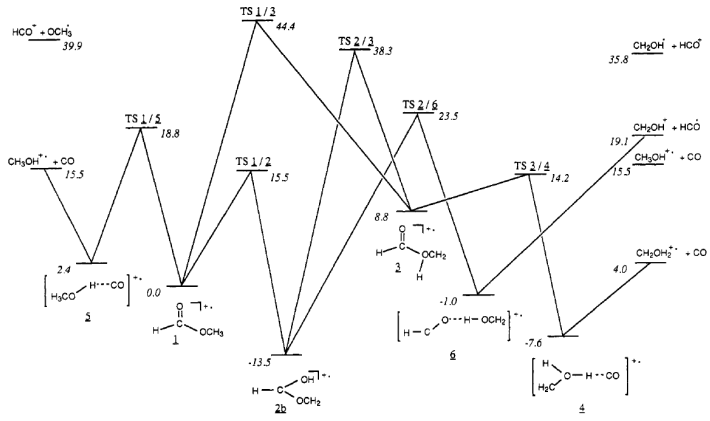

Figure 4.17: Calculated hypersurface for rearrangement and dissociation reactions of MF radical cation (MP3/6-31G**/6-31G*+ZPVE). The energies are given in $\mathrm{kcal\,mol^{-1}}$. The figure is taken from [134].

Chapter 5

The Theoretical Results

"Good time for a change
See, the luck I've had"

Please, Please, Please, Let Me Get What I Want - The Smiths

In this chapter, we report the theoretical investigation on the reactions $He^+ + CH_3OCH_3$ and $He^+ + HCOOCH_3$. We obtain insights into the *dissociative charge electron transfer* mechanism of both reactions by investigating the nature of the non-adiabatic transitions between the relevant potential energy surfaces. The well-known Landau-Zener-Stückelberg model has been used but with an innovative approach. In fact, the attention of the author has been on improving the mentioned model, in order to apply it to the complex systems of an ion-permanent dipole reaction, in which stereo-dynamics might play a crucial role. Three critical elements rule the charge exchange processes: the strong anisotropy of the potential interactions of reagents, the position of the non-adiabatic curve crossings, and the symmetry of the electron density distribution of the neutral reagent orbital from which the electron jumps on the ion. Furthermore, final aims are the cross-section calculation for the mentioned reactions in a wide collision energy range, in order to have rate constants values for the processes from temperatures relevant for the interstellar medium (*i.e.* as low as 10 K) to room temperature (300 K).

The used procedures, the improvements and the results of calculated cross-sections will be reported in detail in the following sections.

5.1 Introduction

As explained previously (Sec. 3.1.1), during the years simplified models to estimate cross-sections for ion-molecule reactions have been proposed, in order to give realistic estimates, particularly in the complete absence of experimental data. Such empirical or semi-empirical models neglect the detailed knowledge of the PESs, their short-range behaviors and the existence of crossings between entrance and exit channels of the diabatic curves. They focus exclusively on an effective potential that only includes the long-range attraction of reactants, controlling their approaching, and the centrifugal potential (Sec. 3.1.1) to create the so called centrifugal barrier. The cross-sections

so evaluated are defined by a *capture model* (Sec. 3.1.1), according to which all trajectories having enough energy to cross the centrifugal barrier will lead to reaction, thus providing an upper limit to the actual value, especially in the range of thermal and sub-thermal collision energies. In the case of point charge cations interacting with non-polar neutrals, the model leads to the well-known Langevin expression (Eqn. 3.31), while in the case of neutrals with a dipole moment the dependence of the potential on the dipole orientation should be taken into account (Eqn. 3.33). While for simple systems the mentioned models give good estimation of integral cross-sections, the present investigation demonstrates that this is not always the case, and the dynamics of non-dissociative and dissociative charge transfer processes often require a more complete treatment for a correct evaluation of the relevant observables. In fact, in Figure 5.1 total absolute σ (green dots) measured as a function of the collision energy (see Chapter 4) for the reaction $He^+ + CH_3OCH_3$ (on the left) and for the reaction $He^+ + HCOOCH_3$ (on the right) are reported together with the expected dependence based on a simple Langevin model (red dashed line) and on the locked-dipole (blue dashed line) approximations. Remarkably, experimental σ values do not follow the expected trend based on simplified capture models, with a decrease in the cross-section with increasing energy that is less steep than what was predicted by models. It is therefore intriguing to understand the causes of such deviations exploiting a semi-empirical formulation of the involved PESs, providing a proper analytic representation of the interaction in the full space of the configurations, and a quantitative treatment of the charge transfer dynamics.

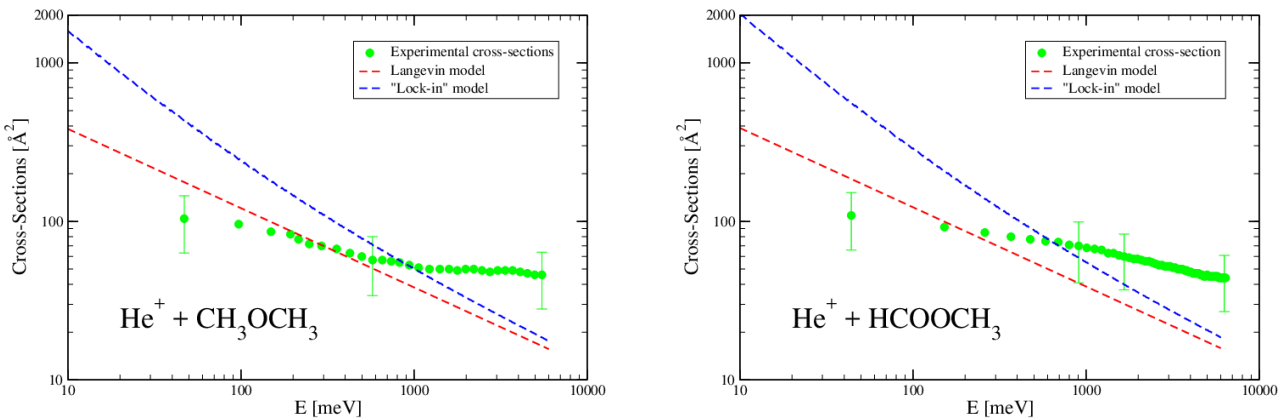

Figure 5.1: Total absolute cross-sections (in Å^2) for the reactions of He^+ with DME (on the left) and with MF (on the right) as a function of the collision energy in the CM frame. Experimental cross-sections (green dots) have been obtained by summing contributions from the various channels with BRs (Table 4.2 for DME and Table 4.5 for MF). The red dashed line results from Langevin model (capture from ion-induced dipole interactions only and blue dashed line results from locked-dipole model (capture from ion-induced dipole plus ion-dipole with dipole locked at the position of maximum attraction).

5.2 Dynamics of the *dissociative charge transfer process* for the reaction $He^+ + CH_3OCH_3$

5.2.1 The PESs

In order to calculate the cross-sections with a Landau-Zener approach (see Sec. 3.1.2), the critical point is the accurate description of the PESs, correlating asymptotically with the entrance and exit charge transfer states (He^+ + DME and He^+ + $DME^{\bullet+}$, respectively).

Before reporting the details on the parametrization of the interaction potentials, it is necessary to conveniently define the geometry of the $[He-DME]^+$ using a reference frame centered on the CM of the molecule, and the $C_\alpha-O-C_\beta$ molecular plane coincident with the *xy* plane. The He^+ and DME system is shown in Figure 5.2.

For the interaction potential, C_α and C_β are considered as *effective atoms*, each having the mass (15 u) and the polarizability of a methyl group. This "wrapping" of carbon and hydrogens in only one atom corresponds to the *united atom* approximation, in which the interaction site coincides with a specific functional group of the molecule and not with the single atoms that form it (*all atoms* description) [91]. Since the description of the interaction potential is built on the assumption of the pairwise atom-atom-like additivity (see Eqn. 3.95 in Sec. 3.2.5), the main advantage is the reduction of the number of centers to consider.

In order to build the long range potential, it is fundamental to report the partition of the molecular polarizability in the functional groups polarizabilities. The DME polarizability is equal to $5.16\,\text{Å}^3$ [135] and it can be partitioned into three components, two assigned to the effective atoms C_α and C_β (each one $2.20\,\text{Å}^3$), and one to the O atom ($0.76\,\text{Å}^3$). Already here, we can anticipate that the molecular ion is formed in an excited state, by ejection of one electron from a inner valence molecular orbital. For this reason, the polarizability (and the size) of $DME^{\bullet+}$ might be determined by the energy and number of the most external electronic clouds and it is assumed that this physical property is the same as for neutral DME. Therefore, it is partitioned in the same way of the neutral DME. Regarding the geometry [136], a value of 1.41 Å is used for the C–O bond length and 111.3° for the $C_\alpha-O-C_\beta$ bond angle. In this reference frame, the Cartesian coordinate (*x*, *y*, *z*) matrix has been defined as:

$$\begin{bmatrix} x_O & y_O & z_O \\ x_{C_\alpha} & y_{C_\alpha} & z_{C_\alpha} \\ x_{C_\beta} & y_{C_\beta} & z_{C_\beta} \end{bmatrix} = \begin{bmatrix} 0 & -0.510 & 0 \\ -1.175 & +0.272 & 0 \\ +1.175 & +0.272 & 0 \end{bmatrix} \tag{5.1}$$

The potential has been developed in terms of polar coordinates R, θ and φ (as shown in Figure 5.2). The vector R connects the CM of the molecule with the position of He^+ in the entrance channel, which is equivalent to the position of the He atom in the exit channel. The polar angle θ defines the direction of the incoming He^+ ion with respect to the *z* axis. For example, $\theta = 0°$ corresponds to the He^+ approaching perpendicular to *xy* plane, while with $\theta = 90°$ the ion approaches co-planar to the molecular plane. Finally, φ specifies the projection of the R vector on the *xy* plane, *e.g.* $\varphi = 0°$ corresponds to the positive value of the *x* axis (on the CH_3-group of the C_α side).

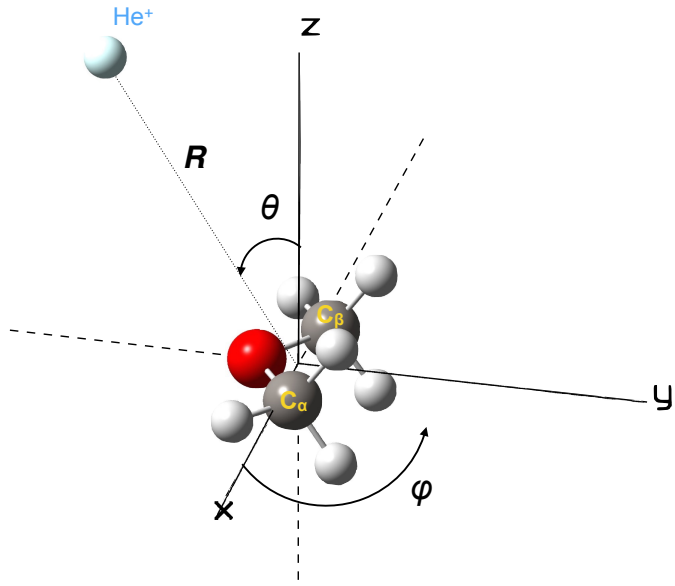

Figure 5.2: Illustration of the relevant coordinates used to represent the interaction potential between the He^+ and DME. The axes origin is positioned at the CM of the DME molecule and the xy plane coincides with the plane defined by the C_α–O–C_β atoms.

Furthermore, it is convenient to define the distances in terms of Cartesian coordinates between He^+/He and O, C_α and C_β (R_O, R_{C_α}, R_{C_β}, respectively). The expressions for R_O, R_{C_α}, R_{C_β} are the following:

$$R_O = \quad R_{O-He} = R_{O-He^+} = \quad \sqrt{(x_{He}-x_O)^2+(y_{He}-y_O)^2+(z_{He}-z_O)^2}$$
$$R_{C_\alpha} = \quad R_{C_\alpha-He} = R_{C_\alpha-He^+} = \quad \sqrt{(x_{He}-x_{C_\alpha})^2+(y_{He}-y_{C_\alpha})^2+(z_{He}-z_{C_\alpha})^2}$$
$$R_{C_\beta} = \quad R_{C_\beta-He} = R_{C_\beta-He^+} = \quad \sqrt{(x_{He}-x_{C_\beta})^2+(y_{He}-y_{C_\beta})^2+(z_{He}-z_{C_\beta})^2}$$

The x, y, z Cartesian coordinates of O, C_α and C_β are the matrix elements of 5.1, while the set of Cartesian coordinates (x_{He}, y_{He}, z_{He}) for the He^+/He atom is given by the relationship with polar coordinates:

$$x_{\mathrm{He}} = x_{\mathrm{He^+}} = Rsin\theta cos\varphi$$
$$y_{\mathrm{He}} = y_{\mathrm{He^+}} = Rsin\theta sin\varphi$$
$$z_{\mathrm{He}} = z_{\mathrm{He^+}} = Rcos\theta$$

Ranges of the polar coordinates are:

- $R \in [0, +\infty)$
- $\theta \in [0, \pi)$
- $\varphi \in [0, 2\pi)$

Due to the symmetry of the DME molecule, the PESs are symmetrical with respect to the *xy* and *zy* planes, where PES values are repeated. Hence, the polar angle ranges can be reduced to:

- $\theta \in \left[0, \frac{\pi}{2}\right]$
- $\varphi \in \left[-\frac{\pi}{2}, \frac{\pi}{2}\right]$

Entrance channel: He^+ + DME

The PES of the He^+ ion interacting with DME is described in terms of the electrostatic potential (V_{Electr}) and the non-electrostatic one ($V_{NElectr}$) (see the specific sections in Sec. 3.2).

The electrostatic component is defined as sum of Coulomb contributions between the He^+ and the charges on O, C_α and C_β. Since the dipole moment (μ_D) of DME is $1.3\,\mathrm{Debye}$, it is possible to calculate the charges of all the atoms of the molecule. The resulting effective atomic charges in terms of the electric charge, e [1], are $-0.35e$ for O and $+0.175e$ for C_α and C_β. Therefore, the electrostatic component (Eqn. 3.74) of the total interaction potential can be expressed as:

$$\begin{aligned} V_{Electr} &= \frac{e}{4\pi\varepsilon_0}\left(-\frac{q_{\mathrm{O}}}{R_{\mathrm{O}}} + \frac{q_{\mathrm{C}_\alpha}}{R_{\mathrm{C}_\alpha}} + \frac{q_{\mathrm{C}_\beta}}{R_{\mathrm{C}_\beta}}\right) \\ &= cost \times \left(-\frac{0.35}{R_{\mathrm{O}}} + \frac{0.175}{R_{\mathrm{C}_\alpha}} + \frac{0.175}{R_{\mathrm{C}_\beta}}\right) \end{aligned}$$

If $cost = 14400$, the Coulomb potential is given in meV.

The non-electrostatic component includes induction and dispersion potentials, active at large distances, combined with the size repulsion effective at short distances. Hence, the $V_{NElectr}$ is defined as a sum of contributions, due to the ion-neutral interaction pair, between the He^+ ion and each of the effective groups (O, C_α and C_β) [91]. To describe this non-covalent interaction between neutral and ionic partners, the improved Lennard-Jones model (V_{ILJ}) has been chosen for the advantages explained in Sec. 3.2. Since, in the entrance channel, a small atomic ion interacts with a large neutral molecule, the induction component is the most relevant long-range component in the $V_{NElectr}$. For this reason, the m parameter of Eqn. 3.87 in Sec. 3.2 has been selected as 4, and the values of ε and r_m (depth and position of the potential well, respectively) have been predicted by the *correlation formulas*, developed for ion-neutral systems and given in terms of polarizabilities

[1] $1.6021 \times 10^{-19}\,\mathrm{C}$

Table 5.1: Potential parameters ε and r_m defining V_{ILJ} potentials for the pair of interest in the entrance channel.

Interacting system	ε (meV)	r_m Å
$He^+ - O$	125	2.39
$He^+ - C_\alpha$ $He^+ - C_\beta$	312	2.58

of the interacting partners (see equations 3.92 and 3.93). The ε and r_m values of the relevant interaction pairs are summarized in Table 5.1. In addition, β (Eqn. 3.88) has been chosen to be equal to 7.

Therefore, the non-electrostatic component is then the sum of the three contributions:

$$V_{NElectr}(R,\theta,\varphi) = V_{ILJ}(R_O) + V_{ILJ}(R_{C_\alpha}) + V_{ILJ}(R_{C_\beta})$$

where R_O, R_{C_α}, and R_{C_β} are the same as previously defined. It is interesting to note that in the entrance channel the long range interaction is dominated by the electrostatic component (dotted curve in Figure 5.3).

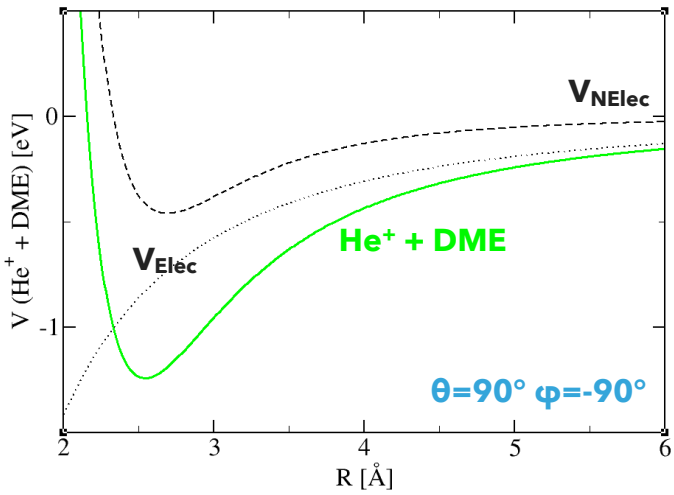

Figure 5.3: The resulting entrance channel (He^+ + DME) potential (green continuous line) for θ = 90° and φ = −90°, defined as sum of electrostatic potential (V_{Electr}, dotted black line) and no-electrostatic potential ($V_{NElectr}$, dashed black line).

Table 5.2: Potential parameters ε and r_m defining V_{ILJ} potentials for the pair of interest in the exit channel.

Interacting system	ε (meV)	r_m Å
He – O	1.7	3.38
He – C_α	2.3	3.69
He – C_β		

Exit channel: He + $DME^{\bullet+}$

The PES in the exit channel (*i.e.* after the electron transfer from DME to He^+) depends exclusively on the balance of the non-electrostatic contributions, *i.e.* induction (V_{Ind}) and dispersion components, that control the long-range interaction, combined with the size repulsion of short range distances. The dispersion potential can be defined as *van der Waals* interaction (V_{vdW}) and it is expressed again by the improved Lennard-Jones function, describing the interaction pairs between the He atom and each of the effective groups (O, C_α and C_β).

$$V_{vdW}(R,\theta,\varphi) = V'_{ILJ}(R_{\mathrm{O}}) + V'_{ILJ}(R_{\mathrm{C}_\alpha}) + V'_{ILJ}(R_{\mathrm{C}_\beta})$$

In this case, the dispersion component is the most relevant in V_{ILJ}. Therefore, $m = 6$ and $\beta = 9$ have been used, whereas the values of ε and r_m parameters have been again predicted by *correlation formulas*, given in terms of polarizabilities of the interacting partners and reported in Table 5.2.

On the contrary, the induction contribution V_{Ind} is independent of the polar angles, since it describes the interaction between a point charge on the DME and the He atom, the least polarizable neutral atomic partner. The V_{Ind} formula has been already defined (Eqn. 3.78 in Sec. 3.2). To obtain V_{Ind} in meV, we have:

$$V_{Ind}(R) = -7200\frac{\alpha_{\mathrm{He}}}{R^4}$$

where R is in angstrom and α_{He} is the polarizability of the He atom, amounting to $0.2\,\text{Å}^3$. As shown in Figure 5.4, the V_{vdW} is the dominant interaction both at intermediate and at short range for the exit channel, while the ion-induced dipole contribution (V_{Ind}) is added only as a perturbative term.

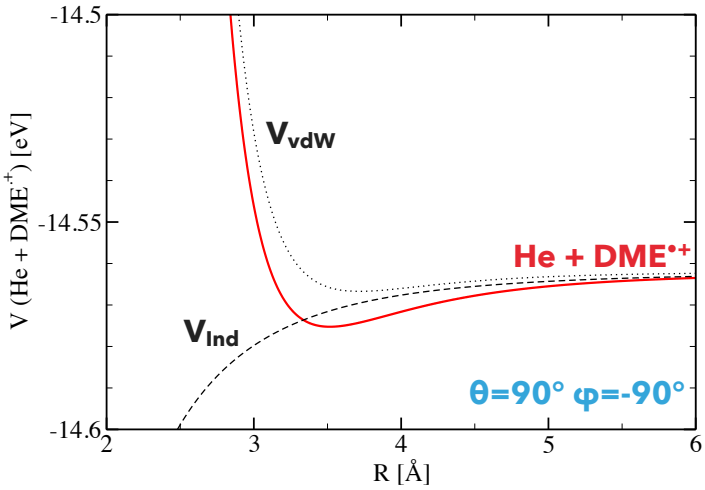

Figure 5.4: The resulting exit channel (He + $DME^{\bullet+}$) potential (red continuous line) for $\theta = 90^\circ$ and $\varphi = -90^\circ$, defined as sum of *van der Waals* potential (V_{vdW}, dotted black line) and induction potential (V_{Ind}, dashed black line). On the basis of the $\Delta_r H$ for the reaction $He^+ + DME \longrightarrow He + DME^{\bullet+}$, the asymptotic value of the potential has been fixed at $14.56\,eV$.

Anisotropy of the PES

Due to the polarity of the molecule, the resulting PES is strongly anisotropic. To highlight such a feature, the attractive and repulsive contributions have been represented using different colors in Figure 5.5 (*i.e.* blue and orange, respectively, while white symbols specify the area where the potential energy is zero).

The PES cut of Figure 5.5 is for the entrance channel, with the He^+ ion approaching DME in *xy* plane (*i.e.* θ=90°). For the chosen geometry, the interaction anisotropy is such that a deep potential well ($\sim -1.25\,eV$) located at distance of ~ 2 Å from the O atom is present when He^+ ion collides on the O-side of DME (φ=−90°). When He^+ ion approaches from the methyl side (φ=90°) at the same distance from the O atom the potential is only $-0.370\,eV$. Therefore, the most attractive geometry is when He^+ lies on the DME plane on the oxygen side (*i.e.* θ=90°, φ=−90°). We can already anticipate that the PES anisotropy plays a relevant role in the reaction dynamics, especially at low collision energy, by orienting the DME molecule in a "natural" way at long distances.

To shed more light on the anisotropy of the PES, θ and φ dependence of the PES at fixed values of R (corresponding to 3.0 Å, 5.0 Å, 10.0 Å, 15.0 Å and 20.0 Å) have been reported in Figure 5.6.

The figure on the left shows the anisotropy on the molecular plane (θ is fixed at 90°): even at intermediate and large distances ($R \geq 5$ Å), the PES is strongly repulsive when He^+ approaches

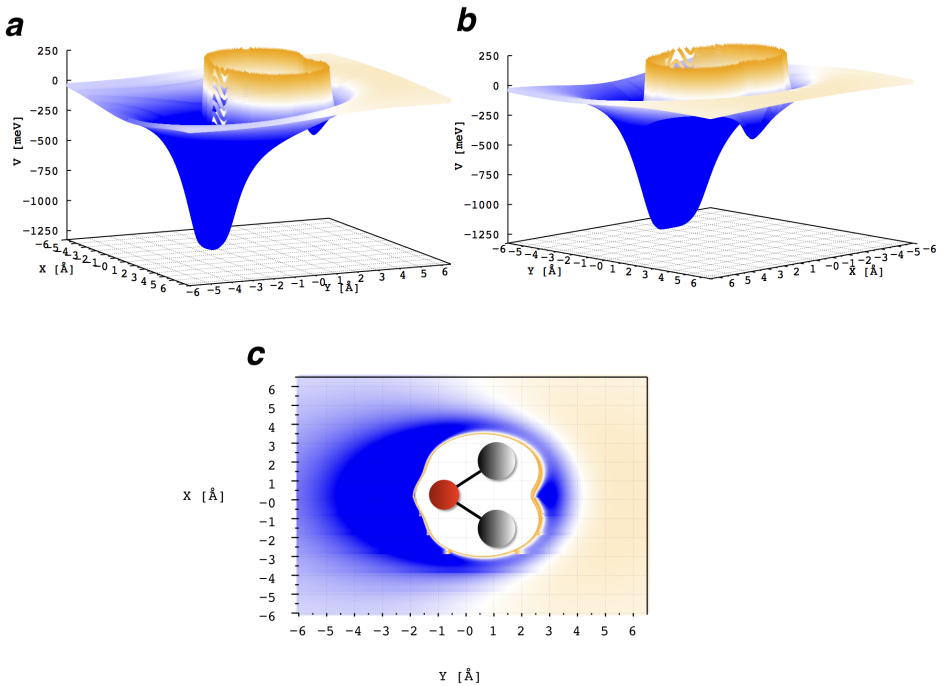

Figure 5.5: Different views for the PES of the entrance channel in the xy plane (θ=90°): panel ***a*** looking from the O-side (φ=−90°), panel ***b*** from the methyl groups (φ=90°), panel ***c*** from the top. Negative potential values are shown in blue and the positive ones are in orange, while the zero values are reported in white. In the top view, a pictorial imagine of the DME structure is reported.

Figure 5.6: *On the left*: cuts of the PES for the He^+ – DME entrance channel for a fixed value of θ=90° (corresponding to the He^+ ion being constrained on the *xy* C_α–O–C_β molecular plane, *i.e.* the first mirror plane of the C_{2v} molecule) and five different R values corresponding to 3.0 Å, 5.0 Å, 10.0 Å, 15.0 Å and 20.0 Å (in different colors) plotted as a function of φ. *On the right*: cuts of the PES for the He^+ – DME entrance channel for fixed values of φ=−90° (left side) and 90° (right side) and five different R values corresponding to 3.0 Å, 5.0 Å, 10.0 Å, 15.0 Å and 20.0 Å (in different colors) plotted as a function of θ. The cuts correspond to the He^+ ion being constrained on the *yz* (*i.e.* the second mirror plane of the C_{2v} molecule).

from the methyl sides and strongly attractive on the O atom side, mainly because of the electrostatic component of the interaction.

It is convenient to define the PES anistropy $\Delta V(R)$ as the difference between the energy values of the least and most stable configurations, for fixed R values. Interestingly $\Delta V(R)$ is still $\sim$ $22\,\mathrm{meV}$ at 20.0 Å. Furthermore, in the region between the two methyl groups (φ=90°), the potential becomes attractive at short distances (albeit being repulsive at large distances), although much less than on the O-side (φ=$-90°$): at 3.0 Å the potential is around $-1000\,\mathrm{meV}$ on the O-side and around $-250\,\mathrm{meV}$ on the CH_3^+-side, while the PES anisotropy $\Delta V(R)$ is much larger ($-5300\,\mathrm{meV}$). The right panel of Figure 5.6 presents the interaction when He^+ approaches in a plane perpendicular to the molecular one, *i.e.* the *yz* plane.

The most important consequence of that strong anisotropy of the entrance channel PES is that the polar DME molecule can be induced spontaneously (*i.e.* without applied external fields) to orient itself in the electric field gradient associated with the interaction with the He^+ ion. For gaining a better understanding of this phenomenon, it is useful to compare the PES anisotropy ($\Delta V(R)$) with the mean rotational energy of DME ($E_r = 3/2k_BT$), which amounts to $\sim 39\,\mathrm{meV}$ at T=300 K. As already mentioned, the potential anisotropy $\Delta V(R)$ is $\sim 22\,\mathrm{meV}$ at 20.0 Å and increases to $\sim 40\,\mathrm{meV}$ and $90\,\mathrm{meV}$ for R = 15.0 Å and 10 Å, respectively. At very large distances (several tens of $\mathrm{angstrom}$) the DME molecule can freely rotate (left panel of Figure 5.7), while the rotations may be partially hindered already at a distance of 5.0 Å, mainly for low rotational states. Rotations may become completely impeded at 10.0 Å, where the potential anisotropy is almost twice the mean rotational energy (see right panel of Figure 5.7). Under these conditions, the molecular collision complex is confined to a *pendular state* [137, 138], in which the hindered molecular rotations transform into bending vibrations of the collision complex.

At 2-3 Å, the anisotropy can be even higher than $1\,\mathrm{eV}$. The transformation of free rotations into pendular states, driven by the natural electric field gradient generated by the interaction potential anisotropy, has been experimentally demonstrated *via* molecular beam scattering experiments among water molecules or other polar molecules [139, 140]. In the present case, where the ion-permanent dipole interaction is involved, the transformation must be much more efficient since the potential anisotropy is at least ten times larger than the cited cases.

As explained in the following, it is expected that the strong anisotropic interaction between the He^+ and the DME controls the selective trapping of reagents in the entrance channel and drives the charge transfer process only from selected configurations. In other words, during the collision with He^+, most of the DME molecules will be channeled within narrow angular cones confined around the most attractive configuration of the interacting system.

In addition to energy considerations, it is interesting to note also the time scale of the collisions. In fact, the probability of formation of pendular states is higher when the collision time is larger or comparable with the average period of pendular motions, the latter being in the range $10^{-13}\,\mathrm{s}$ to $10^{-14}\,\mathrm{s}$ (*i.e.* the standard timings for bending modes). Average collision times change with the collision energy (hence, the velocity) and can be estimated by calculating the time taken by the system to travel twice a distance of 15 Å, *i.e.* the largest distance at which the molecules are trapped in the pendular states. In the collision energy range of the experiment, the average collision times are in the range $\sim 4 \times 10^{-12}\,\mathrm{s}$ to $2 \times 10^{-13}\,\mathrm{s}$ and therefore, satisfy the condition of being longer than the pendular motions, at least in the low and intermediate collision energy regimes. At high collision energies, the interaction time between the colliding partners might be too short to obtain a high degree of molecular orientation towards the most stable configurations because a substantial

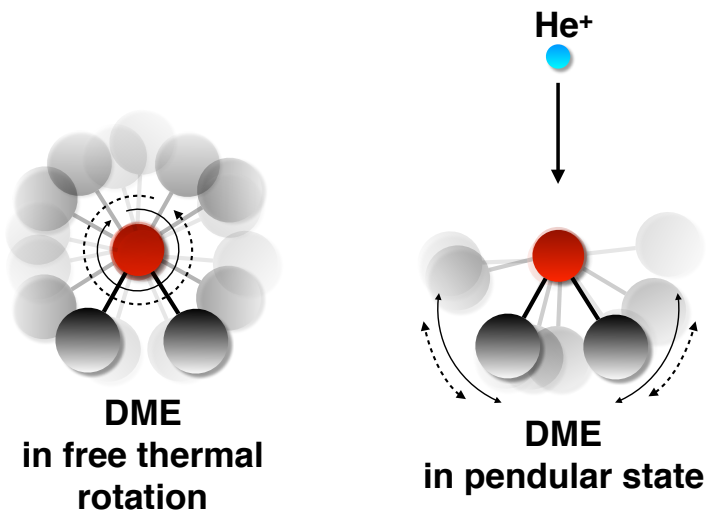

Figure 5.7: Pictorial views of the thermal rotations of DME with respect to an imaginary axis centered in the O atom and of the formation of a pendular state in presence of the He^+ ion.

fraction of molecules will have enough energy to escape from the "pendular trap", extending to a wider region the narrow reactive cone.

5.2.2 Crossings between the entrance and exit channels

As already explained in Sec. 3.1.2, within the collision energy range ($0.050\,\mathrm{eV}$ to $7\,\mathrm{eV}$) operative in our experiment, the transfer of the electron from DME to He^+ occurs *via* non-adiabatic transitions located at the crossings between the entrance and the exit channels, *i.e.* between the associated PESs formulated in the diabatic representation. However, the charge transfer reaction is highly exothermic, by $(14.562 \pm 0.025)\,\mathrm{eV}$, due to the significant difference in ionization energy between He and CH_3OCH_3, $24.587\,41\,\mathrm{eV}$ and $10.025 \pm 0.025\,\mathrm{eV}$, respectively [141, 116]. Assuming that the transferred electron is ejected by the HOMO (*Highest Occupied Molecular Orbital*) of the DME forming a ground state of the radical cation, the entrance and exit channels do not cross. To exemplify the situation, a cut of the PESs, in the entrance (green solid curve) and exit (red solid curve) channels with the DME radical cation formed in its electronic state, is represented in Figure 5.8, where the potential curves have been obtained by fixing θ=90° and φ=−90°.

This geometry has been chosen since it represents the most attractive configuration, as said already above, and things do not change much if other geometries are considered, since for all geometries entrance and exit channels do not cross. On the contrary, if the electron is removed from an inner orbital (as already hypothesized in Sec. 4) having a higher ionization potential, the

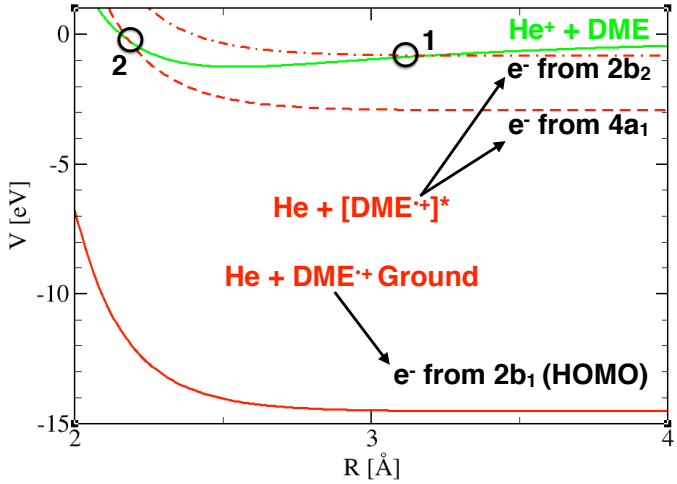

Figure 5.8: Potential energy curves of the entrance He^+ + DME (green curve) and exit He + $DME^{\bullet+}$ (red continuous curve) channels for θ=90° and φ=−90°, with the DME radical cation formed in its electronic ground state. The red dashed and red dot-dashed curves represent the exit channels assuming the removal of an electron from the inner valence orbitals $4a_1$ or $2b_2$, respectively. In this case the DME radical cation is formed in a excited electronic state ($[DME^{\bullet+}]^*$).

reduced exothermicity allows the entrance and exit channels to cross at distances suitable for the charge exchange.

The electronic configuration of DME in its ground state can be written as

$$(\text{core})^6 \underbrace{(3a_1)^2(2b_2)^2(4a_1)^2}_{\text{inner valence}} \underbrace{(1b_1)^2(5a_1)^2(3b_2)^2(1a_2)^2(4b_2)^2(6a_1)^2(2b_1)^2}_{\text{outer valence}}$$

The experimental (e, 2e) ionization potential spectrum of DME is well known and here, the results at the impact energy of 1200 eV of Miao *et al.* are reported and shown in Figure 5.9 [142].

The resolved ionization bands are seven (with 0.7 eV as energy resolution). The first four orbitals ($2b_1$, $6a_1$, $4b_2$ and $1a_2$) have ionization potentials equal to 10.1 eV, 11.8 eV, 13.3 eV and 14.2 eV, respectively. Unfortunately, orbitals $3b_2$, $1b_1$, $5a_1$ are too close to be resolved (maximum at 16.2 eV). Finally, the $4a_1$ and $2b_2$ orbitals are located at 21.2 eV and 23.3 eV, respectively. These last orbitals have the appropriate energy to promote the reaction by electron exchange. Assuming that the electron transferred to He^+ belongs to either one of the inner valence orbitals ($4a_1$ or $2b_2$), the asymptotic value of the exit channel can be re-scaled accordingly to obtain the red dashed and red dot-dashed curves in Figure 5.8. The reaction exothermicity is thus reduced to about

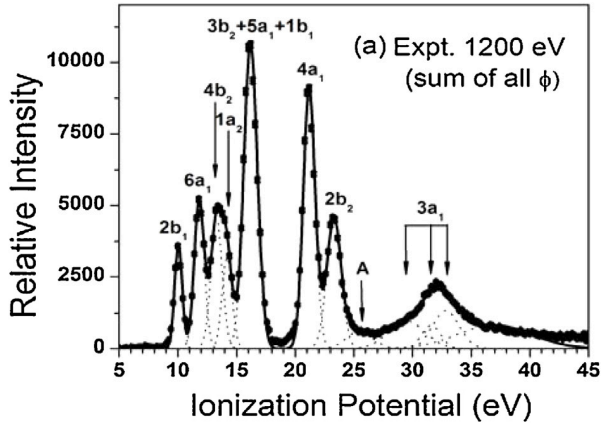

Figure 5.9: The experimental (e,2e) ionization potential spectrum of DME at the impact energy of $1200\,\mathrm{eV}$ (with $0.7\,\mathrm{eV}$ as energy resolution)[142]. The labels over-written on the peaks indicate the relative orbital from which the electron is removed.

$3.4 \pm 0.7\,\mathrm{eV}$ and $1.3 \pm 0.7\,\mathrm{eV}$, respectively. In all dynamics calculations, zero energy has been fixed to the asymptotic value of the entrance channel.

In general, for a fixed geometry of the $[He-DME]^+$ system, there are three diabatic potential energy curves to be considered: the entrance channel (He^+ – DME) and the two excited exit channels (He – $[DME(4\,a_1)^{\bullet+}]^*$ and He – $[DME(2\,b_2)^{\bullet+}]^*$). Therefore, the nascent DME radical cation has a high energy content, and it is expected to dissociate almost instantaneously.

At this level of the discussion, it is of interest to have some insights on the electron density distribution of the DME molecular orbitals, from which the electron is removed. Furthermore, we can anticipate that the electron density of those orbitals plays a role in defining the probability of charge transfer to He^+, since it affects the overlap between the orbitals involved in the electron exchange. Hence, the electron densities of the relevant molecular orbitals $4a_1$ and $2b_2$ have been calculated with NBO analysis (see Sec. 3.3) and the the results are shown in Figure 5.10.

The minimum energy structure of neutral DME has been determined with DFT, using the M06-2X functional with the basis-set cc-pVTZ (for details see Appendix B). The results are shown in Figure 5.11 and are in agreement with the experimental values reported in [136]. For the calculated C–O bond the difference with respect to the experimental one is $0.008\,$Å (corresponding to 0.6%), for the C–H bond is $0.002\,$Å (corresponding to 0.2%) and for the bond angle C–O–C is 0.4° (0.9%). In addition to the electron densities of the molecular orbitals, the NBO analysis has allowed to determine of which atomic orbitals the involved MO are combination. Actually, the orbital $2b_2$, the most involved in the reaction for its crossing parameters and with the highest contribution to the cross-sections according to our calculations, is combination of only C (33.93%) and O (66.07%) atomic orbitals, whereas the orbital $4a_1$ is the lone pair of the oxygen. This result is

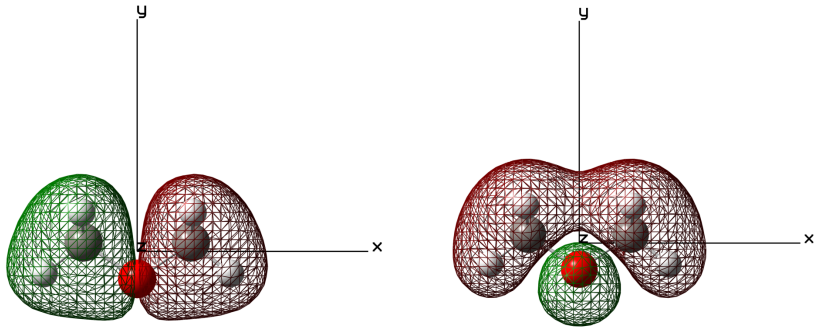

Figure 5.10: Electron densities of $2b_2$ (on the left) and $4a_1$ (on the right) molecular orbitals of neutral DME.

perfectly in agreement with the products obtained by the title reaction. In fact, in Sec. 4.1 we concluded that a C−O break bond should be the responsible of the BRs of the reaction between He^+ and DME. Now, we can confirm this experimental evidence correlating a specific orbital with the charge transfer process and finding out that this MO corresponds precisely with our hypothesis.

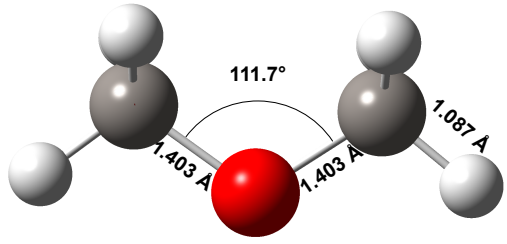

Figure 5.11: Neutral DME optimized at the M06-2X/cc-pVTZ level. The significant bond distances (in Å) and bond angle are reported. The data are in agreement with literature values [136].

Therefore, at this point it is possible to define the most significant geometries in order to have the crossing parameters (see Sec. 3.1.2). In fact, for the dynamics of the process we assume that the orientation effects (Sec. 5.2.1) control the reaction. For this reason, the most attractive configurations, *i.e.* those corresponding to the He^+ ion approaching the DME plane in the proximity of the O-side (as already said, the highest attraction is exhibited by the co-planar configuration, defined by θ=90° and φ=−90°), have the most significant contribution to the cross-section calculation. Hence, it is possible to define an "effective cone" , that is confined around the C_{2v} symmetry axis of DME and is not symmetric, *i.e.* it is more open in the *yz* plane than in the *xy* plane, due to the repulsion of the methyl groups.

In addition to the anisotropy, the position and energy of crossings between the non-adiabatic curves also need to be taken into account to define the most relevant θ and φ values. In fact, while for the most stable co-planar configuration both the crossings are exothermic and therefore are open at all the explorable collision energies, when He^+ approaches, still from the O-side, but closer to the methyl groups ($-90° < \theta < 0°$), the exothermicity of the crossings decreases and eventually they become highly endothermic, thus no longer contributing to the charge transfer process. As expected, the reaction probability is non-zero only in a narrow cone confined on the yz plane in the direction opposite to the methyl groups.

For the dynamic calculations, a limited number of configurations, confined in this narrow angular cone, have been selected. They must be considered as the most representative and efficient geometries to carry out extensive integral cross-section calculations to be compared to the experimental data. The values of polar angles defining the selected configurations for both exit channel curves (i = 1 and 2 for the $2b_2$ and $4a_1$ crossings, respectively) are reported in Table 5.3, together with the position R_i, value of energy E_i, and absolute difference of slope Δ_i. Furthermore, a pictorial view of the effective cone is represented in Figure 5.12, in which the polar angle values are reported. For the sake of completeness, we report also the parameters for the most (*i.e.* θ=90° and φ=−90°) and less (*i.e.* θ=90° and φ=90°) attractive geometries. Finally, at each collision energy in the CM frame, cross-sections from the different configurations are averaged to compare with the experimental data.

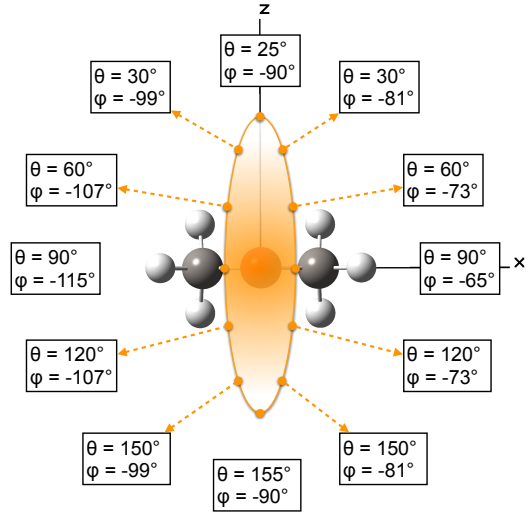

Figure 5.12: Pictorial view of the base of the effective cone used to calculate the cross-sections. It is a narrow non-symmetrical slice of the space around the molecule, more open in the yz plane than in the xy plane, due to the repulsion of the methyl groups. The y-axis is perpendicular to the figure plane.

Table 5.3: Position R_i, energy E_i, and absolute difference of slopes Δ_i for crossing i between the entrance and exit diabatic curves at selected and fixed θ and φ values.

θ	φ	i=1			i=2		
		R_i [Å]	E_i [meV]	Δ_i [meV Å^{-1}]	R_i [Å]	E_i [meV]	Δ_i [meV Å^{-1}]
90°	−65°, −115°	3.15	-801	785	2.11	353	6474
60°	−73°, −107°	3.08	-805	791	2.07	18	6493
30°	−81°, −99°	2.86	-802	872	1.85	400	6153
25°, 155°	−90°	2.81	-801	891	1.81	585	6062
90°	−90°	3.20	-807	741	2.18	-230	6811
90°	90°	1.14	53998	23728	1.08	67455	39661

5.2.3 Calculation of cross-sections

A treatment based on the Landau-Zener-Stückelberg approach (see Chapter 3) has been used to calculate transition probabilities at crossings between different electronic curves in a one dimensional model, that is considering specific cuts of the PESs, in which, for fixed values of θ and φ angles, the reaction coordinate is given by the polar coordinate R. Vibronic couplings have not directly been taken into account, since the vibrational levels of DME to be considered are several and closely spaced in energy, making their resolution impossible under the experimental conditions adopted.

According to Eqn. 3.63, the probability of single diabatic passage through the i-th crossing between two diabatic curves is:

$$p_i(E,\theta,\varphi,l) = exp\left(-\frac{2\pi H_i^2}{\hbar v_R(l,E)\Delta_i}\right) \tag{5.2}$$

where E is the collision energy, l is the quantum number representing the orbital angular momentum of the collision complex, H_i is the non-adiabatic coupling term between the two potential curves, Δ_i as defined previously is the absolute value of the difference in slopes of the diabatic potential curves calculated at the crossing point and v_R is the radial velocity (Eqn. 3.64), that in terms of l is given by:

$$v_R^2 = \frac{2}{\mu}\left[E\left(1-\frac{l(l+1)}{k^2R_i^2}\right)-E_i\right] \tag{5.3}$$

in which the impact parameter b has been substituted knowing the relation:

$$b = \frac{[l\,(l+1)]^{1/2}}{k}$$

where k is the wavenumber defined as:

$$k = \frac{(2E\mu)}{\hbar}$$

In Eqn. 5.3, E_i is the value of the potential energy at the crossing ($E_i < 0$ for an exothermic crossing), R_i is the position of the crossing and μ is the reduced mass of the He-DME system.

For each geometry (fixed θ and φ) and collision energy E, the total cross-section for charge transfer to the i-th exit channel can be written as a sum of contributions from each l:

$$\sigma_i(E,\theta,\varphi) = \frac{\pi}{k^2}\sum_{i=0}^{l_{max}}(2l+1)\,P_i\,(E,\theta,\varphi,l) \tag{5.4}$$

l_{max} of Eqn. 5.4 can be defined as the maximum value of l for which the system has sufficient energy to overcome the centrifugal barrier and reach the crossing point located at R_i. For high collision energies, l_{max} is given by the maximum value of l for which the radial velocity v_R is real:

$$l_{max} = kR_i\sqrt{1-\frac{E_i}{E}} \tag{5.5}$$

On the contrary, for exothermic crossings ($E_i < 0$) and low collision energies, l_{max} found by Eqn. 5.5 generates a centrifugal barrier located at $R_{max} \gg R_i$, higher than the available collision energy (see Sec. 3.1.1). In Figure 5.13, the effective potential V_{eff} (sum of the interaction potential V and the centrifugal one V_C) for the most attractive geometry (θ=90° and φ=−90°) for two different l at E=100 meV (dashed red line) is represented: the first curve (turquoise continuous line) is the effective potential with l_{max} calculated by Eqn. 5.5 and it is evident that the generated centrifugal barrier (at 4 Å) is impossible to overcome with the available collision energy. For this

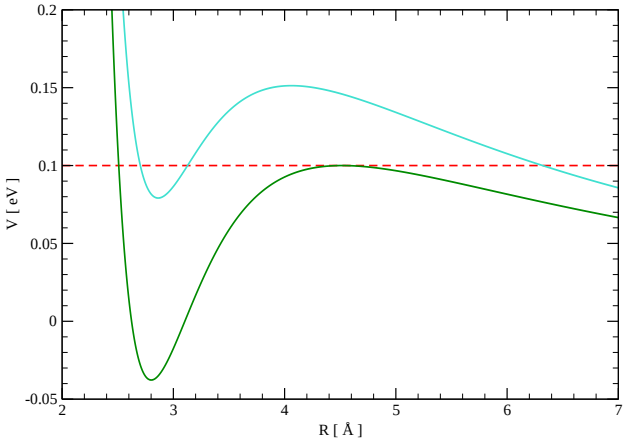

Figure 5.13: In the figure, the effective potential V_{eff} is represented for the most attractive geometry (θ=90° and φ=−90°) at fixed E=100 meV (dashed red line). The turquoise curve is the effective potential with l_{max} calculated by Eqn. 5.5 and it is evident that the generated centrifugal barrier (at 4 Å is impossible to overcome with the available collision energy. Using Eqn. 5.6, the l_{max} generates a smaller barrier (green curve) surmountable with E=100 meV.

reason, l_{max} should be reduced in order to avoid the formation of a high centrifugal barrier (green curve in Figure 5.13). Since the interaction potential V is represented in a complex analytic form, an analytic expression for l_{max} can not be obtained. Therefore, for each energy E the maximum value of l was calculated computationally. The adopted procedure was based on the solution of Eqn. 5.6 in l, after finding R_{max} (the coordinate R in which V_{eff} is maximum) from the derivative of V_{eff}. The corresponding l that satisfies Eqn. 5.6 in R_{max} (*i.e.* that specific l value for which the effective potential is smaller than the collision energy E) is l_{max}, used then for calculating the

cross-section.

$$V_{eff}(R_{max}, \theta, \varphi, l) < E$$
$$V(R_{max}, \theta, \varphi) + \frac{\hbar l\,(l+1)}{2\mu R_{max}^2} < E \tag{5.6}$$

In Eqn. 5.4, $P_i\,(E, \theta, \varphi, l)$ is the total probability for formation of $[DME]^{\bullet+*}$ in one of the two excited states and takes into account the flux branching at each crossing adjusting Eqn. 3.66 in Chapter 3. In this case, for each E, θ, φ, l and to form $[DME]^{\bullet+*}$ removing the electron from the $2b_2$ orbital, we should have:

$$P_1 = (1-p_1)p_1 + p_1p_2^2(1-p_1) + p_1(1-p_2)^2(1-p_1) \tag{5.7}$$

where p_1 and p_2 are given by Eqn. 5.2. Using Figure 5.8, we can define:

- the first term $(1-p_1)p_1$ is the probability to jump once at the first crossing to the $2b_2$ product curve, remaining on this after the turning point;
- the $p_1p_2^2(1-p_1)$ is the probability to jump to the $4a_1$ product curve at the second crossing and to move to the $2b_2$ product at the first crossing;
- $p_1(1-p_2)^2(1-p_1)$ is about the probability to jump twice at the second crossing, forming the $2b_2$ product at the first crossing.

On the contrary, for $[DME]^{\bullet+*}(4a_1)$, the total probability should be:

$$P_2 = p_1[2p_2(1-p_2)] \tag{5.8}$$

since to have $4a_1$ product it is necessary not to jump at the first crossing (p_1), but jumping only at second crossing ($2p_2(1-p_2)$, according to Eqn. 3.66).

Equations 5.7 and 5.8 should be correct, if our charge transfer process was not dissociative. Since the experimental evidence is that the reaction between He^+ and DME is completely dissociative, equations 5.7 and 5.8 are not valid and the following expressions should be used instead:

$$P_1 = (1-p_1)(1+p_1p_2^2) \tag{5.9}$$

$$P_2 = p_1(1-p_2)(1+p_2) \tag{5.10}$$

In fact, the new expressions for P_1 and P_2 are built considering that once the non-adiabatic transition from the entrance to one of the exit curves is operative, a fast electronic rearrangement in the excited $[DME]^{\bullet+}$, leading to fragmentation, is triggered. It occurs on a much shorter time-scale compared to the time taken by the collision partners to travel in the crossing region. For a comparison of timings, we note that the transit time of the collision partners over a distance of 0.5 Å is in the range from 3×10^{-14} s to 3×10^{-15} s (for collision energies in the experimental range from 0.050 eV to 7 eV), while electron relaxation times are in the order of 10^{-15} s - 10^{-17} s. Therefore, once the electron is transferred (jump to the product curve) the fragmentation of the molecule takes place instantaneously and the system has no time to travel up to the *turning point*. For this reason, the contribution in equations 5.7 and 5.8 of terms regarding the probabilities to stay on the same curve or to jump on the other one, after the jump on the product curve, are neglected, obtaining equations 5.9 and 5.10. Furthermore, it should be noted that in equations 5.9 and 5.10 a

p_i value equal to 1 signifies that the system remains on the diabatic curve, which means no charge transfer reaction. On the other hand, p_i=0 means that the non-adiabatic transition is complete.

To obtain the total cross-section, the cross-sections obtained from Eqn. 5.4 are summed over i:

$$\sigma(E,\theta,\varphi) = \sum_{i=1}^{2} \sigma_i(E,\theta,\varphi) \tag{5.11}$$

The H_i term of Eqn. 5.4 is still undefined. This is the non-adiabatic coupling at each crossing between the entrance and exit potential curves and it is introduced as a perturbation term that promotes the non-adiabatic events. In general for collisions in low energy range, the *Franck-Condon factor* can be negleted in the non-adiabatic coupling formulation [143]. In fact, this factor originates from the idea that, during the electron transition, the nuclei distances and their relative momentum do not vary, they remain unchanged due to the fact that the electron velocities are larger than those for the nuclei. It is already demonstrated in Sec. 3.1.2 that for charge transfer processes in ion-neutral molecule collisions the nuclear velocities can not be neglected, breaking the Born-Oppenheimer approximation. Therefore, in cases when the nuclear velocity is comparable to the electron one, during the transition the nuclei distances can strongly vary since the non-adiabatic process can not be considered instantaneous, and also the Franck-Condon principle is not valid.

From this general starting point for the non-adiabatic coupling, we need to distinguish the role of H_i in the inner (i = 2) and the outer (i = 1) case because of the different symmetries of the molecular orbitals involved in the electron exchange process (see Figure 5.10). In particular, the i=1 case is notable because of the nodal plane exhibited by the molecular orbital $2b_2$ along the approach direction of He^+ towards the most attractive configuration (θ=90° and φ=−90°). More in detail, we expect that the $2b_2$ molecular orbital (MO) gives the largest contribution to the charge transfer cross-section due to the energetically favorable positions of crossings for all the geometries. Unfortunately, this MO presents a node in the *yz* plane, that means a very small overlap with the spherically symmetric atomic orbital of He^+ (*i.e.* $^2S_{1/2}$). Hence, the case implies the paradox that the most attractive geometry (corresponding to He^+ approaching the DME plane from the O-side) is also the least efficient for the charge transfer process when molecular orbital symmetries are considered.

Following previous investigation [144] and the treatment of Landau [68] of transitions between non-symmetric systems, we have decided to represent the non-adiabatic coupling H_1 as Coriolis coupling (Eqn. 5.12), since the electron is transferred between orbitals with different symmetry and therefore the crossings are *heterogeneous*.

$$H_1(l,E,\theta,\varphi) = H_C = \frac{\hbar^2 l}{\mu R_1^2} M \tag{5.12}$$

where l, μ and R_1 have been already defined. Furthermore, the Landau formula has been appropriately extended to include the dependence of the H_1 coupling on the strong stereo-chemistry involved in the process and hence, the dependence on the collision energy E and on the original molecular orientation within the collision complex. In fact, the dependence of H_1 on the collision energy is expected to play a crucial role in the reaction: at low collision energies, the "natural" orientation of DME, promoted by the electric field gradient associated with the strongly anisotropic inter-molecular potential, is high, but it becomes inefficient at increasing values of E since molecules have sufficient energy to escape from the potential gradient. Therefore, H_1 should

tend to be small when the molecules are oriented and the Coriolis coupling becomes weak. For these reasons, the M term of Eqn. 5.12 has been extended to:

$$M = C\left(\left|\frac{E}{E_1}\right|\right)^{\gamma} \tag{5.13}$$

where the dimensionless parameter C and the exponent γ have been chosen to obtain the best agreement with the experimental data (while E and E_1 have been already defined). For this reason, C has been fixed to be equal to 6 and γ equal to $1/4$.

It is intriguing to note that in the thermal collision energy range ($\sim 50\,\mathrm{meV}$ to $100\,\mathrm{meV}$) the M value is in the 2-3.5 interval, in qualitative agreement with the expectations from theory [145, 146, 147, 148] that suggests $M \sim 1$ for the pure Coriolis coupling. At the highest energy, the value of M becomes equal to ~ 9 and it increasingly accounts for the possibility that the non-adiabatic transitions occur *via* a different mechanism, controlled by the overlap between the relevant atomic and molecular orbitals.

On the contrary, the coupling H_2 at the crossing with the He – $DME^{\bullet+*}(4a_1)$ exit channel, the electron density of the involved $4a_1$ orbital is isotropic and gives a favorable overlap for several geometries close to the most stable configuration of the collision complex. Hence, an explicit dependence on the collision energy is not necessary. For the sake of simplicity, we have decided to fix H_2 at a constant value equal to $200\,\mathrm{meV}$.

Using equations 5.4 and 5.11, cross-sections $\sigma_1(E)$, $\sigma_2(E)$ and total $\sigma(E)$ have been calculated as a function of the collision energy E for the chosen geometry (see Figure 5.12). The results are shown in Figure 5.14 in which the contribution of both crossings i =1,2 and their sum are represented (in blue, red and black line, respectively) for each configuration. It is interesting to note that the crossing i=1 gives the major contribution to the total cross-section in the whole energy range investigated, while the crossing i=2 is a threshold process, giving lower cross-section values. The experimental total cross-sections (green dots) are compared with the calculated ones (black line) in Figure 5.16. The calculated cross-sections are in a very good agreement with the experimental results. The deviation at high collision energies is attributed to the omission of strongly endothermic crossings, which are effective at high collision energy. In fact, other configurations falling outside the "effective cone" defined above can now contribute to the cross-section, and a wider cone should be considered in the calculations (see Appendix C).

Furthermore, in Figure 5.16 the result assuming no preferential orientation of the reactants has been also reported with black dashed line. In this case, the cross-sections have been calculated by using the same Landau-Zener model discussed above, but without considering stereo-chemical effects (*e.g.* the strong alignment of the colliding system and the pendular state formation) in order to demonstrate their crucial role in the reaction. The new calculation differs from the mentioned one for the number of considered crossings (corresponding to different approaching positions of He^+) and for the expression of the non-adiabatic coupling. Furthermore, it is worth to note that this calculation is completely different from the capture model such as the Langevin one (see Section 3.1.1) for the following reasons:

1. the used opacity function in the cross-section expression (Eqn. 3.7 in Section 3.1.1) is the one theorized by Landau-Zener-Stückelberg for a non-adiabatic transition (Equations 3.63 and 3.66 in Section 3.1.2), while in the capture model the opacity function is simply assumed to be 1 if the colliding system has sufficient translational energy to overcome the centrifugal barrier;

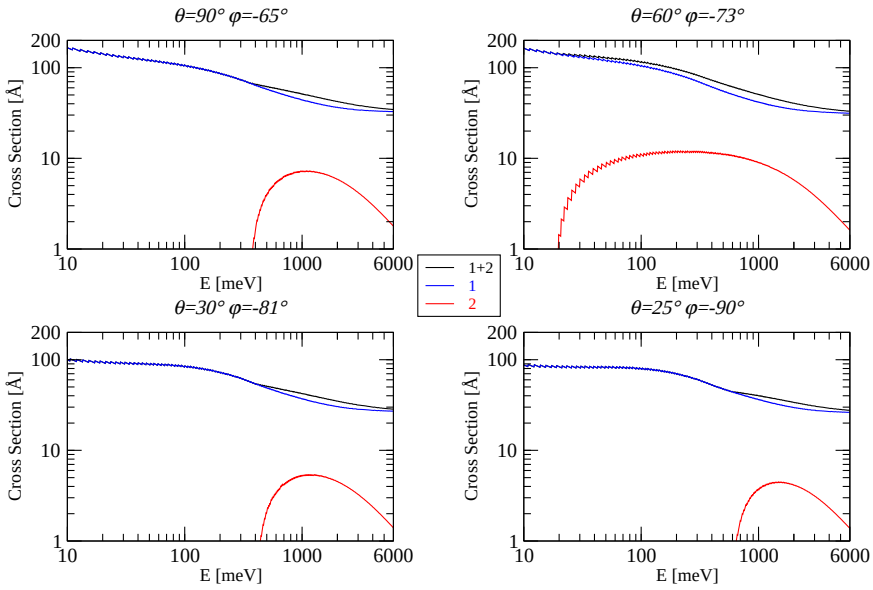

Figure 5.14: Calculated contributions to the total cross-section for the title reaction for selected configurations (fixed θ, φ values, as indicated on top of each of the four graphs) confined in the narrow angular cone most effective for the reaction. In blue is $\sigma_1(E)$, in red is $\sigma_2(E)$ and in black is their sum $\sigma(E)$.

2. in the capture model only the long-range dispersion potential is taken into account, while in our calculation we use a realistic PES, sum of several contributions (electrostatic, dispersion and inductive potential) as already explained. In our representation, the short-range contribution is considered with the long-range one in the dispersion potential (ILJ potential);
3. in the no-alignment calculations, the considerations on the electron density of the involved MOs remains, whereas the capture model does not account for them.

Since in our model the alignment of the colliding system has been taken into account by the Coriolis coupling (Equations 5.12 and 5.13), a new expression for the coupling H_1 has been chosen in order to neglect the stereo-chemical effects, but to consider the unfavorable overlap between the atomic s orbital of He^+ and the involved $2b_2$ molecular orbital of DME, anyway. Therefore, the coupling term H_1 has been represented as a constant value (H_0=200 meV, according to the coupling chosen for the second crossing) modulated by a $(cos\varphi)^2$ (according to previous treatments

[149, 150, 151]) term. The latter brings the coupling to zero for geometries (*e.g.* φ=90°, −90°) giving null overlap between the involved orbitals, while it makes the coupling maximum for geometries (*e.g.* φ=0°, 180°) giving the best overlap (corresponding to maximum of electron density in the $2b_2$ MO). Finally, the total cross-sections have been calculated by averaging cross-sections for an appropriate number of φ, θ couples representing different but equally probable directions of approach for the He^+ on the whole sphere surrounding the DME molecule.

The values of each φ, θ couple has been calculated by the following procedure. Considering a sphere of radius r which is centered in the CM of the molecule, it is possible to divide it in n "parallels", characterized by a specific value of θ (namely θ_i) (the green circle in panel **a** of Figure 5.15). The circumference of each parallel is:

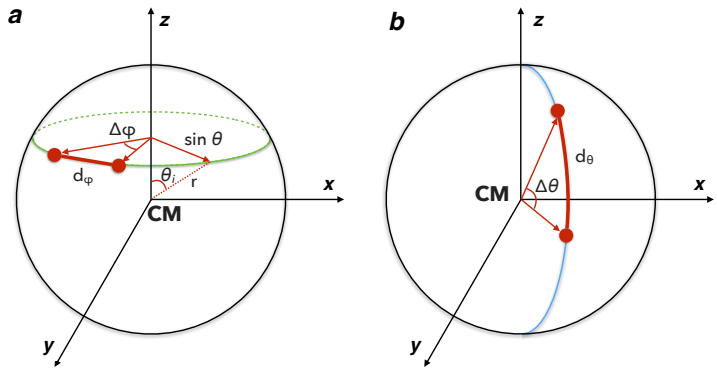

Figure 5.15: Sphere of radius r and centered in the CM of the molecule. In panel **a** the parameters fundamental to define the "parallel" are reported, while in panel **b** the meridian is represented.

$$C_{parallel} = 2\pi r sin\theta_i \tag{5.14}$$

Furthermore, a meridian of semi-circumference $C_{meridian} = \pi r$ must also be considered (the blue semicircle in panel **b** of Figure 5.15). Defining n_θ as the number of points on the meridian and n_φ as those on the parallel, the distances between two consecutive points on the parallel (d_φ) and on

the meridian (d_θ) can be written as:

$$d_\varphi = \frac{C_{parallel}}{n_\varphi} = \frac{2\pi r sin\theta_i}{n_\varphi}$$
$$d_\theta = \frac{C_{meridian}}{n_\theta} = \frac{\pi r}{n_\theta}$$

Since an uniform distribution of points on the sphere is requested, d_φ must be equal to d_θ:

$$d_\varphi = d_\theta$$
$$\frac{2\pi \cancel{r} sin\theta}{n_\varphi} = \frac{\pi \cancel{r}}{n_\theta}$$

Defining the ratio $\frac{\pi}{n_\theta}$ as the angle subtended by d_θ, $\Delta\theta$, the number of points on the parallel is:

$$n_\varphi = \frac{2\pi sin\theta}{\Delta\theta} \tag{5.15}$$

$\Delta\varphi$ is subsequently obtained by the following expression:

$$\Delta\varphi = \frac{2\pi}{n_\varphi} \tag{5.16}$$

Using $n_\theta = 10$ ($\Delta\theta$ =18°), a set of 108 equally distributed points on the sphere around the molecule has been obtained.

As shown in Figure 5.16, the resulting data exhibit a really different trend compared to the experimental one. The disagreement might be used as the further evidence that the dynamics treatment should take into account the relevant role of the strong anisotropy of the PES in the entrance channel.

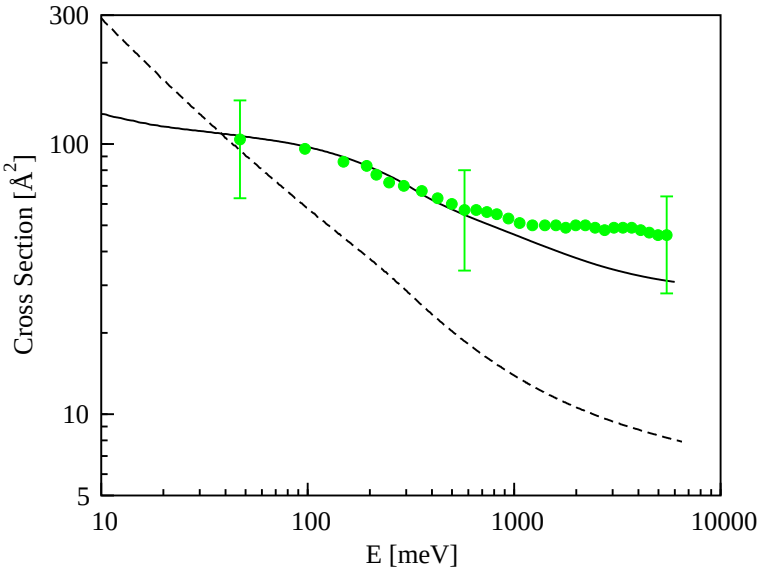

Figure 5.16: Comparison between calculated (in black) and experimental (in green) total cross-sections for the reaction He^+ + DME. Error bars represent an estimate of the accuracy of the absolute values of the cross-section (40%) and account for systematic errors. For the sake of clarity, the error bars have been reported only on three experimental points. The black dashed line results from the discussed model assuming that during the reaction the reactants have not preferential orientations. It is evident that the stereo-chemistry in the charge exchange process plays a crucial role in the dynamics.

5.3 Dynamics of the *dissociative charge transfer process* for the reaction $He^+ + HCOOCH_3$

5.3.1 The PESs

The geometry of the $[He-MF]^+$ interacting complex is conveniently defined using a reference frame centered on the CM of the MF, and the $H-C(=O_\alpha)-O_\beta$ molecular plane coincident with the *xy* plane, as shown in Figure 5.17. As already done with the DME molecule, the $-CH_3$ group is simplified in the "effective atom" C, having the mass and the polarizability of a methyl group. The MF polarizability is equal to $5.050\ \text{Å}^3$ [135] and its dipole moment is (1.77 ± 0.03) Debye [152]. The polarizability has been further partitioned into five components, one for each group of the molecule. For the $O_\beta-CH_3$ section, the same values of DME have been used (*i.e.* $0.76\ \text{Å}^3$ for O_β and $2.20\ \text{Å}^3$ for CH_3). On the other side, for the $H-C=O_\alpha$ section we have chosen $0.38\ \text{Å}^3$, $0.76\ \text{Å}^3$ and $1.21\ \text{Å}^3$ for H, C, O_α, respectively.

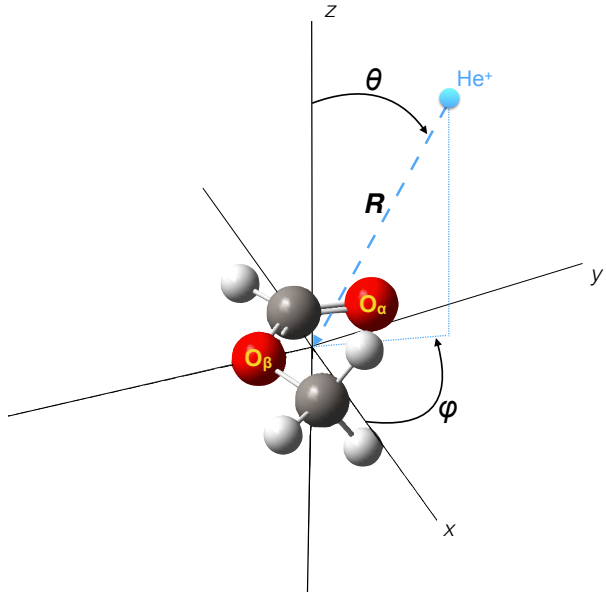

Figure 5.17: Illustration of the relevant coordinates used to represent the interaction potential between He^+ and *cis*-MF. The axes origin is positioned at the CM of the MF molecule and the *xy* plane coincides with the plane defined by the $O_\beta-C-O_\alpha$ atoms.

Since the RF power dissipation of the octople has a minimal effect on the temperature inside the scattering cell [58], we can assume that the reaction is carried out close to room temperature

Table 5.4: Bond lengths in Å and bond angles in degrees for the *cis*-methyl formate.

Description	Value
$C{=}O_\alpha$	1.200 Å
$C{-}O_\beta$	1.334 Å
$C{-}H$	1.101 Å
$H_3C{-}O_\beta$	1.437 Å
$O_\alpha{=}C{-}O_\beta$	125.9°
$O_\alpha{=}C{-}H$	109.3°
$C{-}O_\beta{-}CH_3$	114.8°

with an upper limit on the gas temperature inside the scattering cell of about 305 K [58]. Since the energy separation between the *cis* and *trans* isomers of the neutral MF is of 0.14 eV [153, 154], it is reasonable to assume that only the *cis* conformer is present in the experiment and only this isomer has been used to represent the interaction potential. Therefore, for the representation of the interaction potential, the experimental geometry values of the *cis*-MF structure reported by Hellwege *et al.* [155] have been adopted and the internal coordinates are summarized in Table 5.4.

In the CM frame, it is possible to define the Cartesian coordinates (x, y, z) as:

$$\begin{bmatrix} x_H & y_H & z_H \\ x_C & y_C & z_C \\ x_{O_\alpha} & y_{O_\alpha} & z_{O_\alpha} \\ x_{O_\beta} & y_{O_\beta} & z_{O_\beta} \\ x_{CH_3} & y_{CH_3} & z_{CH_3} \end{bmatrix} = \begin{bmatrix} -1.89 & -0.42 & 0 \\ -0.85 & -0.09 & 0 \\ -0.85 & +1.11 & 0 \\ +0.23 & -0.87 & 0 \\ +1.48 & -0.17 & 0 \end{bmatrix} \tag{5.17}$$

Also for the MF, the interaction potential of the system [He – MF]$^+$ has been developed in terms of the polar coordinates R, φ and θ (Figure 5.17), that are already defined in Sec. 5.2.1. While θ defines the direction of the incoming He^+ ion with respect to the z axis (θ = 0° and 90° correspond to the He^+ approaching perpendicularly and in the xy plane, respectively), φ indicates the projection of the R vector on the xy plane. For example, $\varphi = 0°$ corresponds to He^+ approaching on to the CH_3-side, while φ = 180° corresponds to He^+ approaching on to the H-side. Since the set of Cartesian coordinates (x_{He}, y_{He}, z_{He}) is the same defined for the DME case in Sec. 5.2.1, the distances in terms of Cartesian coordinates between He^+/He and H, C, O_α, O_β, CH_3 are the

following:

$$R_{\mathrm{H}} = R_{\mathrm{H-He}} = R_{\mathrm{H-He^+}} = \sqrt{(x_{\mathrm{He}} - x_{\mathrm{H}})^2 + (y_{He} - y_{\mathrm{H}})^2 + (z_{He} - z_{\mathrm{H}})^2}$$
$$R_{\mathrm{C}} = R_{\mathrm{C-He}} = R_{\mathrm{C-He^+}} = \sqrt{(x_{\mathrm{He}} - x_{\mathrm{C}})^2 + (y_{He} - y_{\mathrm{C}})^2 + (z_{He} - z_{\mathrm{C}})^2}$$
$$R_{\mathrm{O}_\alpha} = R_{\mathrm{O}_\alpha\mathrm{-He}} = R_{\mathrm{O}_\alpha\mathrm{-He^+}} = \sqrt{(x_{\mathrm{He}} - x_{\mathrm{O}_\alpha})^2 + (y_{\mathrm{He}} - y_{\mathrm{O}_\alpha})^2 + (z_{\mathrm{He}} - z_{\mathrm{O}_\alpha})^2}$$
$$R_{\mathrm{O}_\beta} = R_{\mathrm{O}_\beta\mathrm{-He}} = R_{\mathrm{O}_\beta\mathrm{-He^+}} = \sqrt{(x_{\mathrm{He}} - x_{\mathrm{O}_\beta})^2 + (y_{\mathrm{He}} - y_{\mathrm{O}_\beta})^2 + (z_{\mathrm{He}} - z_{\mathrm{O}_\beta})^2}$$
$$R_{\mathrm{CH_3}} = R_{\mathrm{CH_3-He}} = R_{\mathrm{CH_3-He^+}} = \sqrt{(x_{\mathrm{He}} - x_{\mathrm{CH_3}})^2 + (y_{\mathrm{He}} - y_{\mathrm{CH_3}})^2 + (z_{\mathrm{He}} - z_{\mathrm{CH_3}})^2}$$

where the x,y,z Cartesian coordinates of H, C, O_α, O_β, CH_3 are the matrix elements of 5.17.

Since the molecule has C_s symmetry, the PESs are symmetrical only with respect to the xy plane and therefore, the range of θ can be reduced to $[0, \pi/2]$ because PES values are repeated. Due to the smaller symmetry of MF with respect to the DME molecule, the range of φ must be $[0, \pi/2)$.

Since no literature data are available to the authors' knowledge, the effective partial charges and the electron densities of the molecular orbitals have been obtained by NBO calculation (Sec. 3.3) on the minimum energy structure of the neutral *cis*-MF, optimized at M06-2X/cc-pVQZ level. Resulting bond lengths and bond angles are shown in Figure 5.18 and they are in a good agreement with the literature data reported by Hellwege [155] (shown in Table 5.4). The percentage differences between calculated and experimental bonds are in the range 0.2%-0.6%, while for the angles they are 0.3-0.4%. The calculated dipole moment is 1.87 Debye close to the experimental one, differing only by about 6% from the previously mentioned experimental value.

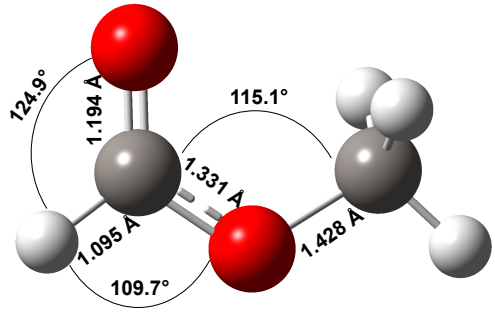

Figure 5.18: Optimized geometry of the neutral *cis*-MF at the M06-2X/cc-pVQZ level. The significant bond distances (in Å) and bond angles are reported.

Entrance channel: He^+ + MF

Also in this case, the PES of the interacting system He^+ – MF can be written in terms of electrostatic (V_{Electr}) and non-electrostatic ($V_{NElectr}$) components. As already defined above, the electrostatic

component is defined as a sum of Coulomb contributions between the He^+ ion and the calculated partial charges of each group of the MF molecule.

Hence, the electrostatic contribution can be factorized as:

$$V_{Electr} = 14400 \times \left(-\frac{0.585}{R_{O_\alpha}} - \frac{0.495}{R_{O_\beta}} + \frac{0.646}{R_C} + \frac{0.125}{R_H} + \frac{0.308}{R_{CH_3}} \right)$$

where the effective atomic charges are in terms of electric charge and have been obtained with the procedure described above. Using the 14 400 factor and the distances in Å, V_{Electr} is obtained in meV.

As already defined for DME, $V_{NElectr}$ arises from the ion-neutral interaction, *i.e.* between the He^+ and each of the atoms or effective groups of the MF molecule (namely H, C, O_α, O_β, CH_3). Each contribution is described by the improved Lennard-Jones model $V_{ILJ}(R_i)$, with R_i equal to R_H, R_C, R_{O_α}, R_{O_β} and R_{CH_3}. While the m and β parameters are the same used to describe the $V_{NElectr}$ of the system [He–DME]$^+$ (m=4 and β=7, specific values for the ion-permanent dipole interaction), the depth and the position of the potential well (r_m and ε, respectively) have been calculated by the *correlation formulas* and are summarized in Table 5.5. Hence, the non-electrostatic potential is calculated as:

$$V_{NElectr}(R,\theta,\varphi) = V_{ILJ}(R_H) + V_{ILJ}(R_{O_\alpha}) + V_{ILJ}(R_{O_\beta}) + V_{ILJ}(R_C) + V_{ILJ}(R_{CH_3})$$

The total entrance channel potential and the single contributions for $\theta = 90°$ and $\varphi = 90°$ are shown in Figure 5.19 as example.

Table 5.5: Potential parameters ε and r_m defining V_{ILJ} potentials for the pair of interest in the entrance channel.

Interacting system	ε (meV)	r_m Å
He^+ – H	94.9	2.15
He^+ – C	200.2	2.38
He^+ – O_α	158.1	2.25
He^+ – O_β	125.3	2.39
He^+ – CH_3	312.2	2.58

Exit channel: He + $MF^{\bullet+}$

The exit channel is again the sum of *van der Waals* potential (V_{vdW}, dispersion component) and of the induction (V_{Ind}) one. Similarly to what has been done with DME and the entrance channel, the improved Lennard-Jones model has been used to describe the V_{vdW}. Since the interaction is between the He atom and each of the atoms/effective groups (H, C, O_α, O_β, CH_3), we have:

$$V_{vdW}(R,\theta,\varphi) = V'_{ILJ}(R_H) + V'_{ILJ}(R_{O_\alpha}) + V'_{ILJ}(R_{O_\beta}) + V'_{ILJ}(R_C) + V'_{ILJ}(R_{CH_3})$$

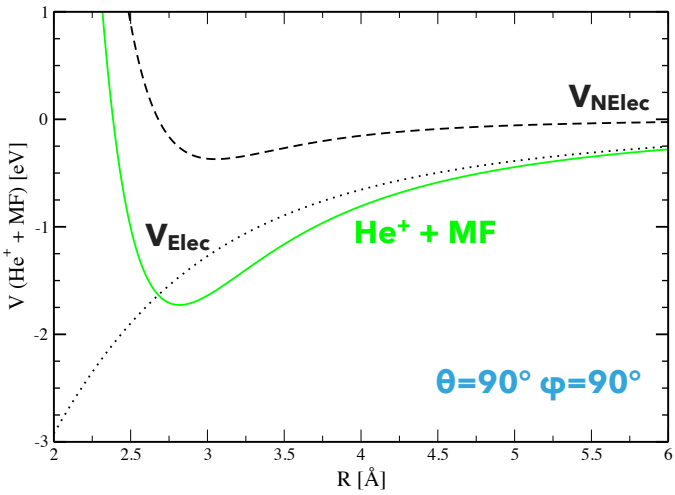

Figure 5.19: The resulting entrance channel (He^+ + MF) potential (green continuous line) for $\theta = 90°$ and $\varphi = 90°$, defined as sum of electrostatic potential (V_{Electr}, dotted black line) and non-electrostatic potential ($V_{NElectr}$, dashed black line).

In this case, the m and β are equal to 6 and 9 and the fundamental parameters are summarized in Table 5.6. The ion-induced dipole contribution is the same as defined in Sec. 5.2.1. All the contributions and the total exit channel interaction $\theta = 90°$ and $\varphi = 90°$ are represented in Figure 5.20.

Table 5.6: Potential parameters ε and r_m defining V'_{ILJ} potentials for the pair of interest in the exit channel.

Interacting system	ε (meV)	r_m Å
He – H	1.06	3.09
He – C	2.04	3.40
He – O_α	2.10	3.22
He – O_β	1.70	3.38
He – CH_3	2.31	3.69

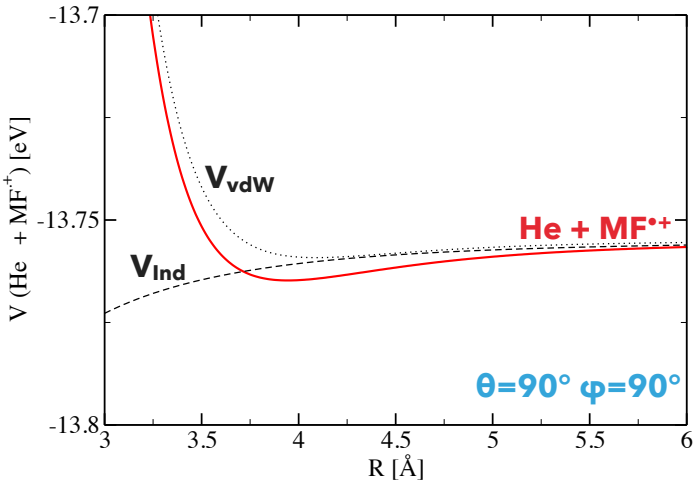

Figure 5.20: The resulting exit channel (He + $MF^{\bullet+}$) potential (red continuous line) for $\theta = 90°$ and $\varphi = 90°$, defined as sum of *van der Waals* potential (V_{vdW}, dotted black line) and induction potential (V_{INd}, dashed black line).

Anisotropy of the PES

Following the lines of the DME case, also in the case of MF it is interesting to analyze the anisotropy of the interaction potential. Considering the He^+ that approaches in the molecular plane (θ = 90°), the cut of the multidimensional PES for the entrance channel (shown in Figure 5.21) presents two deep potential wells (of about $-1.73\,eV$ and $-0.70\,eV$) located at a distance of $2.8\,Å$ from the O_α atom of the carbonyl group and of $2.9\,Å$ from the O_β atom of the ester group. While the interaction on the O_α-side is completely attractive, the second one is surrounded by a weak repulsive potential. In panel **b** of Figure 5.21 it is clearly represented that the blue O_β well is completely isolated by the light-orange (repulsive) potential. For θ= 90° and φ = 270°, this barrier is $\sim 30\,meV$ at $\sim 8\,Å$, as shown in Figure 5.22. Therefore, the most attractive geometries are when He^+ lies on the MF plane at the two oxygen side (θ= 90°, φ =90°, 270°), favoring at low collision energy the O_α-side.

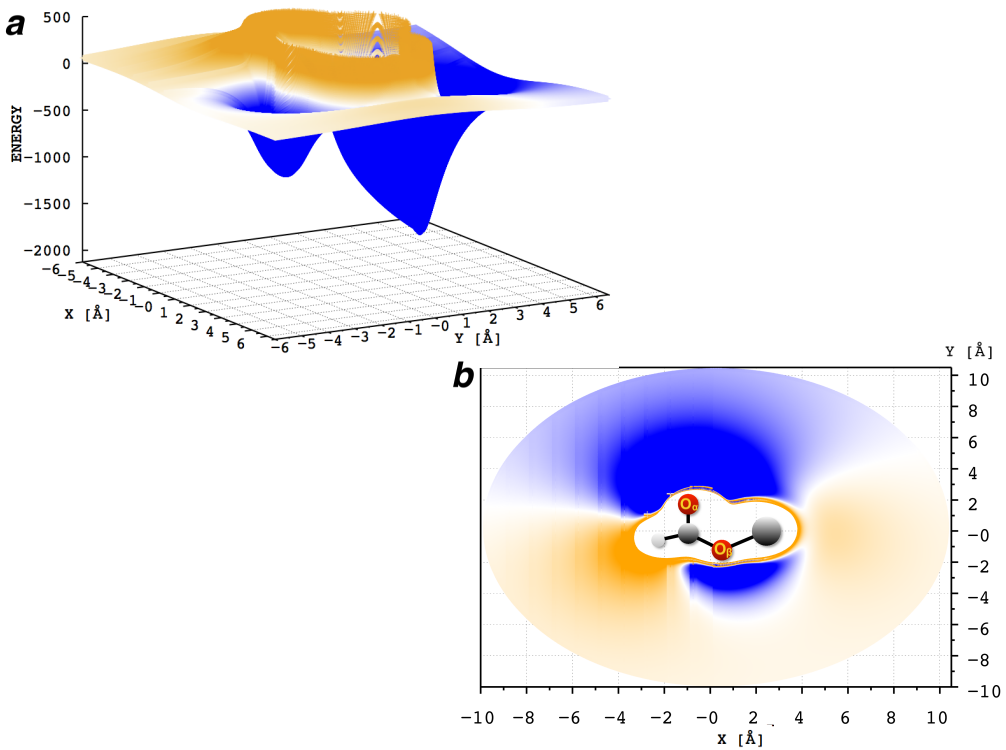

Figure 5.21: Different views for the PES of the entrance channel in the xy plane (θ=90°): panel ***a*** looking from the $O_\beta-CH_3$ side (φ=315°) and panel ***b*** from the top. Negative potential values are shown in blue and the positive ones are in orange, while the zero values are reported in white. In the top view, a pictorial imagine of the MF structure is reported.

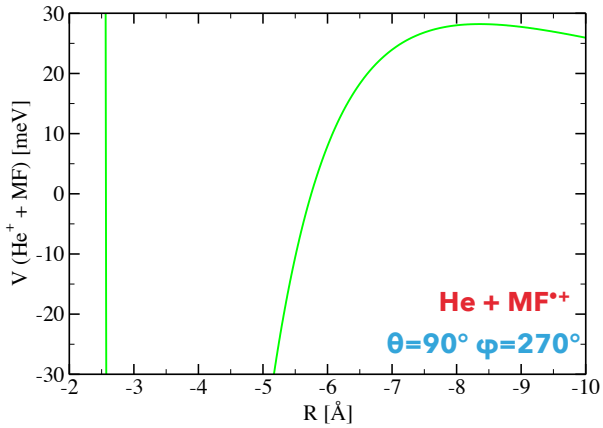

Figure 5.22: Interaction potential for θ= 90° and φ = 270°: to achieve the well, it is necessary to overcome a repulsive barrier $\sim$ 30 meV at $\sim$ 8 Å.

Similarly to the DME case, the potential anisotropy is such that the orientation of the MF molecule is possible already at long distances. In fact, the electric field generated by He^+ ion is able to orient the permanent dipole of the polar MF molecule in the configuration of minimum energy. Even at large distance (around 17 Å), the anisotropy equals the mean rotational energy of MF ($\sim$ 39 meV at 300 K) forcing the molecule in the most attractive geometries and confining the colliding system in the already defined pendular state, in which molecular rotations are transformed into bending vibrations of the collision complex (Figure 5.23). Therefore, the strong anisotropy of the interaction between He^+ and MF controls the reaction driving the process only through the most attractive configurations.

A more quantitative representation of the attractive and repulsive regions of the PES is shown in Figure 5.24, where the interaction potential is plotted as a function of φ and θ at fixed values of R (corresponding to 3 Å, 5 Å, 10 Å, 15 Å and 20 Å). In the top panel, the PES on the *xy* molecular plane (with θ=90°) shows a strong repulsive behavior when He^+ approaches from the methyl side and from the proton side, but a strong attractive behavior on the two O atom sides. In particular, it is possible to estimate the ratio between the negative potential areas, that will be of fundamental importance to calculate the total cross-section of the charge exchange process. The obtained result shows that the O_α-side is 9.9 times more attractive than the O_β-side, normalized to 1 in the ratio 0.9/0.1. This means that the He^+ prefers to collide with the neutral MF from the O_α-side (the most attractive region of the PES), even if during the collision it might approach from either of the two oxygen atoms. Even at large distances (20 Å), $\Delta V(R)$ (defined as the difference between the energy values of the least and most stable configurations) is still $\sim$ 29 meV, exhibiting a stronger anisotropy than the DME case. Furthermore, it is interesting to note that the H atom region is more repulsive than the methyl one at short distances, but for higher R they build the repulsive barrier around the attractive potential of the O_β-side (*i.e* for $180° \leq \varphi \leq 360°$) together. This repulsive potential is already active at 10 Å, where it fluctuates from 45 meV (φ = 200°, H-side) to 22 meV

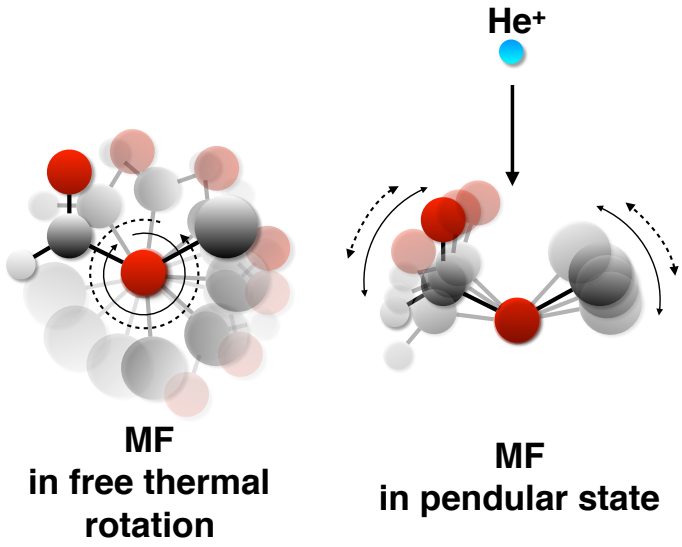

Figure 5.23: Pictorial representation of the formation of a pendular state during collision between He^+ and MF. *On the left*: at large distances the MF molecule can freely rotate (only rotation around one imaginary axis centered in the O_β is represented for clarity). *On the right*: at shorter distances MF is "trapped" in its preferential orientation where only bending vibrations of the collision complex are possible.

and $30\,\mathrm{meV}$ ($\varphi = 290^\circ$ and 340°, O_β- and CH_3-sides, respectively). That means that the reaction can be carried out from the O_β-side only when the collision energy is higher than these threshold energies. The other two panels on the bottom present the interaction when He^+ approaches in the two planes perpendicular to the molecular one, *i.e.* the xz and yz planes.

Figure 5.24: *On the left*: Cuts of the PES for the He^+ – MF entrance channel for a fixed value of θ=90° (corresponding to the He^+ ion being constrained on the xy molecular plane of MF and five different R values corresponding to 3 Å, 5 Å, 10 Å, 15 Å and 20 Å (in different colors) plotted as a function of φ. *On the middle*: Cuts of the PES for the He^+ – MF entrance channel for fixed values of φ=180° and 0° and five different R values corresponding to 3 Å, 5 Å, 10 Å, 15 Å and 20 Å (in different colors) plotted as a function of θ. The cuts correspond to He^+ being constrained on the xz molecular plane of MF, perpendicular to the molecular plane. *On the right*: Cuts of the PES for the He^+ – MF entrance channel for fixed values of φ=270° and 90° and five different R values corresponding to 3 Å, 5 Å, 10 Å, 15 Å and 20 Å (in different colors) plotted as a function of θ. The cuts correspond to He^+ being constrained on the yz molecular plane of MF, perpendicular to the molecular plane.

5.3.2 Crossings between the entrance and exit channels

At the collision energies used in our experiments, the electron transfer might be operative only when the PESs of the entrance and exit channels given in the diabatic representation cross at distances for which the non-adiabatic coupling between the surfaces at the crossing is non-zero. As Figure 5.25 shows, due to the significant difference in ionization energy between He (IE=24.58741 eV [141]) and MF (IE= 10.835eV [156]), assuming that the transferred electron is ejected by the HOMO of MF (exothermic of $(13.755 \pm 0.025)\,\mathrm{eV}$), the entrance (green solid line in Figure 5.25) and exit (red solid line in Figure 5.25) curves do not cross. The curves of Figure 5.25 have been obtained by fixing θ= 90° and φ=90°. This geometry was chosen since it represents the most attractive configuration, however things do not change much if other geometries are considered (for all geometries entrance and exit channels do not cross). Hence, to promote reaction the exchanged electron should involve inner MOs of MF, having higher ionization energies than the HOMO, as in the DME reaction and in accord to what has been found out in Sec. 4.2.

Given the electronic configuration of MF having C_s symmetry in its electronic ground state [154],

$$(\text{core})^8(5a')^2(6a')^2(7a')^2(8a')^2(9a')^2(10a')^2(1a'')^2(11a')^2(2a'')^2(12a')^2(3a'')^2(13a')^2$$

it is possibile to reconduce the experimental ionization potentials of the two valence orbitals 8a′ and 7a′ to $19.9 \pm 0.1\,\mathrm{eV}$ and $23.6 \pm 0.1\,\mathrm{eV}$ [157, 158], respectively. When such orbitals are considered, the asymptotic value of the exit channels can be re-scaled accordingly to obtain the red dot-dashed and red dashed curves of Figure 5.25, whose crossings with the entrance curve are marked with black circles in Figure 5.25. The reaction exothermicity is reduced to about $(4.69 \pm 0.10)\,\mathrm{eV}$ and $(0.99 \pm 0.10)\,\mathrm{eV}$, respectively. In all dynamical calculations, the zero energy has been fixed to the asymptotic value of the entrance channel. There are then two relevant crossing points that for convenience are numbered i=1, 2, the first being the crossing occurring at larger R values, *i.e.* the one leading to the [He−MF$^{\bullet+}$]*(7a′) exit channel.

As said previously, the electron densities of the involved orbitals have been calculated by NBO analysis with DFT-M06-2X method. The results highlight that the inner valence orbitals 7a′ and 8a′ of MF show a series of nodal planes (Figure 5.26), being the electrons highly localized around some specific atoms or atomic groups. As a consequence, when the molecular ion [MF$^{\bullet+}$]* is formed in a highly electronically excited state, the dynamics immediately following the charge transfer occurs on an exit PES that is only mildly attractive and anisotropic. In any case, the nascent [MF$^{\bullet+}$]* has a high-energy content, and it is therefore expected to dissociate almost instantaneously, in agreement with the measured branching ratios (Table 4.5) and the hypothesis done in Sec. 4.2. Furthermore, from the NBO analysis the two MOs are formed by combination of only C and O orbitals. This is in accord with the conclusions of Sec. 4.2, in which type of products and the BRs have been explained in terms of only C−O bond breaks.

At this level of the discussion, it is possible to define the "effective cones" having, due to the orientation effects explained above, the most significant contributions in the cross-section calculation. The most attractive geometries are those corresponding to the He^+ ion approaching the MF plane in the proximity of the O_α- and O_β-sides (*i.e.* θ=90° and φ=90°, 270°). The two cones have been chosen around these geometries and they are symmetric and with the same angular opening. In order to consider the different depth and extension of the potential wells in the two configurations, the total cross-sections have been obtained properly averaging the contributions coming

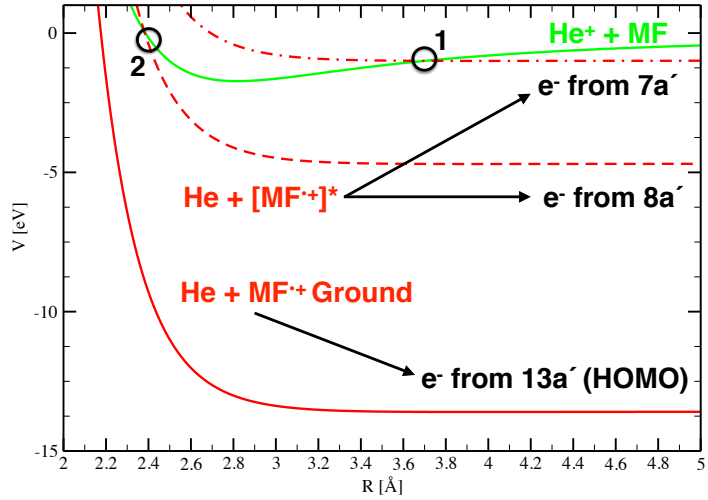

Figure 5.25: Potential energy curves of the entrance He^+ + MF (green curve) and exit He + $MF^{\bullet+}$ (red continuous curve) channels for θ= 90° and φ=90°, with the MF radical cation formed in its electronic ground state. The red dashed and dot-dashed curves represent exit channels assuming the removal of an electron from the inner valence orbitals 7a′ or 8a′.

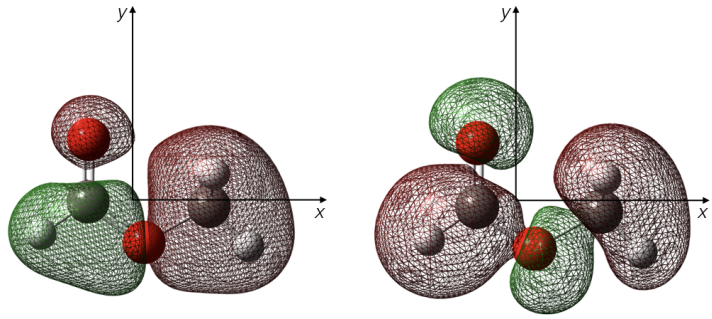

Figure 5.26: Electron densities of 7a′ (on the right) and 8a′ (on the left) MOs of neutral *cis*-MF.

from the two different effective cones, *i.e.* using the weighted average with the ratio 0.9/0.1 for the O_α- and O_β-side. For the dynamical calculations a limited number of configurations, confined in the narrow angular cones, have been selected. They must be considered as the most representative

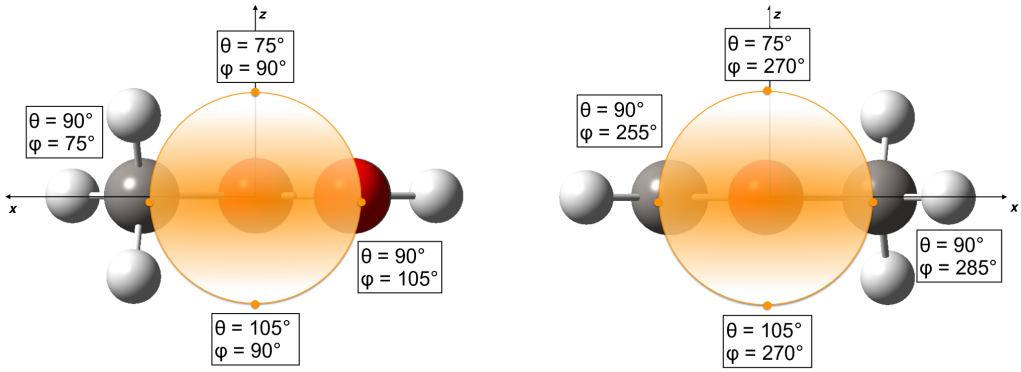

Figure 5.27: Pictorial view of the effective cones used to calculated the cross-sections. They are narrow symmetrical slices of the space around the molecule: on the left the O_α-side cone is represented, while on the right the O_β-side cone. The y-axis is orthogonal to the plane of the figure.

and efficient geometries to carry out extensive integral cross-section calculations to be compared with the experimental data. The values of polar angles (θ and φ) defining the selected configurations are reported in Figure 5.27 and summarized in Table 5.7, together with the position R_i, value of energy E_i, and absolute difference of slopes Δ_i for the various crossings i.

Table 5.7: Position R_i, energy E_i, and absolute difference of slopes Δ_i for crossing i between the entrance and exit diabatic curves at selected and fixed θ and φ values.

Side	θ	φ	i=1			i=2		
			R_i [Å]	E_i [meV]	Δ_i [meV Å^{-1}]	R_i [Å]	E_i [meV]	Δ_i [meV Å^{-1}]
C=O_α	90°	105°	3.99	-995.1	767.4	2.72	62.0	13321
	90°	75°	3.26	-998.9	818.8	1.90	741.1	9654
	75°,105°	90°	3.62	-996.9	772.0	2.31	143.0	11675.3
C−O_β−CH_3	90°	255°	2.71	-467.2	1937	2.18	4291	22750
	90°	285°	3.08	-807.0	1469	2.39	3166	20739
	75°,105°	270°	2.90	-721.7	1605	2.29	3315	21478
	90°	90°	3.70	-997.7	761.8	2.38	69.9	11857
	90°	270°	2.95	-728.9	1605	2.29	3315	21478

5.3.3 Calculation of cross-sections

The Landau-Zener-Stückelberg model is the same used to calculate the DME cross-sections (see Sec. 5.2.3). In fact, the MF case is almost similar to the DME one: the charge transfer is dissociative, there are two crossings (i=1,2) to be considered with two involved MOs, on which the non-adiabatic coupling H_i depends. The formulas used to calculate the single probability of non-adiabatic transition and the total probabilities for i=1,2 crossings are equal to equations 5.2, 5.10 and 5.10 of Sec. 5.2.3. We also point out again that cross-sections are mostly due to collisions occurring with large orbital angular momentum quantum numbers. However, at large distances the centrifugal barrier can prevent the interacting partners to reach, in the low collision energy range, the distance at which the crossing between entrance and exit channel is positioned, thus posing a limitation to the quantum numbers contributing to the cross-sections (Eqn. 5.6).

The non-adiabatic coupling H_i at each crossing i has been defined with the same formulation. In fact, in this case it is not necessary to distinguish the role of the inner (i = 2) from the outer (i = 1) case (as done with the non-adiabatic coupling for the DME) because, due to their symmetries, the molecular orbitals involved in the electron exchange present similar nodes in the electron densities. Both molecular orbitals have a nodal plane (see Figure 5.26) along the approach direction of He^+ towards the most attractive configurations. The 7a′ and 8a′ orbitals present a node in the yz plane, and therefore small overlaps with the spherically symmetric atomic orbital of $He^+(^2S_{1/2})$. Thus, the stereo-chemical paradox occurs also in this reaction: the most attractive geometries (θ = 90° and φ =90°, 270°, corresponding to He^+ approaching on the MF plane from the O_α- and O_β-side, respectively) are the least efficient for the charge transfer process when MO symmetries are taken into account. Therefore, the reaction can be essentially promoted by the coupling between the rotational angular momentum of the nuclei within the collision complex and the orbital angular momentum of the electron (Coriolis coupling, Eqn. 5.12). In the formulation of this type of non-adiabatic coupling, the dependence on the collision energy has been again added in order to consider the orientation effects promoted by the strong anisotropy of the PES and the small overlap between the involved MOs and the s atomic orbital of He^+.

In the cross-section calculation for the $He^+ + HCOOCH_3$ reaction, the dimensionless parameter C of Eqn. 5.13 acquires a further new significance respect to the DME case. In fact, different C values might be properly chosen for the two effective cones in order to consider the efficiency of the overlap between the MO of the MF and the s atomic orbital of He^+. For example, we focus on the 7a′ MO. The electron density of this orbital is mainly distributed on the O_β-side (φ = 270°), while it is more "rarefied" on the O_α-side (φ = 90°). This means that the C parameter must be higher for the He^+ approaching on the O_β-side and lower for the He^+ approaching on the O_α-side. Since the electron densities distribution of 7a′ MO is quite similar to the $2b_2$ MO of the DME molecule, we can assume that C must be equal to 6 when He^+ collides with the MF molecule on the O_β-side (corresponding to He^+ that approaches the DME on the O-side). On the contrary, a value of 4.75 has been chosen to represent the less efficient case, *i. e.* when He^+ collides with the MF molecule on the O_α-side. This treatment of the parameter C can be successfully extended also to the 8a′ MO, since the electron densities show similar maxima and minima distributions.

For the chosen geometries (summarized in Figure 5.27 and in Table 5.7) and for both the O_α, O_β atom sides, cross-sections $\sigma_1(E)$ and $\sigma_2(E)$, as well as the total cross-section $\sigma(E)$ have been calculated as a function of the collision energy E and results are shown in Figure 5.28. For each configuration, the contributions of both crossings i=1,2 and their sum are represented (in blue, red and black). It is interesting to note that the crossing i=1 (corresponding to remove the electron from

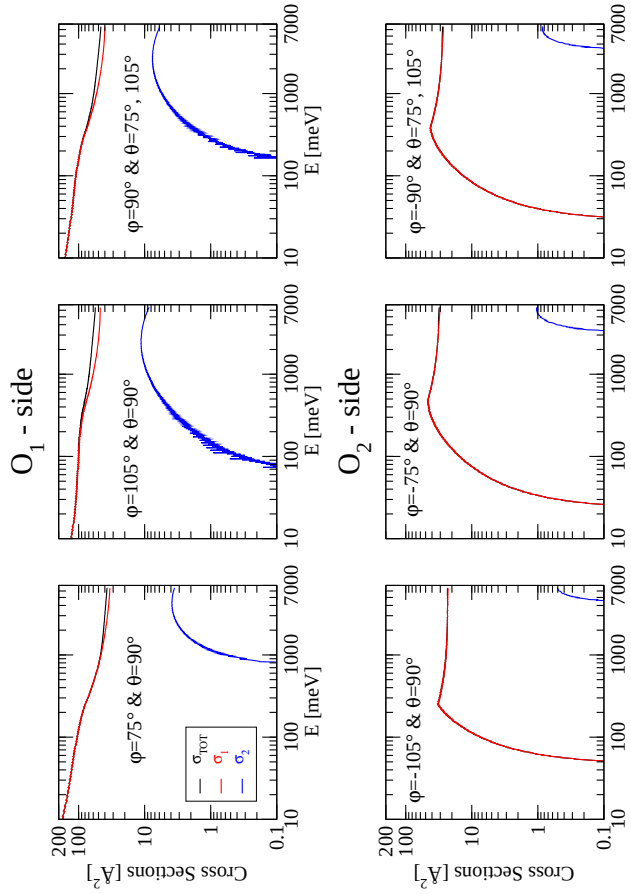

Figure 5.28: Calculated contributions to the total cross-section for the title reaction for selected configurations (fixed values, as indicated in each of the six graphs) confined in the two narrow angular cones on O_α- and O_β-sides most effective for the reaction (see text for details). In blue: $\sigma_1(E)$; in red: $\sigma_1(E)$ and in black their sum $\sigma(E)$.

the 7a′ MO) gives the major contribution to the total cross-section at the whole collision energy range, despite the low value of the C parameter. The cross-section for the two cones, representing the geometries for which the He^+ approaches the MF on the O_α- (orange line) and O_β-side (dark green line) (see Figure 5.29) are obtained averaging the single contributions. In Figure 5.30, the

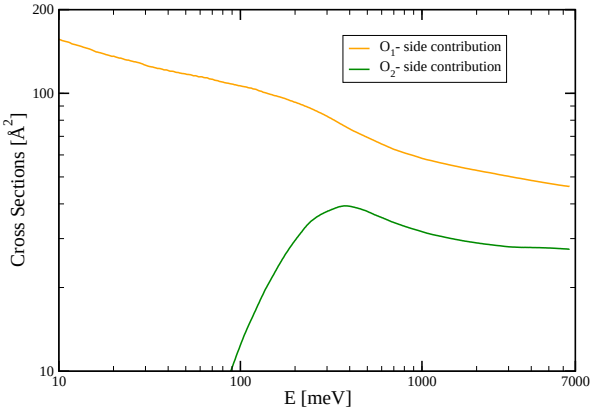

Figure 5.29: Calculated contributions for the two geometries of interaction, O_α- (orange line) and O_β-side (dark green line).

experimental total cross-sections (green dots) are compared with the calculated ones (black line), obtained according to the procedure discussed above. As done for the DME total cross-sections, the result (blue line) obtained without the assumption of the strong stereo-chemical effect in the reaction is shown in Figure 5.30. In this case, the total cross-sections have been obtained averaging the cross-section for an appropriate combination of θ and φ, in order to consider the whole sphere around the MF molecule. θ and φ couples (108 couples) have been obtained following the procedure already mentioned in Sec. 5.2.3. We remind that H_i is not defined as Coriolis coupling and without the explicit dependence from E. Accordingly with the electron densities of the molecular orbitals and with what has been done for the DME reaction, we have decided to represent H_i for i=1,2 as a function of the angle φ:

$$H_i = cost \times (cos\varphi)^2$$

where $cost$ is $200\,\mathrm{meV}$. With this definition, H_i is equal to zero for geometries with φ=90° and 270°, where the involved molecular orbitals 7a′ and 8a′ have the electron density node, and it is equal to the constant for geometries with φ=0° and 180°, where the electron densities have their maximum. As Figure 5.30 shows, the cross-sections calculated with our model are in excellent agreement with the experimental results. The disagreement of the results obtained without the "alignment assumption" shows the importance of including stereo-chemical effects in the dynamics treatment.

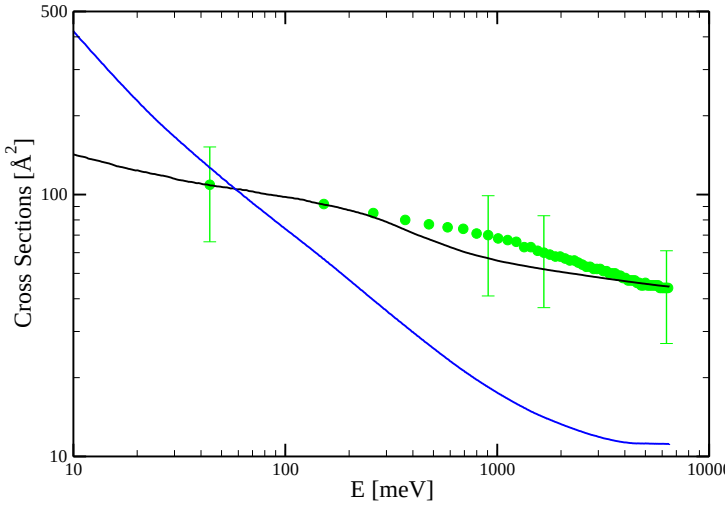

Figure 5.30: Comparison between calculated (black line) and experimental (green dots) total cross-sections for the reaction He^+ + MF. Error bars represent an estimate of the accuracy of the absolute values of the cross-section (40%) and account for systematic errors. For the sake of clarity, the error bars have been reported only on four experimental points. The blue line results from the discussed model assuming that during the reaction the reactants have not preferential orientations. It is evident that the stereo-chemistry in the charge exchange process plays a crucial role in the dynamics.

Summarizing on the basis of the excellent results obtained for the DME/MF reactions, it is possible to outline the following general guidelines for modeling the charge transfer between He^+ and a polar organic molecule:

- the total probability of non-adiabatic transition must take into account the dissociative nature of the process (see for instance Equations 5.9 and 5.10);
- according to the anisotropy of the reactant potential energy hyper-surface, it must be evaluated whether the reaction occurs in preferential configurations of the ion-molecule system. Therefore, stereo-dynamical effects must be included in the model considering a reactive narrow cone confined in a well defined region of the neutral molecule. Eventually, two or

more reactive cones can be taken into account, if the entrance potential presents more than one attractive well;

- the l_{max} calculation must be carried out carefully. In fact, it has been found out that the constrain on the l_{max} (Eqn. 5.5) of the classic Landau-Zener model is not sufficient at very low energy. In this case, values of l are included allowing the formation of a centrifugal barrier higher than the collision energy. For this reason, it is necessary to reduce further the angular momentum quantum number by putting the new constrain expressed in Eqn. 5.6;
- the electron densities of the MOs involved in the process must be evaluated, because they play a decisive role in the expression of the non-adiabatic coupling. In fact, it is possible to report two cases:

    1. if the electron density distribution of the MO has the correct symmetry to overlap with the electron density distribution of the AO of the ion accepting the electron, the coupling can be treated as a constant;
    2. if the MO presents a node along the most attractive configuration, it is necessary to consider the low efficiency of the charge transfer due to the small overlap between the involved MO and AO of the ion. Therefore, the non-adiabatic coupling must be represented by using the Coriolis coupling (Eqn. 5.12), that allows the transition considering a rotational contribution *via* the angular momentum quantum number l. Since the l_{max} value increases at high collision energies, the Coriolis coupling has the same trend: the lower is the collision energy, less efficient is the transition. Furthermore, to include also the strong alignment due to the anisotropy of the PES, a new term has been implemented in the Coriolis formula, making stronger the dependence on the collision energy. The M parameter of Eqn. 5.12 is now a function of a power (γ) of E up to a multiplicative constant C (Eqn. 5.13), in which γ and C are fitting parameters. For reactions between He^+ and an oxygen-bearing polar molecule, it can be suggested to take γ equal to $1/4$, while $C \leq 6$.

Chapter 6

The Rate Constants and the Astrochemical Network Databases

"Ora le stelle stanno cadendo,
le nostre mura stanno tremando
e camminando e camminando
a piedi nudi ballano i Santi... "

I Santi - A. Branduardi

In this chapter, the branching ratios and rate constant values for DME/MF reactions present in astrochemical databases are reviewed and compared with results from our experiments (for BRs) and from our calculations (for rate constants). It will be highlighted the striking differences between the experimental branching ratios and the estimates used in the astrochemical network databases. As explained in the previous chapter, the calculated cross-sections come from more accurate evaluation of the conditions in which the helium cation collides with the methyl formate and dimethyl ether. Hence, the rate constants obtained from our model might be considered a more reasonable estimate with respect to the models used until now.

6.1 Introduction

In the KIDA database [77, 159] (KInetic Database for Astrochemistry), the suggested values for rate constants as a function of temperature for He^+ reactions with DME and MF are based on a modified Arrhenius equation, using the parameters from the OSU2009 gas-phase chemistry database of E. Herbst [160].

$$k(T) = \alpha \left(\frac{T}{300} \right)^{\beta} e^{-\gamma/T} \quad [\mathrm{cm}^3\,\mathrm{s}^{-1}] \tag{6.1}$$

where α is a parameter specific for each reaction, while the other two parameters are usually assumed as β=-0.500, γ=0.00 and T in the range from $10\,\mathrm{K}$ to $280\,\mathrm{K}$. It should be noted that the above expression is an approximation (valid for low temperatures) of a more general expression, which derives from an analytical fit of thermal rate coefficients calculated using the classical trajectory method [76, 161]. The rate coefficients obtained by the classical trajectory method depend only on the reduced mass of the reactants, on the polarizability and permanent dipole moment of the neutral reactant. More generally, it is possible to calculate rate constants as a function of temperature using the formulas already reported in Sec. 3.1.1 (equations 3.25 and 3.27).

In UMIST (University of Manchester Institute of Science and Technology) database for astrochemistry [162, 163], rate constants exhibit the same temperature dependence of OSU model (*i.e.* $T^{-0.5}$), but they are scaled to a measured or estimated value at $300\,\mathrm{K}$. The Eqn. 6.1 is reduced to:

$$k(T) = k_{300\,\mathrm{K}} \left(\frac{T}{300} \right)^{\beta} \quad [\mathrm{cm^3\,s^{-1}}] \tag{6.2}$$

where β=-0.500 and T in the range from $10\,\mathrm{K}$ to $41\,000\,\mathrm{K}$. A factor 2 accuracy in the rate constant is also reported [25].

6.1.1 $He^+ + CH_3OCH_3$ reaction

In KIDA, the reaction of He^+ ions with DME is reported to give only two ionic products, each with a branching ratio of 50.0%. The proposed reactions are the following:

$$\mathrm{He^+ + CH_3OCH_3 \longrightarrow He + H + H_2CO + {CH_3}^+} \tag{6.3}$$

$$\mathrm{He^+ + CH_3OCH_3 \longrightarrow He + CH_3 + H_2COH^+} \tag{6.4}$$

On the contrary, in the UMIST database only React. 6.3 is reported with a CH_3^+ yield of 100%. The experimental evidence supported by the BRs of Table 4.2 in Sec. 4.1 (indicating that the most abundant product is HCO^+ with BR of 0.536 and that CH_3^+, $CH_2^{\bullet+}$, OCH_3^+ have BRs of 0.385, 0.073 and 0.004) rebuts these estimations, revealing a serious lack on the astrochemical database estimates.

The Langevin rate constant for the process is k_L=$2.77 \times 10^{-9}\,\mathrm{cm^3\,s^{-1}}$. The KIDA database proposes k=$7.23 \times 10^{-9}\,\mathrm{cm^3\,s^{-1}}$ for both reactions 6.3 and 6.4 at $10\,\mathrm{K}$, with a total k for the title reaction equal to $1.45 \times 10^{-8}\,\mathrm{cm^3\,s^{-1}}$. The used α parameter is 1.32×10^{-9}. At $280\,\mathrm{K}$ (upper limit of Eqn. 6.1), the model gives a total k equal to $2.74 \times 10^{-9}\,\mathrm{cm^3\,s^{-1}}$. In the UMIST database, the $k_{300\,\mathrm{K}}$ is fixed to $2.00 \times 10^{-9}\,\mathrm{cm^3\,s^{-1}}$, giving a rate constant at $10\,\mathrm{K}$ equal to 1.10×10^{-8} and $2.07 \times 10^{-9}\,\mathrm{cm^3\,s^{-1}}$ at $280\,\mathrm{K}$. KIDA and UMIST rate constant values at $10\,\mathrm{K}$ and $280\,\mathrm{K}$ are summarized in the left panel in Figure 6.1 with red diamonds and blue circles.

6.1.2 $He^+ + HCOOCH_3$ reaction

In the KIDA database, the reaction of He^+ ions with MF is reported to give only the following channel (hence with a branching ratio of 100.0%):

$$\mathrm{He^+ + HCOOCH_3 \longrightarrow He + CH_3 + HCOO^+} \tag{6.5}$$

Also the UMIST database, gives React. 6.5 as the sole product channel for collisions of He^+ ions with MF. Again the BRs estimations disagree with the experimental data, indicating that the most abundant product is HCO^+ with BR of 0.880 with CH_3^+, $CH_2^{\bullet+}$, OCH_3^+ have BRs of 0.054, 0.023 and 0.043.

The Langevin rate constant for the title reaction is k_L=2.78 $\times 10^{-9}\,\mathrm{cm^3\,s^{-1}}$, while the KIDA value assuming α=3.54 $\times 10^{-9}$ is equal to $1.94 \times 10^{-8}\,\mathrm{cm^3\,s^{-1}}$ at 10 K and equal to 3.66×10^{-9} $\mathrm{cm^3\,s^{-1}}$ at 280 K. In the UMIST database, the $k_{300\,\mathrm{K}}$ is fixed to $3.00 \times 10^{-9}\,\mathrm{cm^3\,s^{-1}}$, giving a rate constant at 10 K equal to 1.64×10^{-8} and $3.11 \times 10^{-9}\,\mathrm{cm^3\,s^{-1}}$ at 280 K. KIDA and UMIST rate constant values at 10 K and 280 K are summarized in the right panel Figure 6.1 with red diamonds and blue circles.

6.2 Resulting Rate Constants and Comparison with the Database Values

Thermal rate constants as a function of temperature ($k(T)$) have been obtained by averaging the total cross-sections (calculated in sections 5.2.3 and 5.3.3) over a Maxwell-Boltzmann distribution of collision energies E (Eqn. 2.16 in Sec. 2.3.5). The treatment based on the Landau-Zener-Stückelberg approach defines the energy range within which cross-sections calculated using a semi-classical method are meaningful. In particular, the validity of the adopted semi-classical methodology is satisfied when the *de Broglie* wavelength λ_{DB} for the relative motion of the colliding partners is smaller than the distances at which the potential wells in the entrance and exit channels are located. For example for DME, such distances are in the range 1.5 Å to 3 Å, while for MF they are in the range 2 Å to 4 Å. Crossings among the entrance and exit potential energy curves are located within the same range. To get a conservative estimate, it is assumed that λ_{DB}=1.5 Å, resulting in a minimum energy E about 10 meV: below this value, the semi-classical treatment is not reliable. On the other hand, Wakelam and co-workers [164] state that semi-classical models might be used even for low T in the range 1 K to 10 K, in which the transition between classical and semi-classical behavior of the rotational motions occurs. At lower T ($\ll$ 1 K), a full quantum mechanical treatment must be used, while at higher temperatures (10 K to 20 K) the rotational motion might be considered fully classical, allowing to apply classical trajectory methods. However, to get a meaningful estimate of $k(T)$ at low T without errors coming from numerical artifacts, cross-section values at energies smaller than 10 meV should be included. Since the energy range is determining in rate constant calculation using Eqn. 2.16, Langevin rate constants for the reaction $He^+ + CH_3OCH_3$ at 10 K and 300 K have been calculated by using the expression already reported in Chapter 3 (Eqn. 3.31):

$$k_{Langevin}(T) = \frac{2\pi q}{4\pi\varepsilon_0}\sqrt{\frac{\alpha}{\mu}} = 2.77 \times 10^{-9}\,\mathrm{cm^3\,s^{-1}} \tag{6.6}$$

This value has been compared with that obtained integrating the cross-section over the M-B distribution:

$$k(T)^* = \left(\frac{1}{\pi\mu}\right)^{1/2} \cdot \left(\frac{2}{k_B T}\right)^{3/2} \cdot \int_{E_{min}}^{E_{max}} \sigma_{Langevin}(E) \cdot E \cdot e^{-E/k_B T} dE \tag{6.7}$$

Table 6.1: Percentage error obtained comparing the real Langevin rate constant for DME reaction (k_L=2.77 $\times$ 10^{-9} cm^3 s^{-1}) with the results calculated by integrating over a Maxwell-Boltzmann distribution the total cross-sections in different energy ranges. While the upper limit energy has been fixed at E_{max}=10 000 meV, the lower limit (E_{min}) has been varied from 10 meV to 0.001 meV.

E_{min}	Error (%)	
	10 K	300 K
10 meV	100.0	14.4
1 meV	49.1	0.56
0.1 meV	2.8	0.02
0.01 meV	0.1	0.0
0.001 meV	0.0	0.0

where $\sigma_{Langevin}(E) = q\sqrt{\frac{\pi\alpha}{2\varepsilon_0 E}}$ and all the terms are already defined in Chapter 3. Fixing the upper limit at E_{max}=10 000 meV, the error as a function of the lower limit energy (E_{min}) has been calculated comparing the $k(T)^*$ values with the Langevin rate constant for DME reaction and results are reported in Table 6.1. As shown in Table 6.1, while at 300 K the numerical error on the calculated rate constant is negligible already starting from 0.1 meV, for $k(10\,\mathrm{K})$ it is necessary to decrease the lower limit energy to 0.01 meV to have a relative error equal to the 0.1% and to 0.001 meV for zero error. Therefore, to avoid numerical errors and assuming that our model is a very well estimation of reactive behavior of the studied colliding systems, the cross-sections have been guessed in the energy range 0.01 meV to 10 meV with our developed model. Furthermore, to estimate the differences on rate constants when cross-sections have different trends in this very low energy range, an upper and lower limits for the cross-sections have been guessed in the 0.01 meV to 10 meV energy range for the DME case, by assuming the following two different behaviors for:

1. cross-sections increasing with energy E: a function $\propto E^2$ has been chosen to represent σ in the discussed energy range (see results labeled "our model: case 1" and represented by dotted turquoise line in the right panel of Figure 6.1);
2. increasing cross-sections with decreasing the energy E: in this case, the developed Landau-Zener-Stückelberg treatment has again been used, but the strength of the already mentioned H_1 coupling has been modulated (using C=7.4 in Eqn. 5.13 of the previous Chapter) by obtaining calculated cross-section at the upper limit of the experimental determinations (see results labeled "our model: case 2" and represented by dotted magenta line in the right panel of Figure 6.1);

With cross-sections estimated by case 1, the resulting rate constant at 10 K is lower by a factor of 0.13 with respect to the one calculated with our model (black continuous line in the right panel of Figure 6.1), whereas at 300 K the two values coincide. The upper limit rate constant (case 2) is higher by a factor of 1.5-1.4 in the whole range of temperature. Simulations for MF have not been

carried out, but we expect that the rate constants can vary also in this case in the same range of values.

Finally, rate constants $k(T)$ resulting from our estimates in the temperature range $10\,\mathrm{K}$ to $300\,\mathrm{K}$ are compared with recommended values from KIDA and UMIST and are shown in Figure 6.1, where on the left the He^+ – DME case is presented, while on the right the He^+ – MF case is reported. The differences between the calculated rate constant and the estimates of KIDA and UMIST databases are evident.

For DME, we obtain k=5.69 $\times\ 10^{-10}\,\mathrm{cm^3\,s^{-1}}$ at $10\,\mathrm{K}$ and k=1.41 $\times\ 10^{-9}\,\mathrm{cm^3\,s^{-1}}$ at $280\,\mathrm{K}$ (at $300\,\mathrm{K}$ k=1.44 $\times\ 10^{-9}\ \mathrm{cm^3\,s^{-1}}$). At $10\,\mathrm{K}$, the KIDA database overestimates by a factor of ~ 26, while the UMIST value is ~ 20 times higher with respect to our calculations. At around $300\,\mathrm{K}$, the differences decrease between the calculated and estimated rate constants and the KIDA value becomes ~ 2 times higher than our value, while the UMIST one is ~ 1.5 higher.

For MF, we obtain k=7.05 $\times\ 10^{-10}\,\mathrm{cm^3\,s^{-1}}$ at $10\,\mathrm{K}$ and k=1.44 $\times\ 10^{-9}\,\mathrm{cm^3\,s^{-1}}$ at $280\,\mathrm{K}$ (at $300\,\mathrm{K}$ k=1.48 $\times\ 10^{-9}\ \mathrm{cm^3\,s^{-1}}$). At $10\,\mathrm{K}$, KIDA and UMIST recommend values ~ 21, ~ 24 times higher than our value. Around $300\,\mathrm{K}$, KIDA and UMIST overestimate the rate constants respectively by a factor ~ 2.5, ~ 2. Therefore, the results show a high overestimation of the database values, especially at $10\,\mathrm{K}$. In MF case, the calculation of rate constants in the hypothesis of no orientation of the reactants has been performed, giving, as expected, an overestimation of the rate constant.

It is worth noting that the estimate of the astrochemical network database rate constants exhibit a negative temperature dependence (*anti*-Arrhenius behavior), while the calculated ones show an Arrhenius dependence (*i.e.* a positive dependence on T) even though the present charge transfer is an exothermic barrier-less process. This unexpected behaviour as a function of the temperature has been observed in other systems [165], in which Ar^+ and $N_2{}^+$ ions react with interhalogens (ICl, ClF) leading exclusively to dissociative and non-dissociative charge transfer processes. Results of Shuman *et al.* [165] have been interpreted as consequences of the long-range anisotropic interactions that affect specific surface crossings. In another investigation of rovibrationally selected H_2O^+ ions reacting with H_2, stereodynamic effects related to charge and dipole-induced multipole anisotropic interactions have been invoked to explain reactivity [166]. Opposite trends in the rate constants can alternatively be foreseen when long-range interaction potentials reorient the reacting couple into preferred configurations that are also the most facile for reaction [167].

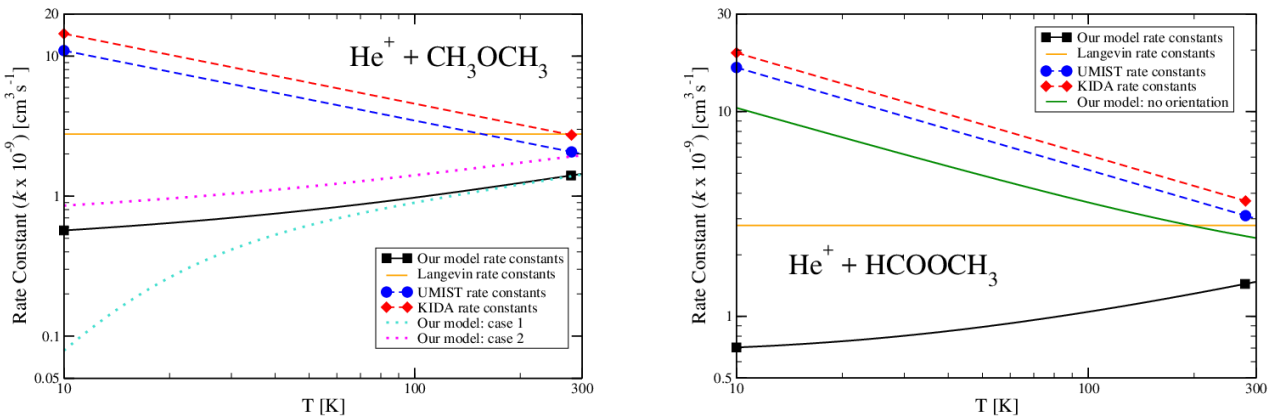

Figure 6.1: Temperature dependence of the total rate constant k (black line) for reactions He^+ + DME (on the left) and He^+ + MF (on the right) calculated by our improved version of the Landau-Zener-Stückelberg model (values at 10 K and 280 K are highlighted with black squares). Values recommended by KIDA database obtained by Eqn. 6.1 are reported with red dashed line (values at 10 K and 280 K are highlighted with red diamonds) , while the UMIST values (Eqn. 6.2) are represented by the blue dashed line (values at 10 K and 280 K are highlighted with blue circles). The orange continuous line is the Langevin rate constant calculated for He^+ – DME and He^+ – MF systems. For He^+ – MF, rate constants in the hypothesis of no orientation of the reactants have been calculated and reported in figure with green continuous line. For He^+ – DME, turquoise and magenta dotted lines refer to our calculation in the lower and upper limit estimates.

Chapter 7

Conclusions

"I would say I'm sorry
If I thought that it would change your mind
But I know that this time
I have said too much. "

Boys Don't Cry - The Cure

The work of this thesis is focused on two ion-neutral molecule reactions that play a significant role in astrochemistry. The involved species are He^+, one of the most relevant interstellar cations, and dimethyl ether (DME) and methyl formate (MF), two of the most abundant complex organic molecules, detected in star-forming region and in pre-stellar cores [13, 14, 15, 16, 17, 18, 19, 20, 21, 22, 23, 24, 168, 169, 170, 171]. Since these O-bearing species can act as building blocks for sugars and other bio-molecules, they can be considered as *pre-biotic* molecules. For this reason, the mechanism of their formation, destruction and distribution within our Galaxy is of paramount importance in the development of theories about the origin of life on Earth [172].

These reactions are an example of charge transfer processes, in which an electron is transferred from the neutral molecule to the ionic reactant. To the authors' knowledge, results on these reactions are the first experimental measurements, and the experimental cross-sections and product branching ratios can be used by theoreticians for achieving better modeling of the abundances of complex organic molecules in the ISM.

The first result obtained by the guided ion beam experiments demonstrates that, due to the differences between the respective ionization energies, the reactions of He^+ are strongly exoergic, causing the complete fragmentation of the molecular radical cation formed by the electron exchange. This means that the considered reactions are no simple charge transfers, but also dissociative processes, in which the neutrals are destroyed after the collision with helium cations. Therefore, relative yields of the ionic products are important data obtained by this thesis work, casting light on these reactions, until now unknown. Furthermore, the process efficiency is quantitatively determined with measures of the absolute cross-section values at thermal and hyperthermal energy range.

The theoretical investigations support the experimental evidences, confirming that the charge transfer reaction between He^+ and DME/MF can not produce the parent cation but only fragment

ions. Indeed, the analysis of the interaction potential energy surfaces reveals that the diabatic reactant surface does not cross the product surface that correlates asymptotically with the ground state of both $CH_3OCH_3^{\bullet+}$ and $HCOOCH_3^{\bullet+}$. Thus, an additional result is the discovery that the nascent molecular radical cation in both reactions is formed in excited states that quickly dissociate. The reason of this surplus in energy is that the charge exchange process is promoted by the removal of an inner-valence electron: the instantaneous electronic rearrangement produces an highly excited state of the molecular radical cation and it causes its explosion into fragments.

Another important aspect of the detailed representation of the PESs is the quantification of the anisotropy of the interaction, that, in the studied cases, generates important stereo-dynamical effects. In fact, the two polar molecules are forced to be oriented in a natural way during the collision by the electric field gradient arising from the interaction with He^+. The reaction dynamics are hence limited to few geometries confined around the most stable configurations of the collision complex systems (*i.e.* $[He-DME]^+$ and $[He-MF]^+$). These geometries are consistent, especially at low collision energies, with the assumption of formation of a "pendular state", which arises from the transformation of free/hindered molecular rotations in bending motion within the colliding systems.

Since we find out that, at low collision energies, the most significant contribution to the reactions between He^+ and DME/MF molecules comes from the most attractive configurations, also the electron density distributions of the involved MOs play a further important role in the dynamics treatment. In the mentioned most attractive geometries, the symmetry of the MOs are unfavorable, implying a small and inefficient overlap with the *s* atomic orbital of the helium ion. For this reason, the reactions are driven by the *Coriolis coupling* rather than by the orbital overlap. Moreover, due to the formation of pendular states, the Coriolis coupling must become progressively weaker at low collision energies. Such insights on the molecular orientation and on the poor orbital overlaps suggest the surprising paradox that the most attractive geometries are also the least reactive. This conclusion makes the charge transfer reaction at low collision energy less efficient than what predicted by a standard Landau-Zener treatment. This behavior is contradictory to the usual assumption that cross-sections of exothermic barrier-less processes, as ion-molecule reactions usually are, increase at low collision energy. As demonstrated, the thorough investigation of the most important factors involved in the proposed reactions is the only way to obtain calculated cross-sections in excellent agreement with experimental ones.

Furthermore, the slack rise of the calculated cross-section values for decreasing collision energies is reflected in an Arrhenius behavior (*i.e.* positive dependence on the temperature) of the so obtained rate constants. This result is in contrast with the models used by the astrochemical network databases to estimate rate constants. In fact, the KIDA and UMIST databases recommend for He^+ + MF/DME reactions rate constants based on a modification of the Arrhenius equation supported by the well-known capture models. The resulting rate coefficients show an anti-Arrhenius behavior (*i.e.* negative dependence on the temperature) that implies a relevant overestimation (especially at 10 K) if compared with the results of this thesis. As a consequence, the astrochemical models, that try to determine accurately the abundances of DME and MF especially in cold interstellar environments, are based on inaccurate assumptions of the rates for dissociation promoted by He^+ ions. Therefore, the immediate update of the network databases with the results of this work is warmly suggested to improve, at least partially, the astrochemical models.

The absence of experimental data on the reaction between He^+ and DME/MF suggests that the dissociative charge exchange processes promoted by the helium cation are largely overlooked by

the astrochemical databases. Therefore, this thesis represents a starting point to extend the study to other COMs such as methanol CH_3OH, ethanol C_2H_5OH (isomer of DME), acetic acid CH_3COOH and glycolaldehyde CH_2OHCHO (isomers of MF), acetaldehyde CH_3COH and ethylene oxide ($c-C_2H_4O$), acetone (CH_3COCH_3) and propanal (C_2H_5COH).

Appendix A

The multiple collisions

In any GIB-MS experiment, there is the possibility that the reactant ion can undergo more than one collision with the neutral target or that a product of the first collision can undergo a collision with the neutral. In fact, a sufficient neutral target gas pressure is necessary to be able to detect the weaker single collision channels with sufficient statistics in a finite experimental run time. Inevitably, there is then the possibility that reactive ions formed in the major channels can undergo secondary reactions. For most early apparatuses, the experiments were not particularly sensitive to these phenomenon. By improving of the sensitivity, these processes were more often observed and it has been demonstrated that they could be characterized by their pressure dependence [59]. The prediction of the absolute intensity of ions coming from multiple collisions depends on the cross-sections for these higher order reactions [61]. In general, it is not possible to assume that the cross-sections for subsequent collisions and reactions are invariant. Collisions alter the kinetic energy of the ions, which will affect the cross-section and changes in the subsequent reaction thermochemistry can drastically influence the cross-section. [61]

If the cross-section for subsequent collisions is assumed to be invariant, then the relative intensities of ions undergoing x or more collisions are given by the following equation:

$$I_x = I_R \cdot [1 - exp(-\rho \cdot \sigma_{rxn} \cdot l)]^x \tag{A.1}$$

where I_R is the intensity of the reactant ion, ρ is the density of the neutral target and l the effective length of the scattering cell. The relative intensity of ions that have undergone exactly x number of collisions is $I_x - I_{x+1}$. In the *thin-target limit*, Eqn. A.1 is simplified to:

$$I_x = I_R \cdot (\rho \cdot \sigma_{rxn} \cdot l)^x \tag{A.2}$$

Eqn. A.2 is generally not accurate for larger values of $\rho\sigma_{rxn}l$.

When planning GIB-MS experiments, appropriate pressure values in the scattering cell should be used so that the weaker single collision channels are visible and secondary reactions are kept to a minimum. However, because it is impossible to completely remove the effects of secondary collisions using experimental methods, cross-sections corresponding to single-collision conditions could be acquired by linear extrapolating to zero pressure or by adding the cross-section for the secondary products to those of the primary product [59].

According to Eqn. A.2, the cross-section as a function of the pressure will have a linear trend when it is due to a primary process, while it will have a quadratic dependence when the reactant

collides twice. These different behaviors of product trends are shown in Figure A.1, in which the protonated DME ($HO(CH_3)_2^+$ (open blue circles)) is formed by secondary collisions of the most abundant primary products (HCO^+ (closed red squares)) with DME, in the reaction of He^+ + $O(CH_3)_2$ (DME). In fact, the protonated DME yield shows a quadratic dependence from density, a clear indication of secondary collision.

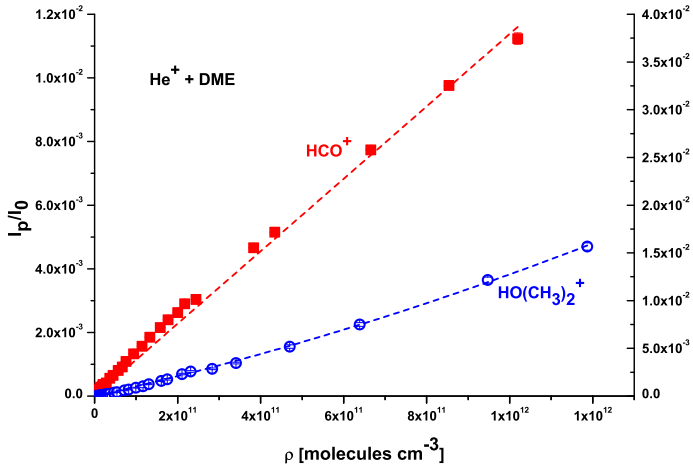

Figure A.1: Ion intensities (I_P) of HCO^+ (closed red squares), $HO(CH_3)_2^+$ (open blue circles) relative to the ion intensity ($I_0 = I_R$) for reaction of He^+ + $O(CH_3)_2$ (DME) at a collision energy in the CM frame of about $1.6\,\mathrm{eV}$ as a function of the DME reactant density. The lines show linear and quadratic models of the density dependencies.

Apparently, intensity of secondary collision products should be lower than primary collision ions in the whole range of studied neutral pressures. This assumption has been called into question during the calibration of the instrument with the reference reaction Ar^+ + CH_4 [173, 174]. In this case, as the mass spectra show in Figure A.3 an unusual relative abundance between primary and secondary products, CH_3^+ ($15\,\mathrm{m/z}$) and $C_2H_5^+$ ($29\,\mathrm{m/z}$), has been observed . More specifically, the primary collision reaction that leads to methyl ion is:

$$Ar^+ + CH_4 \longrightarrow Ar + {CH_3}^+ + H \tag{A.3}$$

while $C_2H_5^+$ might result from the reaction of CH_3^+ with methane *via* a highly efficient process (k in the range $1.0 \times 10^{-9}\,\mathrm{cm^3 molecule^{-1} s^{-1}}$ to $1.2 \times 10^{-9}\,\mathrm{cm^3 molecule^{-1} s^{-1}}$ at $300\,\mathrm{K}$ [175, 176, 177, 178, 179, 180, 181, 182, 183]):

$${CH_3}^+ + CH_4 \longrightarrow {C_2H_5}^+ + H_2 \tag{A.4}$$

Furthermore, while in Tosi *et al.* [173, 174] a small amount (15%) of $CH_2^{\bullet+}$ at *m/z* 14 is detected, in our experiment the ionic product $CH_2^{\bullet+}$ is not observed. The differences in BRs can be explained in terms of internal energy of the produced methane radical cation [184, 174]. In fact, as reported in the breakdown curves for methane (IE=12.61(1)eV [185], Figure A.2, adapted from [184, 174]), obtained by using a threshold photoelectron-photoion coincidence technique in the photon energy range13.8-16.4 eV [184], the fragmentation pattern of the molecular ion is related to its internal energy. Figure A.2 shows that only $CH_4^{\bullet+}$ ions are produced if the nascent ion is formed with an internal energy below 14.3 eV, while above this threshold CH_3^+ appears and $CH_4^{\bullet+}$ begin to decrease. The $CH_2^{\bullet+}$ ions start to appear at a threshold energy $\sim$ 15.2eV and their branching ratio increases as the internal energy of $CH_4^{\bullet+}$ increases. Coming back to Ar^+ experiments, the BRs of the Ar^+ + CH_4 suggest that in Tosi *et al.* experiment the the internal energy of methane radical cation is $\sim$ 2.7 eV (corresponding to have 85% of CH_3^+ and 15% of $CH_2^{\bullet+}$ in the photo-ionization breakdown diagram as shown by the red line in Figure A.2), whereas in our experiment the methyl radical cation is formed with a lower internal energy ($\sim$1.9-2.4 eV energy range corresponding to have 100% of CH_3^+as shown by the green area in Figure A.2).

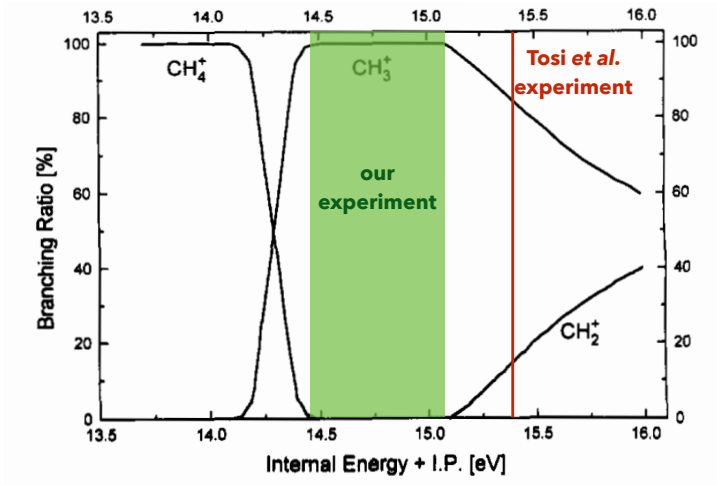

Figure A.2: Breakdown curves (Figure A.2, adapted from [184, 174]) in the 13.8-16.4 eV energy range for methane (IE=12.61(1)eV [185]), obtained by using a threshold photoelectron-photoion coincidence technique [184].

The behavior of the secondary product at 29 m/z is uncommon: it is more abundant than the primary products in the studied methane pressure range and it shows a linear dependence on the neutral density, as well. Verified the absence of impurities at same *m/z* value, it has been tried to explain this unusual behavior modeling the product formation and destruction processes. Since

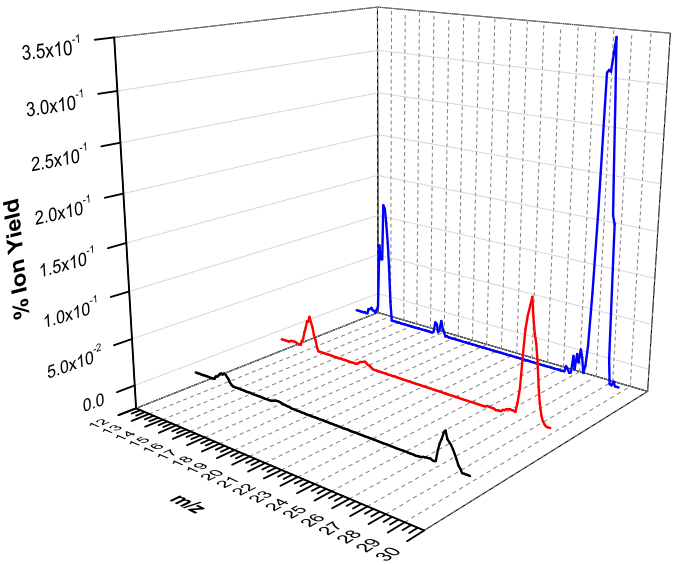

Figure A.3: Mass spectra of selected Ar^+ ions reacting with CH_4 at different pressures inside the reaction octopole: 8.0×10^{-7} mbar (black), 2.2×10^{-6} mbar (red) and 5.3×10^{-6} mbar (blue). The signal intensity of the Ar^+ ion (100 %) is not shown.

the reactive system is simplified to:

$$\mathrm{R} + \mathrm{N} \rightarrow \mathrm{P}_1$$
$$\mathrm{P}_1 + \mathrm{N} \rightarrow \mathrm{P}_2$$

with R being the ion reagent intensity, N the neutral target intensity, P_1 and P_2 the primary and secondary product intensities, and on the basis of the *Lambert-Beer Law*, the following initial conditions have been fixed:

- $\frac{dR}{dx} = -\sigma_1 NR$
- $\frac{dP_1}{dx} = -\frac{dR}{dx} - \frac{dP_2}{dx}$
- $\frac{dP_2}{dx} = \sigma_2 NP_1$
- $\frac{d[R+P_1+P_2]}{dx} = -\sigma_1 NR + \sigma_1 NR - \sigma_2 NP_1 + \sigma_2 NP_1 = 0$ (Q.E.F.)

The depletion of the ionic reactant is obtained integrating the first expression:

$$\int_{R_0}^{R} \frac{d\bar{R}}{\bar{R}} = -\sigma_1 N \int_0^x d\bar{x}$$
$$\ln(\bar{R})\Big|_{R_0}^{R} = -\sigma_1 N\bar{x}\Big|_0^x$$
$$\ln(\frac{R}{R_0}) = -\sigma_1 Nx$$

from which is possible to obtain the following equation equivalent to Eqn. 2.7 in Sec. 2.3.4 to calculate the ionic reactant intensity after the first collision as a function of the effective length of the scattering cell *x*:

$$R(x) = R_0 exp(-\sigma_1 Nx) \tag{A.5}$$

For the first collision product (P_1) we have that:

$$\frac{d\bar{P_1}}{d\bar{x}} = \sigma_1 N R(x) - \sigma_2 N \bar{P_1} \tag{A.6}$$

considering Eqn. A.5, it is possible to expand in:

$$\frac{d\bar{P_1}}{d\bar{x}} + \sigma_2 N \bar{P_1} = \sigma_1 N R_0 exp(-\sigma_1 N\bar{x}) \tag{A.7}$$

To resolve the ODE (*Ordinary Differential Equation*) it is necessary to multiply both member for $e^{\sigma_2 N\bar{x}}$:

$$exp(\sigma_2 N\bar{x})\frac{d\bar{P_1}}{d\bar{x}} + \sigma_2 N exp(\sigma_2 N\bar{x})\bar{P_1} = \sigma_1 N R_0 exp(\sigma_2 N\bar{x}) exp(-\sigma_1 N\bar{x})$$
$$\frac{d}{d\bar{x}}\left[exp(\sigma_2 N\bar{x})\bar{P_1}\right] = \sigma_1 N R_0 exp\left[N\bar{x}(\sigma_2 - \sigma_1)\right] \tag{A.8}$$

Integrating, we obtain:

$$exp(\sigma_2 Nx)P_1 = \sigma_1 N R_0 \int_0^x exp\left[N\bar{x}(\sigma_2 - \sigma_1)\right] d\bar{x}$$
$$P_1 = \sigma_1 \cancel{N} R_0 exp(-\sigma_2 Nx) \cdot \frac{exp\left[N(\sigma_2 - \sigma_1)x\right] - 1}{\cancel{N}(\sigma_2 - \sigma_1)}$$
$$P_1 = R_0 \frac{\sigma_1}{\sigma_2 - \sigma_1} \cdot [exp(\cancel{\sigma_2 Nx} - \sigma_1 Nx - \cancel{\sigma_2 Nx}) - exp(-\sigma_2 Nx)]$$

and finally,

$$P_1(x) = R_0 \frac{\sigma_1}{\sigma_2 - \sigma_1} \cdot [exp(-\sigma_1 Nx) - exp(-\sigma_2 Nx)] \tag{A.9}$$

To check the truthfulness of this expression, it is considered the special case in which secondary collisions are avoid ($\sigma_2 = 0$): the Eqn. A.9 must be equal to Eqn. 2.9.

$$P_1(x) = R_0 \frac{\sigma_1}{0 - \sigma_1} \cdot [exp(-\sigma_1 N x) - exp(0)]$$
$$P_1(x) = R_0 - \frac{\cancel{\sigma_1}}{\cancel{\sigma_1}} \cdot [exp(-\sigma_1 N x) - 1]$$
$$P_1(x) = R_0 \left[(1 - exp(-\sigma_1 N x)\right] \quad (Q.E.D.)$$

For P_2 we have:

$$\frac{d\bar{P}_2}{d\bar{x}} = \sigma_2 N P_1(x)$$

$$\frac{d\bar{P}_2}{d\bar{x}} = \sigma_2 N R_0 \frac{\sigma_1}{\sigma_2 - \sigma_1} \cdot [exp(-\sigma_1 N \bar{x}) - exp(-\sigma_2 N \bar{x})]$$
$$\int_0^{P_2} d\bar{P}_2 = \sigma_2 N R_0 \frac{\sigma_1}{\sigma_2 - \sigma_1} \cdot \left[\int_0^x exp(-\sigma_1 N \bar{x}) d\bar{x} - \int_0^x exp(-\sigma_2 N \bar{x}) d\bar{x}\right] =$$
$$= \cancel{N} R_0 \frac{\cancel{\sigma_1}\cancel{\sigma_2}}{\sigma_2 - \sigma_1} \cdot \left\{ -\frac{1}{\cancel{N}\cancel{\sigma_1}} [exp(-\sigma_1 N x) - 1] + \frac{1}{\cancel{N}\cancel{\sigma_2}} [exp(-\sigma_2 N x) - 1] \right\}$$

and rather,

$$P_2 = R_0 \frac{\sigma_1}{\sigma_2 - \sigma_1} [exp(-\sigma_2 N x) - 1] - R_0 \frac{\sigma_2}{\sigma_2 - \sigma_1} [exp(-\sigma_1 N x) - 1]$$

from which we obtain the expression for $P_2(x)$:

$$P_2(x) = \frac{R_0}{\sigma_2 - \sigma_1} [\sigma_2 - \sigma_1 + \sigma_1 exp(-\sigma_2 N x) - \sigma_2 exp(-\sigma_1 N x)]$$

If $\sigma_2 = 0$, $P_2(x)$ should be equal to 0:

$$P_2(x) = \frac{R_0}{0 - \sigma_1} [0 - \sigma_1 + \sigma_1 exp(-0 \cdot N x) - 0 \cdot exp(-\sigma_1 N x)]$$
$$P_2(x) = -\frac{R_0}{\sigma_1} [-\sigma_1 + \sigma_1]$$
$$P_2(x) = 0 \quad (Q.E.D.)$$

In Figure A.4, the comparison between the experimental data (blue diamonds and orange squares for CH_3^+ and $C_2H_5^+$) as a function of the neutral density and the modeled ones is shown. Having reasonable values of R_0=1.9 $\times$ 10^5, σ_1=27 $Å^2$ and σ_2=23 $Å^2$, both the linear trend and the higher signal of the secondary product $C_2H_5^+$ with respect to the one of CH_3^+ are well modeled (continuous blue and orange lines) assuming that $l_{\sigma_2} > l_{\sigma_1}$ (9 and 8 cm). The difference in effective length of the scattering cell might mean that the kinetic energy of the primary and secondary collision products is quite different causing different residing times in the scattering cell. Despite the premises, the modeled relative intensity of $C_2H_5^+$ is underestimated.

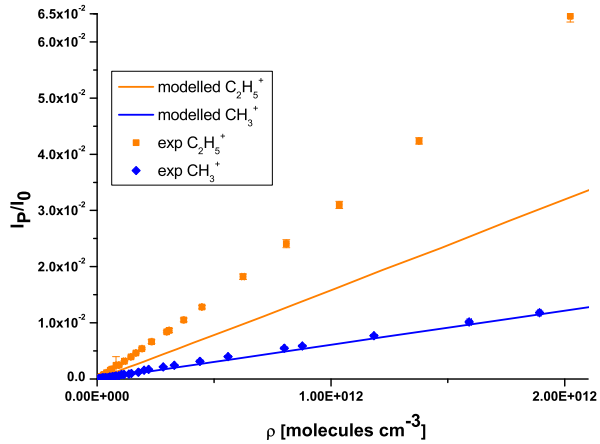

Figure A.4: Experimental CH_3^+ and $C_2H_5^+$ yields as a function of the neutral density are reported with blue diamonds and orange squares. Blue and orange continuous lines are the results obtained by the developed model (details in the text) assuming R_0=1.9 $\times$ 10^5, σ_1=27 Å^2, σ_2=23 Å^2, l_{σ_2}=9 cm and l_{σ_1}=8 cm.

Appendix B

The M06-2X and the cc-pVTZ/cc-pVQZ

For the work of this thesis, the M06-2X [186, 187, 188, 189] functional has been used.

Briefly, the DFT is a quantum theory formulated by Kohn and Sham in 1965 [190], in which the many-body effect of electron correlation is modelled by a function of the electron density [191], $\rho(r)$, that can be also defined as probability density, *i.e.* the probability to find one of the any N electrons of the system in a volume element dr. The electron density has several important properties: [190, 192]

- $\rho(r)$ is always a positive physical quantity;
- it depends only on the spatial variables;
- $\rho(r) \to 0$ for $r \to \infty$;
- its integral defines the N number of electrons;
- the cusps in the density define the position of the nuclei and their heights the nuclear charges;
- it is a physical observable and it can be obtained by *X-Ray diffraction* experiments.

The main impact of the DFT method, illustrated by the *first Hohenberg-Kohn theorem* [193], is to establish a connection between the energy of a system and its electron density, declaring that the first one is *functional* [1] of the second one. From this theorem and from the exact electron density, all the properties of the ground state of a system can be obtained.

For a many body system under the BO approximation, the time-independent Schrödinger equation can be written as:

$$\widehat{H}\Psi = \left[\widehat{T} + \widehat{V} + \widehat{U}\right] = E\Psi \tag{B.1}$$

[1] A *function* is a prescription for producing a number from a set of variables, *e.g.* the coordinates of a system. A *functional* is a prescription for producing a number from a *function*, which depends on variables. Therefore, we can define the wave function and the electron density as functions, while the energy depending on the wave function or on the electron density is a functional. The functional is denoted with $F[f]$. [191]

where $\widehat{H}$ is the Hamiltonian, E the total energy, $\widehat{T}$ the kinetic energy, $\widehat{V}$ the potential energy of the external field and $\widehat{U}$ the electron-electron interaction energy (for a detailed description of the Hamiltonian and the BO approximation see Sec. 3.1.2). In DFT, the Ψ_0 of the ground state is defined as functional of the ground state density $\rho(r)_0$:

$$\Psi_0 = \Psi\left[\rho_0\right] \tag{B.2}$$

So, for the ground state, the electron energy $E[\rho_0]$ can be expressed as:

$$E_0 = E[\rho] = \langle \Psi\left[\rho_0\right] | \widehat{T} + \widehat{V} + \widehat{U} | \Psi\left[\rho_0\right] \rangle \tag{B.3}$$

The functionals $T[\rho]$ and $U[\rho]$ are called *universal functionals*, while $V[\rho]$ is the *non-universal functional*, because it depends on the specific system of interest. Therefore, working on a specific system, $V[\rho]$ is known and the problem can be solved minimizing the functional $E[\rho]$, having reliable expressions for $T[\rho]$ and $U[\rho]$.

At this point, the suggestion of Kohn and Sham [190] was to consider a reference system, in which the N electrons are non-interacting and exposed to the same external potential. The energy functional becomes:

$$E_s[\rho] = \langle \Psi_s\left[\rho\right] | \widehat{T}_s + \widehat{V}_s | \Psi_s\left[\rho\right] \rangle \tag{B.4}$$

where $\widehat{T}_s$ is the kinetic energy operator of the non-interacting system and $\widehat{V}_s$ is a external effective potential in which the particles move. The relation $\rho_s(r) = \rho(r)$ is valid only if $\widehat{V}_s = \widehat{V} + \widehat{J} + \widehat{T} - \widehat{T}_s$. In general, the DFT energy expression can be re-written as:

$$E_{DFT}[\rho] = T_s[\rho] + V[\rho] + J[\rho] + E_{xc}[\rho] \tag{B.5}$$

where $T_s[\rho]$ is the kinetic energy of non-interacting electrons, $J[\rho]$ is the classical Coulomb potential energy and $E_{xc}[\rho]$ is the *exchange correlation energy*, due to interacting electrons. E_{xc} can be represented as sum of kinetic energy deviation from the reference system ($\Delta T[\rho]$, kinetic correlation energy of the electrons) and the electron-electron interaction deviation from the classical system ($\Delta U[\rho]$, potential exchange-correlation energy):

$$E_{xc}[\rho] = \Delta T[\rho] + \Delta U[\rho] = (T[\rho] - T_s[\rho]) + (U[\rho] - J[\rho]) \tag{B.6}$$

The challenge of Kohn-Shame theory is to approximate formulations of the unknown E_{xc} term. From the different forms of that term, it is possible to obtain:

- *Local Density Approximation* (LDA), in which it is assumed that the density can be treated locally as a uniform gas. In general, if α and β spin densities are not equal, it is used the *Local Spin Density Approximation* (LSDA).
- *Generalized Gradient Approximation* (GGA): to improve the LSDA method is necessary to consider a non-uniform electron gas; for this reason, it is requested that the E_{xc} does not depend only on the electron density, but also on its derivative, including the first derivative as variable. The GGA methods are non-local methods.
- *meta-Generalized Gradient Approximation* (m-GGA): the E_{xc} depends on higher order derivatives of the electron density.

Table B.1: *Mean Signed Error* (MSE) and *Mean Unsigned Error* (MUE) in $\mathrm{kcal\,mol^{-1}}$ for ionisation potential (IP), electron affinity (EA), proton affinity (PA) and in $\mathrm{kcal\,mol^{-1}}$ per bond (PB) for atomization energy (AE). Average (DFT) is the average of several DFT methods, while Average (All) is the average of DFT and HF methods reported in the original table [189].

Method	AE		IP		EA		PA	
	MSEPB	MUEPB	MSE	MUE	MSE	MUE	MSE	MUE
M06-2X	-0.18	0.40	1.06	2.54	1.30	2.07	-0.19	1.75
Average (DFT)	-0.47	1.32	1.45	3.62	1.24	2.85	0.93	1.83
Average (All)	-2.27	3.05	0.34	4.46	2.76	4.27	1.04	1.91

- *hybrid-Generalized Gradient Approximation* (h-GGA): the E_{xc} is written as a combination of LSDA and a gradient correction term.

The functional used for the work reported in this thesis (the M06-2X) is one of the hybrid-GGA methods developed by Zhao and Thrular in Minnesota since 2005: all the functionals have the same name form, *i.e.* M*yz* or M*yz*-suffix, in which M indicates *Minnesota* or *meta* and the *yz* indicates the year (20*yz*) [194]. The M06-2X depends on three variables:

- the spin density (ρ_σ);
- the gradient of the spin density ($x_\sigma = \frac{|\Delta\rho_\sigma|}{\rho_\sigma^{3/4}}$);
- the density of spin kinetic energy ($\tau_\sigma = \frac{1}{2}\sum_i^{Occ} |\bigtriangledown \Psi_{i\sigma}|^2$).

The exchange- correlation energy is written as:

$$E_{xc} = \frac{X}{100}E_x^{HF} + (1 - \frac{X}{100})E_x^{DFT} + E_c^{DFT} \tag{B.7}$$

where E_x^{HF} is the non-local exchange HF energy, X is the percentage of the HF exchange in the hybrid functional, E_x^{DFT} and E_c^{DFT} are the exchange and correlation DFT energies. In M06-2X, the exchange percentage value X is 54% [194].

From *Mean Signed Error* (MSE) and *Mean Unsigned Error* (MUE) in $\mathrm{kcal\,mol^{-1}}$ for ionisation potential (IP), electron affinity (EA), proton affinity (PA) and in $\mathrm{kcal\,mol^{-1}}$ per bond (PB) for atomization energy (AE) (reported in Table B.1), this functional shows an improvement of $\sim$ 9-13% with respect to the average of the other DFT functionals [186, 187, 188, 189].

For the DFT calculations of this thesis work, the cc-pVTZ and cc-pVQZ (*correlation consistent polarized Valence Triple/Quadrupole Zeta*) basis sets have been used. This type of basis set was proposed by Dunning and co-workers [195, 196]. The acronym *cc* (correlation consistent) refers to the correlation energy of the valence electrons: the functions of these basis sets include a contribution similar to that due to correlation energy, independent of the function type. This type of basis set is, therefore, geared towards recovering the correlation energy of the valence electrons and it is designed so that functions that contribute similar amounts of correlation energy are included at

the same stage. The *s*- and *p*- basis sets exponents are optimized at HF level for the atoms, while the polarization exponents are optimized at the CISD level (Configuration Interaction including single and double excitations from occupied to unoccupied orbitals). The *V* refers to the fact that only valence orbital functions, that are involved in molecular bond, are multiplied, neglecting the core orbitals, essentially independent of the chemical environment (*split valence basis*). Finally, the letter *x* indicates the different sizes in terms of final number of contracted functions.

Appendix C

Classical trajectory: The He^+ + DME case

The strong anisotropic non-covalent interaction between He^+ and a polar species, such as DME, induces a pronounced stereo-chemical effect in the ion-molecule reaction (as already explained in detail in Chapter 5). Thus, the charge transfer process takes place at low collision energy only from selected configurations confined in the region where the interaction is highly attractive (the O-side for the DME molecule). To have a further evidence of this phenomenon, the classical trajectory for the reaction He^+ + DME have been studied sampling the position of the He^+ in proximity of the DME molecule. Since for the mentioned collision system the rotational motion of the target molecule has to be taken into account together with the translational motion of the ion, the study has been carried out using a modified velocity Verlet algorithm [197] that improves the velocity Verlet with considering the rotational motion. The work has been performed in collaboration with Dr. G. Garberoglio, senior researcher at the FBK-ECT*-LISC center in Trento.

Before explaining this upgraded method, it results convenient to report the "normal" velocity Verlet algorithm, formulated to solve the Newton equation of motions with assigned positions ($\overrightarrow{x}(t)$) and velocities ($\overrightarrow{v}(t)$) at a certain time t_0 (for the sake of simplicity the vector symbol will be omitted from now). In a interacting system in which is active a potential $V(x)$, the acceleration is expressed as a position-dependent force term:

$$\frac{d^2x(t)}{t^2} = a(t) = \frac{1}{m}F(x(t)) = -\frac{1}{m}\nabla V(x(t)) \tag{C.1}$$

The steps to perform the velocity Verlet algorithm are:

1. Advance the velocity at a time $t + \delta t/2$:

$$v(t + \delta t/2) = v(t) + \frac{1}{2m}F(t)\delta t \tag{C.2}$$

2. Advance the positions at time $t + \delta t$:

$$x(t + \delta t) = x(t) + v(t + \delta t/2)\delta t \tag{C.3}$$

3. Calculate the new force at time $t + \delta t$:

$$F(t + \delta t) = -\nabla V(x(t + \delta t)) \tag{C.4}$$

4. Complete the velocity move at time $t + \delta t$:

$$v(t + \delta t) = v(t + \delta t/2) + \frac{1}{2m} F(t + \delta t)\delta t \tag{C.5}$$

As said above, the modified velocity Verlet [197] includes the rotations of a rigid body (in this case the DME molecule), target of a body that moves with a translational motion (the ion). This method involves the use of *quaternions* (denoted by q_k with k =0 $\cdots$ 3) for representing orientations and rotations of the rigid molecule in the three dimension [1]. Therefore, the rotation matrix that allows to transform the coordinates of a vector from the laboratory reference frame to the molecular frame is the following:

$$E(q) = \begin{bmatrix} q_0^2 + q_1^2 - q_2^2 - q_3^2 & 2(q_1 q_2 + q_0 q_3) & 2(q_1 q_3 - q_0 q_2) \\ 2(q_1 q_2 - q_0 q_3) & q_0^2 - q_1^2 + q_2^2 - q_3^2 & 2(q_2 q_3 + q_0 q_1) \\ 2(q_1 q_3 + q_0 q_2) & 2(q_2 q_3 - q_0 q_1) & q_0^2 - q_1^2 - q_2^2 + q_3^2 \end{bmatrix} \tag{C.6}$$

Consequently, the equation of motion for the quaternions is:

$$\dot{q} = \begin{bmatrix} \dot{q}_0 \\ \dot{q}_1 \\ \dot{q}_2 \\ \dot{q}_3 \end{bmatrix} = \frac{1}{2} \begin{bmatrix} q_0 & -q_1 & -q_2 & -q_3 \\ q_1 & q_0 & -q_3 & q_2 \\ q_2 & q_3 & q_0 & -q_1 \\ q_3 & -q_2 & q_1 & q_0 \end{bmatrix} \begin{bmatrix} 0 \\ w_x^m \\ w_y^m \\ w_z^m \end{bmatrix} = Q(q) W^m \tag{C.7}$$

where w_i^m is the i-component of the angular velocity in the molecular frame (indicated by the superscript m, while from now the laboratory frame is indicated by the superscript l), that can be easily evaluated by the angular momentum of the rigid molecule L and the rotation matrix C.6:

$$w^m = I^{-1} E(q) L^l \tag{C.8}$$

I is the inertia tensor expressed in the molecular frame, where it is diagonal.

Given the basis for the rotational motion, the modified velocity Verlet algorithm evolves as follows [197]:

1. The first step of the velocity Verlet for the center of mass coordinates have to be performed (Eqn. C.2);
2. The angular velocities and the quaternion derivative at time t (using Eqn. C.8 and Eqn. C.7, respectively) have to be calculated:

$$\dot{q}(t) = \frac{1}{2} Q(q(t)) \left[I^{-1} E(q(t)) L(t) \right] = \frac{1}{2} Q(q(t)) w^m(t) \tag{C.9}$$

[1] Quaternions are preferred with respect to the *Euler angles* (commonly used to describe the angular velocities of a rigid body). In fact, the representation of a rotation matrix with Euler angles can lead to the loss of one degree of freedom in a three dimensional (*a.k.a.* **gimbal lock**), causing serious effects in any numerical integration.

3. Evaluate the quaternions at mid-step ($t + \delta t/2$):

$$q(t + \delta t/2) = q(t) + \dot{q}(t)\delta t/2 \tag{C.10}$$

4. Advance the angular momentum at mid-step using the torques N [2] at time t:

$$L(t + \delta t/2) = L(t) + N(t)\delta t/2 \tag{C.11}$$

5. Calculate the angular velocity and quaternion derivative at mid-step ($t + \delta t/2$):

$$w^m(t + \delta t/2) = I^{-1}E(q(t + \delta t/2))L(t + \delta t/2) \tag{C.12}$$

$$\dot{q}(t + \delta t/2) = \frac{1}{2}Q(q(t + \delta t/2))w^m(t + \delta t/2) \tag{C.13}$$

6. From the quaternion derivative calculated in the previous step, advance quaternions at time $t + \delta t$:

$$q(t + \delta t) = q(t) + \dot{q}(t + \delta t/2)\delta t \tag{C.14}$$

7. Advance the velocity and angular momentum from the forces and torques at time $t + \delta t$.

Therefore, to perform the algorithm for the specific He⁺ + DME system the following input are necessary:

- The He⁺ position in Cartesian coordinates with respect to the CM of the molecule, far enough so that the interaction potential is negligible (*e.g.* [50.0 Å 0 0]).
- The He⁺ velocity, of which only the *x*-component has been considered. The approximation is allowed since the molecule rotates freely with a random initial position. The translation depends on the collision energy (E_{CM}) of the ions as the following expression shows:

$$v_x = \sqrt{\frac{2E_{CM}}{m_{He}}} \tag{C.15}$$

  where m_{He} is the mass of helium. Since the E_{CM} of the calculated cross-sections is in the range from 0.010 to 6 eV, v_x ranges from $\sim 6.95 \times 10^2$ to $1.70 \times 10^4\,\mathrm{m\,s^{-1}}$.
- Position of the CM and translational velocity of DME that are set equal to zero;
- The Cartesian coordinates reported in Chapter 5 are used to set the position of the atoms of DME with respect the CM of the molecule (molecular frame):

$$\begin{bmatrix} \mathrm{O} \\ \mathrm{C}_\alpha \\ \mathrm{C}_\beta \end{bmatrix} = \begin{bmatrix} 0 & -0.510 & 0 \\ 1.175 & 0.272 & 0 \\ -1.175 & 0.272 & 0 \end{bmatrix} \tag{C.16}$$

- To calculate the acceleration and therefore the force in Eqn. C.1, it is necessary to know the potential of interaction for the examined system. Obviously, in this case the potential representation for the He⁺ + DME reported in detail in Chapter 5 has been used.

[2] Torque is defined as the cross product of the distance vector and the force vector.

- The inertia tensor (diagonal in the molecular frame) has been calculated as follows:

$$I = \begin{bmatrix} I_{xx} & 0 & 0 \\ 0 & I_{yy} & 0 \\ 0 & 0 & 0I_{zz} \end{bmatrix} = \\ = \begin{bmatrix} 6.38 & 0 & 0 \\ 0 & 41.42 & 0 \\ 0 & 0 & 47.80 \end{bmatrix} \tag{C.17}$$

  where $I_{xx} = m_O(d_O^y)^2 + 2m_{\mathrm{CH_3}}(d_{\mathrm{CH_3}}^y)^2$, $I_{yy} = 2m_{\mathrm{CH_3}}(d_{\mathrm{CH_3}}^x)^2$ and $I_{zz} = m_O(d_O^y)^2 + m_{\mathrm{CH_3}}\left[(d_{\mathrm{CH_3}}^x)^2 + (d_{\mathrm{CH_3}}^y)^2\right]$. d_O^i and $d_{\mathrm{CH_3}}^i$ are the distances between the O atom/methyl groups with respect to the CM of the molecule, and m_O and $m_{\mathrm{CH_3}}$ are the masses of the O atom and the methyl groups, respectively.

- The quaternions that are chosen random by using the MT19937 generator developed by M. Matsumoto and T. Nishimura [198]. Constraint is that the valid values are contained in a sphere of radius equal to 1.

- The angular momentum of the molecule that depends on its rotational temperature (about 300 K). The Gaussian distribution of random variables generated by MT19937 has been used. The function has mean zero and standard deviation equal to the angular momentum (σ_L) at room temperature:

$$\sigma_L = \sqrt{k_B T I_i}$$

  where k_B is the Boltzmann's constant, T the temperature and I is the moment of inertia.

- the Verlet step has been chosen equal to 0.01: from this value the calculated trajectories converge. Since the fixed *natural units* are the mass (m=1 uma), the energy (E=1 eV) and the distance (r=1 Å), it results that:

$$t = \sqrt{\frac{m \cdot r^2}{E}}$$

  from which the typical time of the Verlet algorithm is 10^{-14} s.

Since the final aim of the trajectory study is to demonstrate the strong stereo-dynamical effect at low energy, it has been decided to sample the position of He^+ at 2.3 Å with respect to the CM at the lowest (0.010 eV) and highest (6 eV) energy to verify if the ion approaches the molecule in preferred directions. The 2.3 Å distance has been chosen to include the potential well on the O-side and the number of simulated trajectories for each energy to have an acceptable statistic is one thousand.

Results are shown in Figure C.1 and they confirm (at least partially) our hypothesis. The three 2D-panels (from the left to the right: *xz*, *xy* and *yz* planes) of Figure C.1 show where He^+ hits the "imaginary" sphere of 2.3 Å radius at E_{CM}=0.010 eV (black dots) and at E_{CM}=6 eV (red dots). It is clear that at 0.010 eV the ion prefers to hit the area characterized by negative values of the *y*-axes (O-side of the molecule), while it avoids the methyl-side (characterized by positive values of the *y*-axes) as the high concentration of black dots demonstrates in the central and right panels of Figure C.1. The difference between the low and high energy results is significant: in fact, the

red dots are more distributed around the molecule (except for the repulsive area occupied by the methyl) than the black ones. This means that at high energy the ion-molecule system has not enough time to align and to approach along the most attractive geometry. For these reasons, it is evident (left and right panels) that at high energy a wider reactive cone should be consider in order to take into account the differences between the low and high energy cases. Furthermore, it is interesting to note that our cone (qualitatively estimated as reported in Chapter 5 and shown in Figure C.1 with green diamonds) is in good agreement with the one estimated with the trajectory method at 0.010 eV, even if the latter is quite wider and have a less tapered shape that the former [3]. This comparison suggests the power of the trajectory method for estimating the reactive cone and it represents an interesting starting point for further developments of the "Improved Landau-Zener method" reported in this doctoral thesis.

[3]It is worth noting that in our model we approximated using only the external points of the cone: since the solid angle should also taken into account in the weighted average of the cross-section, the σ calculated along the perimeter of the cone would be heavier in the average than the internal ones.

Figure C.1: Impact points of He^+ with respect to an "imaginary" sphere of radius 2.3 Å (from the CM) that surrounds the DME molecule. These results are obtained for E_{CM}= 0.010 eV (black dots) and 6 eV (red dots) by using the data of one thousand trajectory simulations for each energy. The panels are the 2D-projections on the three dimension planes: xz (left panel), yz (central panel) and yz (right panel). On the xy-plane representation, points of our reactive cone (details in Chapter 5) are reported with green diamonds.

Bibliography

[1] Planck Collaboration, P. A. R. Ade, N. Aghanim, C. Armitage-Caplan, M. Arnaud, M. Ashdown, F. Atrio-Barandela, J. Aumont, C. Baccigalupi, A. J. Banday, R. B. Barreiro, J. G. Bartlett, E. Battaner, K. Benabed, A. Benoît, A. Benoit-Lévy, J.-P. Bernard, M. Bersanelli, P. Bielewicz, J. Bobin, J. J. Bock, A. Bonaldi, J. R. Bond, J. Borrill, F. R. Bouchet, M. Bridges, M. Bucher, C. Burigana, R. C. Butler, E. Calabrese, B. Cappellini, J.-F. Cardoso, A. Catalano, A. Challinor, A. Chamballu, R.-R. Chary, X. Chen, H. C. Chiang, L.-Y. Chiang, P. R. Christensen, S. Church, D. L. Clements, S. Colombi, L. P. L. Colombo, F. Couchot, A. Coulais, B. P. Crill, A. Curto, F. Cuttaia, L. Danese, R. D. Davies, R. J. Davis, P. de Bernardis, A. de Rosa, G. de Zotti, J. Delabrouille, J.-M. Delouis, F.-X. Désert, C. Dickinson, J. M. Diego, K. Dolag, H. Dole, S. Donzelli, O. Doré, M. Douspis, J. Dunkley, X. Dupac, G. Efstathiou, F. Elsner, T. A. Enßlin, H. K. Eriksen, F. Finelli, O. Forni, M. Frailis, A. A. Fraisse, E. Franceschi, T. C. Gaier, S. Galeotta, S. Galli, K. Ganga, M. Giard, G. Giardino, Y. Giraud-Héraud, E. Gjerløw, J. González-Nuevo, K. M. Górski, S. Gratton, A. Gregorio, A. Gruppuso, J. E. Gudmundsson, J. Haissinski, J. Hamann, F. K. Hansen, D. Hanson, D. Harrison, S. Henrot-Versillé, C. Hernández-Monteagudo, D. Herranz, S. R. Hildebrandt, E. Hivon, M. Hobson, W. A. Holmes, A. Hornstrup, Z. Hou, W. Hovest, K. M. Huffenberger, A. H. Jaffe, T. R. Jaffe, J. Jewell, W. C. Jones, M. Juvela, E. Keihänen, R. Keskitalo, T. S. Kisner, R. Kneissl, J. Knoche, L. Knox, M. Kunz, H. Kurki-Suonio, G. Lagache, A. Lähteenmäki, J.-M. Lamarre, A. Lasenby, M. Lattanzi, R. J. Laureijs, C. R. Lawrence, S. Leach, J. P. Leahy, R. Leonardi, J. León-Tavares, J. Lesgourgues, A. Lewis, M. Liguori, P. B. Lilje, M. Linden-Vørnle, M. López-Caniego, P. M. Lubin, J. F. Macías-Pérez, B. Maffei, D. Maino, N. Mandolesi, M. Maris, D. J. Marshall, P. G. Martin, E. Martínez-González, S. Masi, M. Massardi, S. Matarrese, F. Matthai, P. Mazzotta, P. R. Meinhold, A. Melchiorri, J.-B. Melin, L. Mendes, E. Menegoni, A. Mennella, M. Migliaccio, M. Millea, S. Mitra, M.-A. Miville-Deschênes, A. Moneti, L. Montier, G. Morgante, D. Mortlock, A. Moss, D. Munshi, J. A. Murphy, P. Naselsky, F. Nati, P. Natoli, C. B. Netterfield, H. U. Nørgaard-Nielsen, F. Noviello, D. Novikov, I. Novikov, I. J. O'Dwyer, S. Osborne, C. A. Oxborrow, F. Paci, L. Pagano, F. Pajot, R. Paladini, D. Paoletti, B. Partridge, F. Pasian, G. Patanchon, D. Pearson, T. J. Pearson, H. V. Peiris, O. Perdereau, L. Perotto, F. Perrotta, V. Pettorino, F. Piacentini, M. Piat, E. Pierpaoli, D. Pietrobon, S. Plaszczynski, P. Platania, E. Pointecouteau, G. Polenta, N. Ponthieu, L. Popa, T. Poutanen, G. W. Pratt, G. Prézeau, S. Prunet, J.-L. Puget, J. P. Rachen, W. T. Reach, R. Rebolo, M. Reinecke, M. Remazeilles, C. Renault, S. Ricciardi, T. Riller, I. Ristorcelli, G. Rocha, C. Rosset, G. Roudier, M. Rowan-Robinson, J. A. Rubiño-Martín, B. Rusholme, M. Sandri, D. Santos, M. Savelainen, G. Savini, D. Scott, M. D. Seiffert, E. P. S. Shellard, L. D. Spencer, J.-L. Starck, V. Stolyarov, R. Stompor, R. Sudiwala, R. Sunyaev, F. Sureau, D. Sutton, A.-S. Suur-Uski, J.-F. Sygnet, J. A. Tauber, D. Tavagnacco, L. Terenzi, L. Toffolatti, M. Tomasi, M. Tristram, M. Tucci, J. Tuovinen,

M. Türler, G. Umana, L. Valenziano, J. Valiviita, B. Van Tent, P. Vielva, F. Villa, N. Vittorio, L. A. Wade, B. D. Wandelt, I. K. Wehus, M. White, S. D. M. White, A. Wilkinson, D. Yvon, A. Zacchei, and A. Zonca, "Planck 2013 results. XVI. cosmological parameters," *A & A*, vol. 571, p. A16, 2014.

[2] G. Hinshaw, D. Larson, E. Komatsu, D. N. Spergel, C. L. Bennett, J. Dunkley, M. R. Nolta, M. Halpern, R. S. Hill, N. Odegard, L. Page, K. M. Smith, J. L. Weiland, B. Gold, N. Jarosik, A. Kogut, M. Limon, S. S. Meyer, G. S. Tucker, E. Wollack, and E. L. Wright, "Nine-year wilkinson microwave anisotropy probe (WMAP) observations: Cosmological parameter results," *The Astrophysical Journal Supplement Series*, vol. 208, no. 2, p. 19, 2013.

[3] S. Yamamoto, *Introduction to Astrochemistry. Chemical Evolution from Interstellar Clouds to Star and Planet Formation*. 7, Springer Japan, 1 ed., 2017.

[4] M. Asplund, N. Grevesse, A. J. Sauval, and P. Scott, "The Chemical Composition of the Sun," *Annual Review of Astronomy and Astrophysics*, vol. 47, pp. 481–522, 2009.

[5] A. Shaw, *Astrochemistry: From Astronomy to Astrobiology*. Wiley, 2007.

[6] T. Snow and V. Bierbaum, "Ion chemistry in the interstellar medium," *Annual Review of Analytical Chemistry*, vol. 1, pp. 229–259, 2008.

[7] S. G. Lias, "Ionization energy evaluation," in *NIST Chemistry WebBook, NIST Standard Reference Database Number 69* (P. J. Linstrom and W. G. Mallard, eds.), Gaithersburg MD: National Institute of Standards and Technology, 2017.

[8] "ESO-European Southern Observatory," 2017. http://www.eso.org/public/about-eso/esoglance/.

[9] H. S. P. Müller, S. Thorwirth, D. A. Roth, and G. Winnewisser, "The cologne database for molecular spectroscopy, CDMS," *A & A*, vol. 370, no. 3, pp. L49–L52, 2001.

[10] H. S. P. Müller, F. Schlöder, J. Stutzki, and G. Winnewisser, "The cologne database for molecular spectroscopy, CDMS: a useful tool for astronomers and spectroscopists," *Journal of Molecular Structure*, vol. 742, no. 1, pp. 215 – 227, 2005.

[11] H. S. P. Müller, "The cologne database for molecular spectroscopy (CDMS) catalog," 2017. http://www.astro.uni-koeln.de/cdms/catalog.

[12] E. Herbst and E. F. van Dishoeck, "Complex organic interstellar molecules," *Annual Review of Astronomy and Astrophysics*, vol. 47, no. 1, pp. 427–480, 2009.

[13] C. Vastel, C. Ceccarelli, B. Lefloch, and R. Bachiller, "The origin of complex organic molecules in prestellar cores," *The Astrophysical Journal Letters*, vol. 795, no. 1, p. L2, 2014.

[14] E. Gibb, A. Nummelin, W. M. Irvine, D. C. B. Whittet, and P. Bergman, "Chemistry of the organic-rich hot core G327.3-0.6," *The Astrophysical Journal*, vol. 545, no. 1, p. 309, 2000.

[15] M. Ikeda, M. Ohishi, A. Nummelin, J. E. Dickens, P. Bergman, A. Hjalmarson, and W. M. Irvine, "Survey observations of c$-C_2H_4O$ and CH_3CHO toward massive star-forming regions," *The Astrophysical Journal*, vol. 560, no. 2, p. 792, 2001.

[16] S. E. Bisschop, J. K. Jørgensen, E. F. van Dishoeck, and E. B. M. de Wachter, "Testing grain-surface chemistry in massive hot-core regions," *A & A*, vol. 465, no. 3, pp. 913–929, 2007.

[17] S. Cazaux, A. G. G. M. Tielens, C. Ceccarelli, A. Castets, V. Wakelam, E. Caux, B. Parise, and D. Teyssier, "The hot core around the low-mass protostar IRAS 16293–2422: Scoundrels rule!," *The Astrophysical Journal Letters*, vol. 593, no. 1, p. L51, 2003.

[18] S. Bottinelli, C. Ceccarelli, B. Lefloch, J. P. Williams, A. Castets, E. Caux, S. Cazaux, S. Maret, B. Parise, and A. G. G. M. Tielens, "Complex molecules in the hot core of the low-mass protostar NGC 1333 IRAS 4A," *The Astrophysical Journal*, vol. 615, no. 1, p. 354, 2004.

[19] M. A. Requena-Torres, J. Martín-Pintado, S. Martín, and M. R. Morris, "The galactic center: The largest oxygen-bearing organic molecule repository," *The Astrophysical Journal*, vol. 672, no. 1, p. 352, 2008.

[20] M. A. Requena-Torres, J. Martín-Pintado, A. Rodríguez-Franco, S. Martín, N. J. Rodríguez-Fernández, and P. de Vicente, "Organic molecules in the galactic center - hot core chemistry without hot cores," *A & A*, vol. 455, no. 3, pp. 971–985, 2006.

[21] K. I. Öberg, S. Bottinelli, J. K. Jorgensen, and E. F. van Dishoeck, "A cold complex chemistry toward the low-mass protostar B1-b: Evidence for complex molecule production in ices," *The Astrophysical Journal*, vol. 716, no. 1, p. 825, 2010.

[22] J. Cernicharo, N. Marcelino, E. Roueff, M. Gerin, A. Jiménez-Escobar, and G. M. M. Caro, "Discovery of the methoxy radical, CH_3O, toward B1: Dust grain and gas-phase chemistry in cold dark clouds," *The Astrophysical Journal Letters*, vol. 759, no. 2, p. L43, 2012.

[23] A. Bacmann, V. Taquet, A. Faure, C. Kahane, and C. Ceccarelli, "Detection of complex organic molecules in a prestellar core: a new challenge for astrochemical models," *A & A*, vol. 541, p. L12, 2012.

[24] A. A. Jaber, C. Ceccarelli, C. Kahane, and E. Caux, "The census of complex organic molecules in the solar-type protostar IRAS16293-2422," *The Astrophysical Journal*, vol. 791, no. 1, p. 29, 2014.

[25] T. Millar, E. Herbst, and S. Charnely, "The formation of oxygen-containing organic-molecules in the orion compact ridge," *Astrophysical Journal*, vol. 369, no. 1, pp. 147–156, 1991.

[26] S. B. Charnley, A. G. G. M. Tielens, and T. J. Millar, "On the molecular complexity of the hot cores in Orion A - Grain surface chemistry as 'The last refuge of the scoundrel'," *Astrophysical Journal*, vol. 399, pp. L71–L74, 1992.

[27] P. Caselli, T. I. Hasegawa, and E. Herbst, "Chemical differentiation between star-forming regions - The Orion Hot Core and Compact Ridge," *Astrophysical Journal*, vol. 408, pp. 548–558, 1993.

[28] R. T. Garrod and E. Herbst, "Formation of methyl formate and other organic species in the warm-up phase of hot molecular cores," *A & A*, vol. 457, no. 3, pp. 927–936, 2006.

[29] N. Balucani, C. Ceccarelli, and V. Taquet, "Formation of complex organic molecules in cold objects: the role of gas-phase reactions," *Monthly Notices of the Royal Astronomical Society*, vol. 449, pp. L16–L20, 2015.

[30] R. Johnsen, A. Chen, and M. A. Biondi, "Dissociative charge transfer of He^+ ions with H_2 and D_2 molecules from 78 to 330 K," *The Journal of Chemical Physics*, vol. 72, no. 5, pp. 3085–3088, 1980.

[31] H. Böhringer and F. Arnold, "Measurements of ion-molecule reaction rate coefficients with an ion drift-tube method at temperatures from 18 to 420 K," in *Molecular Astrophysics: State of the Art and Future Directions* (G. H. F. Diercksen, W. F. Huebner, and P. W. Langhoff, eds.), pp. 639–647, Dordrecht: Springer Netherlands, 1985.

[32] M. M. Schauer, S. R. Jefferts, S. E. Barlow, and G. H. Dunn, "Reactions of H_2 with He^+ at temperatures below 40 K," *The Journal of Chemical Physics*, vol. 91, no. 8, pp. 4593–4596, 1989.

[33] B. R. Rowe, J. B. Marquette, and G. Dupeyrat, "Measurements of ion-molecule reaction rate coefficients between 8 and 160 K by the CRESU technique," in *Molecular Astrophysics: State of the Art and Future Directions* (G. H. F. Diercksen, W. F. Huebner, and P. W. Langhoff, eds.), pp. 631–638, Dordrecht: Springer Netherlands, 1985.

[34] T. B. McMahon and J. L. Beauchamp, "A versatile trapped ion cell for ion cyclotron resonance spectroscopy," *Review of Scientific Instruments*, vol. 43, no. 3, pp. 509–512, 1972.

[35] W. T. Huntress Jr. and R. F. Pinizzotto Jr., "Product distributions and rate constants for ion-molecule reactions in water, hydrogen sulfide, ammonia, and methane," *The Journal of Chemical Physics*, vol. 59, no. 9, pp. 4742–4756, 1973.

[36] I. Smith, S. Faber, and E. VanDishoeck, "Laboratory astrochemistry: Gas-phase processes," *Annual Review of Astronomy and Astrophysics*, vol. 49, pp. 29–66, 2011.

[37] S. E. Barlow, G. H. Dunn, and M. Schauer, "Radiative association of CH_3^+ and H_2 at 13 K," *Phys. Rev. Lett.*, vol. 52, pp. 902–905, 1984.

[38] S. E. Barlow, J. A. Luine, and G. H. Dunn, "Measurement of ion-molecule reactions between 10 and 20 K," *International Journal of Mass Spectrometry and Ion Processes*, vol. 74, no. 1, pp. 97 – 128, 1986.

[39] G. H. Dunn, "Ion-electron and ion-neutral collisions in ion traps," *Physica Scripta*, vol. 1995, no. T59, p. 249, 1995.

[40] D. Gerlich and S. Horning, "Experimental investigation of radiative association processes as related to interstellar chemistry," *Chemical Reviews*, vol. 92, no. 7, pp. 1509–1539, 1992.

[41] D. Gerlich, "Ion-neutral collisions in a 22-pole trap at very low energies," *Physica Scripta*, vol. 1995, no. T59, p. 256, 1995.

[42] D. Gerlich, "The study of cold collision using ion guides and traps," in *Low Temperatures and Cold Molecules* (I. Smith, ed.), pp. 121–174, London: Imperial College Press, 2008.

[43] R. Wester, "Radiofrequency multipole traps: tools for spectroscopy and dynamics of cold molecular ions," *Journal of Physics B: Atomic, Molecular and Optical Physics*, vol. 42, no. 15, p. 154001, 2009.

[44] E. E. Ferguson, F. C. Fehsenfeld, and A. L. Schmeltekopf, "Flowing afterglow measurements of ion-neutral reactions," in *Advances in Atomic and Molecular Physics* (D. Bates and I. Estermann, eds.), vol. 5, pp. 1 – 56, Academic Press, 1969.

[45] F. C. Fehsenfeld, A. L. Schmeltekopf, P. D. Goldan, H. I. Schiff, and E. E. Ferguson, "Thermal energy ion—neutral reaction rates. I. some reactions of helium ions," *The Journal of Chemical Physics*, vol. 44, no. 11, pp. 4087–4094, 1966.

[46] D. B. Dunkin, F. C. Fehsenfeld, A. L. Schmeltekopf, and E. E. Ferguson, "Ion–molecule reaction studies from 300 to 600 K in a temperature-controlled flowing afterglow system," *The Journal of Chemical Physics*, vol. 49, no. 3, pp. 1365–1371, 1968.

[47] N. Adams and D. Smith, "The selected ion flow tube (SIFT); a technique for studying ion-neutral reactions," *International Journal of Mass Spectrometry and Ion Physics*, vol. 21, no. 3, pp. 349 – 359, 1976.

[48] N. G. Adams and D. Smith, "Product-ion distributions for some ion-molecule reactions," *Journal of Physics B: Atomic and Molecular Physics*, vol. 9, no. 8, p. 1439, 1976.

[49] A. A. Viggiano, R. A. Morris, F. Dale, J. F. Paulson, K. Giles, D. Smith, and T. Su, "Kinetic energy, temperature, and derived rotational temperature dependences for the reactions of $Kr^+(^2P_{3/2})$ and Ar^+ with HCl," *The Journal of Chemical Physics*, vol. 93, no. 2, pp. 1149–1157, 1990.

[50] J. C. Poutsma, A. J. Midey, and A. A. Viggiano, "Absolute rate coefficients for the reactions of O_2^- + N ($^4S_{3/2}$) and O_2^- + O (^3P) at 298 K in a selected-ion flow tube instrument," *The Journal of Chemical Physics*, vol. 124, no. 7, p. 074301, 2006.

[51] B. R. Rowe, G. Dupeyrat, J. B. Marquette, and P. Gaucherel, "Study of the reactions $N_2^+ + 2\,N_2 \longrightarrow N_4^+ + N_2$ and $O_2^+ + 2\,O_2 \longrightarrow O_4^+ + O_2$ from 20 to 160 K by the CRESU technique," *The Journal of Chemical Physics*, vol. 80, no. 10, pp. 4915–4921, 1984.

[52] G. Dupeyrat, J. B. Marquette, and B. R. Rowe, "Design and testing of axis-ymmetric nozzles for ion-molecule reaction studies between 20 K and 160 K," *The Physics of Fluids*, vol. 28, no. 5, pp. 1273–1279, 1985.

[53] B. Rowe and J. Marquette, "CRESU studies of ion-molecule reactions," *International Journal of Mass Spectrometry and Ion Processes*, vol. 80, pp. 239 – 254, 1987.

[54] P. Gaucherel, J. Marquette, C. Rebrion, G. Poissant, G. Dupeurat, and B. Rowe, "Temperature dependence of slow charge-exchange reactions: $N_2^+ + O_2$ from 8 to 163 K," *Chemical Physics Letters*, vol. 132, no. 1, pp. 63 – 66, 1986.

[55] B. R. Rowe, J. B. Marquette, G. Dupeyrat, and E. E. Ferguson, "Reactions of He^+ and N^+ ions with several molecules at 8 K," *Chemical Physics Letters*, vol. 113, no. 4, pp. 403 – 406, 1985.

[56] C. Rebrion, B. R. Rowe, and J. B. Marquette, "Reactions of Ar^+ with H_2, N_2, O_2, and co at 20, 30, and 70 K," *The Journal of Chemical Physics*, vol. 91, no. 10, pp. 6142–6147, 1989.

[57] A. Canosa, F. Goulay, I. Sims, and B. Rowe, "Gas phase reactive collision at very low temperature: Recent experimental advances and perspectives," in *Low Temperatures and Cold Molecules* (I. Smith, ed.), pp. 55–120, London: Imperial College Press, 2008.

[58] K. M. Ervin and P. B. Armentrout, "Translational energy-dependence of $Ar^+ + XY \longrightarrow ArX^+ + Y$ (XY=H_2, D_2, HD) from thermal to 30 eV CM," *Journal of Chemical Physics*, vol. 83, no. 1, pp. 166–189, 1985.

[59] P. B. Armentrout, "Kinetic energy dependence of ion-molecule reactions: Guided ion beams and threshold measurements," *International Journal of Mass Spectrometry*, vol. 200, no. 1-3, pp. 219–241, 2000.

[60] P. B. Armentrout, "Mass spectrometry - not just a structural tool: The use of guided ion beam tandem mass spectrometry to determine thermochemistry," *Journal of the American Society For Mass Spectrometry*, vol. 13, no. 5, pp. 419–434, 2002.

[61] P. B. Armentrout, "Fundamentals of ion-molecule chemistry," *Journal of Analytical Atomic Spectrometry*, vol. 19, no. 5, pp. 571–580, 2004.

[62] D. Gerlich, "Inhomogeneous RF-fields - a versatile tool for the study of processes with slow ions," *Advances in Chemical Physics*, vol. 82, pp. 1–176, 1992.

[63] C.-Y. Ng, "State-selected and state-to-state ion-molecule reaction dynamics," *The Journal of Physical Chemistry A*, vol. 106, no. 25, pp. 5953–5966, 2002.

[64] D. Ascenzi, N. Cont, G. Guella, P. Franceschi, and P. Tosi, "New insights into the reaction mechanisms of phenylium ions with benzene," *Journal of Physical Chemistry A*, vol. 111, no. 49, pp. 12513–12523, 2007.

[65] P. Franceschi, L. Penasa, D. Ascenzi, D. Bassi, M. Scotoni, and P. Tosi, "A simple and cost-effective high voltage radio frequency driver for multipolar ion guides," *International Journal of Mass Spectrometry*, vol. 265, no. 2-3, pp. 224–229, 2007.

[66] M. Instrument, "Spinning rotor vacuum gauge," *Instruction Manual*, 2004.

[67] D. Skoog, D. West, F. Holler, and S. Crouch, *Fundamentals of Analytical Chemistry*. Belmont, USA: Mary Finch, 2013.

[68] L. Landau and E. Lifshitz, *Quantum Mechanics*. Oxford: Pergamon Press, 1965.

[69] M. Brouard and C. Vallance, *Tutorials in Molecular Reactions Dynamics*. Cambridge: RSCPublishing, 2010.

[70] P. Langevin, "Une formule fondamentale de théorie cinétique," *Annales de Chimie et de Physique*, vol. 5, 1905.

[71] G. Gioumousis and D. P. Stevenson, "Reactions of gaseous molecule ions with gaseous molecules. V. Theory," *The Journal of Chemical Physics*, vol. 29, no. 2, pp. 294–299, 1958.

[72] L. P. Theard and W. H. Hamill, "The energy dependence of cross sections of some ion-molecule reactions," *Journal of the American Chemical Society*, vol. 84, no. 7, pp. 1134–1139, 1962.

[73] T. F. Moran and W. H. Hamill, "Cross sections of ion-permanent-dipole reactions by mass spectrometry," *The Journal of Chemical Physics*, vol. 39, no. 6, pp. 1413–1422, 1963.

[74] S. K. Gupta, E. G. Jones, A. G. Harrison, and J. J. Myher, "Reactions of thermal energy ions. VI. hydrogen-transfer ion–molecule reactions involving polar molecules," *Canadian Journal of Chemistry*, vol. 45, no. 24, pp. 3107–3117, 1967.

[75] T. Su and M. T. Bowers, "Theory of ion-polar molecule collisions. Comparison with experimental charge transfer reactions of rare gas ions to geometric isomers of difluorobenzene and dichloroethylene," *The Journal of Chemical Physics*, vol. 58, no. 7, pp. 3027–3037, 1973.

[76] T. Su and W. J. Chesnavich, "Parametrization of the ion–polar molecule collision rate constant by trajectory calculations," *The Journal of Chemical Physics*, vol. 76, no. 10, pp. 5183–5185, 1982.

[77] V. Wakelam, E. Herbst, J. Loison, I. Smith, V. Chandrasekaran, B. Pavone, N. Adams, M. Bacchus-Montabonel, A. Bergeat, K. Beroff, V. Bierbaum, M. Chabot, A. Dalgarno, E. van Dishoeck, A. Faure, W. Geppert, D. Gerlich, D. Galli, E. Hebrard, F. Hersant, K. Hickson, P. Honvault, S. Klippenstein, S. Le Picard, G. Nyman, P. Pernot, S. Schlemmer, F. Selsis, I. Sims, D. Talbi, J. Tennyson, J. Troe, R. Wester, and L. Wiesenfeld, "A kinetic database for astrochemistry (KIDA)," *Astrophysical Journal Supplement Series*, vol. 199, no. 1, pp. 21–30, 2012.

[78] D. P. Ridge, "Capture collision theory," in *Structure/Reactivity and Thermochemistry of Ions* (P. Ausloos and S. G. Lias, eds.), pp. 1–13, Dordrecht: Springer Netherlands, 1987.

[79] R. Levine, *Molecular Reaction Dynamics*. Cambridge University Press, 2009.

[80] K. R. Naqvi, "On the non-crossing rule for potential energy surfaces of polyatomic molecules," *Chemical Physics Letters*, vol. 15, no. 4, pp. 634 – 636, 1972.

[81] L. D. Landau, "To the theory of energy transmission in collisions," *Physikalische Zeitschrift der Sowjetunion*, vol. 2, pp. 46–54, 1932.

[82] E. C. G. Stueckelberg, "Theory of inelastic collisions between atoms (theory of inelastic collisions between atoms, using two simultaneous differential equations)," *Helvetica Physica Acta*, vol. 5, pp. 369–422, 1932.

[83] E. E. Nikitin, "Non-adiabatic transitions : What we learned from old masters and how much we owe them," *Annual Review of Physical Chemistry*, vol. 50, no. 1, pp. 1–21, 1999.

[84] E. E. Nikitin and S. Y. Umanskii, *Theory of slow Atomic Collisions*, vol. 30 of *Springer Series in Chemical Physics*. Berlin-Heidelberg-New York-Tokyo: Springer-Verlag, 1984.

[85] R. P. Smith and E. M. Mortensen, "Bond and molecular polarizability tensors. i. mathematical treatment of bond tensor additivity," *The Journal of Chemical Physics*, vol. 32, no. 2, pp. 502–507, 1960.

[86] F. Pirani, D. Cappelletti, and G. Liuti, "Range, strength and anisotropy of intermolecular forces in atom–molecule systems: an atom–bond pairwise additivity approach," *Chemical Physics Letters*, vol. 350, no. 3–4, pp. 286 – 296, 2001.

[87] J. C. Slater and J. G. Kirkwood, "The Van Der Waals forces in gases," *Phys. Rev.*, vol. 37, pp. 682–697, 1931.

[88] K. S. Pitzer, "Inter- and intramolecular forces and molecular polarizability," in *Advances in Chemical Physics*, pp. 59–83, John Wiley and Sons, Inc., 2007.

[89] A. D. Koutselos and E. A. Mason, "Correlation and prediction of dispersion coefficients for isoelectronic systems," *The Journal of Chemical Physics*, vol. 85, no. 4, pp. 2154–2160, 1986.

[90] R. Cambi, D. Cappelletti, G. Liuti, and F. Pirani, "Generalized correlations in terms of polarizability for van der waals interaction potential parameter calculations," *The Journal of Chemical Physics*, vol. 95, no. 3, pp. 1852–1861, 1991.

[91] F. Pirani, M. Alberti, A. Castro, M. Teixidor, and D. Cappelletti, "Atom-bond pairwise additive representation for intermolecular potential energy surfaces," *Chemical Physics Letters*, vol. 394, no. 1-3, pp. 37–44, 2004.

[92] G. Maitland and E. Smith, "A simplified representation of intermolecular potential energy," *Chemical Physics Letters*, vol. 22, no. 3, pp. 443 – 446, 1973.

[93] F. Pirani, S. Brizi, L. Roncaratti, P. Casavecchia, D. Cappelletti, and F. Vecchiocattivi, "Beyond the Lennard-Jones model: a simple and accurate potential function probed by high resolution scattering data useful for molecular dynamics simulations," *Physical Chemistry Chemical Physics*, vol. 10, no. 36, pp. 5489–5503, 2008.

[94] G. Liuti and F. Pirani, "Regularities in van der Waals forces: correlation between the potential parameters and polarizability," *Chemical Physics Letters*, vol. 122, no. 3, pp. 245 – 250, 1985.

[95] V. Aquilanti, G. Liuti, F. Pirani, and F. VecchiocattiviI, "Orientational and spin-orbital dependence of interatomic forces," *Journal of the Chemical Society-Faraday Transactions*, vol. 85, pp. 955–964, 1989.

[96] D. Cappelletti, G. Liuti, and F. Pirani, "Generalization to ion neutral systems of the polarizability correlations for interaction potential parameters," *Chemical Physics Letters*, vol. 183, no. 3-4, pp. 297–303, 1991.

[97] V. Aquilanti, D. Cappelletti, and F. Pirani, "Range and strength of interatomic forces: Dispersion and induction contributions to the bonds of dications and of ionic molecules," *Chemical Physics*, vol. 209, no. 2-3, pp. 299–311, 1996.

[98] R. S. Mulliken, "Electronic population analysis on lcao–mo molecular wave functions. I," *The Journal of Chemical Physics*, vol. 23, no. 10, pp. 1833–1840, 1955.

[99] R. S. Mulliken, "Electronic population analysis on LCAO–MO molecular wave functions. II. Overlap populations, bond orders, and covalent bond energies," *The Journal of Chemical Physics*, vol. 23, no. 10, pp. 1841–1846, 1955.

[100] R. Mulliken and W. Ermler, *Diatomic molecules: results of ab initio calculations*. Academic Press, 1977.

[101] J. B. Collins and A. Streitwieser, "Integrated spatial electron populations in molecules: Application to simple molecules," *Journal of Computational Chemistry*, vol. 1, no. 1, pp. 81–87, 1980.

[102] F. Weinhold and J. E. Carpenter, *The Natural Bond Orbital Lewis Structure Concept for Molecules, Radicals, and Radical Ions*. The Structure of Small Molecules and Ions, Boston, MA: Springer US, 1988.

[103] A. E. Reed, L. A. Curtiss, and F. Weinhold, "Intermolecular interactions from a natural bond orbital, donor-acceptor viewpoint," *Chemical Reviews*, vol. 88, no. 6, pp. 899–926, 1988.

[104] J. Carpenter and F. Weinhold, "Analysis of the geometry of the hydroxymethyl radical by the different hybrids for different spins natural bond orbital procedure," *Journal of Molecular Structure-Theochem*, vol. 46, pp. 41–62, 1988.

[105] A. Reed, R. Weinstock, and F. Weinhold, "Natural-population analysis," *Journal of Chemical Physics*, vol. 83, no. 2, pp. 735–746, 1985.

[106] A. Reed and F. Weinhold, "Natural localized molecular-orbitals," *Journal of Chemical Physics*, vol. 83, no. 4, pp. 1736–1740, 1985.

[107] A. Reed and F. Weinhold, "Natural bond orbital analysis of near-Hartree-Fock water dimer," *Journal of Chemical Physics*, vol. 78, no. 6, pp. 4066–4073, 1983.

[108] J. Foster and F. Weinhold, "Natural hybrid orbitals," *Journal of the American Chemical Society*, vol. 102, no. 24, pp. 7211–7218, 1980.

[109] E. D. Glendening, C. R. Landis, and F. Weinhold, "Natural bond orbital methods," *Wiley Interdisciplinary Reviews: Computational Molecular Science*, vol. 2, no. 1, pp. 1–42, 2012.

[110] P.-O. Löwdin, "Quantum theory of many-particle systems. i. physical interpretations by means of density matrices, natural spin-orbitals, and convergence problems in the method of configurational interaction," *Phys. Rev.*, vol. 97, pp. 1474–1489, Mar 1955.

[111] M. J. Frisch, G. W. Trucks, H. B. Schlegel, G. E. Scuseria, M. A. Robb, J. R. Cheeseman, G. Scalmani, V. Barone, G. A. Petersson, H. Nakatsuji, X. Li, M. Caricato, A. V. Marenich, J. Bloino, B. G. Janesko, R. Gomperts, B. Mennucci, H. P. Hratchian, J. V. Ortiz, A. F. Izmaylov, J. L. Sonnenberg, D. Williams-Young, F. Ding, F. Lipparini, F. Egidi, J. Goings, B. Peng, A. Petrone, T. Henderson, D. Ranasinghe, V. G. Zakrzewski, J. Gao, N. Rega, G. Zheng, W. Liang, M. Hada, M. Ehara, K. Toyota, R. Fukuda, J. Hasegawa, M. Ishida, T. Nakajima, Y. Honda, O. Kitao, H. Nakai, T. Vreven, K. Throssell, J. A. Montgomery, Jr., J. E. Peralta, F. Ogliaro, M. J. Bearpark, J. J. Heyd, E. N. Brothers, K. N. Kudin, V. N. Staroverov, T. A. Keith, R. Kobayashi, J. Normand, K. Raghavachari, A. P. Rendell, J. C. Burant, S. S. Iyengar, J. Tomasi, M. Cossi, J. M. Millam, M. Klene, C. Adamo, R. Cammi, J. W. Ochterski, R. L. Martin, K. Morokuma, O. Farkas, J. B. Foresman, and D. J. Fox, "Gaussian 16 Revision A.03," 2016. Gaussian Inc. Wallingford CT.

[112] S. D. Tanner, G. I. Mackay, A. C. Hopkinson, and A. C. Bohme, "Proton transfer reactions of HCO^+ at 298 K," *International Journal of Mass Spectrometry and Ion Processes*, vol. 29, pp. 153–169, 1979.

[113] M. Kumakura and T. Sugiura, "Thermal ion-molecule reactions in oxygen-containing molecules. condensation-elimination reactions in dimethyl ether-trioxane mixtures," *Zeitschrift für Naturforschung*, vol. 32a, pp. 1533–1540, 1977.

[114] P. Wilson, M. McEwan, and M. Meotner, "Reactions of $CH_3OCH_2^+$ with nitrogen bases - a mechanism for the formation of protonated imines," *International Journal of Mass Spectrometry and Ion Processes*, vol. 132, no. 1-2, pp. 149–152, 1994.

[115] "NIST chemistry webbook, NIST standard reference database," 2015.

[116] J. Butler, D. Holland, A. Parr, and R. Stockbauer, "A threshold photoelectron photoion coincidence spectrometric study of dimethyl ether (CH_3OCH_3)," *International Journal of Mass Spectrometry and Ion Processes*, vol. 58, pp. 1–14, 1984.

[117] T. Nishimura, Q. Zha, P. R. Das, Y. Niwa, and G. G. Meisels, "On the dissociation dynamics of energy-selected dimethylether ions," *International Journal of Mass Spectrometry and Ion Processes*, vol. 113, no. 3, pp. 177 – 189, 1992.

[118] J. Holmes, C. Aubry, and P. Mayer, *Assigning Structures to Ions in Mass Spectrometry*. CRC Press, 2006.

[119] J. D. Dill, C. L. Fisher, and F. W. McLafferty, "Collisional activation and theoretical studies of gaseous COH_3^+ ions," *Journal of the American Chemical Society*, vol. 101, no. 22, pp. 6531–6534, 1979.

[120] P. Burgers and J. Holmes, "The generation of triplet methoxy cations," *Organic Mass Spectrometry*, vol. 19, no. 9, pp. 452–456, 1984.

[121] M. Aschi, J. Harvey, C. Schalley, D. Schroder, and H. Schwarz, "Reappraisal of the spin-forbidden unimolecular decay of the methoxy cation," *Chemical Communications*, no. 5, pp. 531–532, 1998.

[122] P. Burgers, J. Holmes, A. Mommers, J. Szulejko, and J. Terlouw, "Collisionally induced dissociative ionization of neutral products from unimolecular ion fragmentations .1. neutral product structures," *Organic Mass Spectrometry*, vol. 19, no. 9, pp. 442–447, 1984.

[123] J. N. Harvey and M. Aschi, "Spin-forbidden dehydrogenation of methoxy cation: a statistical view," *Phys. Chem. Chem. Phys.*, vol. 1, pp. 5555–5563, 1999.

[124] W. Brown, B. Iverson, E. Anslyn, and C. Foote, *Organic Chemistry*. Cengage Learning, 2013.

[125] T. Schindler, C. Berg, G. Niednerschatteburg, V. Bondybey, C. Lugez, A. Schriver, and L. Schriver, "FT-ICR studies of the reaction of O^+ with methanol," *Journal of Physical Chemistry*, vol. 98, no. 16, pp. 4316–4319, 1994.

[126] V. Anicich, "Evaluated bimolecular ion-molecule gas-phase kinetics of positive-ions for use in modeling planetary-atmospheres, cometary comae, and interstellar clouds," *Journal of Physical and Chemical Reference Data*, vol. 22, no. 6, pp. 1469–1569, 1993.

[127] N. G. Adams, D. Smith, and D. Grief, "Reactions of $HnCO^+$ ions with molecules at 300 K," *International Journal of Mass Spectrometry and Ion Processes*, vol. 26, pp. 405–415, 1978.

[128] G. I. Mackay, A. C. Hopkinson, and D. K. Bohme, "Acid catalysis in the gas phase: dissociative proton transfer to formic and acetic acid," *Journal of the American Chemical Society*, vol. 100, no. 24, pp. 7460–7464, 1978.

[129] C. G. Freeman, P. W. Harland, and M. J. McEwan, "Ion-molecule reactions of formic acid. I. proton-transfer reactions," *Australian Journal of Chemistry*, vol. 31, no. 10, pp. 2157–2160, 1978.

[130] B. Ruscic, "Active Thermochemical Tables (ATcT) values based on ver. 1.118 of the Thermochemical Network," 2015.

[131] D. M. Jackson, N. J. Stibrich, J. L. McLain, L. D. Fondren, N. G. Adams, and L. M. Babcock, "A selected ion flow tube study of the reactions of various nitrogen containing ions with formic acid, acetic acid, and methyl formate," *International Journal of Mass Spectrometry*, vol. 247, no. 1, pp. 55 – 60, 2005.

[132] F. Fantuzzi, S. Pilling, A. C. F. Santos, L. Baptista, A. B. Rocha, and H. M. Boechat-Roberty, "Photodissociation of methyl formate in circumstellar environment: stability under soft X-rays," *Monthly Notices of the Royal Astronomical Society*, vol. 417, no. 4, p. 2631, 2011.

[133] T. Nishimura, Q. Zha, and G. G. Meisels, "Unimolecular dissociation of energy-selected methyl formate ion," *The Journal of Chemical Physics*, vol. 87, no. 8, pp. 4589–4597, 1987.

[134] N. Heinrich, T. Drewello, P. C. Burgers, J. C. Morrow, J. Schmidt, W. Kulik, J. K. Terlouw, and H. Schwarz, "Unimolecular chemistry of methyl formate cation radical. a combined theoretical and experimental study," *Journal of the American Chemical Society*, vol. 114, no. 10, pp. 3776–3783, 1992.

[135] "NIST Computational Chemistry Comparison and Benchmark Database (CCCBDB), NIST Standard Reference Database," 2016.

[136] Y. Niide and M. Hayashi, "Reinvestigation of microwave spectrum of dimethyl ether and rs structures of analogous molecules," *Journal of Molecular Spectroscopy*, vol. 220, no. 1, pp. 65 – 79, 2003.

[137] B. Friedrich and D. Herschbach, "Spatial orientation of molecules in strong electric-fields and evidence for pendular states," *Nature*, vol. 353, no. 6343, pp. 412–414, 1991.

[138] B. Friedrich, D. Pullman, and D. Herschbach, "Alignment and orientation of rotationally cool molecules," *Journal of Physical Chemistry*, vol. 95, no. 21, pp. 8118–8129, 1991.

[139] L. Roncaratti, D. Cappelletti, P. Candori, and F. Pirani, "Polar molecules engaged in pendular states captured by molecular-beam scattering experiments," *Physical Review A*, vol. 90, no. 1, pp. 012705– 012712, 2014.

[140] L. Roncaratti, D. Cappelletti, and F. Pirani, "The spontaneous synchronized dance of pairs of water molecules," *Journal of Chemical Physics*, vol. 140, no. 12, p. 124318, 2014.

[141] P. J. Linstrom and W. G. Mallard, "NIST Chemistry WebBook; NIST Standard Reference Database."

[142] Y. Miao, J. Li, J. Deng, and C. Ning, "High resolution (e, 2e) spectroscopy of dimethyl ether," *Journal of Electron Spectroscopy and Related Phenomena*, vol. 193, pp. 1–5, 2014.

[143] R. Candori, S. Cavalli, F. Pirani, A. Volpi, D. Cappelletti, P. Tosi, and D. Bassi, "Structure and charge transfer dynamics of the $(Ar-N_2)^+$ molecular cluster," *Journal of Chemical Physics*, vol. 115, no. 19, pp. 8888–8898, 2001.

[144] V. Aquilanti, R. Candori, F. Pirani, and C. Ottinger, "On the dynamics of the vibrationally selective electronic-energy transfer from metastable Xenon atoms to nitrogen molecules," *Chemical Physics*, vol. 187, no. 1-2, pp. 171–183, 1994.

[145] C. Melius and W. Goddard, "The theoretical description of an asymmetric, nonresonant charge transfer process; Li + $Na^+ \longrightarrow Li^+$ + Na the two-state approximation," *Chemical Physics Letter*, vol. 15, no. 4, pp. 524–529, 1972.

[146] W. L. McMillan, "Theory of one-electron molecules. I. Li_2^+," *Physical Review A*, vol. 4, no. 1, pp. 69–75, 1971.

[147] W. A. Melius, Carl F. Goddard, "Theoretical studies of nonresonant charge-transfer processes using a multistate molecular wave-function approach: Li + $Na^+ \longrightarrow Li^+$ + Na," *Physical Review Letters*, vol. 29, no. 15, pp. 975–983, 1972.

[148] V. Aquilanti, "A three-state description of excitation and charge transfer in Na^+ – Na collisions," *Zeitschrift für Physikalische Chemie Neue Folge*, vol. 90, pp. 1–7, 1974.

[149] E. A. Gislason and J. G. Sachs, "Multiple-crossing electron-jump model for reactions of metal atoms with diatomic halogen molecules," *The Journal of Chemical Physics*, vol. 62, no. 7, pp. 2678–2689, 1975.

[150] E. A. Gislason, G. Parlant, and M. Sizun, *The Semiclassical Time-Dependent Approach to Charge-Transfer Processes*, pp. 321–421. John Wiley and Sons, Inc., 2007.

[151] S. Falcinelli, M. Rosi, S. Cavalli, F. Pirani, and F. Vecchiocattivi, "Stereoselectivity in autoionization reactions of hydrogenated molecules by metastable noble gas atoms: The role of electronic couplings," *Chemistry – A European Journal*, vol. 22, no. 35, pp. 12518–12526, 2016.

[152] R. F. C. Jr., "Microwave spectrum, barrier to internal rotation, and structure of methyl formate," *The Journal of Chemical Physics*, vol. 30, no. 6, pp. 1529–1536, 1959.

[153] M. Senent, M. Villa, F. Melendez, and R. Dominguez-Gomez, "Ab initio study of the rotational-torsional spectrum of methyl formate," *Astrophysical Journal*, vol. 627, no. 1, pp. 567–576, 2005.

[154] Y. Nunes, G. Martins, N. Mason, D. Duflot, S. Hoffmann, J. Delwiche, M. Hubin-Franskin, and P. Limao-Vieira, "Electronic state spectroscopy of methyl formate probed by high resolution VUV photoabsorption, He(I) photoelectron spectroscopy and ab initio calculations," *Physical Chemistry Chemical Physics*, vol. 12, no. 48, pp. 15734–15743, 2010.

[155] K. H. Hellwege and A. M. Hellwege, "Structure data of free polyatomic molecules," in *Landolt-Bornste in Group II Atomic and Molecular Physics*, vol. 7, Berlin: Springer-Verlag, 1976.

[156] E. Waterstradt, R. Jung, T. Belling, and K. Muller-Dethlefs, "Zero kinetic energy (ZEKE) photoelectron spectrum and coincident mass spectra of methyl formate," *Berichte der Bunsengesellschaft fur physikalische Chemie*, vol. 98, no. 2, pp. 176–179, 1994.

[157] P. H. Cannington and N. S. Ham, "He(I)/He(II) photoelectron band intensity ratios for simple organic-molecules," *Journal of Electron Spectroscopy and Related Phenomena*, vol. 31, no. 2, pp. 175–179, 1983.

[158] P. Cannington and N. Ham, "He(II) photoelectron-spectra of esters," *Journal of Electron Spectroscopy and Related Phenomena*, vol. 36, no. 2, pp. 203–205, 1985.

[159] V. Wakelam, J.-C. Loison, E. Herbst, B. Pavone, A. Bergeat, K. Béroff, M. Chabot, A. Faure, D. Galli, W. D. Geppert, D. Gerlich, P. Gratier, N. Harada, K. M. Hickson, P. Honvault, S. J. Klippenstein, S. D. L. Picard, G. Nyman, M. Ruaud, S. Schlemmer, I. R. Sims, D. Talbi, J. Tennyson, and R. Wester, "The 2014 KIDA Network for Interstellar Chemistry," *The Astrophysical Journal Supplement Series*, vol. 217, no. 2, p. 20, 2015.

[160] E. Herbst, "OSU2009," 2009. http://faculty.virginia.edu/ericherb/research_files/osu_01_2009.

[161] A. Maergoiz, E. Nikitin, and J. Troe, "Capture of asymmetric top dipolar molecules by ions: Rate constants for capture of H_2O, HDO, D_2O by arbitrary ions," *International Journal of Mass Spectrometry*, vol. 280, no. 1–3, pp. 42 – 49, 2009.

[162] D. McElroy, C. Walsh, A. J. Markwick, M. A. Cordiner, K. Smith, and T. J. Millar, "The UMIST database for astrochemistry 2012," *A & A*, vol. 550, p. A36, 2013.

[163] "The UMIST Database for Astrochemistry."

[164] V. Wakelam, I. W. M. Smith, E. Herbst, J. Troe, W. Geppert, H. Linnartz, K. Öberg, E. Roueff, M. Agúndez, P. Pernot, H. M. Cuppen, J. C. Loison, and D. Talbi, "Reaction networks for interstellar chemical modelling: Improvements and challenges," *Space Science Reviews*, vol. 156, no. 1, pp. 13–72, 2010.

[165] N. Shuman, O. Martinez, S. Ard, J. Wiens, N. Keyes, H. Guo, and A. Viggiano, "Surprising behaviors in the temperature dependent kinetics of diatomic interhalogens with anions and cations," *Journal of Chemical Physics*, vol. 146, no. 21, 2017.

[166] A. Li, Y. Li, H. Guo, K. C. Lau, Y. Xu, B. Xiong, Y. C. Chang, and Y. C. Ng, "Communication: The origin of rotational enhancement effect for the reaction of $H_2O^+ + H_2$ (D_2)," *Journal of Chemical Physics*, vol. 140, pp. 011102–011111, 2014.

[167] P. Allmendinger, J. Deiglmayr, K. Höveler, O. Schullian, and F. Merkt, "Observation of enhanced rate coefficients in the $H_2^+ + H_2 \longrightarrow H_3^+ + H$ reaction at low collision energies," *The Journal of Chemical Physics*, vol. 145, no. 24, pp. 244–316, 2016.

[168] Z. Peeters, S. Rodgers, S. Charnley, L. Schriver-Mazzuoli, A. Schriver, J. Keane, and P. Ehrenfreund, "Astrochemistry of dimethyl ether," *Astronomy and Astrophysics*, vol. 445, no. 1, pp. 197–204, 2006.

[169] C. Favre, H. Wootten, A. Remijan, N. Brouillet, T. Wilson, D. Despois, and A. Baudry, "High-resolution expanded very large array image of dimethyl ether $(CH_3)_2O$ in Orion-KL," *Astrophysical Journal Letters*, vol. 739, no. 1, pp. L12–L16, 2011.

[170] D. Friedel and S. Weaver, "Complex organic molecules at high spatial resolution toward Orion-KL. II. Kinematics," *Astrophysical Journal Supplement Series*, vol. 201, no. 2, pp. 17–32, 2012.

[171] R. Choudhury, P. Schilke, G. Stephan, E. Bergin, T. Moller, A. Schmiedeke, and A. Zernickel, "Evolution of complex organic molecules in hot molecular cores synthetic spectra at (sub-)mm wavebands," *Astronomy and Astrophysics*, vol. 575, pp. A68–A87, 2015.

[172] G. A. Olah, T. Mathew, and G. K. S. Prakash, "Chemical formation of methanol and hydrocarbon ("organic") derivatives from CO_2 and H_2-carbon sources for subsequent biological cell evolution and life's origin," *Journal of the American Chemical Society*, vol. 139, no. 2, pp. 566–570, 2017.

[173] P. Tosi, D. Cappelletti, O. Dmitriev, S. Giordani, D. Bassi, D. Latimer, and M. Smith, "Dissochative charge-transfer of argon ions with methane molecules from ultralow to superthermal collision energies," *Journal of Physical Chemistry*, vol. 99, no. 42, pp. 15538–15543, 1995.

[174] P. Tosi, D. Bassi, B. Brunetti, and F. Vecchiocattivi, "Molecular processes in CH_4-H_2 plasmas dilueted with rare gases: reaction of X^* atoms and X^+ ions (X = Ne and Ar) with methane molecules," *International Journal of Mass Spectrometry*, vol. 149, pp. 345–353, 1995.

[175] V. G. Anicich, P. Wilson, and M. J. McEwan, "Termolecular ion-molecule reactions in titan's atmosphere. IV. A search made at up to 1 micron in pure hydrocarbons," *Journal of the American Society for Mass Spectrometry*, vol. 14, no. 8, pp. 900 – 915, 2003.

[176] V. G. Anicich, "Evaluated bimolecular ion-molecule gas phase kinetics of positive ions for use in modeling planetary atmospheres, cometary comae, and interstellar clouds," *Journal of Physical and Chemical Reference Data*, vol. 22, no. 6, pp. 1469–1569, 1993.

[177] N. G. Adams and D. Smith, "Reactions of CHn^+ ions with molecules at 300K.," *Chemical Physics Letters*, vol. 54, pp. 530–534, 1978.

[178] D. Smith and N. Adams, "Reaction of simple hydrocarbon ions with molecules at thermal energies," *International Journal of Mass Spectrometry and Ion Physics*, vol. 23, no. 2, pp. 123 – 135, 1977.

[179] W. T. Huntress and D. D. Elleman, "Ion cyclotron resonance study of the ion-molecule reactions in methane-ammonia mixtures," *Journal of the American Chemical Society*, vol. 92, no. 12, pp. 3565–3573, 1970.

[180] R. P. Clow and J. H. Futrell, "Ion-cyclotron resonance study of the kinetic energy dependence of ion-molecule reaction rates," *International Journal of Mass Spectrometry and Ion Physics*, vol. 4, no. 2, pp. 165 – 179, 1970.

[181] D. Smith, C. V. Goodall, N. G. Adams, and A. G. Dean, "Ion- and electron-density decay rates in afterglow plasmas of argon and argon-oxygen mixtures," *Journal of Physics B: Atomic and Molecular Physics*, vol. 3, no. 1, p. 34, 1970.

[182] R. A. Fluegge, "Ion–molecule reactions in alpha-particle-irradiated methane and water vapor," *The Journal of Chemical Physics*, vol. 50, no. 10, pp. 4373–4380, 1969.

[183] D. A. Kubose and W. H. Hamill, "Velocity dependence of ion-molecule reaction cross sections in a mass spectrometer," *Journal of the American Chemical Society*, vol. 85, no. 2, pp. 125–127, 1963.

[184] R. Stockbauer, "Threshold electron-photoion coincidence mass spectrometric study of CH_4, CD_4, C_2H_6, C_2D_6," *The Journal of Chemical Physics*, vol. 58, no. 9, pp. 3800–3815, 1973.

[185] A. Kramida, Y. Ralchenko, J. Reader, and N. Team, "NIST atomic spectra database (ver. 5.3)," 2016.

[186] Y. Zhao and D. Truhlar, "The M06 suite of density functionals for main group thermochemistry, thermochemical kinetics, noncovalent interactions, excited states, and transition elements: two new functionals and systematic testing of four M06-class functionals and 12 other functionals," *Theoretical Chemistry Accounts*, vol. 120, no. 1, p. 215–241, 2007.

[187] Y. Zhao and D. G. Truhlar, "How well can new-generation density functionals describe the energetics of bond-dissociation reactions producing radicals?," *Journal of Physical Chemistry A*, vol. 112, no. 6, p. 1095–1099, 2008.

[188] Y. Zhao and D. G. Truhlar, "Density functionals with broad applicability in chemistry," *Accounts of Chemical Research*, vol. 41, no. 2, p. 157–167, 2008.

[189] Y. Zhao and D. G. Truhlar, "Exploring the limit of accuracy of the global hybrid meta density functional for main-group thermochemistry, kinetics, and noncovalent interactions," *Journal of Chemical Theory and Computation*, vol. 4, no. 11, p. 1849–1868, 2008.

[190] W. Kohn and L. J. Sham, "Self-consistent equations including exchange and correlation effects," *Phys. Rev.*, vol. 140, pp. A1133–A1138, 1965.

[191] F. Jensen, *Introduction to Computational Chemistry*. Wiley, 2007.

[192] R. Parr and W. Yang, *Density-functional theory of atoms and molecules*. No. 3, John Wiley and Sons, Inc., 1989.

[193] P. Hohenberg and W. Kohn, "Inhomogeneous electron gas," *Phys. Rev.*, vol. 136, pp. B864–B871, 1964.

[194] R. Peverati and D. Truhlar, "Quest for a universal density functional: the accuracy of density functionals across a broad spectrum of databases in chemistry and physics," *Philosophical Transactions of the Royal Society a-Mathematical Physical and Engineering Sciences*, vol. 372, no. 2011, 2014.

[195] T. H. Dunning Jr., "Gaussian basis sets for use in correlated molecular calculations. I. the atoms boron through neon and hydrogen," *The Journal of Chemical Physics*, vol. 90, no. 2, pp. 1007–1023, 1989.

[196] R. A. Kendall, T. H. Dunning Jr., and R. J. Harrison, "Electron-affinities of the 1st-row atoms revisited - systematic basis-sets and wave-functions," *Journal of Chemical Physics*, vol. 96, no. 9, pp. 6796–6806, 1992.

[197] G. Garberoglio, *Dynamical properties of h-bonded liquids: a theoretical and computer simulation study*. PhD thesis, Department of Physics - University of Trento, 2001.

[198] M. Matsumoto and T. Nishimura, "Mersenne twister: A 623-dimensionally equidistributed uniform pseudo-random number generator," *ACM Trans. Model. Comput. Simul.*, vol. 8, pp. 3–30, Jan. 1998.

List of Publications

- A. Cernuto, D. Ascenzi, F. Pirani, L. M. Martini, P. Tosi, "The selective role of long range forces in the stereodynamics of ion-molecule reactions: The He^+ + methyl formate case from guided ion beam experiments", *ChemPhysChem*, DOI: 10.1002/cphc.201701096, 2017.
- A. Cernuto, A. Lopes, C. Romanzin, B. Cunha de Miranda, D. Ascenzi, P. Tosi, G. Tonachini, A. Maranzana, M. Polášek, J. Žabka, C. Alcaraz, "Effects of collision energy and vibrational excitation of CH_3^+", *J. Chem. Phys*, **147**, 154302, 2017.
- A. Cernuto, P. Tosi, L. M. Martini, F. Pirani, D. Ascenzi, "Experimental investigation of the reaction of helium ions with dimethyl ether: stereodinamics of the dissociative charge exchange process", *Physical Chemistry Chemical Physics*, **19**, 19554-19565, 2017.
- P. Fathi, W. D. Geppert, F. Lindén, A. Cernuto, D. Ascenzi, "Ion-neutral reaction of $C_2H_2N^+$ with CH_4: an experimental and theoretical study", *Molecular Astrophysics*, **5**, 9-22, 2016.

Acknowledgements

I acknowledge my tutor Prof. Daniela Ascenzi, my co-tutor Prof. Paolo Tosi, the referees (Prof. David Cappelletti and Prof. Antonio Aguilar Navarro) and Dr. Mario Scotoni. I also thank the whole FAM group and the collaborators, Prof. Fernando Pirani (UniPg), Dr. Giovanni Garberoglio (UniTn), Prof. Glauco Tonachini and Dr. Andrea Maranzana (UniTo).

Trento, 15 Novembre 2017

Sono passati poco più di tre anni e finalmente questa porente= si trentina è quasi vicina al termine.
Sono stati anni lunghi, segnati da qualche gioia e successo, ma anche da tanti pianti e ripensamenti.
È giunta quindi l'ora di ringraziare tutti coloro che sono stati fondamentali durante questo dottorato.

Sinceramente non posso che iniziare dalla FAMILY, cioè da Mamma, Papà e Chiara (più Domenico e il mio arrivato, il piccolo Alessandro), che, nonostante la lontananza, sono sempre riusciti a capire i miei stati d'animo, sostenendo= mi nel giusto e nel sbagliato.
Grazie soprattutto per avermi fatto capire che non ci avrei mai dubitato qualunque cosa avessi preso!

Non posso che continuare ringraziando la mia famiglia trentina. Grazie, quindi, a Emanuele, Marisa, Nadir e Samuele, che ogni giorno mi hanno ricordato quanto sia bella la vita, specialmente di fronte a uno SPRITZ!
Inoltre, grazie per avermi fatto da fratelli (e sorella) aggiuntivi e per essermi sempre preoccupati e presi cura di me: MANCHERETE DAVVERO!
Un ulteriore ringraziamento lo devo fare a Nadir, compagno di avventure, mangiate e bevute, maestro di Fisica e cultura TRASH, impagabile controparte in discussioni su scienza e su cavolate improbabili.

Immancabilmente devo ringraziare i colleghi (più amici che colleghi a dirla tutta), i quali hanno reso il lavoro in Dipartimento meno duro e monotono.
Cesare, Diana, Luca Matteo, Maddalena e Tatev, come avrei fatto senza di voi?
Un ringraziamento speciale va indubbiamente a Luca Matteo, per l'aiuto scientifico e "spirituale" che mi ha regalato nel corso di questi anni. Mi hai sostenuto e difeso anche quando le situazioni si sono fatte difficili e pesanti: grazie per aver creduto in me e per la fiducia e l'amicizia che mi hai dato. È giunta l'ora che anche tu ottenga ciò meglio, TE LO MERITI!!!

In ambito lavorativo vorrei ringraziare il Prof. Pirani, che, inconsapevolmente, non mi ha fatto perdere la speranza, rinnovando la mia passione nella Scienza e nella Scoperta.
Inoltre, voglio dire grazie ad Andrea M. e Gianni T. sempre pronti a darmi consigli da Torino.

Rimanendo sotto la Mole voglio dire grazie a tutti quegli amici che mi hanno sempre pensato! GRAZIE!

Infine, voglio ringraziare Jule, che da molto lontano è stata la più vicina nei momenti belli e brutti di questi tre anni. Grazie per avermi dato la forza di affrontare ogni nuova sfida; grazie per avermi sempre ricordato che non sarei mai stato solo nell'affrontare le difficoltà; grazie per non avermi mai fatto arrendere; grazie per non avermi fatto dimenticare di essere una "A" quando la fiducia in me stesso veniva messa a dura prova! Grazie per farmi amare sempre il buono in tutto e tutti. Grazie per rendermi migliore ogni giorno di più. ... E infine grazie per aver corretto il mio pessimo inglese!

Grazie a tutti,

Andrea